

**FINAL TECHNICAL REPORT**

**TARGET IDENTIFICATION AND DETECTION USING  
IMPULSE RADARS OR ULTRA-WIDEBAND RADARS**

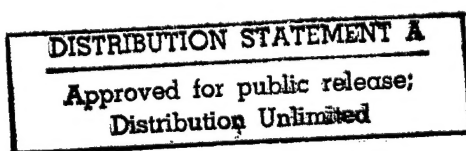
**Grant No. N00014-93-1-11272**

**Reporting period: September 1, 1993 - August 31, 1996**

**Prepared for  
Office of Naval Research  
Department of Navy**

**Kun-Mu Chen, Principal Investigator  
Dennis P. Nyquist, Co-Principal Investigator  
Edward J. Rothwell, Co-Principal Investigator**

**Division of Engineering Research  
Michigan State University  
East Lansing, MI 48824**



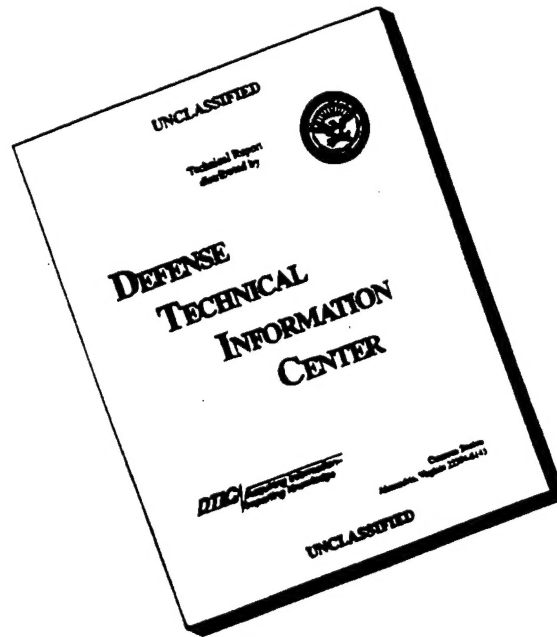
**DTIC QUALITY INSPECTED 4**

**19961016 016**

## REPORT DOCUMENTATION PAGE

1a. REPORT SECURITY CLASSIFICATION Unclassified			1b. RESTRICTIVE MARKINGS N/A	
2a. SECURITY CLASSIFICATION AUTHORITY N/A			3. DISTRIBUTION/AVAILABILITY OF REPORT Approved for public release distribution unlimited.	
2b. DECLASSIFICATION/DOWNGRADING SCHEDULE N/A				
4. PERFORMING ORGANIZATION REPORT NUMBER(S) N/A			5. MONITORING ORGANIZATION REPORT NUMBER(S)	
6a. NAME OF PERFORMING ORGANIZATION Division of Engineering Research Michigan State University		6b. OFFICE SYMBOL (If applicable)		7a. NAME OF MONITORING ORGANIZATION Office of Naval Research
6c. ADDRESS (City, State, and ZIP Code) East Lansing, MI 48824-1226			7b. ADDRESS (City, State, and ZIP Code) Ballstone Tower One 800 N. Quincy St. Arlington, VA 22217-	
8a. NAME OF FUNDING / SPONSORING ORGANIZATION Office of Naval Research		8b. OFFICE SYMBOL (If applicable) ONR		9. PROCUREMENT INSTRUMENT IDENTIFICATION NUMBER N00014-93-1-1272
8c. ADDRESS (City, State, and ZIP Code) Bellstone Tower One 800 N. Quincy St. Arlington, VA 22217-5660			10. SOURCE OF FUNDING NUMBERS	
			PROGRAM ELEMENT NO.	PROJECT NO.
11. TITLE (Include Security Classification) Target Identification and Detection Using Impulse Radars or Ultra-Wideband Radars				
12. PERSONAL AUTHOR(S) Kun-Mu Chen, Dennis P. Nyquist and Edward Rothwell				
13a. TYPE OF REPORT Final		13b. TIME COVERED FROM 9/1/93 TO 8/31/96		14. DATE OF REPORT (Year, Month, Day) 1996, 8, 31
15. PAGE COUNT 232				
16. SUPPLEMENTARY NOTATION				
17. COSATI CODES			18. SUBJECT TERMS (Continue on reverse if necessary and identify by block number) Ultra-wideband/short-pulse radar, Target detection and identification, sea clutter, E-pulse technique, neural network method, time-domain imaging.	
FIELD	GROUP	SUB-GROUP		
19. ABSTRACT (Continue on reverse if necessary and identify by block number) The objectives of this research program are to study the feasibility and to develop schemes for using an ultra-wideband or short-pulse (UWB/SP) reader to (1) detect a target in a sea clutter environment and (2) identify airborne targets. For the first topic, we have conducted a theoretical and experimental study of the transient scattering of a short pulse from sea surfaces of various models and the application of the E-pulse technique to detect a target flying above a disturbed sea surface. For the second topic, we have developed the schemes of target identification using the E-pulse technique, the neural network method, the time-domain imaging and some other related methods. This report summarizes many significant results which may be useful in the design of future UWB/SP radars.				
20. DISTRIBUTION/AVAILABILITY OF ABSTRACT <input checked="" type="checkbox"/> UNCLASSIFIED/UNLIMITED <input type="checkbox"/> SAME AS RPT. <input type="checkbox"/> DTIC USERS			21. ABSTRACT SECURITY CLASSIFICATION Unclassified	
22a. NAME OF RESPONSIBLE INDIVIDUAL Dr. William Miceli			22b. TELEPHONE (Include Area Code) (703) 696-0560	22c. OFFICE SYMBOL ONR (Code 4413)

# DISCLAIMER NOTICE



**THIS DOCUMENT IS BEST  
QUALITY AVAILABLE. THE  
COPY FURNISHED TO DTIC  
CONTAINED A SIGNIFICANT  
NUMBER OF PAGES WHICH DO  
NOT REPRODUCE LEGIBLY.**

## Table of Contents

1.	Introduction	p. 1
2.	Review of Accomplished Results	p. 1
2.1	Target detection in a sea clutter environment	p. 1
2.2	Identification of airborne targets	p. 2
2.3	Publications	p. 3
3.	Personnel	p. 6
4.	Future Plans	p. 6
5.	List of Appendices	p. 7
Appendix 1: Transient scattering of a short pulse from a conducting sinusoidal surface		
Appendix 2: Transient scattering from ocean surface models		
Appendix 3: Enhanced scattering of a target in a sea clutter environment using stepped, ultra-wideband signal and E-pulse clutter cancellation		
Appendix 4: A general E-pulse scheme arising from the dual early-time/late-time behavior of radar scatterers		
Appendix 5: A radar target discrimination scheme using the discrete wavelet transform for reduced data storage		
Appendix 6: Scattering center analysis of radar targets using fitting scheme and genetic algorithm		
Appendix 7: Target discrimination using neural networks with time domain or spectrum magnitude response		
Appendix 8: Time-domain imaging of airborne targets using ultra-wideband or short-pulse radar		
Appendix 9: Time-domain imaging of radar targets using short pulse radars and algorithm for reconstruction from projections		
Appendix 10: Radar identification and detection using ultra-wideband/short-pulse radars		
Appendix 11: Measurement and processing of scattered ultra-wideband/short-pulse signals		
Appendix 12: Ultra-wideband/short-pulse radar for target identification and direction -- Laboratory study		



## 1. Introduction

This is the final technical report for the research program on "Target identification and detection using impulse radars or ultra-wideband radars," supported by the Office of Naval Research under Grant N00014-93-1-1272. This grant consisted of two regular research grants and one ASSERT grant and covered the period of September 1, 1993 to August 31, 1996.

The objectives of this research program were to study the feasibility and to develop schemes for using an ultra-wideband or short-pulse (UWB/SP) radar to (1) detect a target in a sea clutter environment with the E-pulse technique and (2) identify airborne targets with the time-domain imaging, the E-pulse technique or the neural network method. Over the past three years, we have produced a great deal of significant results that were published in the forms of three technical reports, five progress reports and a number of technical journal and conference papers. However, we still have two unfinished studies in the areas of the E-pulse techniques for detecting a target in a sea clutter environment and the time-domain imaging for identifying the target. We plan to continue these studies in the future, hopefully under a new ONR support.

In this report, we will summarize the research results by referring to the published technical reports, appendixing the published technical papers or presenting the study results still in progress.

Overall, we feel that we have produced many significant results which will be useful in the design of future UWB/SP radars.

## 2. Review of Accomplished Results

### 2.1 Target Detection in a Sea Clutter Environment

Two major studies on this topic are (1) the theoretical and experimental study of the transient scattering of a short pulse from sea surfaces of various models, and (2) the application of the E-pulse technique to detect a target flying above a disturbed sea surface.

The first study was completed and the results were reported in Technical Report No. 3 (281 pages) and also published in two journal papers given in Appendices 1 and 2. The second study is still in progress and some up to date results are reported in Appendix 3.

## 2.2 Identification of Airborne Targets

We have conducted three major studies on this topic. They are (1) the target identification using the E-pulse technique and other related schemes, (2) the target identification using the neural network method, and (3) the target identification using the time-domain imaging.

The first study was completed and results were reported in Technical Report No. 1 (296 pages) and also published in three journal papers given in Appendices 4, 5 and 6.

The second study was also completed and the results were reported in Technical Report No. 2 (302 pages) and also published in a journal paper as given in Appendix 7.

The third study on the time-domain imaging is still in progress. The results on the two-dimensional time-domain imaging based on physical optics were published in a journal paper given in Appendix 8, while the three-dimensional time-domain imaging is still under study and some results are given in Appendix 9.

During the past three years, we have also published three papers reporting other study results generated under this research grant. These papers are included in Appendices 10, 11 and 12.

It is noted that Technical Reports 1, 2 and 3 were prepared from Ph.D. theses submitted by Dr. Qing Li, Dr. C.Y. Tsai and Dr. Adam Norman, respectively.

## 2.3 Publications

The following papers reporting the results of this research program have been published in Journals, books or in conferences.

### Papers in Journals and books

1. E.J. Rothwell, K.M. Chen, D.P. Nyquist, J. Ross and R. Bebermeyer, "A radar target discrimination scheme using the discrete wavelet transform for reduced data storage," IEEE Trans. on Antennas and Propagation, vol. 42, no. 7, pp. 1034-1037, July 1994.
2. E.J. Rothwell, K.M. Chen, D.P. Nyquist, P. Ilavarasan, R. Bebermeyer, and Q. Li, "A general E-pulse scheme arising from the dual early-time/late-time behavior of random scatterers," IEEE Trans. on Antennas and Propagation, vol. 42, no. 9, pp. 1336-1341, September 1994.
3. E. Rothwell, K.M. Chen, D.P. Nyquist and J. Ross, "Time-domain imaging of airborne targets using ultra-wideband or short-pulse radar," IEEE Trans. on Antennas and Propagation, vol. 43, No. 3, pp. 327-329, March 1995.
4. K.M. Chen et al, "Radar identification and detection using ultra-wideband/short-pulse radar," proceedings of ultra-wideband, short-pulse electromagnetics 2, pp. 535-542, Edited by L. Carin and L.B. Felsen, Plenum Press, New York, 1995.
5. E. Rothwell, K.M. Chen, D.P. Nyquist, J. Ross and Robert Bebermeyer, "Measurement and processings of scattered ultra-wideband/short-pulse signals," proceedings of SPIE Conference on Radar/Ladar processing and Applications, vol. 2562, pp. 138-149, published by the International Society of Optical Engineering, Box 10, Bellingham, Washington, 98227.
6. K.M. Chen et al, "Ultra-wideband/short-pulse radar for target identification and detection - Laboratory study," Record of IEEE 1995 International Radar Conference, pp. 450-455, 1995.
7. Qing Li, E. Rothwell, K.M. Chen and D.P. Nyquist, "Scattering center analysis of radar targets using fitting scheme and genetic algorithm," IEEE Trans. on Antennas and Propagation, vol. 44, No. 2, pp. 198-207, Feb. 1996.
8. C.Y. Tsai, E. Rothwell and K.M. Chen, "Target discrimination using neural network with time domain and spectrum magnitude response," J. of Electromagnetic Waves and Applications, vol. 10, No. 3, pp. 341-382, 1996.

9. A. Norman, D.P. Nyquist, E. Rothwell, K.M. Chen, J. Ross and P. Ilavarasan, "Transient scattering of a short-pulse from a conducting sinusoidal surface," J. of Electromagnetic Waves and Propagations, vol. 10, No. 4, pp. 461-487, 1996.

#### Conference Papers

1. K.M. Chen, E.J. Rothwell, D.P. Nyquist, J. Ross, P. Ilavarasan, Q. Li, C.Y. Tsai, and A. Norman, "Radar identification and detection using ultra-wideband/short-pulse radars," presented at the Second International Conference on Ultra-wideband, short-pulse electromagnetics, Polytechnic University, New York, April 5-7, 1994.
2. A. Norman, J. Song, D.P. Nyquist, J. Ross, P. Ilavarasan, M. Seneski, K.M. Chen and E.J. Rothwell, "Scattering of transient radiation from an imperfectly-conducting infinite periodic sea surface," presented at the 1994 IEEE/AP-S International Symposium, University of Washington, Seattle, June 19-24, 1994.
3. R. Bebermeyer, J. Ross, E.J. Rothwell, K.M. Chen, D.P. Nyquist, Polarization diversity for reduction of scattering from spatially periodic perfectly conducting surfaces," presented at the 1994 IEEE-APS International Symposium, University of Washington, Seattle, June 19-24, 1994.
4. Q. Li, E.J. Rothwell, K.M. Chen, D.P. Nyquist, J. Ross, and R. Bebermeyer, "Determination of radar target scattering center transfer function from measured data," presented at the 1994 IEEE-APS International Symposium, University of Washington, Seattle, June 19-24, 1994.
5. P. Ilavarasan, E.J. Rothwell, R. Bebermeyer, K.M. Chen, and D.P. Nyquist, "Natural resonance extraction from multiple data sets using a genetic algorithm," presented at the IEEE-APS International Symposium, University of Washington, Seattle, June 19-24, 1994.
6. C.Y. Tsai, K.M. Chen, and E.J. Rothwell, "Radar target discrimination using recurrent dynamic memory and noise tolerant multi-layer feedforward back propagation neural networks," presented at the 1994 URSI Radio Science Meeting, University of Washington, Seattle, June 19-24, 1994.
7. Q. Li, E.J. Rothwell, K.M. Chen, and D.P. Nyquist, "Data storage techniques for use in correlation based early-time radar target discrimination," presented at 1994 URSI Radio Science Meeting, University of Washington, Seattle, June 19-24, 1994.
8. J. Ross, R. Bebermeyer, E.J. Rothwell, K.M. Chen, and D.P. Nyquist, "Aspect angle sensitivity of ultra-wideband target scattering data," presented at the 1994

URSI Radio Science Meeting, University of Washington, Seattle, June 19-24, 1994.

9. K.M. Chen, E.J. Rothwell, D.P. Nyquist, R. Bebermeyer, Q. Li, C.Y. Tsai and A. Norman, "Ultra-wideband/short-pulse radar for target identification and detection-Laboratory study," presented at IEEE International Radar Conference Alexandria, Virginia, May 8-11, 1995.
10. A. Norman, D.P. Nyquist, E.J. Rothwell and K.M. Chen, "Transient scattering from a periodic sea surface," presented at 1995 IEEE/APS and Radio Science International Symposium, Newport Beach, California, June 18-23, 1995.
11. Y. Dai, E.J. Rothwell, D.P. Nyquist and K.M. Chen, "Time-domain imaging of radar target using ultra-wideband or short pulse radar," presented at 1995 IEEE/APS and Radio Science International Symposium, Newport Beach, California, June 18-23, 1995.
12. G. Wallinga, E.J. Rothwell, D.P. Nyquist, K.M. Chen and A. Norman, "Enhanced detection of radar targets in a realistic sea clutter environment using E-pulse clutter cancellation," present at 1995 IEEE/APS and Radio Science International Symposium, Newport Beach, California, June 18-23, 1995.
13. K.M. Chen, E.J. Rothwell, D.P. Nyquist, J. Ross and R. Bebermeyer, "Measurement and processing of scattered ultrawide-band/short-pulse signals," presented at SPIE's 1995 International Symposium, San Diego, CA, July 9-14, 1995.

### 3. Personnel

The following personnel participated in this research program:

1. Kun-Mu Chen, Richard M. Hong Professor of Electrical Engineering, Principal Investigator
2. Dennis P. Nyquist, Professor of Electrical Engineering, Co-Principal Investigator
3. Edward J. Rothwell, Associate Professor of Electrical Engineering, Co-Principal Investigator
4. Adam Norman, Graduate Assistant, graduated in 1996 with a Ph.D. degree
5. Qing Li, Graduate Assistant, graduated in 1995 with a Ph.D. degree
6. C.Y. Tsai, Graduate Assistant, graduated in 1995 with a Ph.D. degree
7. Robert Bebermeyer, Graduate Assistant, graduated in 1994 with a M.S. degree
8. Glen Wallinga, Graduate Assistant, a Ph.D. candidate
9. Y.C. Dai, Graduate Assistant, a Ph.D. candidate
10. Keven Brown, Undergraduate Assistant
11. Mark Seneski, Undergraduate Assistant

It is noted that Adam Norman, Robert Bebermeyer and Glen Wallinga were supported by the ASSERT grant. Adam Norman graduated recently with a Ph.D. degree and will be working for the Naval Underwater Systems Center in Newport, RI in the near future. Robert Bebermeyer graduated with a M.S. degree and is working for the Department of Navy. Glen Wallinga is in the final year of his Ph.D. program. Also the ASSERT grant partially supported two undergraduate students, Keven Brown and Mark Seneski, for their participation in this research program.

### 4. Future Plans

We plan to continue the two unfinished studies on the target detection in a sea clutter environment using the E-pulse technique and on the target identification using three-dimensional time-domain imaging. Hopefully, a new ONR grant will be available to us in the future. If this is the case, we can initiate some new topics in addition to finishing the two unfinished studies.

## 5. List of Appendices

- Appendix 1: Transient scattering of a short pulse from a conducting sinusoidal surface
- Appendix 2: Transient scattering from ocean surface models
- Appendix 3: Enhanced scattering of a target in a sea clutter environment using stepped, ultra-wideband signal and E-pulse clutter cancellation
- Appendix 4: A general E-pulse scheme arising from the dual early-time/late-time behavior of radar scatterers
- Appendix 5: A radar target discrimination scheme using the discrete wavelet transform for reduced data storage
- Appendix 6: Scattering center analysis of radar targets using fitting scheme and genetic algorithm
- Appendix 7: Target discrimination using neural networks with time domain or spectrum magnitude response
- Appendix 8: Time-domain imaging of airborne targets using ultra-wideband or short-pulse radar
- Appendix 9: Time-domain imaging of radar targets using short pulse radars and algorithm for reconstruction from projections
- Appendix 10: Radar identification and detection using ultra-wideband/short-pulse radars
- Appendix 11: Measurement and processing of scattered ultra-wideband/short-pulse signals
- Appendix 12: Ultra-wideband/short-pulse radar for target identification and direction -- Laboratory study

## Appendix 1

*Journal of Electromagnetic Waves and Applications, Vol. 10, No. 4, 461-487, 1996*

### Transient scattering of a short pulse from a conducting sinusoidal surface

A. Norman, D. Nyquist, E. Rothwell, K. M. Chen, J. Ross, and P. Ilavarasan

Department of Electrical Engineering  
Michigan State University  
E. Lansing, MI 48824, USA

**Abstract**—A study on the transient scattering of a short EM pulse from a conducting sinusoidal surface which simulates a sea surface has been conducted. Theoretical analyses were performed for an infinite sinusoidal surface as well as a finite sinusoidal surface for both TE and TM polarized illuminations. A series of experiments was also conducted on a finite sinusoidal surface model to verify the theory. There are some interesting observations due to cut-off and band-pass phenomena of the Floquet modes excited in the periodic surface. It is shown theoretically and experimentally that the backscattered response of a short EM pulse from a conducting sinusoidal surface is a series of periodic peaks representing the reflections of the pulse from the crests of the surface.

#### I. INTRODUCTION

With the advent of Ultra-Wide Band/Short Pulse (UWB/SP) radar, additional studies are needed to gain new insights into the scattering of transient electromagnetic waves from targets in various environments. A two-dimensional perfectly conducting (PEC) sinusoid acting as a scatterer is one such environment. The scattering of continuous wave (CW) radiation from a perfectly conducting (PEC) sinusoidal surface has been analyzed by many authors, but transient scattering of UWB/SP radar signal from such a surface warrants further investigation. Few authors have produced results on transient scattering [19,21], but many have investigated the CW scattering problem [1-17,22-28]. One of the reasons for such a great interest in this problem is that the PEC sinusoidal surface provides an approximation to a sea surface.

Both finite and infinite PEC sinusoidal surfaces will be considered. In addition to theoretical results for both cases experimental results have also been obtained for the finite surface. Our approach will include two different polarization states (TE and TM) and will utilize an Integral Equation (IE) type formulation in conjunction with the Method of Moments. The infinite surface can also be analyzed more classically using the Rayleigh hypothesis, and results from this method will be included as a confirmation of the IE method. Both methods yield frequency domain solutions, therefore the transient results will be synthesized using the inverse Fourier transform (IFT).



Due to the periodicity of the infinite surface the analysis techniques for this surface are centered around Floquet's Theorem. The Rayleigh hypothesis method directly utilizes the theorem to expand the scattered fields, in the IE method the periodicity is embedded in the periodic Green's function. The infinite spatial extent of the surface can therefore be reduced to just one period. This truncation solves one problem (infinite surface), but it creates another problem in convergence [29]. The convergence problem of the PGF is accentuated for shallow (low height) sinusoids, this is one reason for the inclusion of the Rayleigh hypothesis method. The two methods also serve a check against each other.

Research directed towards the finite surface has not been as active as the infinite surface, this is due in part to the strictly numerical nature of the problem, and the lack of apparent applications (sea surface, gratings, etc. can usually be considered infinite for most purposes). There are a few authors examining this and similar problems [21,26,27].

New insights are gained regarding the nature of scattering from a PEC periodic surface. For both TE and TM polarizations, the forward and backscattered time and spectral domain fields are calculated. For the backscatter case, which is of primary interest for many applications (sea clutter, etc) the results exhibit a periodic return of pulses dependent upon the period of the surface. Experimental results help to verify some of the theoretical findings.

## II. TE SCATTERING FROM CONDUCTING SINUSOIDAL SURFACE

Scattering of a plane wave with transversely polarized electric field [ $E_y$ ] as indicated in Fig. 1 is analyzed in the spectral domain. To simplify the problem the surface will be invariant along the  $y$ -direction. As stressed earlier the transient response is to be obtained; this can be accomplished by utilizing the IFT on spectral results of appropriate bandwidth.

### II.1 Infinite PEC Surface

The classical method known as the Rayleigh hypothesis can be applied to this problem. Combining that with Floquet's Theorem to represent the scattered field yields a set of linear equations. The incident and scattered electric fields can be represented by

$$E_i(x, z) = A_0 e^{-j(\beta x - qz)} \quad (1)$$

$$E_s(x, z) = \sum_{n=-\infty}^{\infty} e^{-j\beta_n x} f_n(z) \quad (2)$$

where  $\beta = k \sin \theta_i$ ,  $q = k \cos \theta_i$ ,  $\beta_n = \beta + 2n\pi/L$ , and Floquet's Theorem has been utilized in (2).

Subjecting the fields to the homogeneous Helmholtz equation, and noting the simple periodic  $x$ -dependence, a set of differential equations for  $f_n(z)$  can be obtained. Upon solving these equations the Rayleigh hypothesis is invoked, leaving only one unknown for each Floquet mode. Application of the boundary condition at the conducting surface and using Galerkin's method provide the linear

equations needed to solve for the unknown Floquet mode coefficients. In order to utilize the Rayleigh hypothesis a restriction on the surface slope of the conductor must be met. That is, the surface should be smooth with no slope greater than 0.448. This limits the usefulness of this technique.

### II.1.1 EFIE-MoM Analysis

A more rigorous and general treatment for the scattering of plane waves from a PEC periodic surface, in which the surface need not be sinusoidal (or smooth) has been developed. An integral-operator-based analysis has been employed for this analysis, and will be referred to as EFIE-MoM method. The currents induced on the PEC surface are calculated as solutions to an EFIE with a periodic Green's-function (PGF) kernel. With the surface currents known, it is then possible to determine the scattered fields once again making use of the PGF.

The same notation and configuration as employed for the Floquet mode-matching method will be used in the EFIE-MoM treatment. The scattered field can be solved for in the usual manner, once the induced surface currents are determined, as

$$E_s(x, z) = -jk\eta \int_{C_p} K_y(x', z') G(x, z|x', z') dl' \quad (3)$$

where  $K_y(x, z)$  is the unknown surface current and is the PGF given by [20]

$$G(x, z|x', z') = -\frac{j}{2L} \sum_{n=-\infty}^{\infty} \frac{e^{-j\beta_n(x-x')} e^{-jq_n|z-z'|}}{q_n} \quad (4)$$

The PGF innately accommodates the periodicity of the scattered field and therefore the integral in (3) need only be performed over one period of the surface. Of note in the equations above is the branch cut associated with  $q_n = \sqrt{k^2 - \beta_n^2}$ , by enforcing  $\Im\{q_n\} < 0$  an interesting cut-off phenomenon is created, this will be looked at later in Section IV. An IE for the induced surface current must be solved (via MoM), in order to calculate the field (3). The integral equation for  $K_y(x, z)$  is obtained by enforcing the boundary condition on the surface,

$$\int_{C_p} K_y(x', z') G(x, z|x', z') dl' = \frac{A_0}{j\omega\mu} e^{-j\beta x} e^{jqz} \quad \dots \quad \forall (x, z) \in C_p \quad (5)$$

A MoM numerical solution is implemented by expanding the unknown current  $K_y(x, z)$  in a pulse basis set and point matching on the first surface period  $C_p$ .

There are a number of interesting phenomena associated with this infinite case, both in the frequency and the time domains, and these are discussed in the results section.

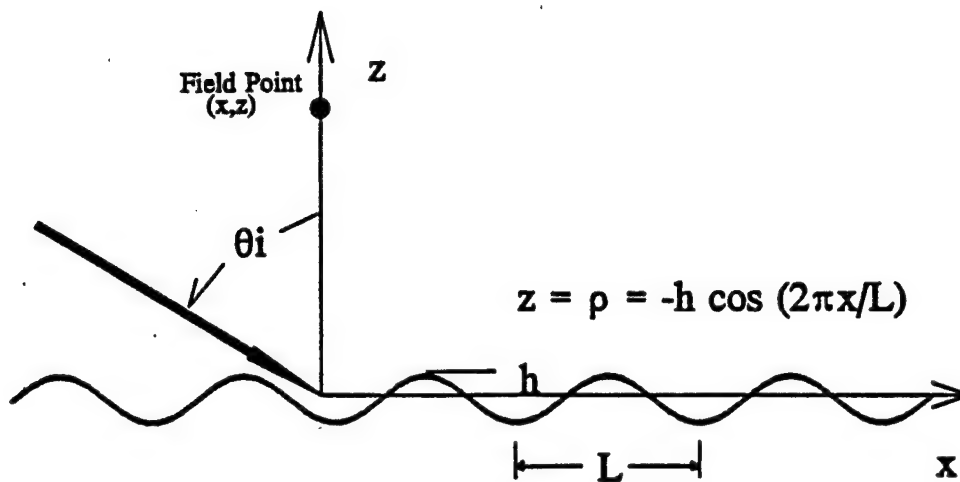


Figure 1a. Infinite, conducting sinusoidal surface scattering geometry.

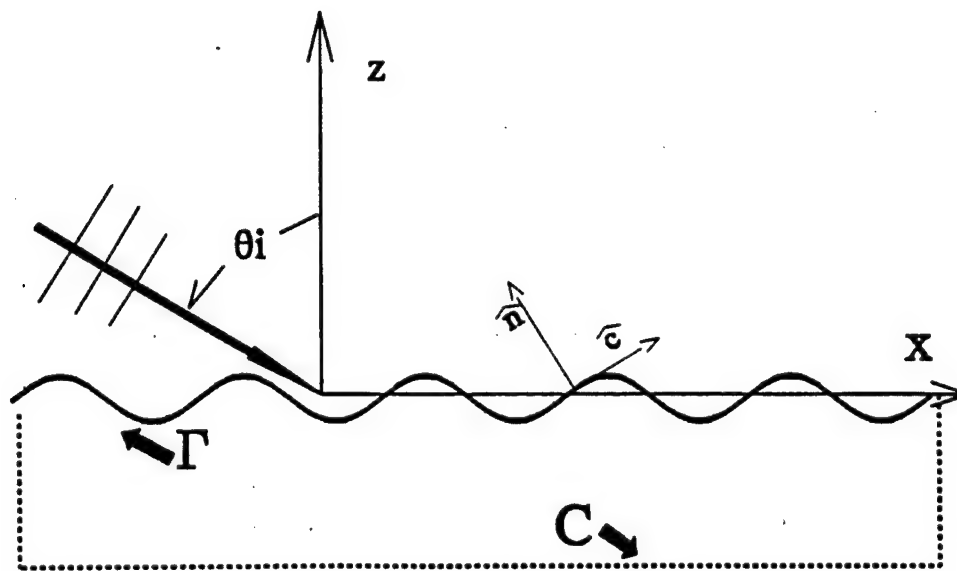


Figure 1b. Finite, conducting sinusoidal surface scattering geometry.

## II.2 TE Scattering from a Finite Conducting Surface

This section is devoted to describing the MoM solution to the EFIE for surface currents required to calculate the fields scattered from a finite-sized, two-dimensional PEC surface. There are no restrictions to the surface curvature (i.e. no slope limitations) the physical size of the scatterer is limited only by numerical consequences (memory, and cpu time); this is due to the fact that the entire surface must be partitioned not just one period as in the PGF case.

The general approach is very similar to the infinite-surface case, in that an IE for the induced surface current must be solved prior to the typical determination

of the scattered field using the 2-D free space Green's function. The configuration and the nomenclature is the same as the infinite case except that the surface is truncated as in Fig. 1b. Since the E-field is polarized transversely, the induced surface current is also only transversely directed as  $\vec{K}(x, z) = \hat{y}K_y(x, z)$ . This current then can be used to find the scattered E-field [18]

$$E_s(x, z) = -\hat{y}\frac{\omega\mu_0}{4}\int_{\Gamma} K_y(x', z')H_0^{(2)}(k|\vec{p}-\vec{p}'|)dl' \quad (6)$$

where  $\vec{p}$  is the position vector in the x-z plane,  $\Gamma$  describes the contour of the surface, and  $H_0^{(2)}$  is the second kind Hankel function of order zero.

To obtain an integral equation for the currents, the boundary condition on the electric field is applied on the conductor surface. Substituting the scattered field into boundary condition equation yields the integral equation for the unknown surface current distribution  $K_y(x, z)$  as

$$\int_{\Gamma} K_y(x', z')H_0^{(2)}(k|\vec{p}-\vec{p}'|)dl' = \frac{4}{k\eta}A_0e^{-j\beta x}e^{jqz} \quad (7)$$

A MoM numerical solution is then implemented to solve the above integral equation. The current is expanded in a set of pulse basis functions and point matching is implemented. This results in a square matrix equation for the unknown current coefficients. In typical fashion the scattered field (6) can be determined numerically subsequent to evaluating the induced currents. For a far-zone scattered field, the asymptotic form of the Hankel function can be used to simplify the numerical integration [18]. Results comparing both cases are provided, and in addition direct comparisons with experimental results can be made, because the finite surface is physically realizable.

### III. TM POLARIZATION

The configuration for this polarization state is the same [see Fig. 1a] except the H-field is now directed transversely as  $\vec{H}(x, z) = \hat{y}H_y(x, z)$  with the E-field parallel to the plane of incidence. Therefore by using  $H_y(x, z)$  as the generating function in the same fashion as  $E_y(x, z)$  was used for the TE polarization, similar analysis techniques may be employed. The electric field components can be found simply utilizing Maxwell's equations for this two-dimensional problem. The infinite PEC surface will be considered first, and once again it is possible to utilize the Rayleigh hypothesis for an adequately shallow sinusoidal surface, while a magnetic field integral equation (MFIE) will be developed for the infinite case.

#### III.1. MFIE-MoM

The scattering of TM polarized plane waves by a perfectly conducting, periodic surface can also be analyzed using an integral-operator-based method. The governing integral equation is in terms of the unknown H-field at the PEC surface, and the kernel consists of the normal derivative of the periodic Green's function

$$\frac{H(x, z)}{2} - PV \int_{C_p} H(x', z') \frac{\partial G(x, z|x', z')}{\partial n'} dl' = H_i(x, z) \quad \dots \forall (x, z) \in C_p \quad (8)$$

where the PGF  $G(x, z|x', z')$  is given by (4), and  $H_i(x, z)$  is the incident plane wave. The notation  $PV$  indicates that the integral must be evaluated in the principal-value sense. The integration path  $C_p$  is one period of the surface, as justified in the Section II.1, because the PGF accounts for the inherent periodicity of the solution.

Subsequent to the solution of the MFIE (8) for the surface fields, the scattered fields away from the surface can be calculated in the usual manner as,

$$H_s(x, z) = \int_{C_p} H(x', z') \frac{\partial G(x, z|x', z')}{\partial n'} dl' \quad (9)$$

A MoM numerical solution is implemented by expanding the unknown surface magnetic field  $H(x, z)$ , in a pulse-function basis set and point matching the MFIE at  $N$  points on the first surface period. Results and comparisons are presented in Section V.

### III.2. TM Finite Surface Scattering

The analysis for the TM plane wave scattering from a finite PEC sinusoidal surface, follows closely to techniques employed for the other integral-operator methods. Considering the geometry in Fig. 1b with an incident H-field in the transverse direction, the scattered H-field can be determined, if the induced surface fields are known,

$$H_s(x, z) = \frac{j}{4} \int_C \vec{K}_s(x', z') \times \nabla H_0^{(2)}(kR) dc' \quad (10)$$

The contour needed for the MFIE is a closed contour and is denoted by  $C$ , and  $\hat{c}$  is the unit vector tangential to the surface. The induced surface current  $\vec{K}_s(x, z)$  can be rewritten as  $\hat{c}(x, z)K_c(x, z)$  and the gradient of the second kind Hankel function can be evaluated (note  $R$  is distance between source and observation points) yielding,

$$H_s(x, z) = \frac{jk}{4} \int_C K_c(x', z') H_1^{(2)}(kR) [\hat{c}' \times \hat{R}] dc' \quad (11)$$

In order to determine the induced current a MFIE is implicated of the form

$$\frac{K_c(x, z)}{2} + \frac{jk}{4} PV \int_C K_c(x', z') H_1^{(2)}(kR) [\hat{c}(x', z') \times \hat{R}] dc' = H_i(x, z) \dots \forall (x, z) \in C \quad (12)$$

where the boundary condition on the tangential H-field has been applied.

A MoM numerical solution is then implemented to solve the above integral equation. The current is expanded in a set of pulse basis functions and point matching is implemented. This results in a square matrix equation for the unknown currents coefficients. The scattered fields (10) can numerically be determined subsequent to performing the MoM numerical solution to the induced surface currents.

### IV. CUT-OFF FREQUENCY PHENOMENA

As alluded to in the previous sections, an interesting cut-off phenomena is associated with the scattered fields of the infinite periodic surface. The scattered

Floquet modes from the infinite surface become evanescent in nature if  $|\beta_n| > k$ , there will be no real power flow away from the surface for such modes. This results in a cut-off frequency for each Floquet mode given as

$$(f_c)_n = \frac{|n|c}{L(1 + \sin \theta_i)} \quad (13)$$

The  $n = 0$  mode (the specular reflection) has no low frequency cutoff, but all the other Floquet modes will exhibit a low frequency cut-off. As more Floquet modes begin to propagate and carry real power, an interference pattern is generated in the spectrum.

Also associated with the cut-off frequency is a maximal frequency for backscattered waves. For a Floquet mode to propagate backwards (-x direction)  $\beta_n < 0$ , and also the mode must be above cut-off frequency. Therefore, there exists a range of frequencies in which backward traveling Floquet modes can propagate. The maximal frequency is given by

$$(f_{\max})_n = \frac{|n|c}{L \sin \theta_i} \quad (14)$$

Of note in the above equations is the lack of dependence on surface shape or height, only the period of the surface and incidence angle are involved. For  $L=0.1016$  m, and an incidence angle of  $85^\circ$  a table of maximal and cut-off frequency for the backward traveling Floquet modes has been provided, in Table 1. These phenomena as applied to results are discussed in the next section.

$n$	$(f_c)_n$ GHz	$(f_{\max})_n$ GHz
-1	1.479	2.964
-2	2.958	5.928
-3	4.438	8.892
-4	5.916	11.86
-5	7.395	14.82

Table 1. Low frequency cutoff and maximal frequency of backward Floquet modes.  $L = .1016$  m,  $85^\circ$  incidence angle.

## V. RESULTS AND EXPERIMENTS

We are interested in the transient scattered field response of a sinusoidal surface. This can be obtained via a Fourier synthesis of the frequency domain results from the previous sections. Much physical insight is provided in the time domain that is not available in the frequency domain.

The goal of the study is to not only understand the transient scattering from both types of surfaces, but to make a connection between the two. This connection will serve as link between the experimental results for the finite surface to the hypothetical experimental results from an infinite surface. The theoretical finite

surface scattering and the experimental finite surface results can be directly compared, then the theoretical finite and infinite surfaces can be compared in order to establish this link.

### V.1 Infinite Surface Results

Two methods of analysis were employed for the infinite surface, the Floquet mode-matching and the integral equation (IE) method. As stated in the previous sections these methods have overlapping regimes of validity. The Floquet mode regime is limited by the surface slope being less than .448, meaning fairly smooth surfaces, this restriction should be strictly enforced for the near-zone fields, however we have noted that the far-zone fields are less effected by this restriction. Extending the Rayleigh hypothesis regime is not the subject of this paper so we will stay within the strict limit set. The IE method has no theoretical limits on surface slope or period length, but there are computational limits, such as matrix size, and matrix ill-conditioning.

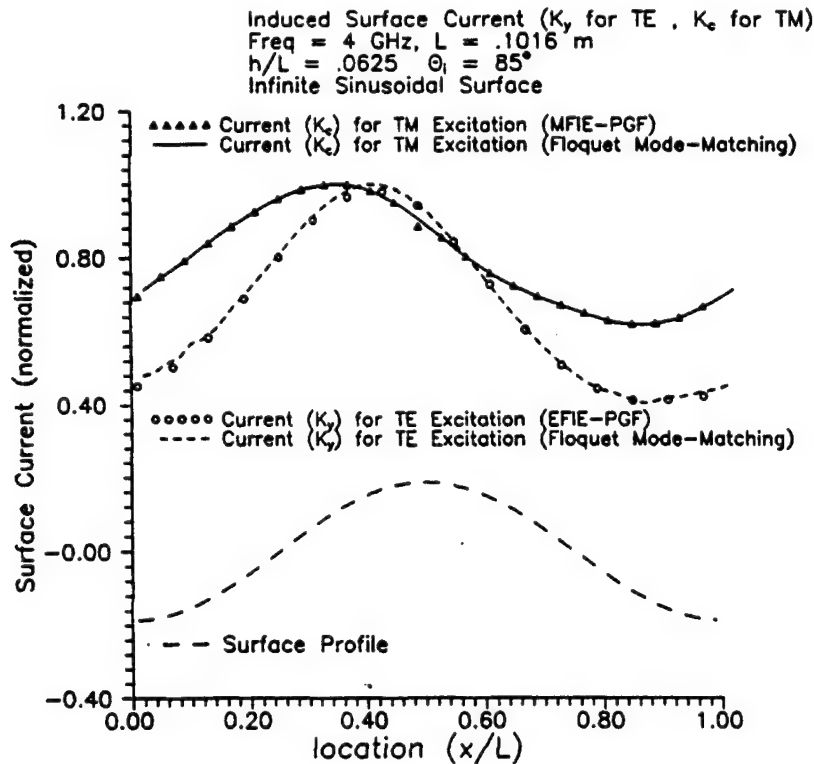


**Figure 2.** Induced surface current on one period of infinite, conducting sinusoidal surface for TE and TM excitation at 4 GHz.

The induced surface currents on one period of the infinite, conducting sinusoidal surface excited by a TE plane wave of 4 GHz at an incidence angle of  $85^\circ$  (near grazing) is shown in Fig. 2. The sinusoidal surface has a period length ( $L$ ) of .1016m which is chosen to match that of the experimentally constructed surface model. In this figure the 'shadowing effect' is observed and the current is maximum in front of the crest of the sinusoidal surface ( the plane wave is incident

from the left). The height ( $h$ ) of the sinusoidal surface is chosen to be  $h/L = .0625$  so that both analytical methods can be applied. In effect, they produced almost identical results as seen in the figure. Figure 2 also shows the corresponding induced surface current excited by a TM plane wave of the same frequency and incident angle on the same surface. It is noted that the induced current in the TM case is in the direction ( $\hat{c}$ ) tangential to the sinusoidal surface. The same 'shadowing effect' is observed for the TM case also.

The spectral domain scattered fields from a conducting sinusoidal surface ( $L=0.1016\text{m}$ ,  $h/L=0.03565$ ) generated by a TE plane wave with an incidence angle of  $85^\circ$  are calculated at an off-surface field point ( $x/L=0$ ,  $z/L=20$ ) as a function of frequency over the bandwidth of 1-7 GHz. The spectral amplitudes of the total scattered field are computed by summing all the Floquet modes and the result is shown in Fig. 3. The spectral amplitude of the backscattered field is computed by summing all Floquet modes propagating in the negative  $x$ -direction, and the result is shown in Fig. 4. There are some interesting phenomena in these results. First, there are the cut-off and band-pass phenomena for the backscattered field as discussed in Section IV. Also of note are the apparent nulls in the frequency domain of the total scattered field, demonstrating the frequency selectivity of the surface. The results shown in Figs. 3 and 4, are produced by the Floquet mode-matching and IE methods, and they give almost identical results.

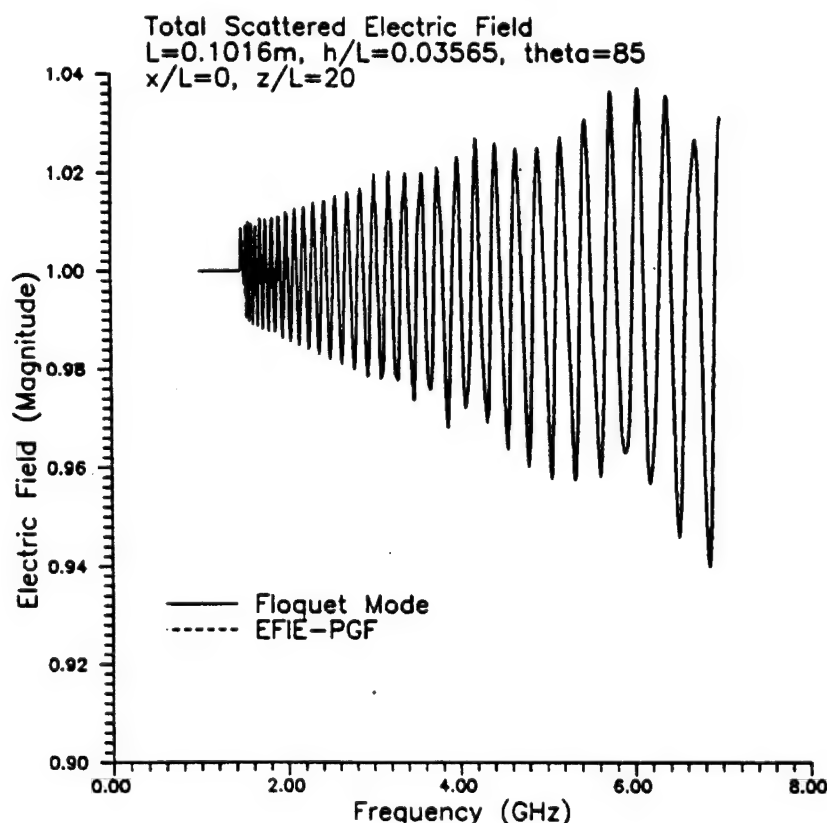


**Figure 3.** Magnitude of total scattered electric field from infinite, conducting sinusoidal surface as a function of frequency for TE excitation.



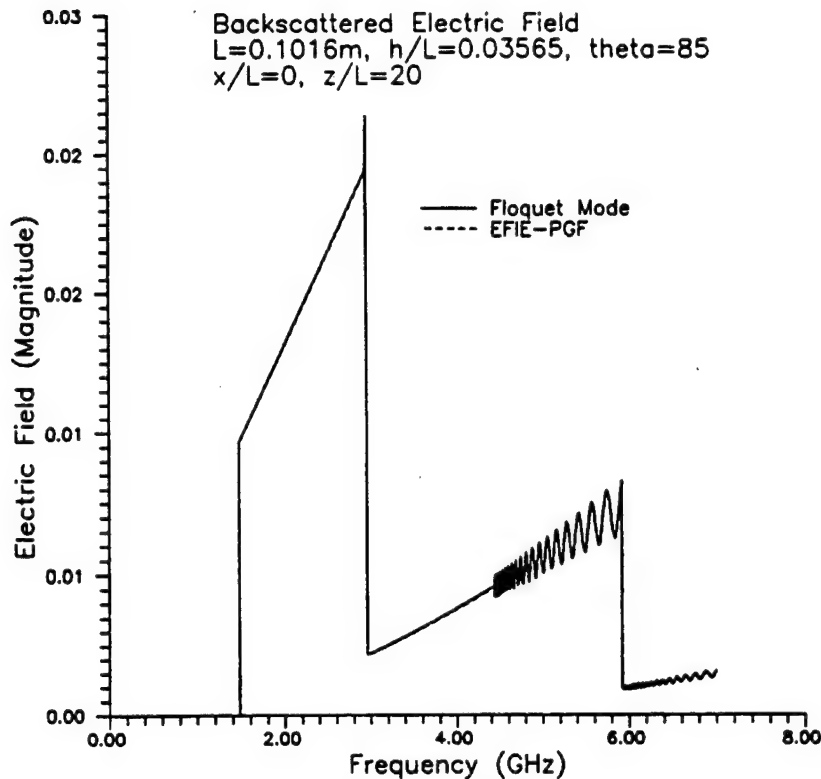


**Figure 4.** Magnitude of backscattered electric field from infinite, conducting sinusoidal surface for TE excitation as a function of frequency.

To find the time-domain, transient scattered field from the conducting sinusoidal surface created by a short pulse, the spectral results of the scattered field are inversely Fourier transformed. The short pulse used in this study is synthesized by inverting a uniform spectral response over a bandwidth of 1-7 GHz with a  $1/8$  cosine taper or a Gaussian Modulated Cosine (GMC) windowings. The shapes of these two short pulses are shown in Fig. 5. Consequently, the time-domain, transient scattered fields created by the short pulse can be obtained by inversely Fourier transforming the spectral results for the scattered field shown in Figs. 3 and 4 with the same windowing. The total scattered transient field created by a short pulse consists of large specular reflection followed by a small non-specular reflection after a time delay, as shown in Fig. 6. For various incidence angles this time delay has been seen to change (see Figure 7). The non-specular reflections are stationary for the various incidence angles. This is because the reflections all originate from directly below the field point and are in fact backscatter. The specular reflection is similar to that generated by a flat surface, although not all the energy is reflected.

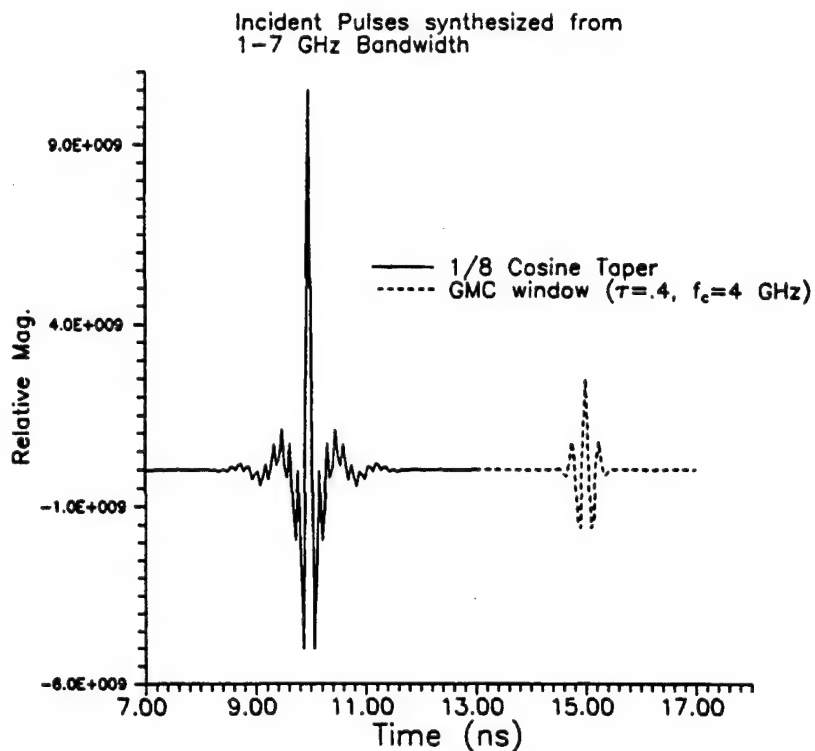


Figure 5. Synthesized pulses used for interrogation of conducting sinusoidal surfaces.

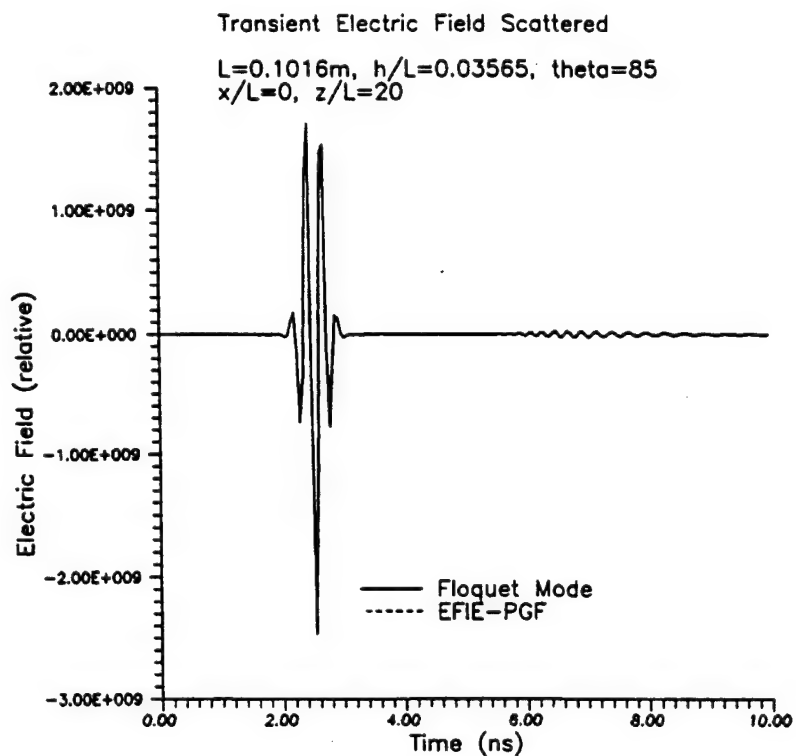
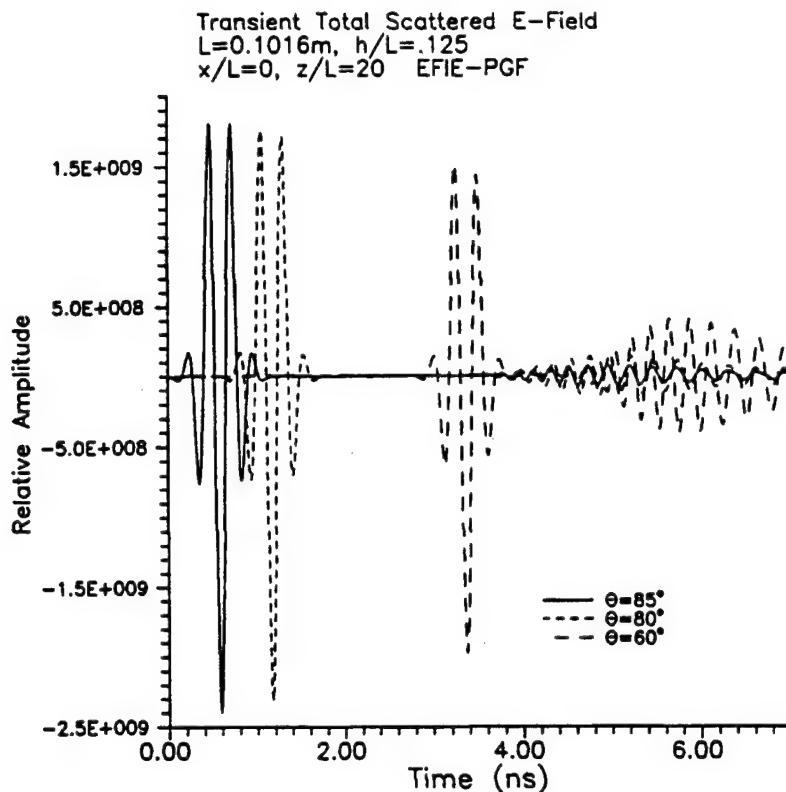


Figure 6. Total scattered electric field created by a GMC pulse from infinite, conducting sinusoidal surface for TE excitation.



**Figure 7.** Comparison of transient total scattered electric fields created by a GMC pulse for various incidence angles upon an infinite sinusoidal surface for TE excitation.

The backscattered, transient field created by a short pulse, which is of major interest in this study, is shown in Fig. 8. It is observed in this figure that the backscattered response of a short pulse exhibits an expected periodic nature with the period correlating to the two-way transit time of the reflected wave between two crests of the sinusoidal surface. This response is dominated by the reflections of the short pulse from crests of the sinusoidal surface.

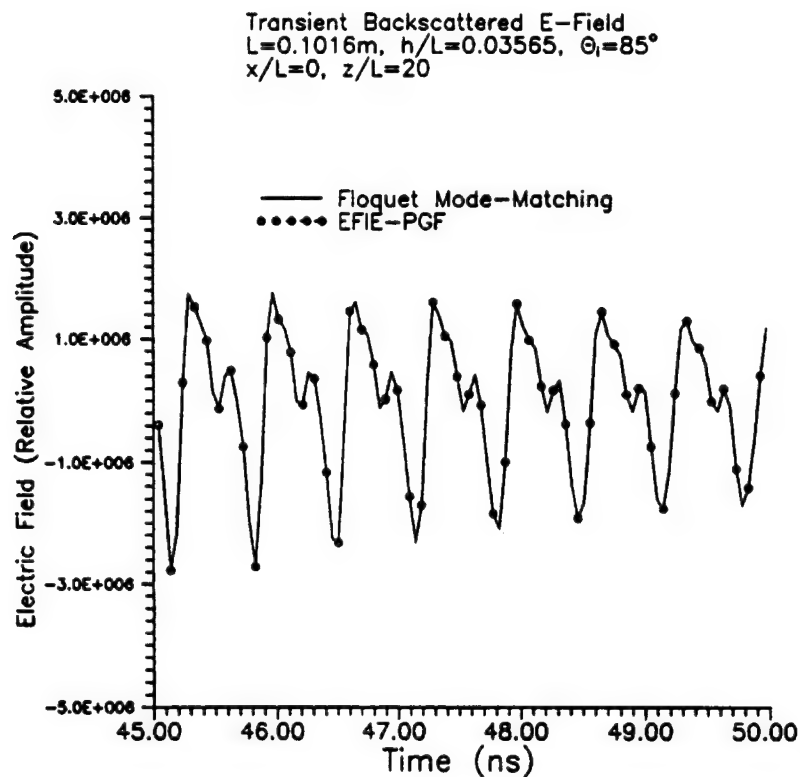


Figure 8. Transient backscattered electric field created by a  $1/8$  cosine pulse from infinite, conducting sinusoidal surface for TE excitation.

In Figure 9 a close up of the non-specular reflection referred to in the total scatter discussion (Figure 7), is actually backscatter. Very interesting is the noticeable change in return pulse periods; this can be explained geometrically by examining the path lengths to the crests nearest to the field point that are contributing to the backscatter. By increasing the height of the sinusoid the backscattered field is enhanced as expected and shown in Fig. 10. In addition, for the larger height sinusoids noticeable pulses are seen within the main crest pulses. This can be explained by the Rayleigh hypothesis. As these sinusoids are outside of the regime of validity, there must be multiple reflections occurring in the trough. Therefore additional reflections can be seen. It is worth noting that the nature of the total scattered field and the backscattered field are entirely different but they are consistent with physical intuition.

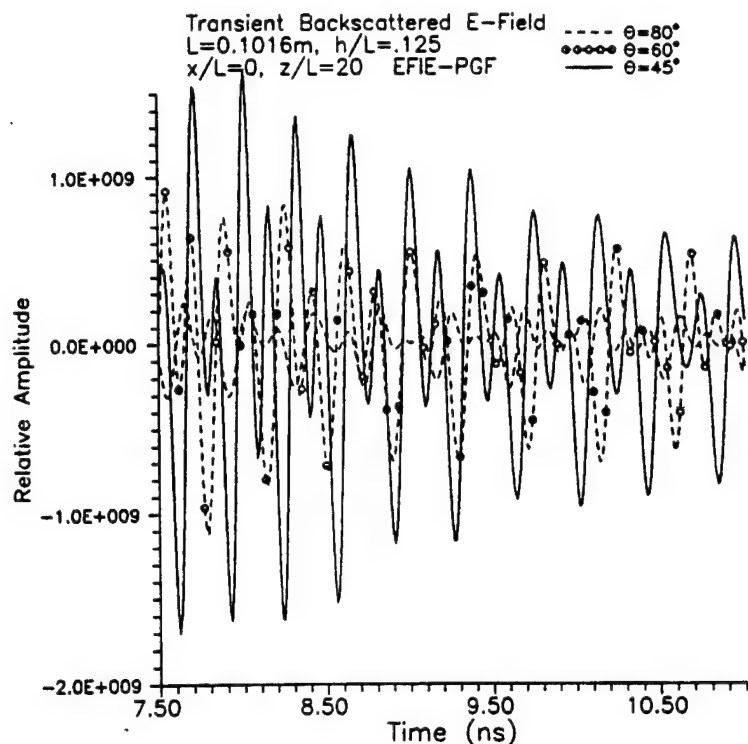


Figure 9. Comparison of transient backscattered electric fields created by a short pulse of various incidence angles upon an infinite sinusoidal surface for TE excitation.

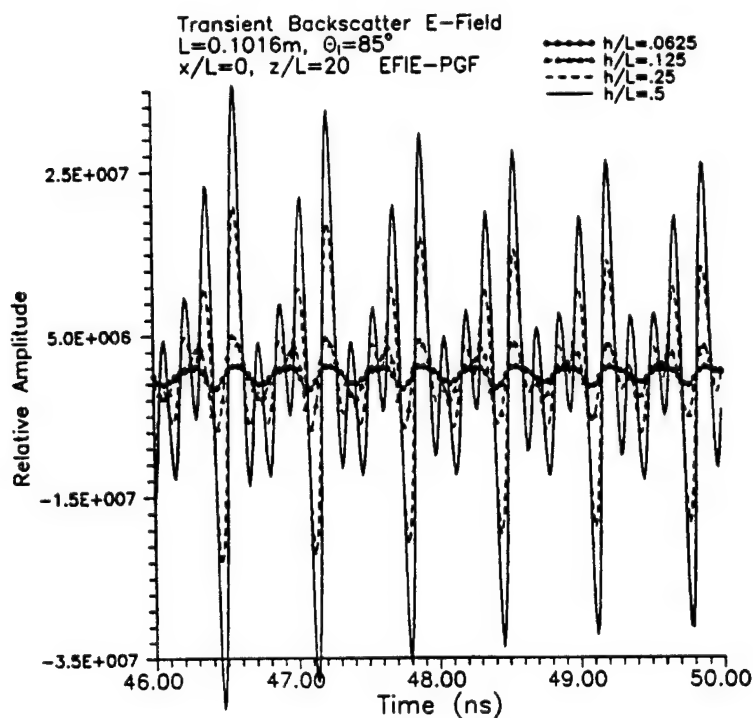


Figure 10. Comparison of transient backscattered electric fields created by a short pulse from various height infinite sinusoidal surfaces for TE excitation.

The dependence on surface period length is examined in Fig. 11, where the transient backscattered fields from two surfaces of differing periods ( $L=.2032\text{m}$  and  $L=.4064\text{m}$ ) and equal crest heights are compared. The separation distance between neighboring return pulses corresponds to the period length, but differing observation heights ( $z/L$ ) lead to the unexpected return pulse period. Although the two surfaces have equal crest heights, it is interesting that the shorter period surface creates larger amplitude return pulses. This phenomena can also be observed in the frequency domain (not shown). The difference in surface slopes lead to a physical explanation. The backscattered field is enhanced with the increased surface slopes, also there is noticeable multiple reflections on the shorter period surface.

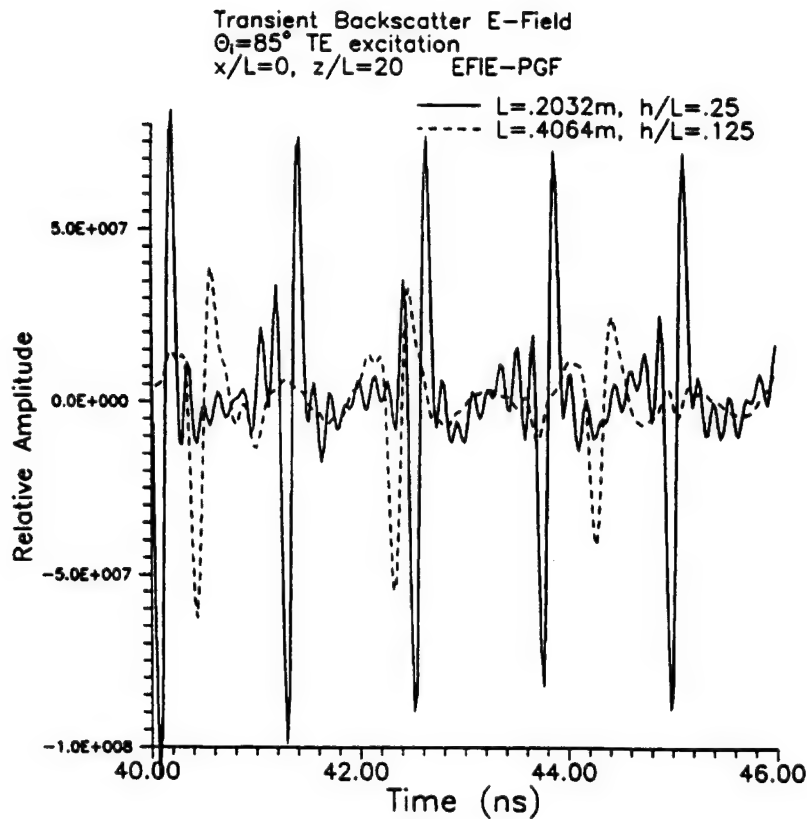


Figure 11. Comparison of transient backscattered electric fields created by a short TE pulse from infinite sinusoidal surfaces of differing periods.

Similar results are obtained for the TM excitation, including the Floquet modes cut-off frequencies, and the frequency selectivity. Only the transient results are shown in Figs. 12 and 13. Where the same phenomena discussed for the TE excitation is observable.

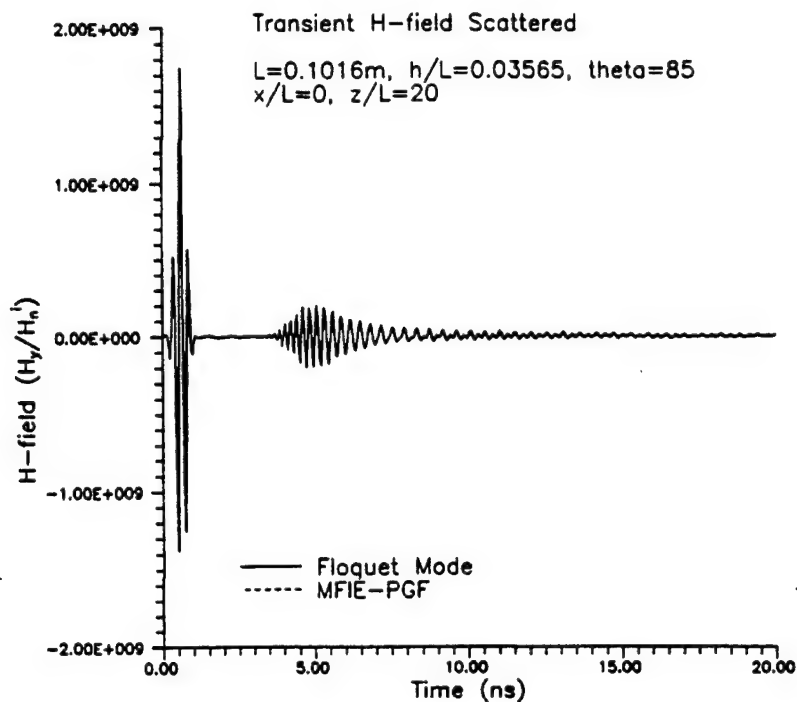


Figure 12. Total scattered magnetic field created by a GMC pulse from infinite, conducting sinusoidal surface for TM excitation.

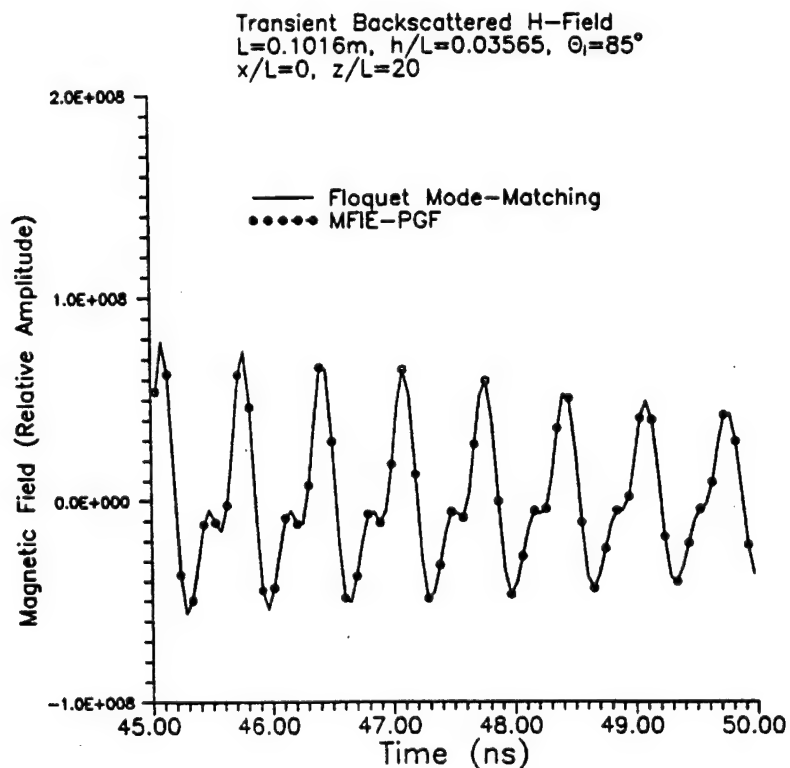


Figure 13. Transient backscattered magnetic field created by a  $1/8$  cosine pulse from infinite, conducting sinusoidal surface for TM excitation.

## V.2 Finite Surface Results

The finite surface analysis consisted of only the IE technique, which has the same shortcomings as the infinite IE method. Figure 14 shows the surface currents excited by a TE plane wave of 4 GHz at an incidence angle of  $-67^\circ$  (i.e. from the right) on two finite sinusoidal surfaces, one with 5 periods and the other with 3 periods, and both have  $L=0.1016$  and  $h/L=0.25$ . The induced current on one period of the corresponding infinite surface is also shown in comparison with that on the finite surfaces. Other than at the edges of the finite surfaces, there are similarities in the induced surface currents between the finite and infinite surface cases. The large spike in the surface currents at the edges of the finite surface is due to the edge effect. Figure 15 shows the surface current induced by a TM plane wave of 2 GHz at an incidence angle of  $-60^\circ$  (from the right) on a sinusoidal surface with 5 periods and  $L=.1016$  and  $h/L=0.125$ . This surface current is compared with that induced on one period of the infinite surface in the same figure. Again there are strong similarities between the surface currents for the finite and infinite surface cases. Because of this agreement in surface currents it is expected that the scattered fields will also have some similarities.

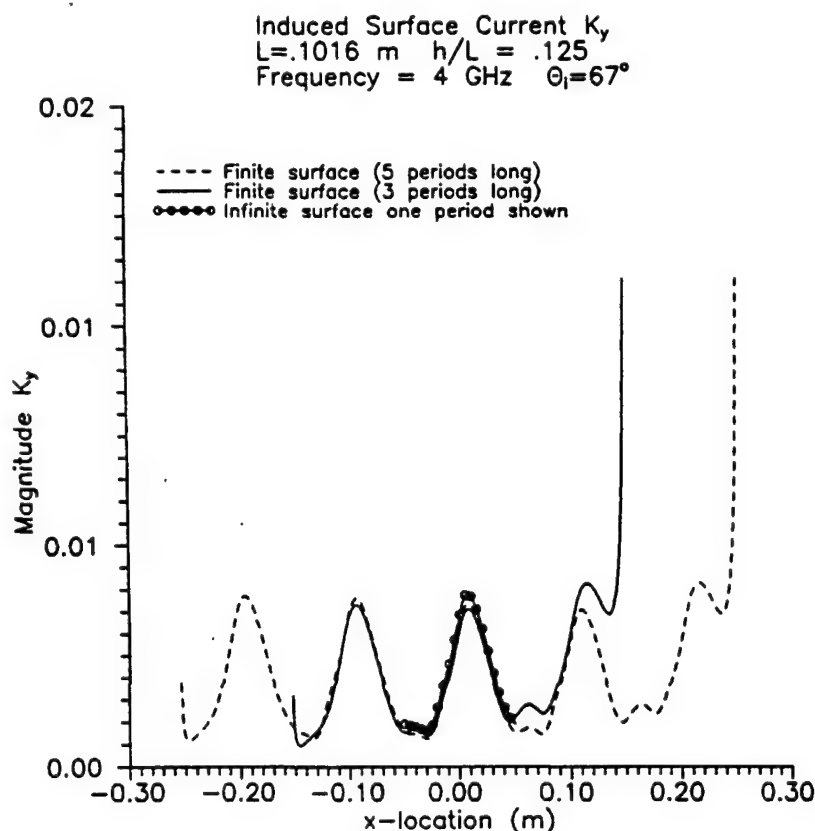
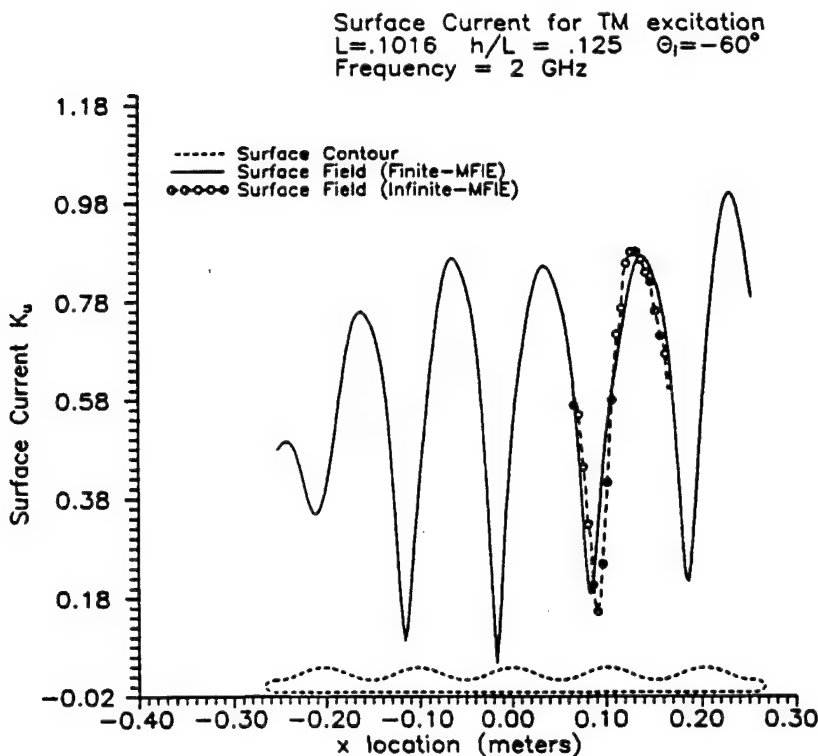


Figure 14. Comparison of induced surface currents on finite and infinite surfaces for TE excitation.





**Figure 15.** Comparison of induced surface currents on finite and infinite surfaces for TM excitation.

The spectral amplitudes of theoretical and experimental backscattered electric fields generated by a TE plane wave at an incidence angle of  $67^\circ$  from finite sinusoidal surfaces are shown in Fig. 16. The finite sinusoidal surface used in the experiment has 6.25 periods while that used in the theoretical calculations has only 5 periods. The dimension of the sinusoidal surface are the same as that used in Fig. 14. Theoretical and experimental results agree quite well, especially at the locations of frequency spikes. When the spectral results of Fig. 16 are inversely Fourier transformed with  $1/8$  cosine windowing, the time domain, transient responses of theoretical and experimental backscattered electric fields created by a short pulse are obtained as shown in Fig. 17. The backscattered response of a short pulse from a finite sinusoidal surface is a number of peaks representing the specular reflections of the pulse from the crests of the surface. Theory and experiment agrees very well except in the number of peaks; theory has 5 and experiment has 6.25.

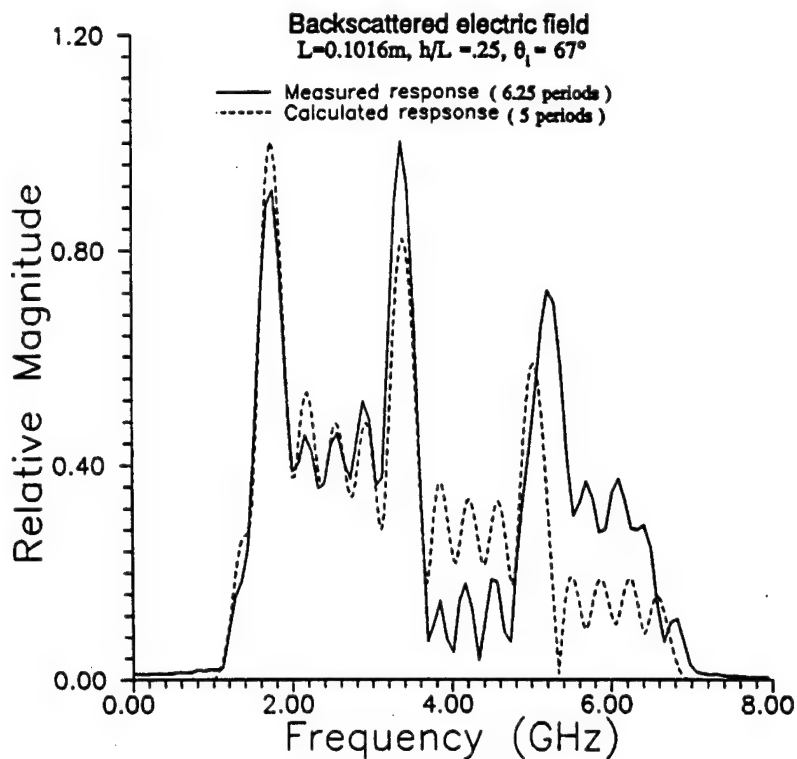


Figure 16. Spectral amplitudes of theoretical and experimental backscattered electric fields from a finite surface for TE excitation.

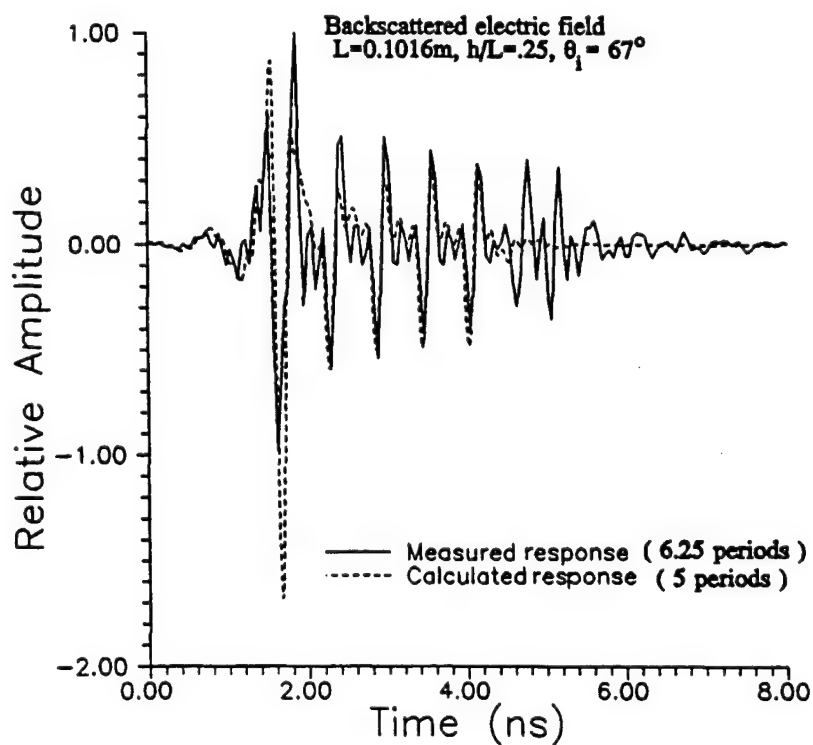
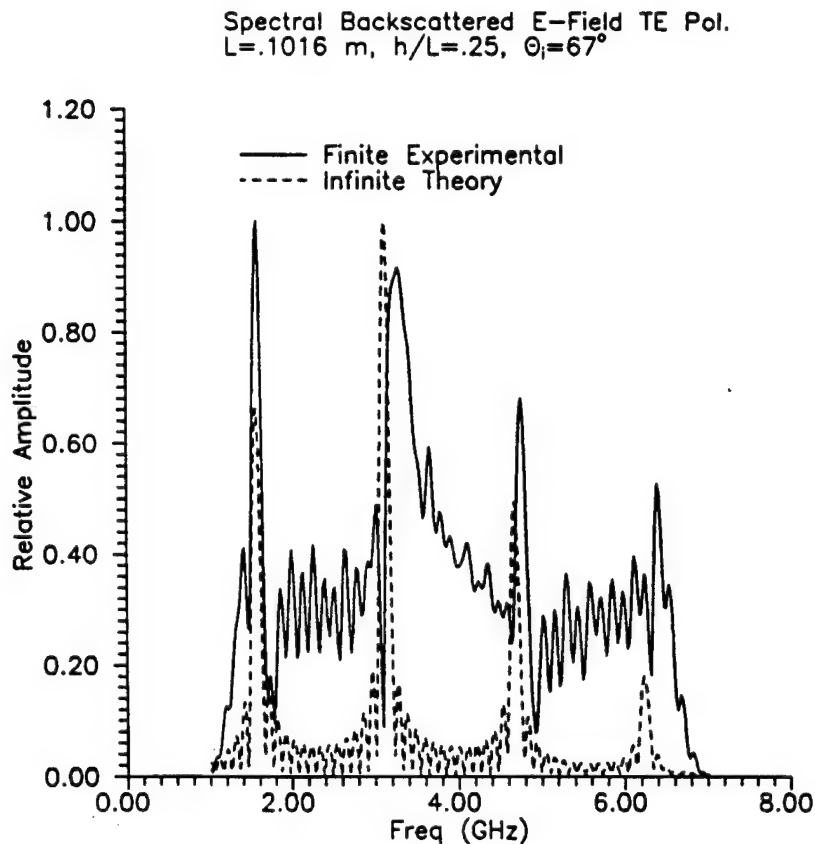
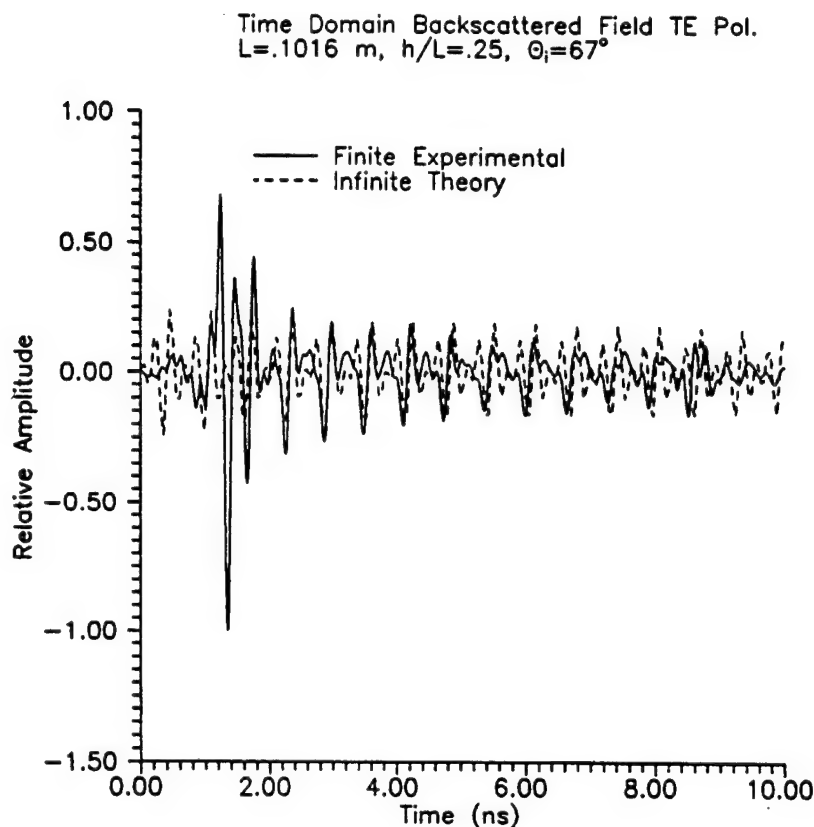


Figure 17. Theoretical and experimental transient backscattered electric fields created by a short pulse from a finite surface for TE excitation.

To seek a link between experimental results from a finite sinusoidal surface and theoretical results based on an infinite sinusoidal surface, an enlarged experimental model of a sinusoidal surface with 11 periods was constructed. There is also a problem in the definition of backscatter from the finite and infinite surfaces. For the finite surface the far-zone scattered fields can be calculated for any given angle in reference to the sinusoidal surface. By choosing this angle to be the same as the incidence angle a backscattered (monostatic) field can be specified. However, the infinite surface does not allow for such an arrangement. The scattered fields are infinitely periodic in the x-direction, therefore location of the field point is unimportant. What allows us to compare the backscattered fields is their transient nature. By geometrically choosing the correct angle from the field point to the surface the path length can be determined. This in turn can be thought of as a time-delay. If the transient backscattered fields from the infinite surface are time shifted by the correct amount a strong agreement should exist. Since this method will only work for one point in space, there will be noticeable differences in the periods of the return pulses.



**Figure 18.** Comparison of experimental backscatter (finite surface) results to theoretical backscatter from an infinite surface for TE excitation.



**Figure 19.** Comparison of transient backscatter created by a short pulse from an infinite surface (theoretical) and a finite surface (experimental) for TE excitation.

The theoretical results on the backscattered electric field in spectral domain and time domain derived on an infinite sinusoidal surface are compared with the corresponding experimental results obtained from the enlarged experimental surface in Figs. 18 and 19. A good qualitative agreement between theoretical results from an infinite surface and experimental results from a finite surface is observed in these figures. In Fig. 18, the frequency spikes observed both in theory and experiment occur at the cut-off frequencies of the Floquet modes signifying the excitation of those modes. In Fig. 19, both theory and experiment predict the backscattered response of a short pulse from a sinusoidal surface to be a series of peaks representing the specular reflections of the pulse from the crests of the sinusoidal surface. To further make a connection between the results of an infinite surface and a finite surface, the computed, transient backscattered electric fields from those two surfaces are compared in Fig. 20. The locations of the peak are completely matched while a minor discrepancy on the shape of the response is observed in Fig. 20. The results shown in Figs. 16 to 19 indicate the experimental verification of theoretical results derived in this paper.

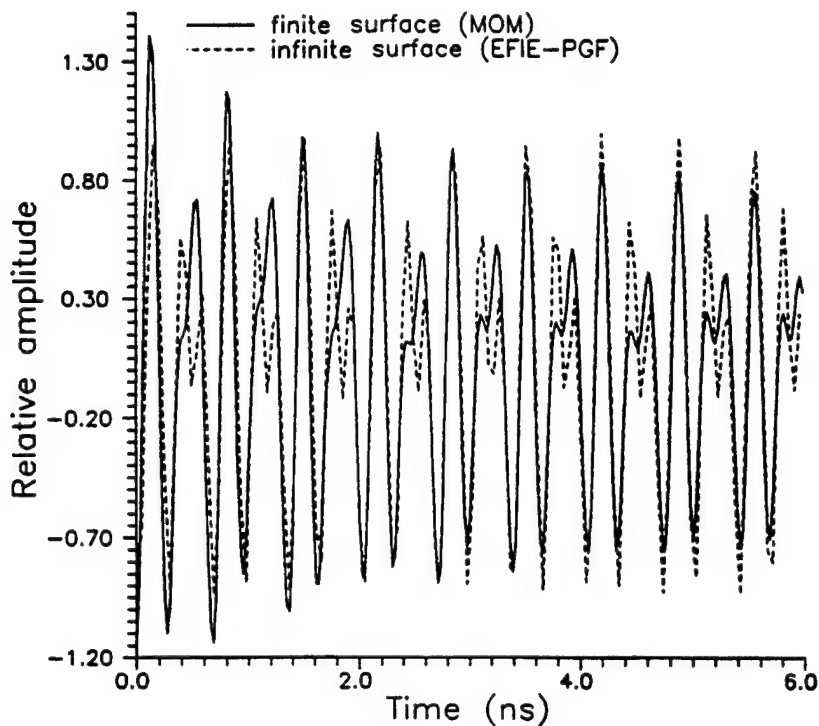


**Figure 20.** Comparison of transient backscattered electric field created by a short pulse from an infinite surface and finite surface for TE excitation.

For completeness, the results for the TM excitation are also included. Figure 21 compares the spectral domain, backscattered magnetic fields obtained from the theory on an infinite surface and the experiment on a finite surface. Figure 22 shows the comparison of the transient backscattered magnetic fields created by a short pulse obtained from the theory on an infinite surface and the experiment on an enlarged finite surface. Finally, theoretical, transient backscattered magnetic fields created by a short pulse from an infinite surface and a finite surface are compared in Fig. 23. From the results in Figs. 21 to 23, there are generally good agreements between experimental and theoretical results from an infinite surface and a finite surface. It is noted that the MFIE employed in the analysis of a finite surface requires a closed surface contour. This may degrade the accuracy of the results on a finite surface by TM excitation.

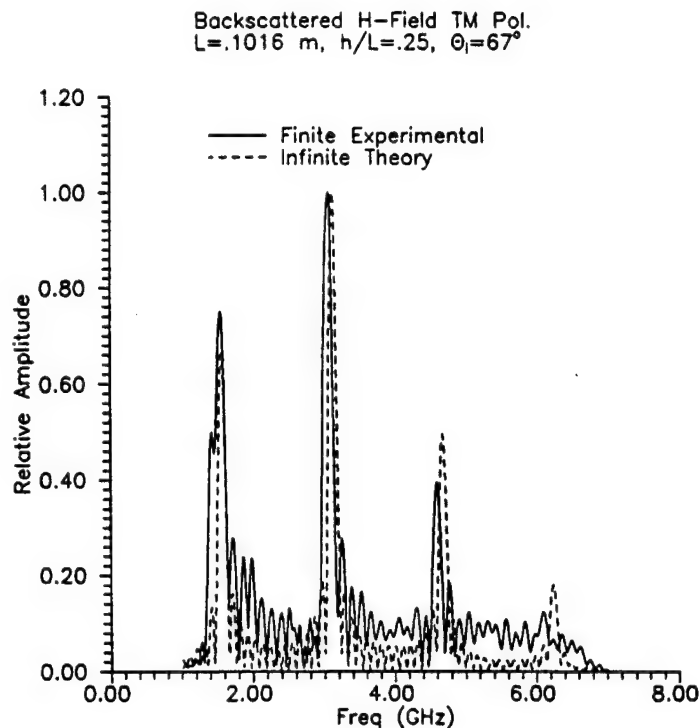


**Figure 21.** Comparison of spectral domain backscattered magnetic field from an infinite surface (theory) and a finite surface (experiment) for TM excitation.

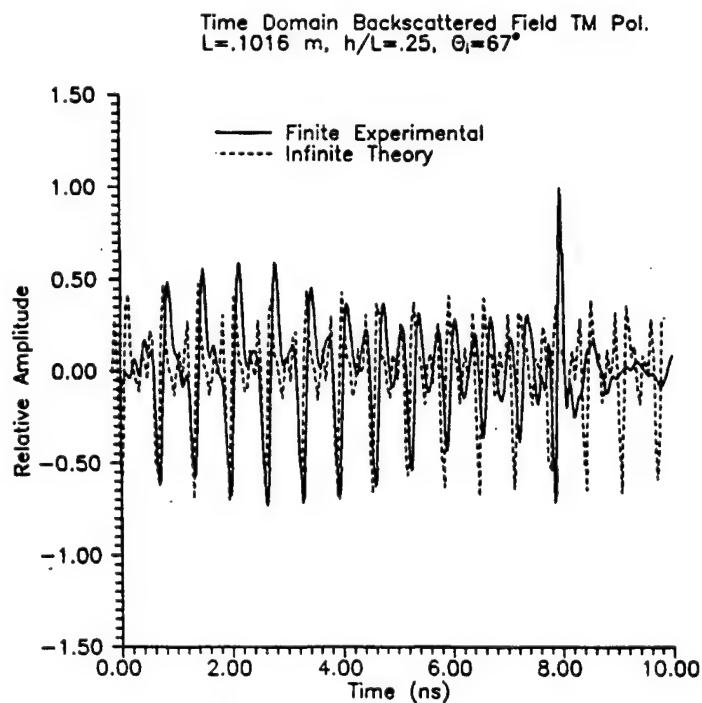


**Figure 22.** Comparison of transient backscattered magnetic field created by a short pulse from an infinite surface (theory) and a finite surface (experiment) for TM excitation.

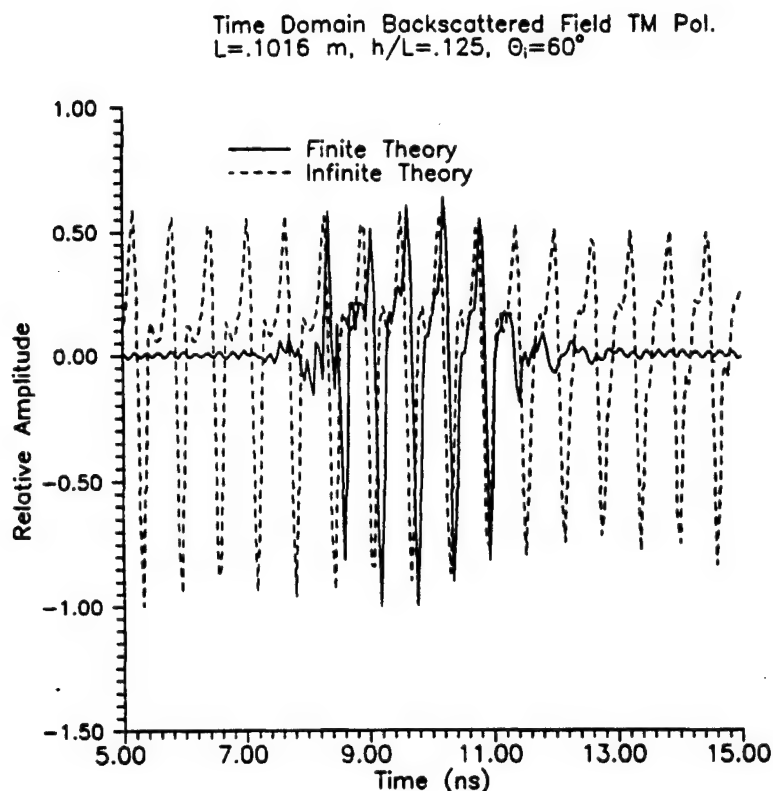


**Figure 23.** Theoretical transient backscattered magnetic field created by a short pulse from an infinite surface and a finite surface for TM excitation.

## VI. CONCLUSIONS

Much has been learned regarding the nature of transient scattering of a short EM pulse from a conducting sinusoidal surface. In this study, theoretical analyses were conducted for an infinite sinusoidal surface and a finite sinusoidal surface for both TE and TM excitations. A series of experiments was also conducted on a finite surface model to verify the theory. There are some interesting observations due to the cut-off and band-pass phenomena of the Floquet modes excited by the periodic sinusoidal surface. It is shown theoretically and experimentally that the backscattered response of a short pulse from a conducting sinusoidal surface is a series of peaks representing the reflections of the pulse from the crests of the surface. A link between the finite and infinite surfaces was established. An argument for the validity of the Rayleigh hypothesis was made by observing the multiple scattering by the higher height sinusoids.

The future extensions of this study is to consider the cases of non-sinusoidal and imperfectly conducting surfaces to better simulate a disturbed sea surface. The studies on those subjects are being conducted and the results will be presented in future publications.

## ACKNOWLEDGMENT

This research was supported by Office of Naval Research under Grant N00014-93-1-1272 and Naval Command, Control and Ocean Surveillance Center under Contract N66001-91-C-6019.

## REFERENCES

1. Ishimaru, A., *Electromagnetic Wave Propagation, Radiation and Scattering*, Prentice Hall, Englewood Cliffs, New Jersey, 1991.
2. Beckmann, P., and A. Spizzichino, *Scattering of Electromagnetic Waves from Rough Surfaces*, Pergamon, London, 1963.
3. Wirgin, A., "Reflection from a corrugated surface," *JASA*, Vol. 68, 692-699, Aug. 1980.
4. DeSanto, J. A., "Scattering from a perfectly reflecting arbitrary periodic surface: An exact theory," *Radio Science*, Vol. 16, 1315-1326, Nov.-Dec. 1981.
5. DeSanto, J. A., "Scattering from a sinusoid: derivation of linear equations for the field amplitudes," *JASA*, Vol. 57, 1195-1197, May 1975.
6. Zipfel, G.G., Jr., and J. A. DeSanto, "Scattering of a scalar wave from a random rough surface: A diagrammatic approach," *J. Math Phys.*, Vol. 13, 1903-1911, Dec. 1972.
7. Zaki, K. A., and A. R. Neureuther, "Scattering from a perfectly conducting surface with a sinusoidal height profile: TE Polarization," *IEEE Trans. Ant. Prop.*, Vol. AP-19, 208-214, Mar. 1971.
8. Schwering, F., and G. Whitman, "Scattering by periodic metal surfaces with sinusoidal height profiles-A theoretical approach," *IEEE Trans. Ant. Prop.*, Vol. AP-25, 869-876, Nov. 1977.
9. Schwering, F., and G. Whitman, "Scattering from a perfectly conducting surface with a sinusoidal height profile: TM Polarization," *IEEE Trans. Ant. Prop.*, Vol. AP-19, 747-751, Nov. 1971.
10. Jordan, A. K., and R. H. Lang, "Electromagnetic scattering patterns from sinusoidal surfaces," *Radio Science*, Vol. 14, 1077-1088, Nov.-Dec. 1979.
11. Waterman, P. C., "Scattering by periodic surfaces," *JASA*, Vol. 57, 791-802, April 1975.
12. Millar, R. F., "On the Rayleigh assumption in scattering by a periodic surface," *Proc. Cambridge Phil. Soc.*, Vol. 65, 773-791, 1969.
13. Millar, R. F., "On the Rayleigh assumption in scattering by a periodic surface II," *Proc. Cambridge Phil. Soc.*, Vol. 69, 217-225, 1971.
14. Millar, R. F., "The Rayleigh hypothesis and a related least-squares solution to scattering problems for periodic surfaces and other scatterers," *Radio Science*, Vol. 8, 785-796, Aug.-Sep. 1973.
15. Utresky, J. L., "The scattering of plane waves from periodic surfaces," *Ann. Phys.*, Vol. 33, 400-427, 1965.
16. van den Berg, P. M., and J. T. Fokkema, "The Rayleigh hypothesis in the theory of reflection by a grating," *JOSA*, Vol. 69, 27-31, Jan. 1979.
17. van den Berg, P. M., and A. T. de Hoop, "Reflection and Transmission of Electromagnetic Waves at a Rough Interface Between Two Different Media," *IEEE Trans. Geosci. Remote Sens.*, Vol. GE-22, 42-52, Jan. 1984.
18. Harrington, R. F., *Time-Harmonic Electromagnetic Fields*, McGraw-Hill, New York, 1961.
19. Veysoglu, M. E., R. T. Shin, and J. A. Kong, "A finite-difference time-domain analysis of wave scattering from periodic surfaces: Oblique incidence case," *JEWA*, Vol. 7, 1595-1607, Dec. 1993.
20. Kong, J. A., *Electromagnetic Wave Theory*, John Wiley, New York, 1990.



21. Carin, L., and L. Felsen, "Time Harmonic and Transient Scattering by Finite Periodic Flat Strip Arrays: Hybrid (Ray)-(Floquet Mode)-(MoM) Algorithm," *IEEE Trans. Ant. Prop.*, Vol. 41, 412-421, April 1993.
22. DeSanto, J. A., "Exact spectral formalism for rough-surface scattering," *JOSA*, Vol. 2, 2202-2206, Dec. 1985.
23. Collin, R. E., "Full Wave theories for rough surface scattering: An updated assessment," *Radio Science*, Vol. 29, 1237-1254, Sep.-Oct. 1994.
24. Collin, R. E., "Electromagnetic Scattering from Perfectly Conducting Rough Surfaces (A New Full Wave Method)," *IEEE Trans. Ant. Prop.*, Vol. 40, 1466-1477, Dec. 1992.
25. Bahar, E., "Full-Wave Solutions for the Scattered Radiation Fields from Rough Surfaces with Arbitrary Slope and Frequency," *IEEE Trans. Ant. Prop.*, Vol. AP-28, 11-21, Jan. 1980.
26. Knotts, M. E., and K. A. O'Donnell, "Multiple scatterings by deep perturbed gratings," *JOSA*, Vol. 11, 2837-2843, Nov. 1994.
27. Depine, R. A., and D. C. Skigin, "Scattering from metallic surfaces having a finite number of rectangular grooves," *JOSA*, Vol. 11, 2844-2850, Nov. 1994.
28. Ott, R. H., et al., "VHF radar sea scatter and propagation at grazing angles less than  $1^\circ$ ," *Radio Science*, Vol. 30, 361-370, Mar.-April 1995.
29. Veysoglu, M. E., et al., "Polarimetric passive remote sensing of periodic surfaces," *JEMWA*, Vol. 5 No. 9, 997-1005, 1991.

**Adam Norman** was born in Garden City, MI, on August 24, 1969. He received the B.S. and M.S. degrees in Electrical Engineering from Michigan State University, East Lansing, 1992 and 1993, respectively, and is currently pursuing the Ph.D. degree in Electrical Engineering at MSU. He is a Research Assistant for the Department of Electrical Engineering, researching transient scattering from ocean-like surfaces. Mr. Norman was the recipient of the Outstanding Graduate Student Award in Electrical Engineering in 1993, and is a member of Eta Kappa Nu.

**John Ross** was born in Westernport, MD, on June 19, 1962. He received the B.S. and M.S. degrees in Electrical Engineering from West Virginia University, Morgantown, in 1984 and 1987, respectively, and the Ph.D. degree in Electrical Engineering from Michigan State University, East Lansing, in 1992. He was an Assistant Engineer in the Illinois Institute of Technology Research Institute, Annapolis, MD. He is currently employed by General Motors R&D Center, Warren, MI. Dr. Ross is a member of Eta Kappa Nu.

**Ponniah Ilavarasan** was born in Puloly, Sri Lanka, on July 27, 1962. He received the B.S. and M.S. degrees in Electrical Engineering in 1986 and 1988, respectively, and the Ph.D. degree in Electrical Engineering from Michigan State University, East Lansing, in 1992. He worked as a Teaching Assistant and as a Research Assistant from 1986 to 1992 in the Department of Electrical Engineering of Michigan State University. He is currently employed by Ford Motor Company, Dearborn, MI. Dr. Ilavarasan is a member of Eta Kappa Nu.

**Dennis P. Nyquist** was born in Detroit, MI, on August 18, 1939. He received the B.S.E.E. and M.S.E.E. degrees in 1961 and 1964, respectively, and the Ph.D. degree in Electrical Engineering from Michigan State University, East Lansing, in 1966. He joined the MSU faculty in 1966 and became Professor in 1979. His current research interests include electromagnetic interactions in integrated electronics, electromagnetic characterization of materials, and transient electromagnetics. Dr. Nyquist is a member of Commission B of URSI, Sigma Xi, Tau Beta Pi and Phi Kappa Phi. He was recipient of the Michigan State University Teacher-Scholar Award in 1969.

**Kun-Mu Chen** received the B.S. degree in Electrical Engineering from National Taiwan University in 1955, and the M.S. and Ph.D. degrees in Applied Physics from Harvard University in 1958 and 1960, respectively. From 1960 to 1964 he was associated with the Radiation Laboratory at the University of Michigan. In 1964 he joined the faculty of Michigan State University as an Associate Professor, and was a Professor of Electrical Engineering for 1967 to 1995. In 1995 he was appointed as Richard M. Hong Professor in Electrical Engineering, an endowed chair professorship. He has published many papers on electromagnetic radiation and scattering, radar target discrimination and bio-electromagnetics. Dr. Chen is a Fellow of IEEE and AAAS. He is the recipient of the Distinguished Faculty Award and Withrow Distinguished Scholar Award from Michigan State University and the Outstanding Achievement Award from the Taiwanese American Foundation.

**Edward Rothwell** was born in Grand Rapids, MI, on September 8, 1957. He received the B.S. degree in Electrical Engineering from Michigan Technological University, Houghton, in 1979, the M.S. degree in Electrical Engineering, and the degree of Electrical Engineer from Stanford University, Stanford, CA, in 1980 and 1982, and the Ph.D. degree in Electrical Engineering from Michigan State University, East Lansing, MI, in 1985, where he held the Dean's Distinguished Fellowship. He worked for Raytheon Co., Microwave and Power Tube Division, Waltham, MA from 1979–1982 on low power traveling wave tubes, and for MIT Lincoln Laboratory, MA, in 1985. He has been at Michigan State University from 1985–1990 as an Assistant Professor of Electrical Engineering and from 1990 as an Associate Professor. He received the John D. Withrow award for teaching excellence from the College of Engineering at Michigan State University in 1991. Dr. Rothwell is a Senior member of the IEEE, and a member of Phi Kappa Phi, Sigma Xi, and Commission B of URSI.

## Appendix 2

### Transient Scattering from Ocean Surface Models

A. Norman, *Student Member, IEEE*, G. Wallinga, D.P. Nyquist, *Senior Member, IEEE*, E.J. Rothwell, *Senior Member, IEEE*, K.M. Chen, *Fellow, IEEE*

Dept of Electrical Engineering  
Michigan State University  
East Lansing, MI 48824

*Abstract* - An experimental study of transient scattering of a short pulse from various ocean models was performed. The measurements confirm previously developed theory and offer insights into the scattering mechanisms of ocean-like waves. The measurements were performed in both the time and frequency domains and the results for TE incident polarization will be examined here.

---

This work was supported by Naval Command, Control and Ocean Surveillance Center, San Diego, CA. under Contract N66001-91-C-6019 and Office of Naval Research under Grant N00014-93-1-1272.

## I. Introduction

The usage of Ultra-Wideband/Short Pulse radar in the ocean environment greatly enhances the range resolution of the radar and allows for "snap shot" type modelling of the ocean. Inherently the improved bandwidth of a radar implies that more information is available. Additional information not possible with conventional CW type radar is obtained in the transient return. There is also new and useful information by examining the spectral returns (via a FFT). This paper will consider transient scattering of short pulse from perfectly conducting (PEC) wave models. In this preliminary investigation the surfaces only contain one-dimensional roughness and are assumed to be infinite in the lateral direction ( $\hat{y}$ ). In order to perform a thorough investigation here, only TE (H-Pol.) incident waves are considered. The TM case has been examined and will be contained in a later publication.

The wave models have been chosen to test a number of scattering mechanisms. There is a Stokes-type wave [1], that has a very large slope (at the crest), and double sinusoid wave that simulates two-scale roughness, and a realistic a-periodic Donelan-Pierson [2,3,4] wave. The Donelan-Pierson wave is constructed from actual ocean statistics and is a function of wind-speed, a periodic swell is superimposed upon the wind roughened waves.

The experimental measurements consist of true time-domain interrogation with a high voltage PPL pulse generator, and of synthesized frequency domain excitation (via a HP 8720B Network Analyzer). The frequency domain synthesis method allows for a much wider bandwidth and a larger dynamic range, resulting in higher quality measurements. These experimental measurements will be examined in the time and frequency domains and will be compared to theoretical models previously developed.

## II. Theory

Although the experimentally obtained results are of primary interest, it is necessary to provide a brief explanation of the theoretical techniques applied to the problem. In a previous publication [5] frequency domain integral equations have been developed for surface models that are either axially ( $\hat{x}$ ) finite or infinite (see Figure 1). The infinite surfaces require periodicity in order to numerically implement the integral equation solution. This periodicity allows the domain of the integral equation to be truncated to a single period, via the periodic Green's function. The finite case has no such restrictions (periodicity), but the numerics (CPU time and memory) limit the physical size of the interrogated surface. Since frequency domain techniques have been utilized, an IFFT is needed to yield the transient (time-domain) backscatter. Therefore, a wide-bandwidth (numerous iterations) of spectral returns is required to produce a short pulse interrogation. This method of solution is analogous to the experimental measurements that are performed in the frequency domain.

The geometry of the problem is shown in Figure 1. The governing integral equation (EFIE) is derived in the standard fashion by applying the boundary condition at the PEC surface,

$$E_y^i(x,z) = -E_y^s(x,z) \quad (1)$$

where  $E_y^i(x,z)$  is the y-component of the TE incident plane wave, and  $E_y^s(x,z)$  is the y-component of the scattered electric field.

The scattered electric field can be found by the 2-D Green's function superposition integral [6], which states that the scattered electric field is produced by the induced surface current ( $K_z(x,z)$ ) excited on the PEC surface, See equation (4) below. Substituting the scattered field (4) into (1) results in an EFIE for the unknown current distribution,

$$\int_{\Gamma} K_z(x', z') H_o^{(2)}(k_o |\vec{\rho} - \vec{\rho}'|) dl' = \frac{4}{k_o \eta} E_y^i(x, z) \quad \forall x, z \in \Gamma \quad (2)$$

where  $H_o^{(2)}$  is the second kind Hankel function of order zero, and  $\vec{\rho}$  is the position vector in the x-z plane, and  $\Gamma$  describes the contour of the surface.

For the infinite case a periodic surface is required, this allows for the use of the periodic Green's function. Physically the induced current due to an incident plane wave will be identical on every period of surface, except for a phase shift. This allows for the reduction in the domain of integration to just one period, and a subsequent summation of the infinite contributions from every period (provided the phase shift is accounted for). The periodic Green's function kernel is given by [7],

$$G(x, z | x', z') = \frac{2}{L} \sum_{n=-\infty}^{\infty} \frac{e^{-j\beta_n(x-x') - jq_n|z-z'|}}{q_n} \quad (3)$$

where  $L$  is period of the surface and  $\beta_n = k_o \sin(\theta_i) + 2n\pi/L$ , and  $q_n^2 = k_o^2 - \beta_n^2$ .

The convergence of (3) is examined in [8,9,10] and can be accelerated for special cases.

The EFIE (Eqn. (2)) is solved via the method of moments by expanding the unknown current distribution into pulse function basis set and then point matching is performed to create the typical MoM matrix solution. Subsequent to the solution of the current distribution the scattered electric field can be determined by,

$$E_y^s(x, z) = -\frac{k_o \eta}{4} \int_{\Gamma} K_y(x', z') H_o^{(2)}(k_o |\vec{\rho} - \vec{\rho}'|) dl' \quad (4)$$

This integral is solved readily using standard techniques.

### III. Measurement Techniques

As alluded to in the previous sections, frequency domain measurements as well as time domain measurements were performed on the ocean surface models. The measurements were all performed in the anechoic chamber at MSU (See Figure 2). The chamber is 24' x 12' x 12' which limits the physical size of the model waves. A bistatic horn arrangement was necessary [11] to produce high quality results. The horns were placed close enough so that comparison with monostatic theoretical results are applicable. Standard gain TEM pyramidal horns were used for transmission and reception in both the frequency domain and time domain techniques.

The wave models were constructed by adhering aluminum foil to precision machined polystyrene. The physical size of the three wave models is 70" by 36". The Stokes wave consisted of 10 periods ( $L=7''$ ) and the double sinusoid had 10 periods with a shorter wavelength (50 periods) superimposed. The Donelan-Pierson wave was constructed with 10 swells with a-periodic wind-driven wave superimposed, therefore the DP surface is not periodic. Figure 3 shows a comparison of all three wave types that will be investigated.

The measurement techniques [11] will be described qualitatively for both the frequency domain synthesis method and the short/pulse time domain method. In the frequency domain method an HP 8720B Network analyser is used to perform the measurements ( $S_{21}$ ). The sending port is amplified with an HP 8349B wide band amplifier and then radiated by the transmitted horn. This creates the incident "plane" wave, which will scatter from the chamber and objects inside the chamber. The receiving horn is then fed into the network analyser's receiving port. The network analyser can very rapidly perform high quality measurements for a large number of frequencies. The speed of the network analyser allows for a great number of measurements to be performed in a relatively short time. Calibration is performed outside (post-processed) the network analyser, and is accomplished using a metallic calibrating sphere. There a four required

measurements. The first two are the measurement of the target (sea-surface model) and the background or target removed. The second set of measurements are of the sphere and the background of the sphere (note that one of the background measurements could be eliminated if there is no change between the target and sphere backgrounds). The background measurements are then subtracted in the frequency domain from the target and sphere measurements. The "corrected" sphere measurement is then utilized as a calibrator, this is accomplished by first computing the theoretical (Mie-Series) scattering from the sphere for the given horn arrangement (bi-static), and then dividing in the frequency domain the measured "corrected" sphere result by the theoretical sphere results. The resultant spectrum is the calibrator or the "system transfer function". The "corrected" target measurement can then be calibrated by dividing out (in the frequency domain) the system transfer function. All subsequent target measurements can be calibrated by this same system transfer function provided that the horns and chamber are not disturbed.

The steps above provide a frequency domain description of the scattering of a plane wave from a target (sea-surface). It is still necessary to synthesize (IFFT) the transient results, a somewhat quicker, and more intuitive approach is to perform the measurements in the time domain. The time-domain measurements require a very high bandwidth sampling oscilloscope and a pulse generator. A PPL 1000B pulse generator and a Tektronix 7854 are used at MSU to perform the true time domain measurements. The pulse generator signal is directly sent to the transmitting horn, while the receiving horn is attached to the oscilloscope. The system used at MSU is far from ideal, and cannot match the performance of the frequency domain synthesis method, but the measurements provide validation of the frequency domain method and are quite instructional and intuitive. The drawbacks of the time-domain system are many-fold, the pulse generator cannot produce as short a pulse as the synthesized, the oscilloscope is also limited in



bandwidth, and the horns perform poorly in the lower frequencies (less than .5 GHz).

The time-domain measurement scheme is ideally much simpler than the frequency domain synthesis method, but due to the horn (system) characteristics a lengthier post-processing technique similar to the synthesis method is needed. The same set of four measurements are performed in the time-domain (target, background, sphere, background). The backgrounds are subtracted and the resultant transient waveforms (target and sphere) are transformed (FFT) into the frequency domain. The frequency domain waveforms are windowed (rectangular) to exclude the lower frequencies (horn difficulties) and an identical set of steps is performed as in the synthesis method. That is, the sphere is used to calibrate in the frequency domain, and the transient results are finally obtained following an IFFT. This roundabout method is post-processed therefore the actual measurements are performed very quickly.

#### **IV. Results/Comparisons**

In general there was very good agreement between the theoretical transient backscatter and measured backscatter from all the sea-surface models. It will be shown later that the theoretical backscatter from the infinite surface has an excellent agreement with the measured results, better than the theoretical finite surface. This was an unexpected results, and can be attributed to the far-field approximation made in calculating the backscatter from the finite surface. The theory for the infinite surface did not contain any such approximations and therefore could better model the cylindrical scattered waves ( $1/r$  loss) and the relative path length variation along the surface, which manifested itself in the spreading of the floquet mode spikes.

##### **a) Experimental Results**

The first results to be considered are a general type (qualitative) angular dependence of the scattered fields. The normalized synthesized transient backscatter from the Stokes wave

model is shown in Figure 4 for incidence angles ranging from near grazing to normal incidence. Normalization was required to enhance the near grazing backscatter, which contained far less energy than the normally incident backscatter. Observable in Figure 4 are the backscatter from each individual peak of the wave, and the change in the two-way transit time versus the incidence angle. The finer structure, such as multiple scatterings, are hard to discern in this plot. The remaining transient results should provide a better glimpse at individual incidence angles.

Accompanying the transient results are the corresponding spectral returns (the actual measurements). In Figure 4 the Floquet mode spikes are evident, and the interference patterns for higher frequencies can be seen. Also of note is the spreading of the Floquet mode spikes as the incidence angle is rotated from near grazing to normal incidence.

The transient scattering of a short pulse from the Double Sinusoid and the Stokes wave models are compared in Figure 5. In Figure 5, only a portion of the transient signal and only the near grazing angles are compared. There are notable differences between the two surface models the double sinusoid exhibits considerable more structure due to the two-scale roughness, however the Stokes wave model has a more pronounced multiple scatter, which is evident in the trough regions. These two observations are intuitively satisfying and will be shown later to agree with the numerical results.

The scattering from the three waves at an incidence angle of  $70^\circ$  are compared in Figures 6 and 7. In Figure 6 the measured frequency domain results are compared. The spikes in the spectral returns are due to periodicity of the surfaces and are called Floquet mode spikes. These spikes are dependent on incidence angle (See Figure 4) and period length, note also that the Donelan Pierson surface lacks the highly defined spikes, this can be attributed to the a-periodic nature of the surface. The overall strength of the returns at this incidence angle are greatest for the Stokes wave this is due to the large slope near the crest of the wave. Also of interest is the

higher frequencies where the spectrum become erratic, this indicates that small structures are nearing resonance or multiple scatterings are occurring.

In Figure 7, the synthesized transient results are compared. The time-domain signals are obtained by IFFT after a Gaussian Modulated Cosine (GMC) window has been applied in the frequency domain. Only a portion of the transient results are shown in order to enhance the resolution of the plot. The plots reveal the differences between the three models. The Stokes wave has the largest return pulses (due to the large slope) and a multiple scatter can be observed in the trough. The multiple scatter spectral content is in the higher frequencies and could be enhanced in the time-domain with a different weighting function that emphasizes the higher frequencies. The double sinusoid wave exhibits the scattering centers from all of the non-shadowed crests, there is also a high frequency content multiple scatter that could be enhanced. The Donelan-Pierson wave has the smallest return amplitude, this is due to the orientation of the wave. The biggest crest was placed at the front edge (See Figure 3), which effectively shadows the remaining crests. The return from the first hump is not shown, but is much larger than the other crests.

#### **b) Comparison with Time-Domain Measurements**

The synthesized transient results that have been discussed, are all of very large bandwidth (i.e. very short pulse). The method of frequency domain synthesis works extremely well for stationary (non-time varying) targets, but is less effective for non-stationary targets. A true short pulse radar can be just as effective on non-stationary targets provided the bandwidth is the same. The time domain system at MSU lacks the large bandwidth of the synthesis system, but is large enough the make some useful and validating comparisons.

In Figure 8 is comparisons of the transient and spectral returns for both the time-domain and frequency domain systems. The Stokes wave model was used for this comparison, although

not shown the other models were compared and similar agreements were observed. The effective bandwidth of the PPL pulse generator is from DC to roughly 2 GHz, and the radar horns are effective down to around .5 GHz. In Figure 8 the spectral returns are compared for both methods, note that the transient measurement had to be transformed (FFT). The agreement between the two methods is excellent over the bandwidth of 0.5-2.0 GHz. Similar agreement can be seen in the transient results. In this case a GMC window was applied to both spectrums and then transformed (IFFT) to time domain. The transient results are seen to contain 11 return pulses, the first pulse is due to the leading edge of the wave model and the remaining 10 pulses are from the wave crests and are separated by the two-way transit time between neighboring crests. These results help to confirm the validity of the synthesis method and provide hope for the future use of short pulse radar.

### **c) Comparison with Theory**

As stated earlier, there was excellent agreement between the theoretical and the experimentally measured backscatter. In Figure 9 the transient backscatter from the Stokes wave model is examined. Only a few periods of the wave are shown, but there is very good agreement between the infinite theoretical backscatter and the measured. These results were obtained by weighting the spectral response with a GMC then transformed into the time-domain.

Although not shown the theoretical transient backscatter from the finite model also matched well with the measured, except the two-way transit times did not vary as they do for the measured result. This was due to the far-field approximation.

In Figure 10, the spectral returns are compared, once again there is excellent agreement. The peaks are due to the periodicity of the wave (Floquet Modes) and are slightly spread out due to the apparent period change as viewed from the field point. The theoretical backscatter from the finite length surface did not exhibit this spreading, and can be attributed to the far-field

approximation.

The double sinusoid wave is considered next, and once again there is a strong agreement between the theory and the measurements. In Figure 11, the transient backscatter is compared. The additional wave structure is evident and accurately depicted by the theoretical results. The spectral returns are not shown but are also in good agreement.

The transient backscatter from the Donelan Pierson wave is compared with the theoretical backscatter from a finite wave. The infinite (periodic) theory can not accurately model the backscatter due to the large shadow produced by the first crest. The finite theory does a fairly good job as seen in Figure 12, but due to the far field approximation the two-way transit times between crests are not correctly depicted. The spectral comparison is also hampered by the far-field approximation, but does show general agreement.

The effects of spectral content are examined in Figures 13 and 14. The synthesized transient backscatter from the double sinusoid wave for an increasing GMC window are shown in Figure 13. The incident pulse can be seen to become very narrow as more  $\tau$  gets smaller, this results in a much enhanced resolution. In Figure 14, the effects of moving constant width GMC window (roughly 1.5 GHz Wide) through the spectral response is shown. Different parts of the wave are more active for different frequency bands, for example the lowest band can only "see" the main swell, but as the window is moved up in frequency ( $f_c$ ) the small ripple becomes more active.

## V. Conclusions

The experimental measurements presented in this paper help to validate the theoretical techniques, and they offer new insights into the scattering from these surface models. The time-frequency nature of the scattering was only qualitatively discussed and will be examined in detail

in the future. The identification of scattering mechanisms helps to further the understanding of the underlying physics of the problem. These mechanisms include the scattering center (or specular reflection), the multiple scatterings, and the sub-structure scattering.

The frequency domain synthesis technique, which was employed for the wide bandwidth measurements, was verified by the true time-domain short pulse method. This experiment reveals the future strengths of the short-pulse radar, which allows one to model the surface as stationary.

Future work will consist of presenting the results for TM polarization and to consider imperfectly conducting ocean surfaces.

## References

- [1] B. Kinsman, *Wind Waves, their generation and propagation on the ocean surface*, Prentice Hall, NJ, 1965.
- [2] M.A. Donelan and W.J. Pierson, "Radar Scattering and Equilibrium Ranges in Wind-Generated Waves with Application to Scatterometry," *JGR*, Vol. 92, No. C5, pp. 4971-5029, May 15, 1987.
- [3] B.J. West, et. al., "A New Method for Surface Hydrodynamics," *JGR*, Vol. 92, No. C11, pp. 11803-11824, Oct. 15, 1987.
- [4] S.L. Broschat, "The Phase Perturbation Approximation for Rough Surface Scattering from a Pierson-Moskowitz Sea-Surface," *IEEE Geoscience and Remote Sensing*, Vol. 31 No. 1, pp. 278-283, Jan. 1993.
- [5] A. Norman, et. al., "Transient scattering of a short pulse from a conducting sinusoidal surface," *JEWA*, Vol. 10, No. 4, pp. 461-487, 1996.
- [6] R.F. Harrington, *Time-Harmonic Electromagnetic Fields*, McGraw-Hill, New York, 1961.
- [7] J.A. Kong, *Electromagnetic Wave Theory*, John Wiley, New York, 1990.
- [8] M.E. Veysoglu, et. al., "Polarimetric Passive Remote Sensing of Periodic Surfaces," *JEWA*, Vol. 5, No. 3, pp.267-280, 1991.
- [9] A.W. Mathis and A.F. Peterson, "A comparison of Acceleration Procedures for the Two-Dimensional Periodic Green's Function," *IEEE AP-S*, Vol. 44 No. 4 pp 567-572, April 1996.
- [10] S. Singh and R. Singh, "A Convergence Acceleration Procedure for Computing Slowly Converging Series," *IEEE MTT*, Vol. 40, No. 1, pp. 168-173, Jan. 1992.
- [11] J.E. Ross, "Application of transient electromagnetic fields to radar target discrimination," PhD Dissertation, Michigan State University, 1992.

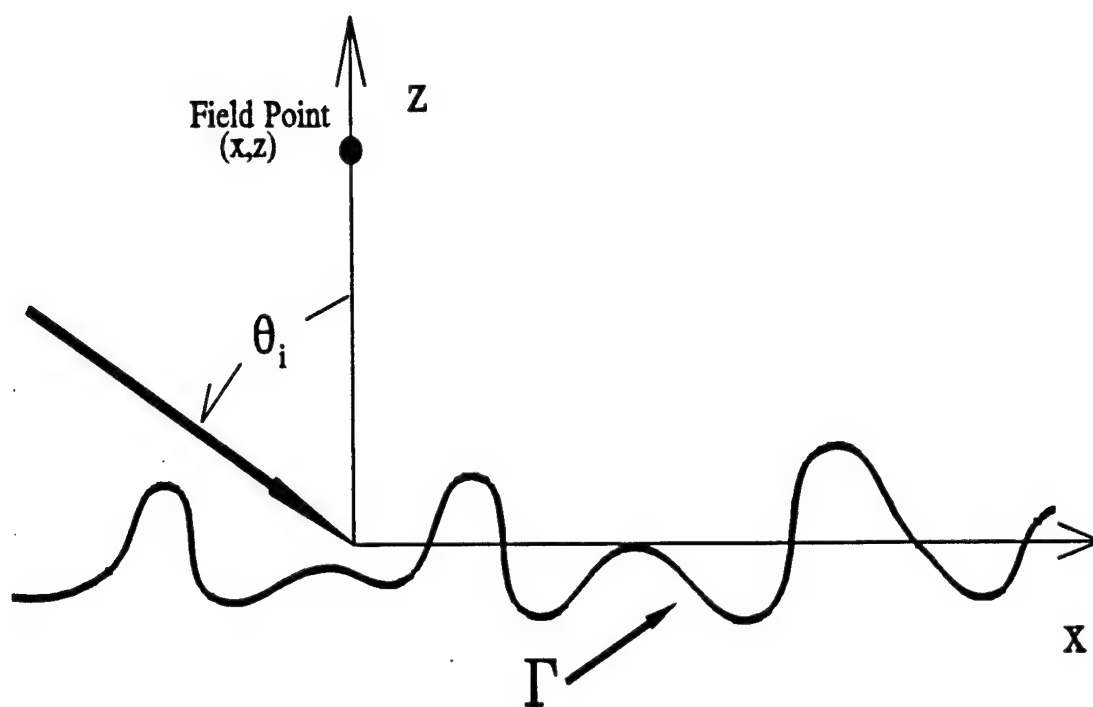


**Figure 1**      **Geometry of Scattering Problem.**



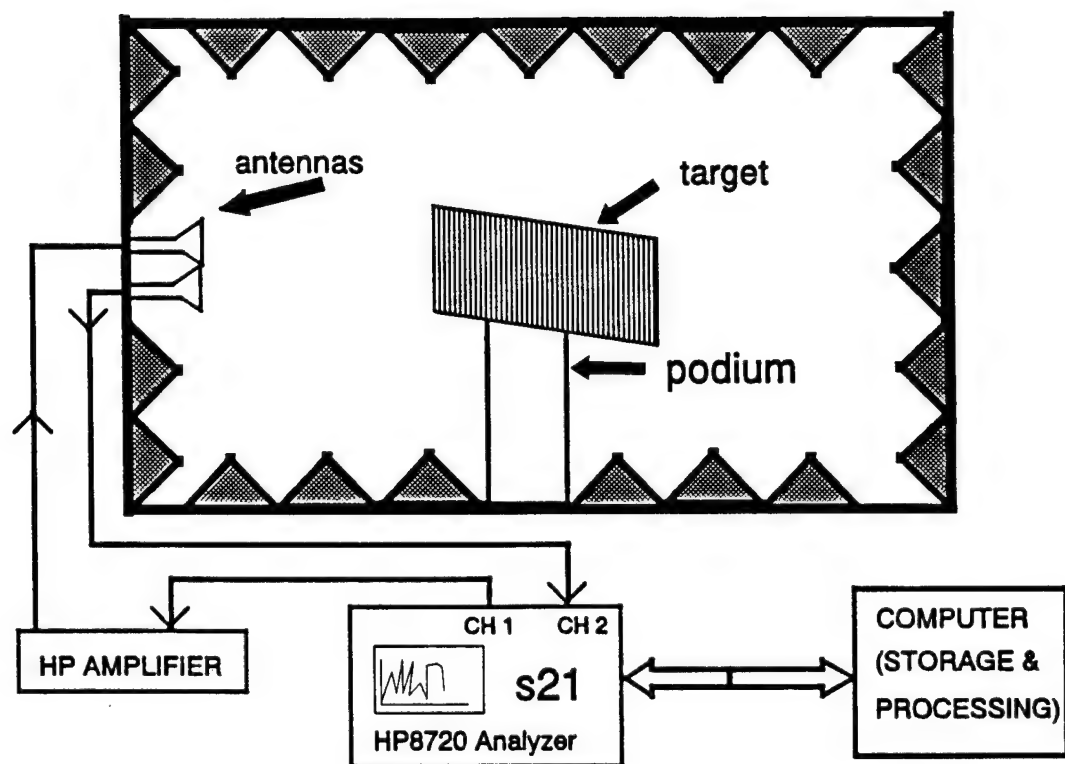


**Figure 2**      **Diagram of the Ultra-wideband Scattering Range at MSU.**

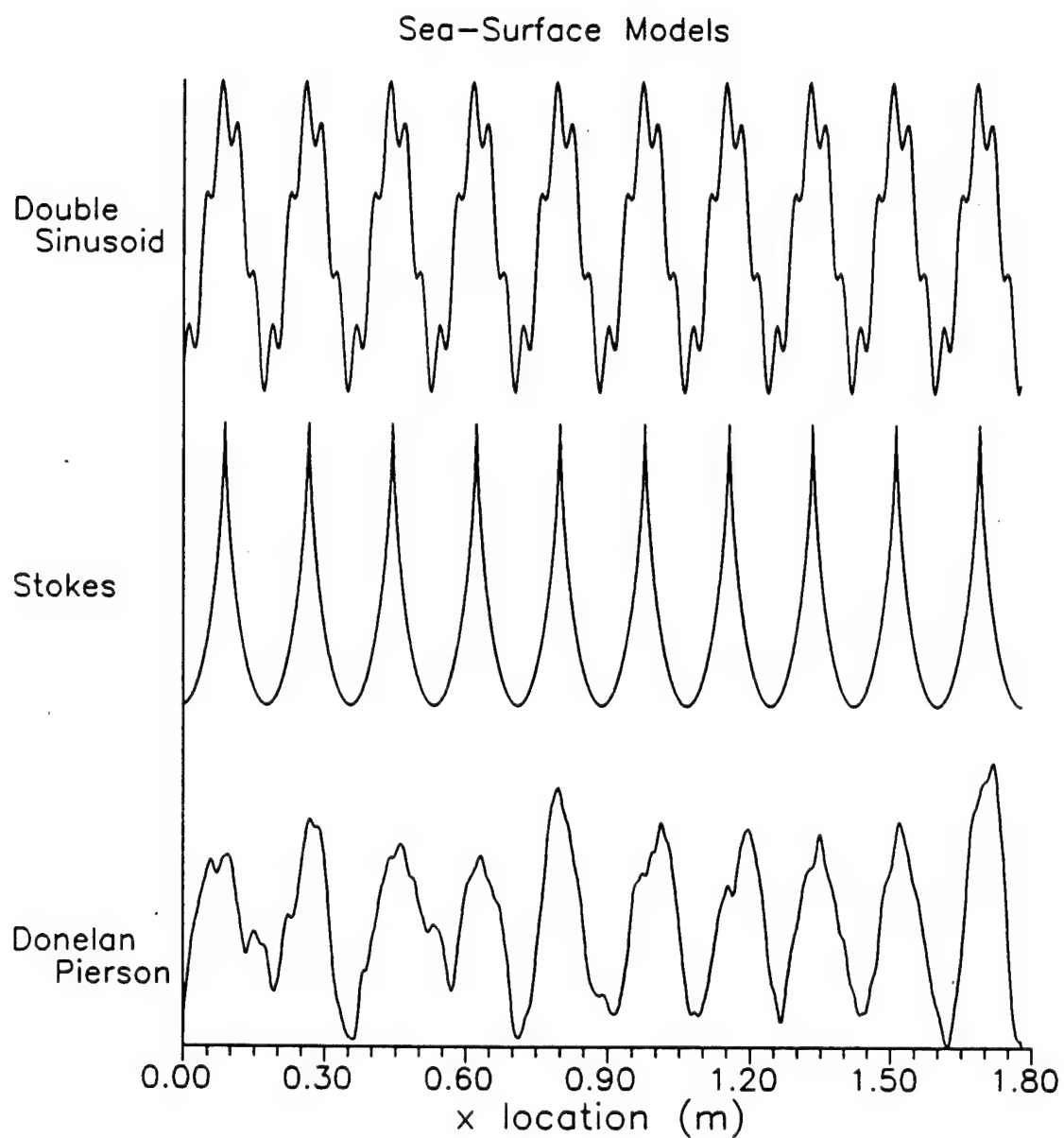


**Figure 3**      **Comparison of Sea-Surface Models.**

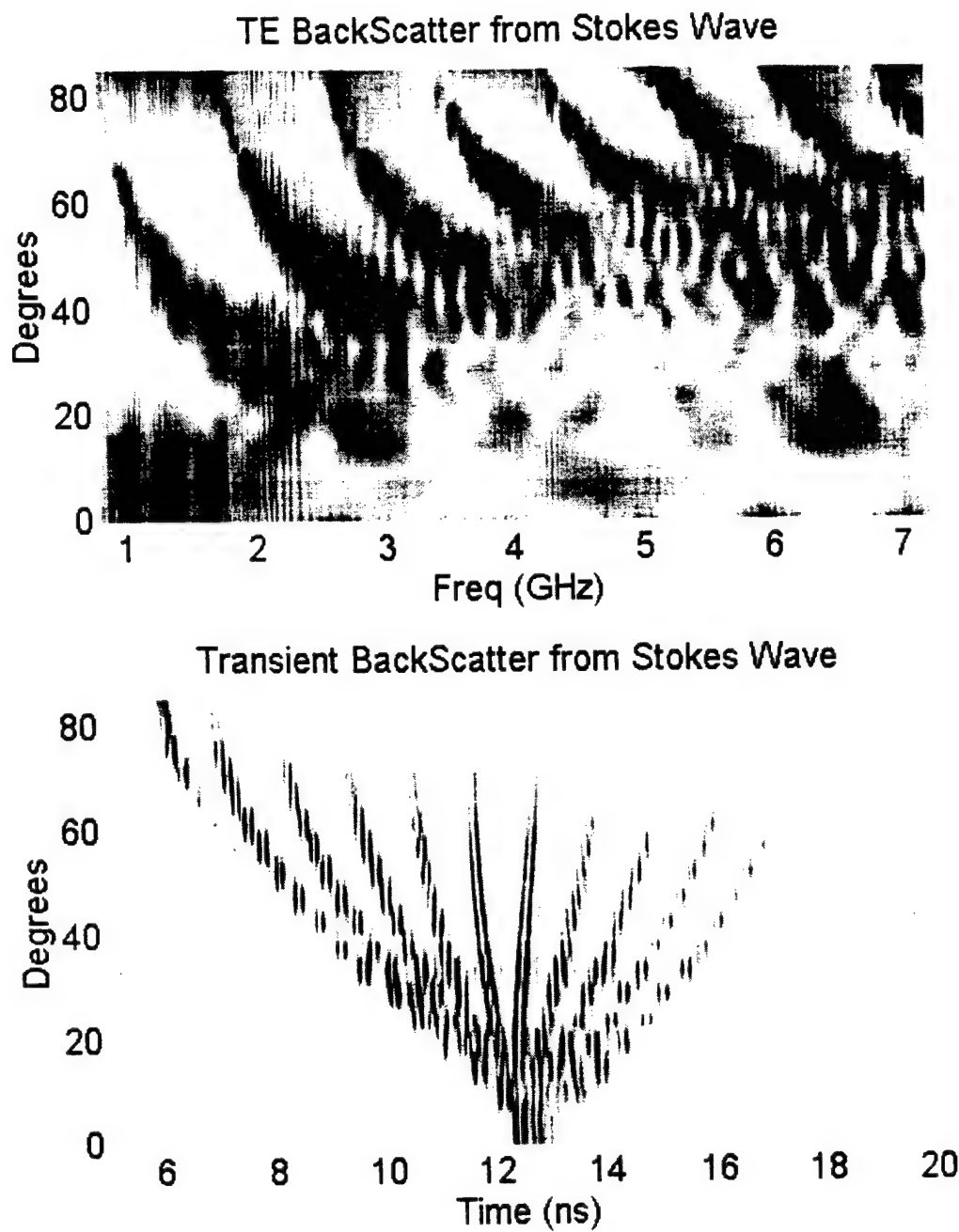


**Figure 4** Experimentally Measured Scattering from the Stokes Wave.

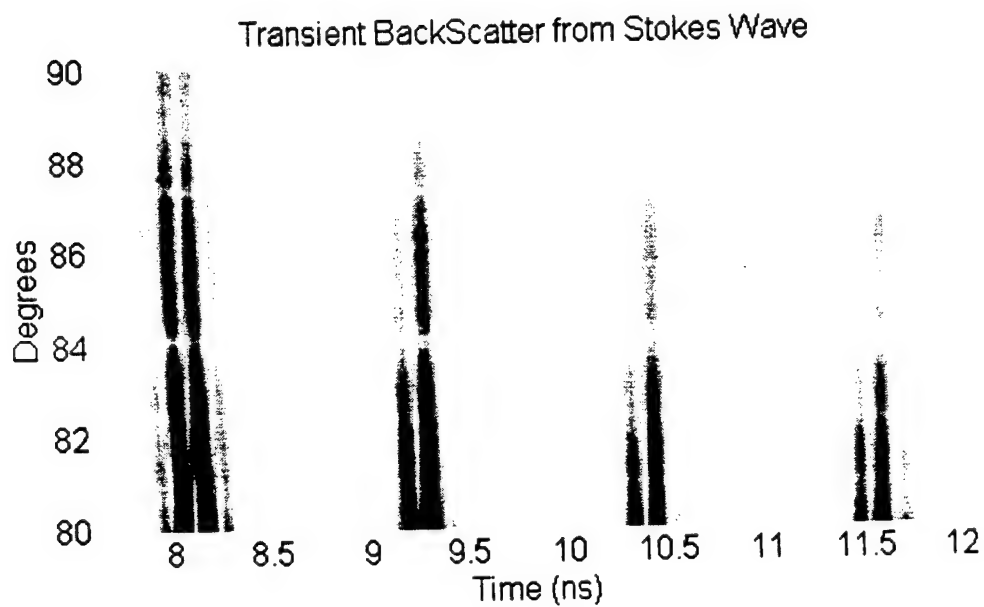
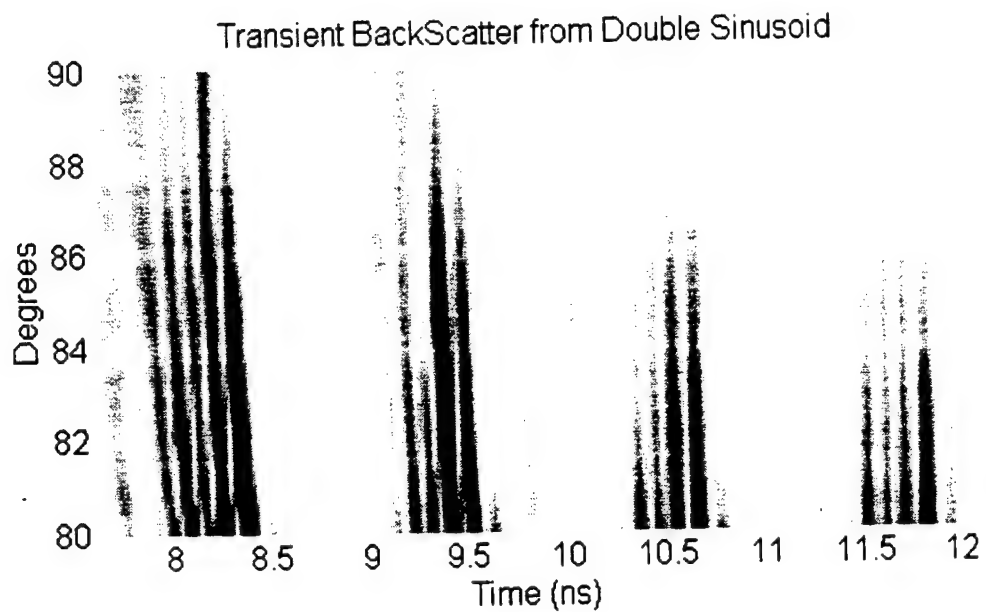


**Figure 5** Comparison of Synthesized TE Transient Backscatter from the Stokes Wave and the Double Sinusoid Wave.

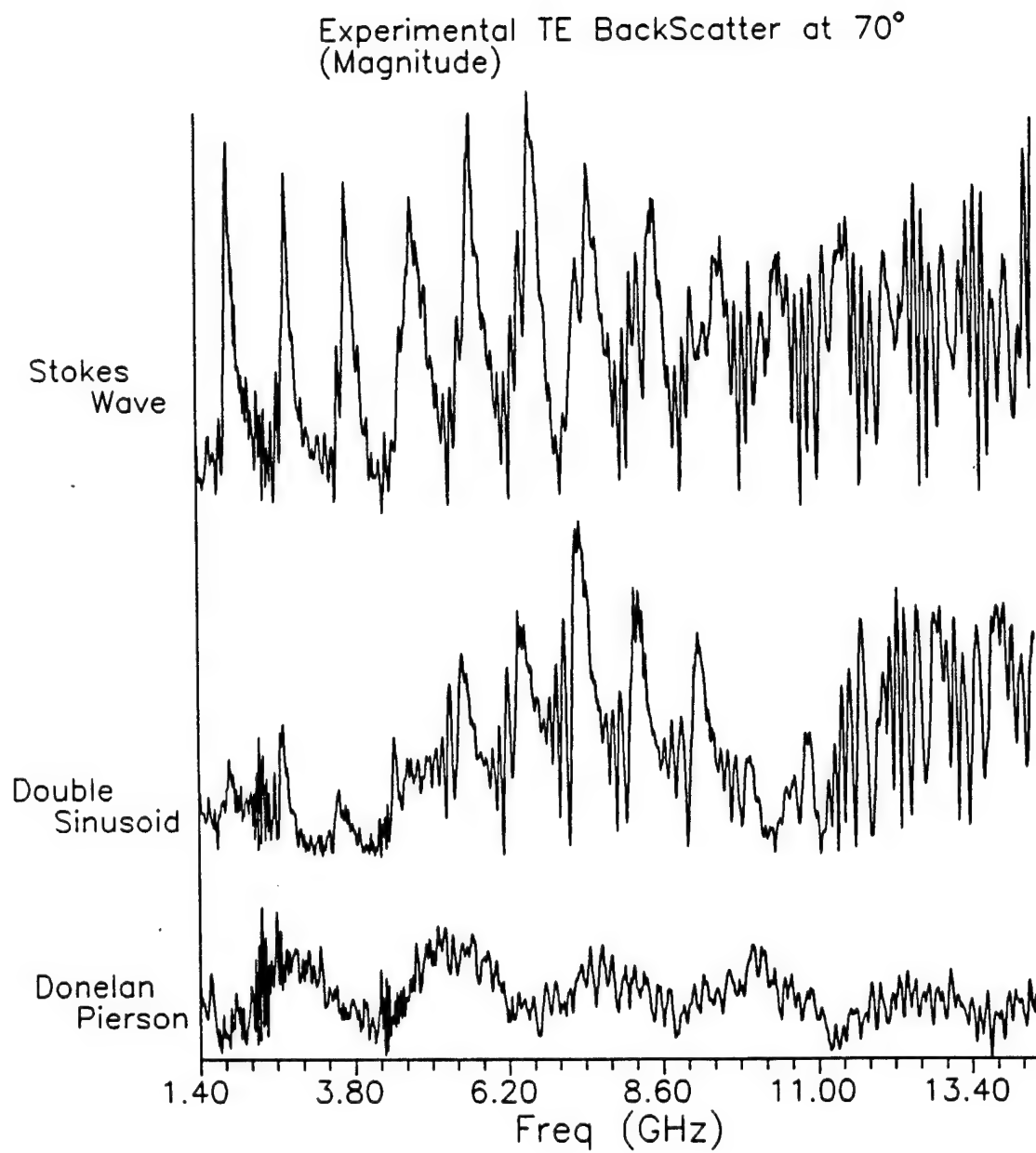


**Figure 6** Experimental TE scattering from various wave models for an incidence angle of 70°.

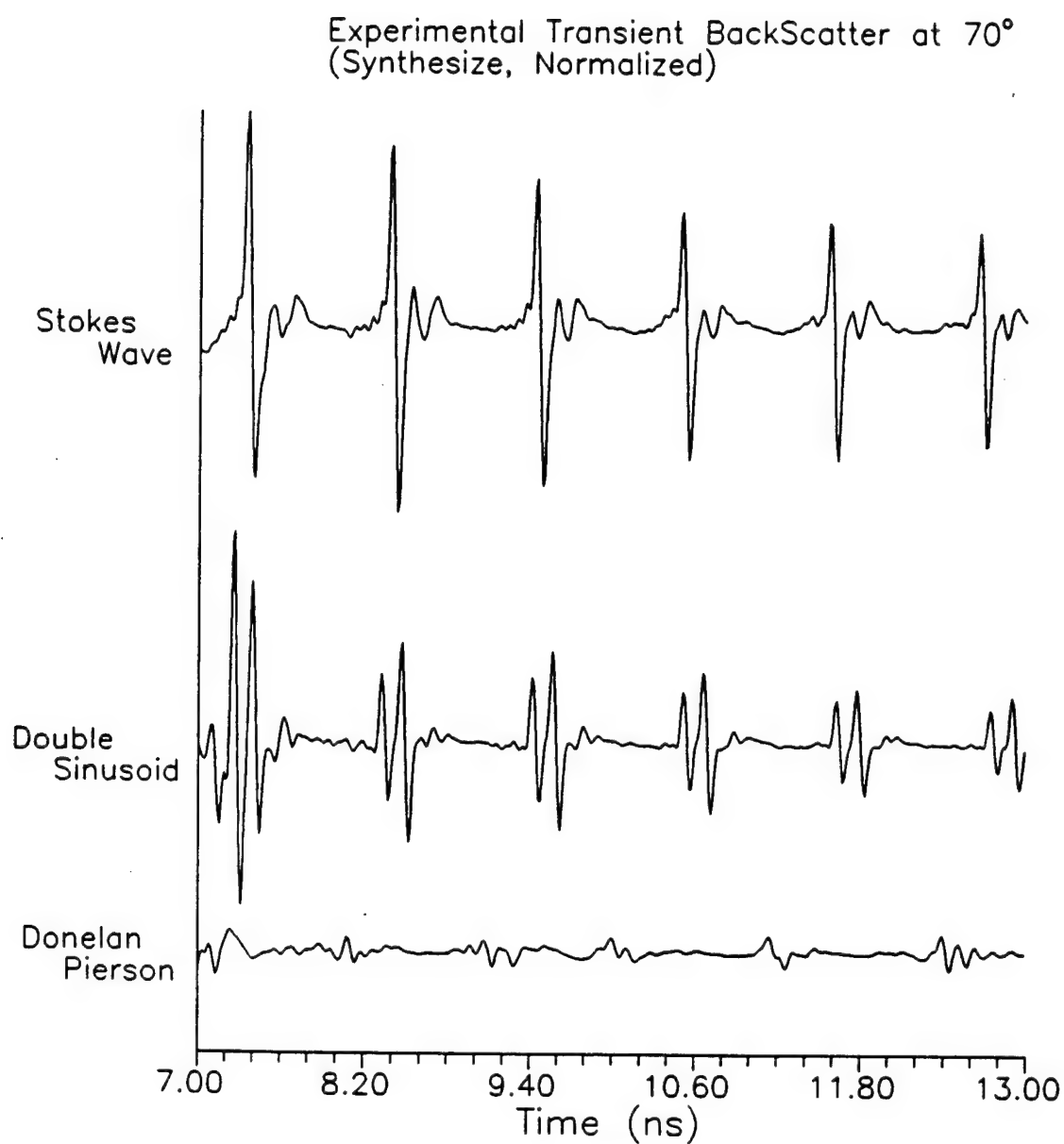


**Figure 7** Experimental synthesized transient scattering from various wave models for an incidence angle of 70°. GMC weighting applied to spectrum before IFFT.

TE Backscatter from Stokes Wave  
Incidence Angle=60°, 0.4–2.96 GHz

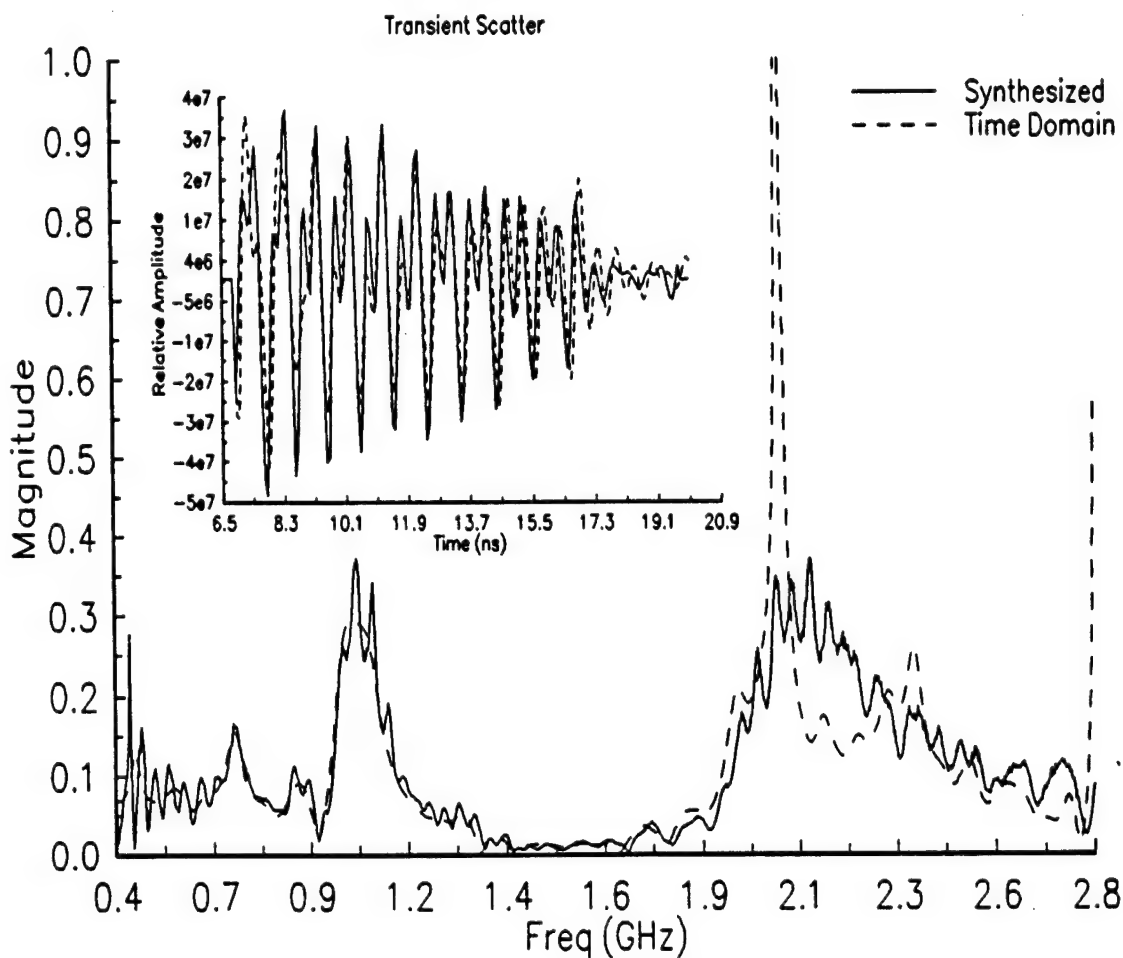


**Figure 8** Comparison of Frequency Domain Synthesis measurement with Time Domain measurement. Both Spectral and Transient returns for Stokes Wave interrogated at 60°.

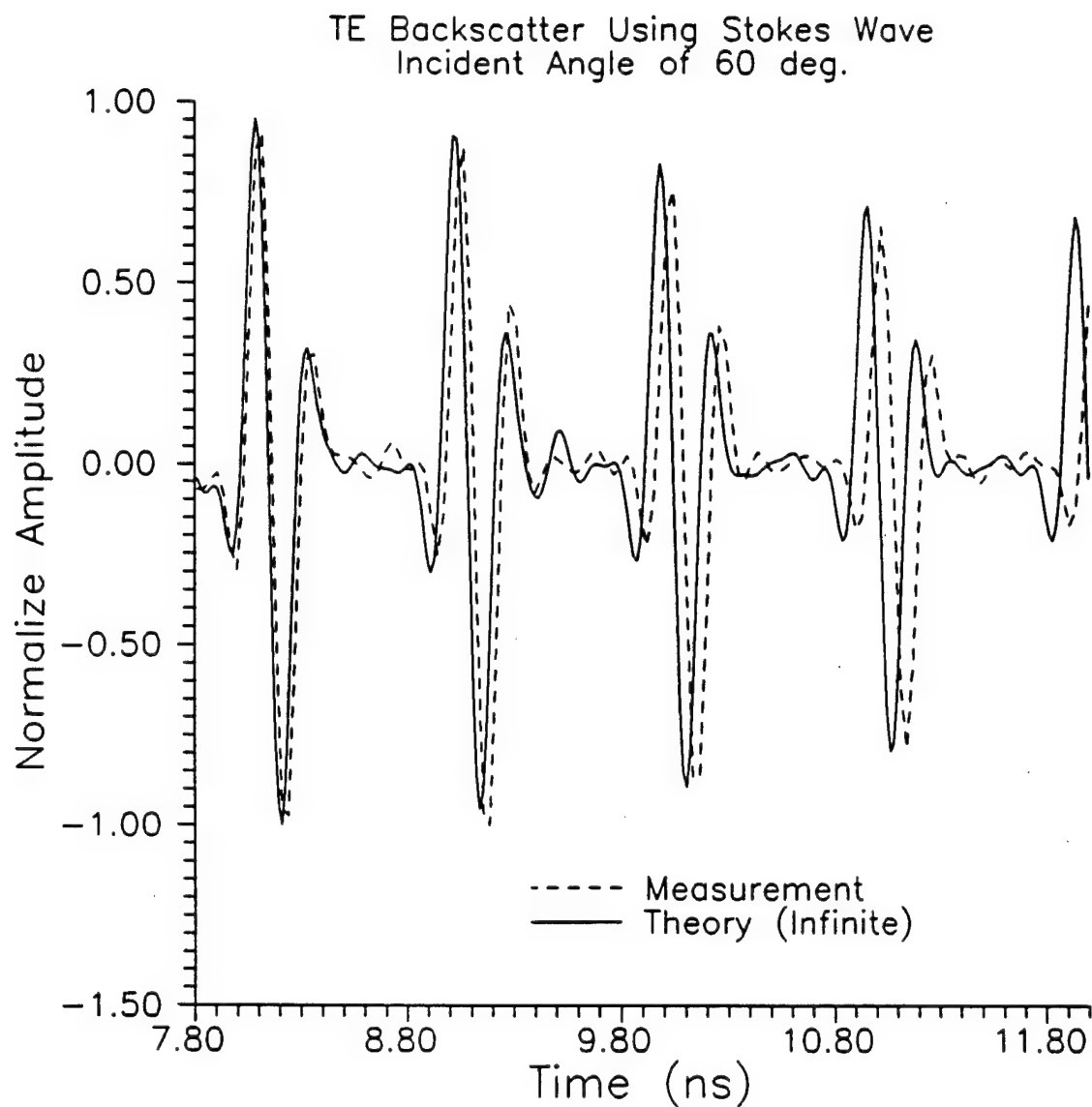


**Figure 9** Comparison of Synthesized transient scattering from Stokes wave with theoretical transient scattering at 60°. Using 0.8-7.2 GHz GMC windowed spectral content.



TE Backscatter Using Stokes Wave  
Incident Angle of 60 deg.

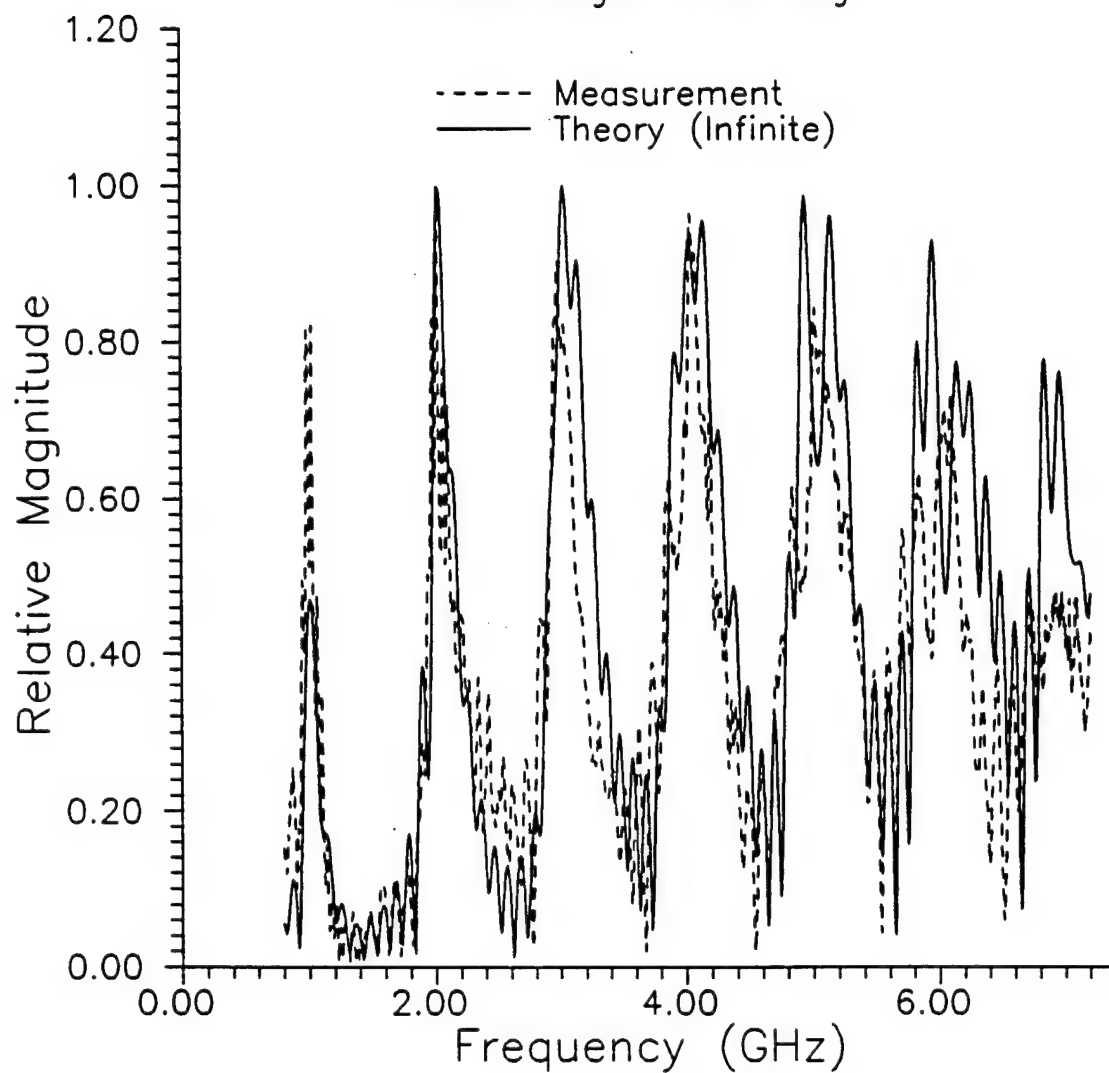


**Figure 10** Comparison of TE scattering from Stokes wave with theoretical scattering at 60°.

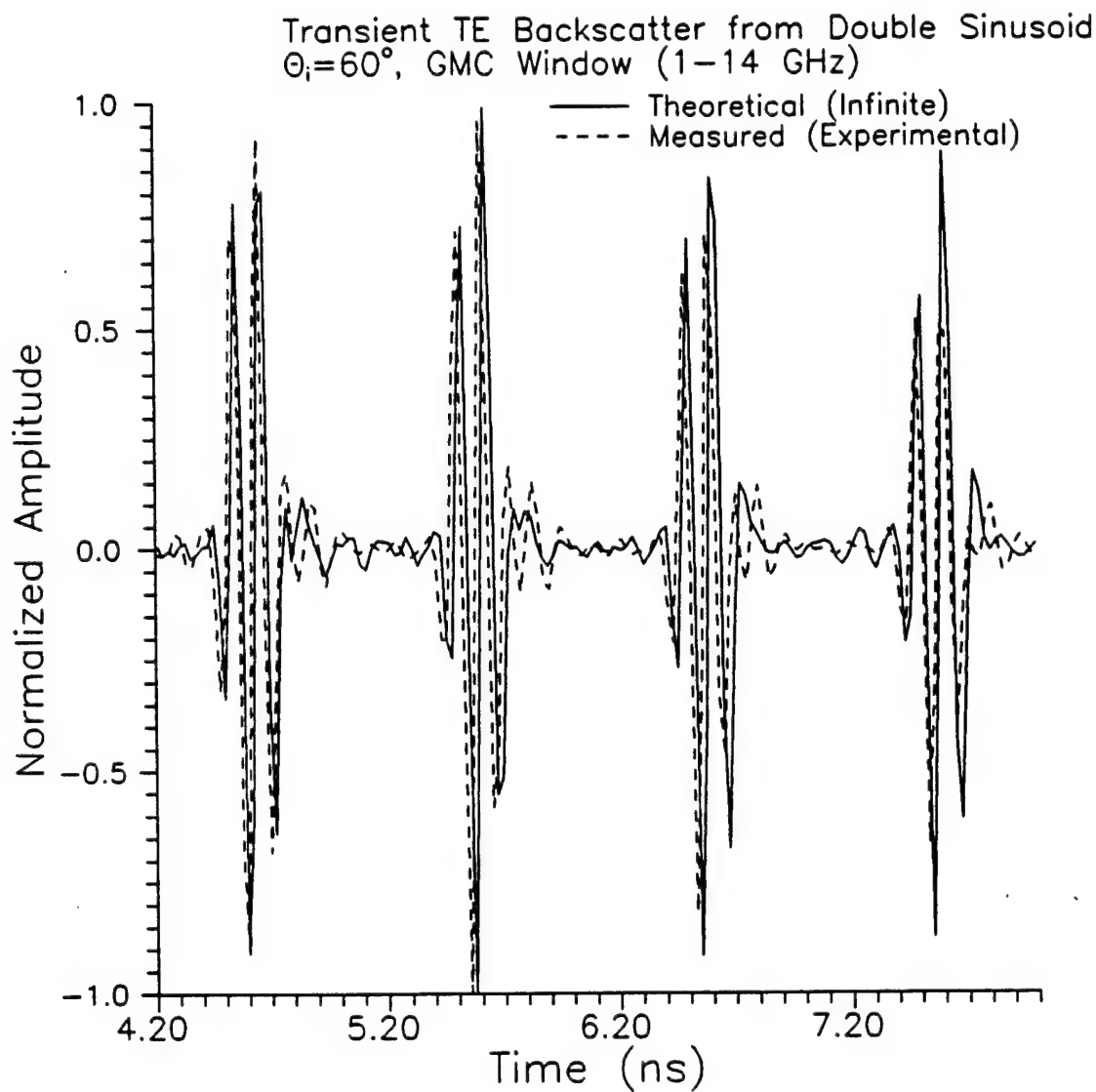


**Figure 11** Comparison of Theoretical and Measured Transient Scattering from the Double Sinusoid Wave. Angle of Incidence is  $60^\circ$ .

TE Scattering From Donelan Pierson Wave  
Incidence Angle of  $60^\circ$ , 0.8–7.2 GHz

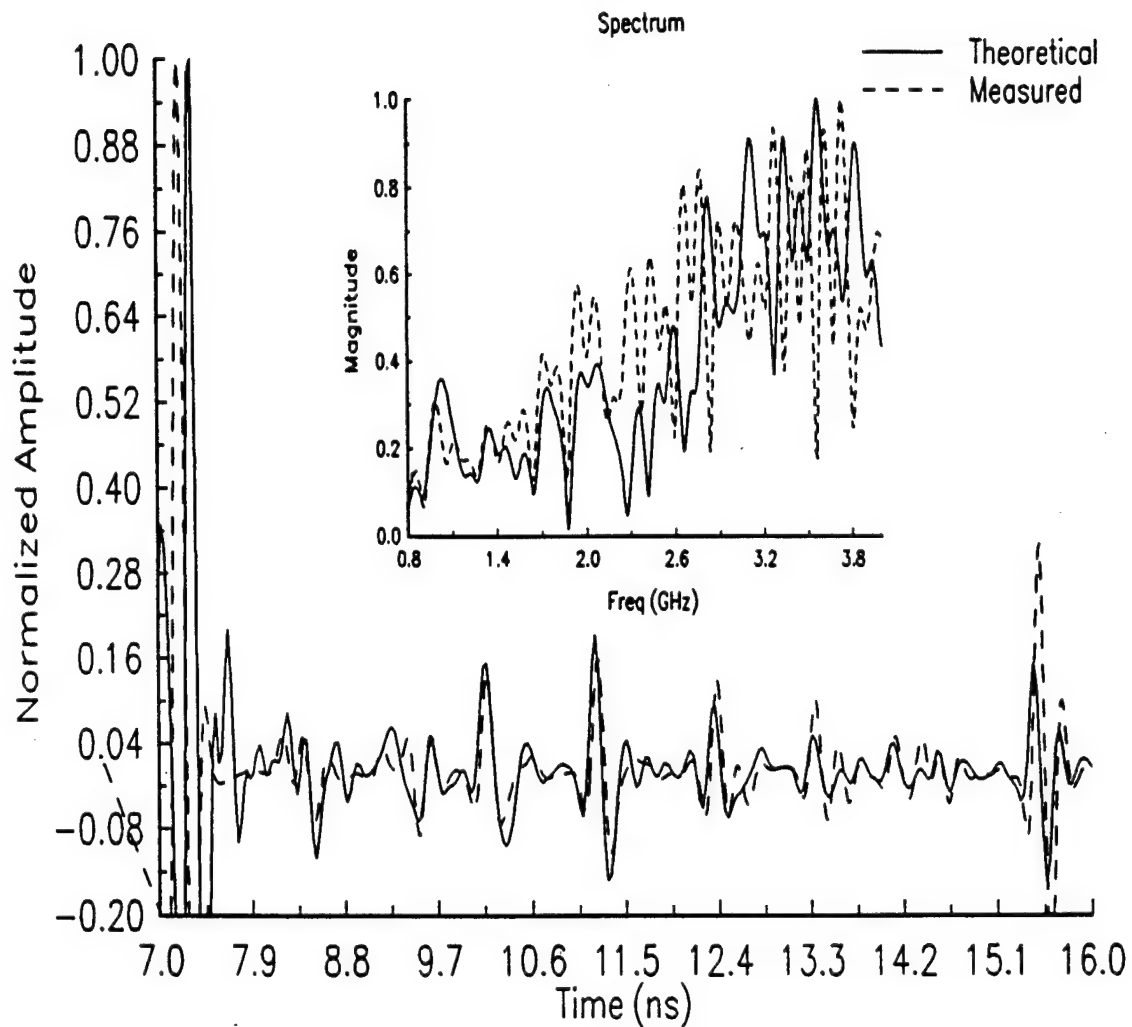


**Figure 12** Comparison of Theoretical and Measured Scattering from the Donelan Pierson Wave. Angle of Incidence is  $60^\circ$ .

Transient TE Scattering from the Double Sinusoid Model  
Field Point is at  $z=1\text{m}$ ,  $\theta_i=85^\circ$

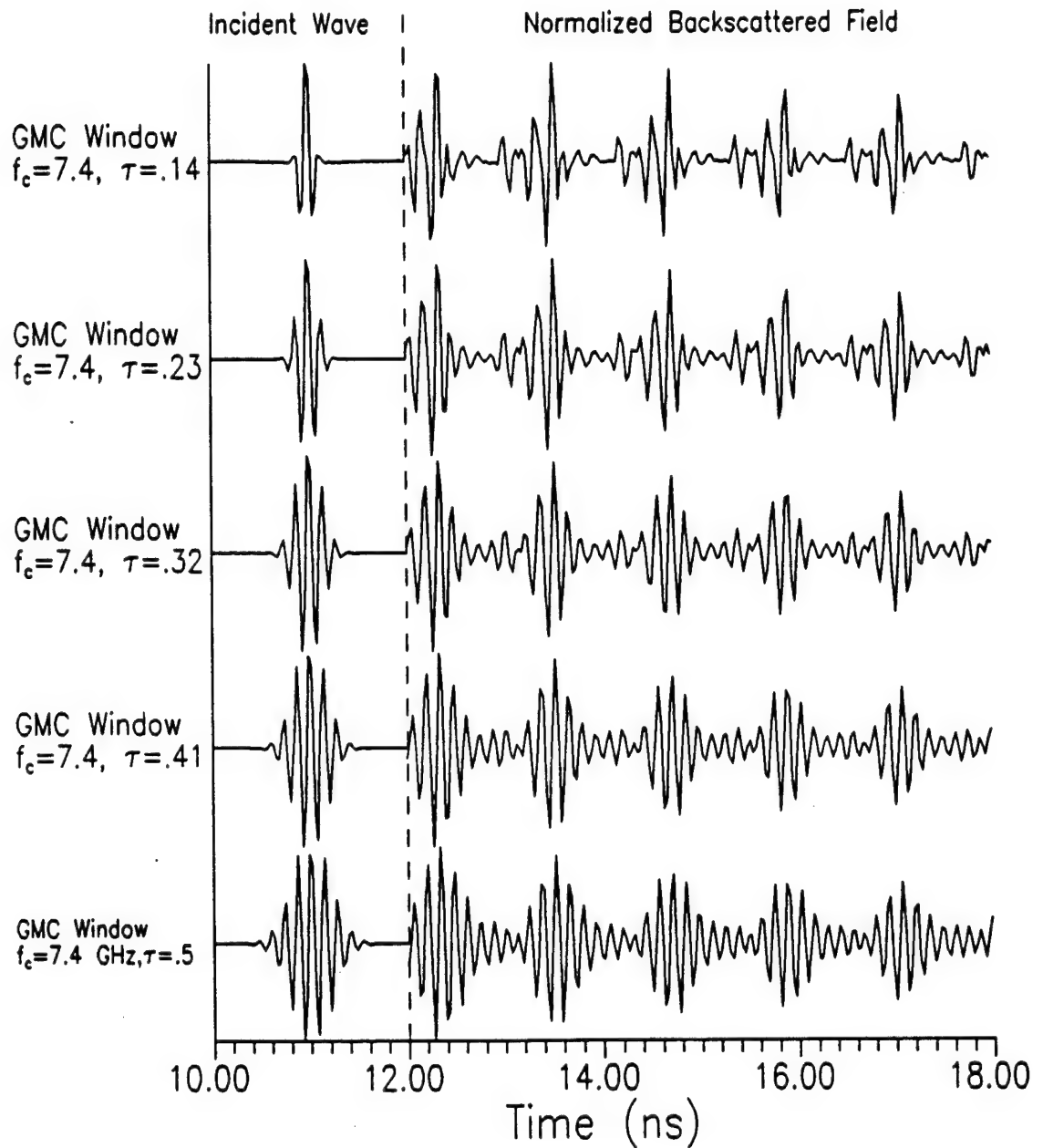


**Figure 13** Theoretical Scattering from Double Sinusoid Wave at  $85^\circ$ , with the effect of GMC window width examined.

Transient TE Scattering from the Double Sinusoid Model  
Field Point is at  $z=1\text{m}$ ,  $\theta_i=85^\circ$

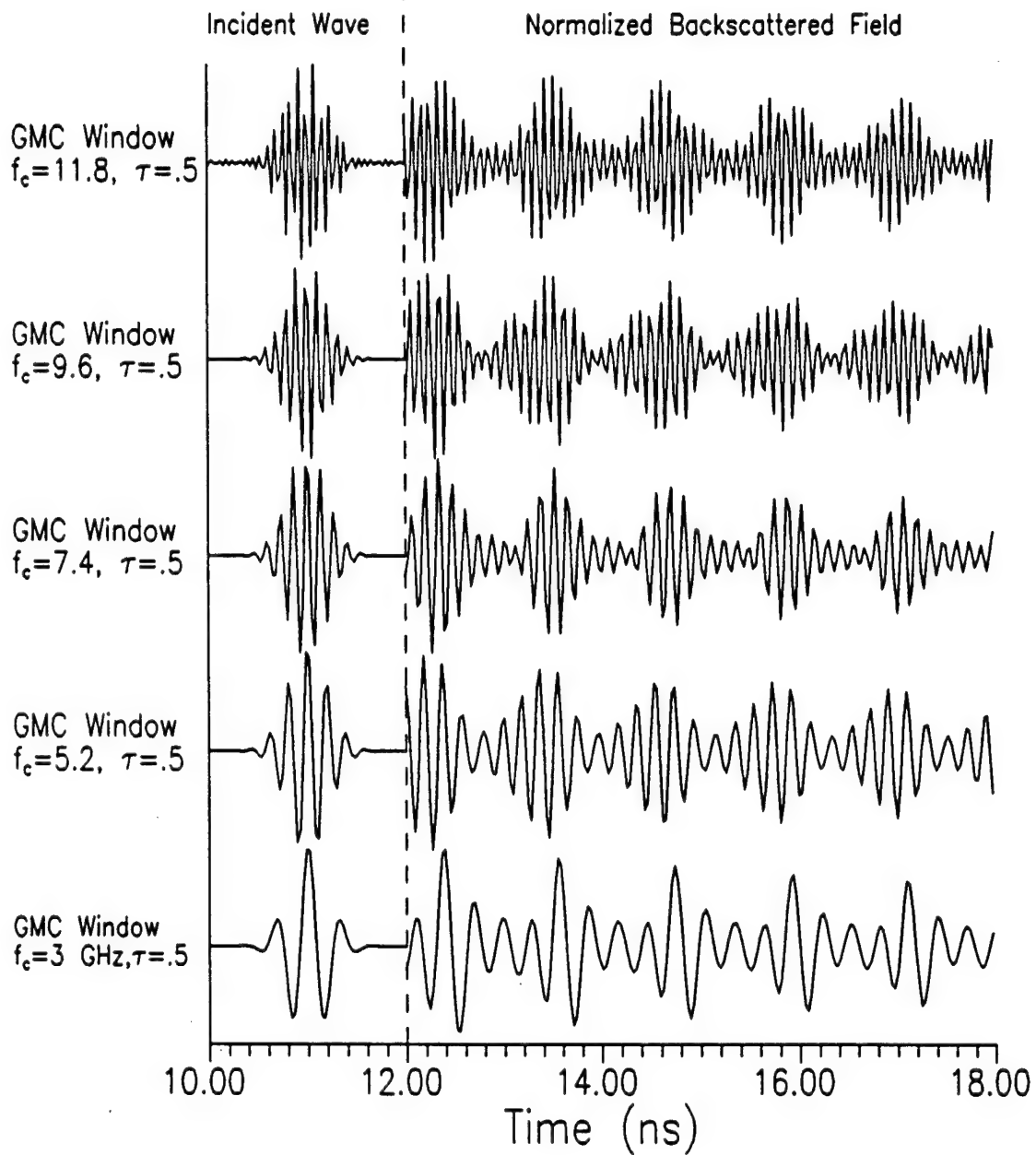


**Figure 14** Theoretical Scattering from Double Sinusoid Wave at  $85^\circ$ , with the effect of GMC window center frequency examined.

## Appendix 3

### Enhanced detection of a target in a sea clutter environment using a stepped, ultra-wideband signal and E-pulse cancellation

G.S. Wallinga, E.J. Rothwell, K.M. Chen, D.P. Nyquist

A new ultra-wideband technique to detect a sea-skimming missile in a sea-surface clutter background is presented. This technique, based on the E-pulse concept, is shown to be effective in maximizing the target to clutter ratio. Results using both measured and theoretical data from scaled surfaces demonstrate the usefulness of this method.

#### I. Introduction

A basic problem faced by on-board ship radar systems is the detection of a sea-skimming missile immersed in background clutter from the sea-surface. Interest in ultra-wideband (UWB) radar systems arise from their potential use for target detection. The use of an UWB system becomes more important when the signal returned by the target is small compared to the background clutter. Using the increased bandwidth (characteristic of UWB radar) and the periodic nature of sea swell one can create a clutter reducing transient waveform (CRTW) which can be used to eradicate the clutter return and enhance the target response.<sup>1</sup>

A new technique, based upon E-pulse concepts<sup>2</sup>, has been devised which allows detection of low signal targets in a sea-clutter environment. One of the inherent difficulties in using the

classical E-pulse method is that when one tries to eradicate merely the sea-clutter return, both the sea-clutter *and* target response are attenuated, resulting in a poor target to clutter ratio. A new approach to the problem is not to eradicate the clutter altogether but to maximize the target to clutter energy ratio.

Several examples will be presented showing the usefulness of this new CRTW technique. The first example uses the measured clutter return from a perfectly conducting (PEC) sea-surface model, in conjunction with the measured scattered return from a small missile model. A CRTW was constructed and applied to a combined sea-surface/target return data set. This first example was designed to show that this new technique works for a simple static situation. Since one is interested in the effect of a changing sea-surface, a second example considers a more realistic model that can evolve over time. In this case, a time-simulation of an evolving sea-surface was created and the scattered fields were numerically calculated. Using the measured missile model a CRTW was calculated for the initial sea-surface. A simulation was then performed in which a missile traveling over the evolving sea-surface was detected using the CRTW technique. Results of that simulation show the effects of an evolving sea-surface on the CRTW technique and the need for periodic updates to an initial CRTW.

## II. Theory

Consider a UWB radar system illuminating a finite portion of the sea-surface where a target is anticipated. If the two-way transit time of the radar signal across the finite portion of the sea-surface is  $W$ , then the transient scattered field is available in the time range  $\tau < t < \tau + W$ , where  $\tau$  is the time of measurement. A CRTW, based on E-pulse concepts, can be

constructed if the clutter return from the sea-surface can be modeled as a series of complex exponentials

$$c(t) = \sum_{n=-N}^N A_n e^{Q_n t} \quad \tau < t < \tau + W \quad (1)$$

where  $A_n$  and  $Q_n$  are complex parameters appearing in complex-conjugate pairs. Furthermore, the CRTW  $e(t)$ , like the E-pulse, is a waveform of finite duration  $T_E$  which when convolved with the sea-clutter signal yields the null result

$$r(t) = e(t) * c(t) = \int_{\tau}^{\tau+W} c(t') e(t-t') dt' = 0 \quad \tau + T_E < t < \tau + W \quad (2)$$

Hence, only a small signal will be returned if the CRTW is radiated in the presence of sea-clutter.

One of the problems arising in the construction of the CRTW is that a target signal embedded in the clutter return is also reduced, often to such a point that the target-to-clutter ratio is not really improved. An alternative to (2) is to construct a CRTW such that the following energy ratio is maximized

$$\epsilon(t, \tau, t') = \frac{\int_{t-\Delta/2}^{t+\Delta/2} \{e(x) * [c(\tau+x) + T(t'+x)]\}^2 dx}{\int_{t-\Delta/2}^{t+\Delta/2} \{e(x) * c(\tau+x)\}^2 dx} \quad T_E + \frac{\Delta}{2} < t < W - \frac{\Delta}{2} \quad (3)$$



In this case the energy ratio is computed in a window of length  $\Delta$  centered at time  $t$ .  $T$  is the time response of an anticipated target and  $t'$  is a parameter which time shifts the target response within the time range bin of the clutter signal. A qualitative argument supporting the use of (3) can be made by observing that the term in the denominator should be quite small as give by (2). On the other hand, the numerator contains two terms: the convolution of the CRTW with the clutter return and the convolution of the CRTW with the time shifted target response. Once again we can consider the term involving the CRTW/clutter convolution to be small, but hopefully the second convolution will not be. The net result is that the energy ratio may be significant for the correct choice of  $e(t)$ .

To envision the detection process one must proceed in the following manner. First at some initial time  $\tau_0$  a measurement is made of the sea-clutter waveform  $c_0(t) = c(\tau_0 + t)$ . A pre-recorded response  $T(t)$  of the anticipated target is then added to the measured sea-clutter waveform. Next, a CRTW is constructed to maximize the energy ratio  $e(t, \tau_0, t')$  in (3). In this case the energy ratio is a function of the parameters  $t$  and  $t'$  where  $t$  represents the position of the energy window and  $t'$  corresponds to the target time-shift. Careful observation of (3) also shows that the energy ratio is a function of the time window width  $\Delta$ . The optimal positions of  $t_m$  and  $t_m'$  represent the window position for maximum energy and optimal target position for detection. In most cases one can expect that  $t_m = t_m'$ .

Once  $e(t)$  has been determined, detection can progress by measuring the sea-surface return at some later time  $\tau > \tau_0$ . At this time an energy ratio given by

$$\bar{\epsilon}(t) = \frac{\int_{t-\Delta/2}^{t+\Delta/2} \{e(x) * c(\tau+x)\}^2 dx}{\int_{t-\Delta/2}^{t+\Delta/2} \{e(x) * c(\tau_0+x)\}^2 dx} \quad T_E + \frac{\Delta}{2} < t < W - \frac{\Delta}{2} \quad (4)$$

is computed. If no target has entered the observation bin and the sea surface remains essentially stationary, the energy ratio will be unity for all  $t$ . Given that the denominator term in (4) remains small one should expect the value of  $\bar{\epsilon}(t)$  to be significantly greater than unity when a target enters the range bin. The value of  $\bar{\epsilon}(t)$  should be large for  $t$  corresponding to the target position and should reach a maximum value when the target reaches the position corresponding to  $t_m$ .

It is important to consider the effect of an evolving sea-surface on  $\bar{\epsilon}(t)$ . For  $\tau > \tau_0$ , the sea-surface will be different than that used to compute  $e(t)$  and the energy ratio computed using (4) will slowly change. As  $\bar{\epsilon}$  rises above unity the ability to detect a target in the range bin will degrade. One then finds it necessary to periodically recompute  $e(t)$ . Figure 1 shows a flowchart for the detection process.

### III. Stationary Surface Demonstration

To demonstrate some of the ideas presented in the preceding section the scattered fields from two PEC surfaces were measured. The surfaces are shown in figure 2. The scattered fields from the two-dimensional surfaces were measured within an anechoic chamber in the band 1 to 17 GHz using 1601 frequency points. The data was then transformed into the time domain to give the clutter signal  $c_0(t)$ . The surfaces should be viewed as a scaled down version of a real

surface. The dimensions of the surface were chosen to allow measurements in the anechoic chamber.

The first surface, known as a Stokes wave<sup>3</sup>, is characterized by steep slopes and is a simple model used to simulate periodic ocean waves. Using an electric field parallel to the wave crest (TE polarization), and an incidence angle of 10° from the horizon, the scattered fields for the Stokes wave is shown in figure 3. As can be seen the scattered field is dominated by reflection from the main crests of the Stokes wave. The second surface is a double sinusoid and was measured under the same conditions as the Stokes wave. This surface is characterized by two scale roughness. The wave profile is give by  $y(x) = .025(1 - \cos 35.4x) + 0.06 \sin 177x$  (m). The scattered field for this surface is shown in figure 4. Once again the scattered fields are dominated by reflection from the sea-wave crests. A scaled 8 cm long Phoenix missile model was used as the expected target. The scattered field from this target is shown in figure 5. In this measurement the electric field was anti-parallel to the long axis of the missile and the angle of incidence was again 10° with respect to the long axis of the missile.

Using the target and clutter responses, scaled to unity, the CRTWs shown in figure 6 were constructed by maximizing the ratio given in (3). The actual construction of the CRTW (maximization of (3)) was implemented using a genetic algorithm. To simulate the detection response, the missile scattered field was scaled by 20% of the clutter maximum value (target to clutter ratio of TCR = -14dB) and added to the sea-clutter surface response. For the Stokes wave the target response was added to the clutter response at two locations:  $t = 4.9$  nsec and  $t = 7.8$  nsec. For the double sinusoid surface the target response was added at locations  $t = 5.6$  nsec and  $t = 11.0$  nsec. The energy ratio response given by (4) was computed for each surface.

The results are shown in figures 7 and 8 for the Stokes and double sinusoid respectively. Also included in these figures is the summed target and clutter response give by  $c(\tau+x)$  in (4). Figure 7 shows that when the target is located at  $t = 5$  nsec the energy ratio  $\bar{\epsilon}$  reaches 22 dB and the target is easily detected. On the other hand a target located at  $t = 8$  nsec has a lower value  $\bar{\epsilon} = 3$  dB indicating that this is not the best location to detect the target. The energy ratio corresponding to the double sinusoid ( fig. 8) shows similar patterns. At  $t = 11$  nsec the ratio is 9 dB indicating a large jump and hence target detection. In contrast, at  $t = 6$  nsec the value of  $\bar{\epsilon}$  is much smaller and not the best location for a target to be detected. In both figures points outside the convolution window have a value of  $\bar{\epsilon}(t)$  equal to unity (0 dB). This follows since the summed signal used in the detection scenario is identical to that used to create  $e(t)$ .

#### IV. Simulated Sea-Surface Demonstration

A more realistic sea-surface profile has been proposed by Kinsman<sup>4</sup>. An evolving sea surface profile  $y(x,t)$  can be computed using the stochastic model

$$y(x,t) = \int_0^{\infty} \cos\left[\frac{\sigma^2}{g}x - \sigma t + \Phi(\sigma)\right] \sqrt{[A(\sigma)]^2 d\sigma} \quad (5)$$

where  $\Phi(\sigma)$  is a phase shift arbitrarily equally distributed between 0 and  $2\pi$ . Here the Neumann spatial frequency spectrum is used

$$[A(\sigma)]^2 = C \frac{\pi}{2} \sigma^{-6} e^{-2g^2 \sigma^{-2} U^{-2}} \quad (6)$$

where  $U$  is the wind speed in m/sec,  $g = 9.81 \text{ m/sec}^2$  is the acceleration due to gravity, and  $C = 3.05 \text{ m}^2/\text{sec}^5$ . A typical spectrum generated using 20 knot winds is shown in figure 9. A numerical measure of the sea-surface evolution can be obtained by calculating the covariance function at a fixed position on the surface. The covariance function<sup>4</sup> may be written as

$$H(t_j, t_k) = \frac{1}{2} \int_0^{\infty} [A(\sigma)]^2 \cos[\sigma(t_k - t_j)] d\sigma \quad (7)$$

In this case we are observing an ensemble of functions  $\{y(t)\}$  at times  $t_j$  and  $t_k$  at a fixed position. It is important to note that the covariance is only a function of the *observation interval*. This follows from the time-invariant statistics or stationarity of the process. For a 20 knot wind, figure 10 shows the covariance function in terms of the observation interval  $T$ . For  $T = 0$  the covariance can be written as

$$H(t_j, t_k = t_j) = \frac{1}{2} \int_0^{\infty} [A(\sigma)]^2 d\sigma \quad (8)$$

Integrating the spectrum over all frequencies gives a measure of the total energy in the wave field, i.e.

$$E = \int_0^{\infty} [A(\sigma)]^2 d\sigma \quad (9)$$

Comparing (8) and (9) we see that

$$E = \frac{1}{2} H(t_j, t_k = t_j) \quad (10)$$

In this case the covariance for a step interval of 0 is directly related to the wave energy through (10). Since the energy can be calculated from (9) one sees that the energy is directly related to the wind speed through (6). The point corresponding to  $T = 0$  in figure 10 coincides with twice the energy given by (10). Since the covariance function is an indicator of sea-surface evolution, figure 10 illustrates the progression of the sea as function of time separation  $T$  at a given point. As shown in this figure the covariance value decreases as a function of time separation. From this figure we see that after about 2 seconds the covariance has dropped to about zero and never returns to its original value, although it does slowly creep up and then returns back to zero. With the covariance information it is possible to get some idea of how often the scattered field must be remeasured. From figure 10 the measurement must certainly be updated more often than once every two seconds. A better update rate would be at least once or twice a second.

A typical surface profile and scattered field generated by the Kinsman model is shown in figure 11. The scattered field for a PEC with this profile was computed using a 2-d Green's function and moment method solution. The polarization is TE and the incidence angle is 10 degrees from the horizon. Due to computational constraints the sea-surface was scaled down by a factor of 50 (from 1000m total length to 20 meter total length) and the field solved for using 1000 segments. A total of 200 frequency points were computed in the band .5 - 1.5 GHz.

To determine the effects of an evolving sea-surface on the CRTW detection technique the following scenario was devised. A series of sea-wave profiles were generated using (5) at intervals of .25 seconds. Each surface was scaled and the scattered field was calculated numerically as described above. The response from the Phoenix missile model was scaled to match the clutter response and a CRTW was computed from the surface profile at  $\tau = 0$  sec. Next, the missile response was amplitude scaled to a TCR of -14dB and added to the evolving sea surface response. In this case the position of the missile with respect to the sea surface was determined by assuming that the missile was flying at 600 knots. The left hand side of figure 12 shows the evolving sea surface profile and the missile position (indicated by the small arrow).

Using the summed response and the initial clutter capture the energy ratio  $\bar{\epsilon}(t)$  was computed for each time step. This is shown on the right hand side of figure 12 where it is assumed that the CRTW computed at  $\tau = 0$  does not change during the simulation. At  $t = 0$  the clutter signal has not changes and hence the energy ratio computed from (4) must be unity (0 dB). At  $t = .25$  sec the surface has evolved but no target has entered the range bin. In this case the energy ratio is no longer unity but has reached a value of 3 dB. As the sea surface continues to evolve the baseline energy ratio (max value) continues to rise. At  $t = .75$  sec the target enters the range bin and  $\bar{\epsilon}(t)$  reaches a max value of 20 dB near the target. Since the baseline value of  $\bar{\epsilon}(t)$  is about 5 dB at  $t = .75$  sec, a target has been detected with a margin of about 15 dB above the baseline level. Continuing with the simulation, the effect of both the moving target and evolving sea surface can be seen. At  $t = 2.0$  sec the sea surface has evolved to the point where only a 10 dB margin exists between the baseline clutter ratio and the target ratio.

## V. Final Discussion

The new CRTW technique, based upon the E-pulse concept, has been shown to be effective using the measured scattered responses from static surfaces and theoretical responses from more realistic sea wave surfaces. Although the static surfaces are not exact representations of ocean waves they are useful in showing the advantages of the CRTW technique. The evolving sea surface simulation shows that the new CRTW technique can be used in an environment that is constantly changing. One important result of this simulation is the need to update the CRTW periodically. Using the above simulation and actual sea surface data one should be able to determine the rate at which to update.

Other items need to be addressed as a result of this study. First can the CRTW be used to detect other targets, i.e. target not used to generate the CRTW ? Second, what are the effects of the window size on the detection algorithm give by (4)? The third issue must address the actual construction of the CRTW. The author has used a genetic algorithm with good results. The advantages here are no initial guesses required for the solution but the disadvantage is the inefficiency of the algorithm. Fourth, this new technique should carefully be compared to some of the other detection algorithms currently being used. Finally, actual scattering data from a UWB radar system is needed to thoroughly test this technique.



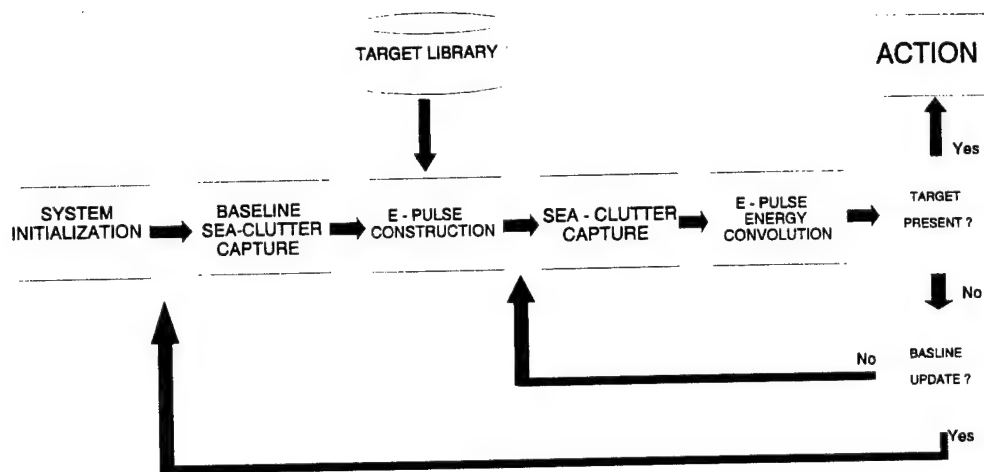


**Figure 1. CRTW Flowchart Process**

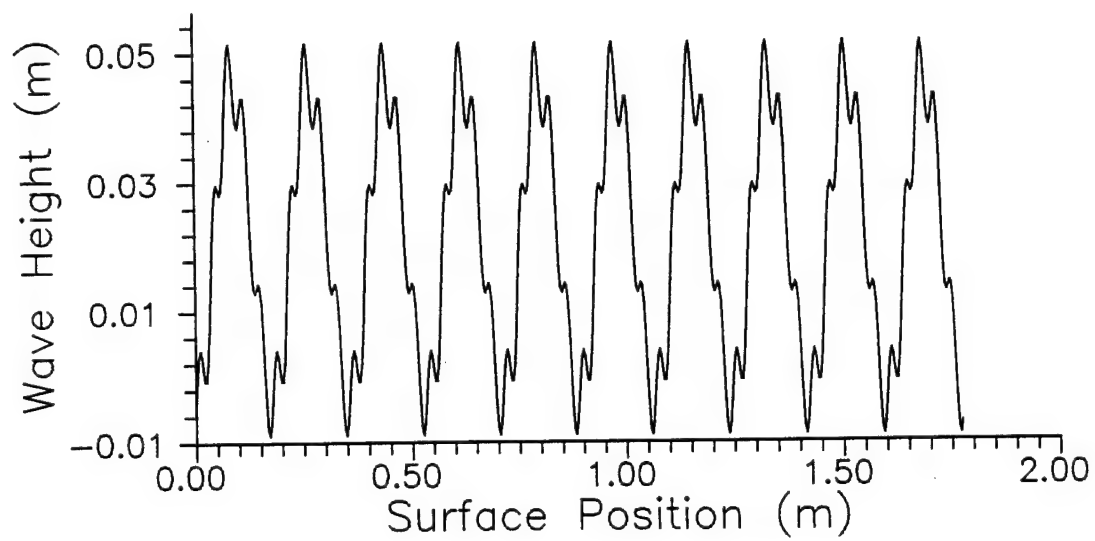
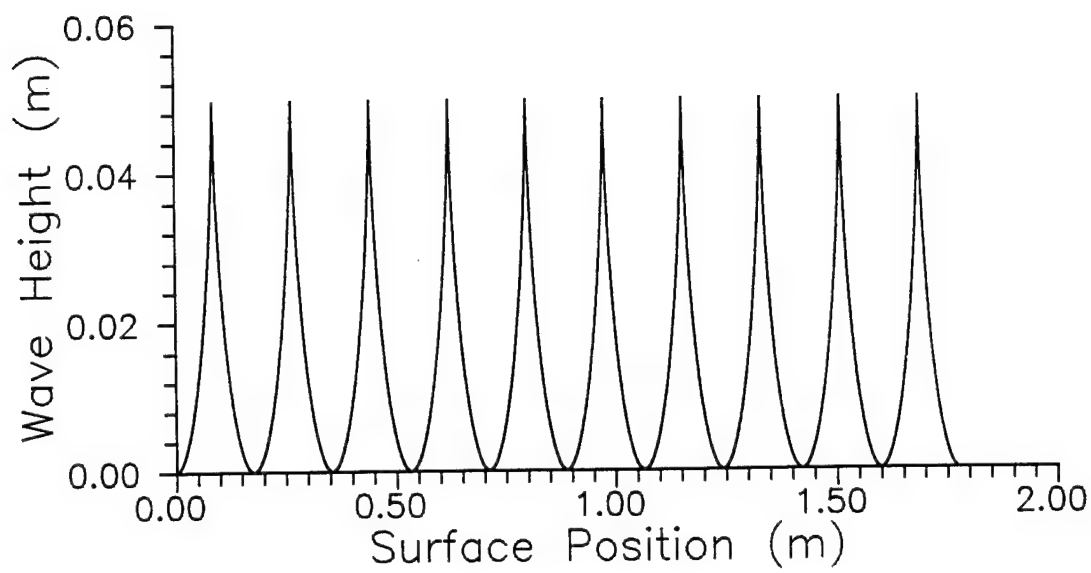


**Figure 2.** Simple PEC Scaled Ocean Surfaces

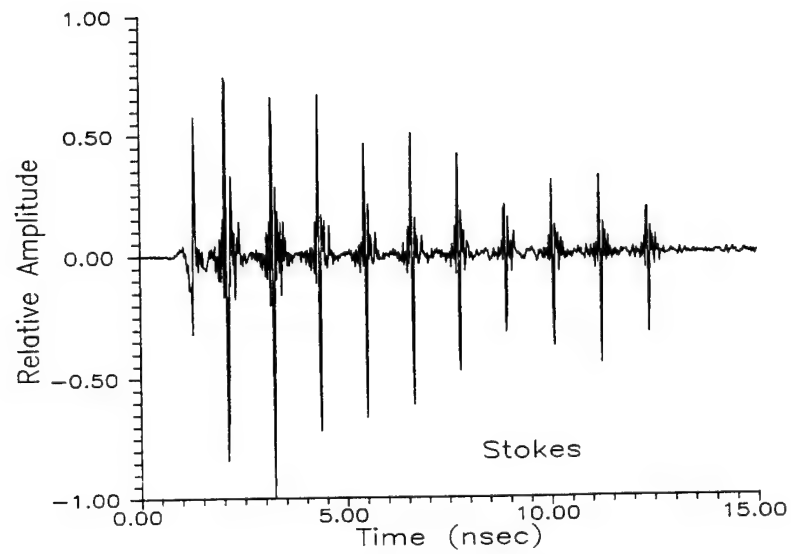


**Figure 3.** Scattered Field from the PEC Stokes Surface

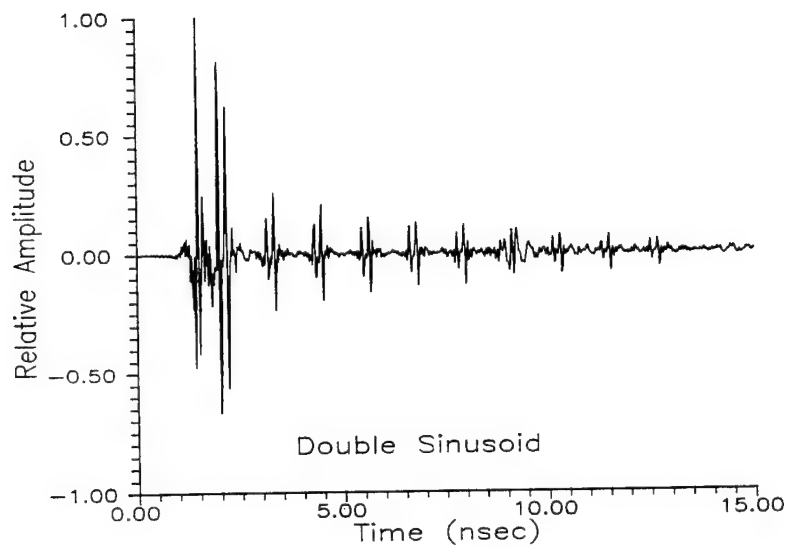


**Figure 4.** Scattered Field from Double Sinusoid Surface

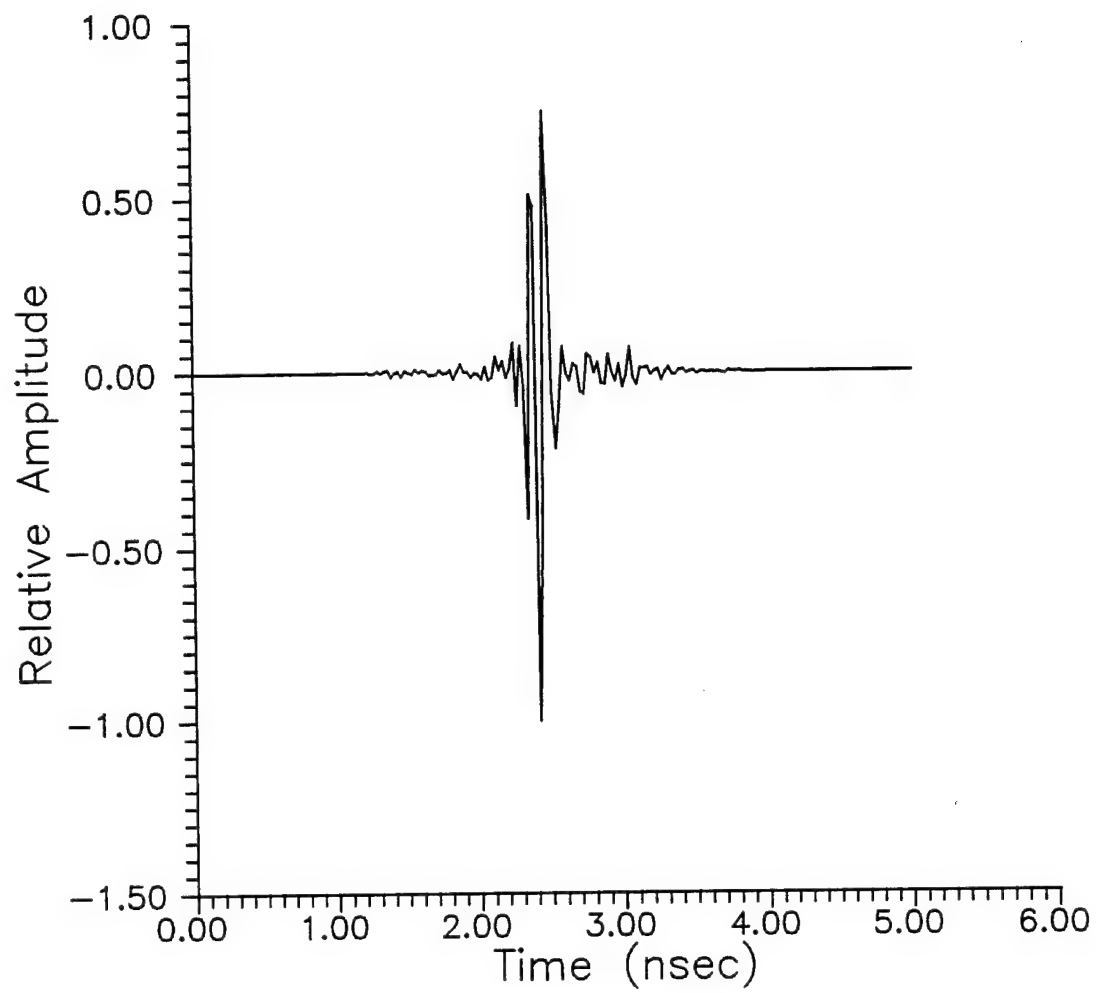


**Figure 5.** Scattered Field from Phoenix Missile Model

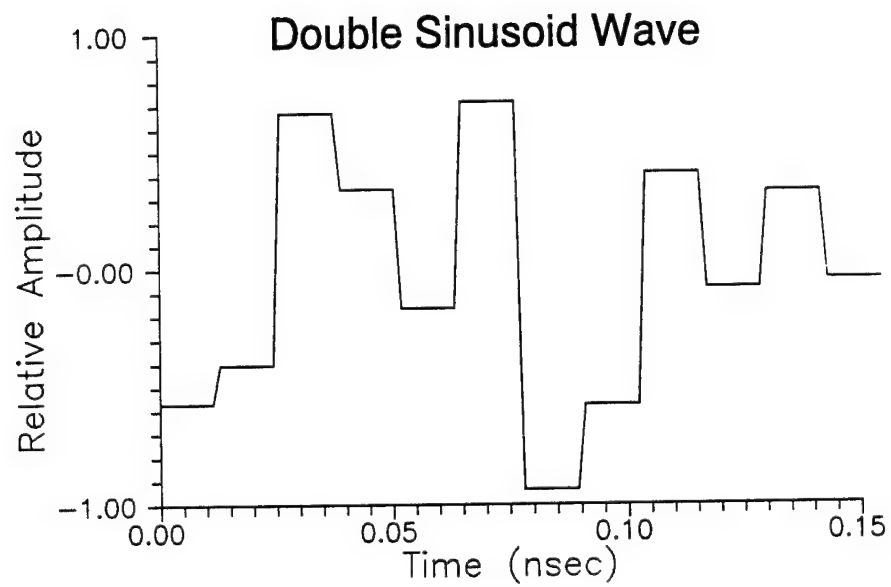
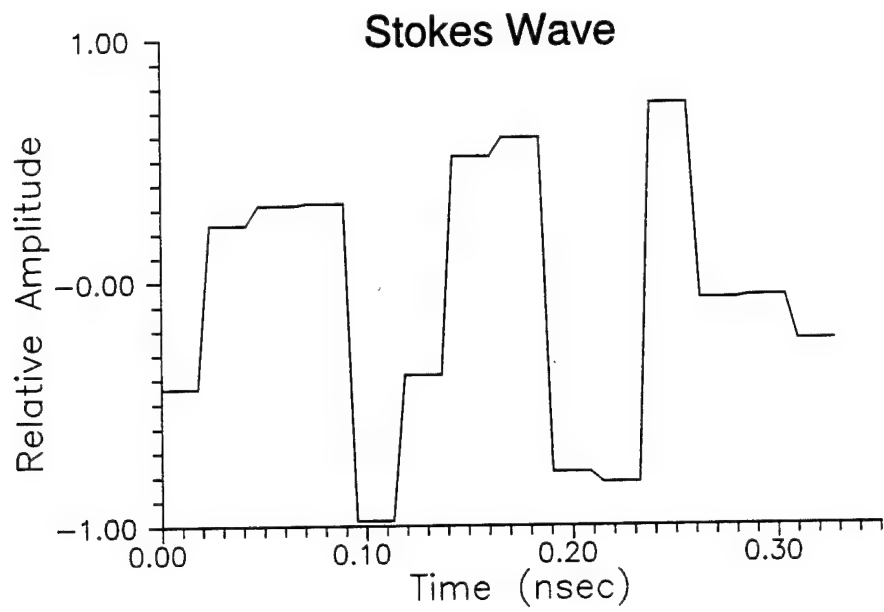


**Figure 6.** Constructed CRTWs for Measured Surfaces

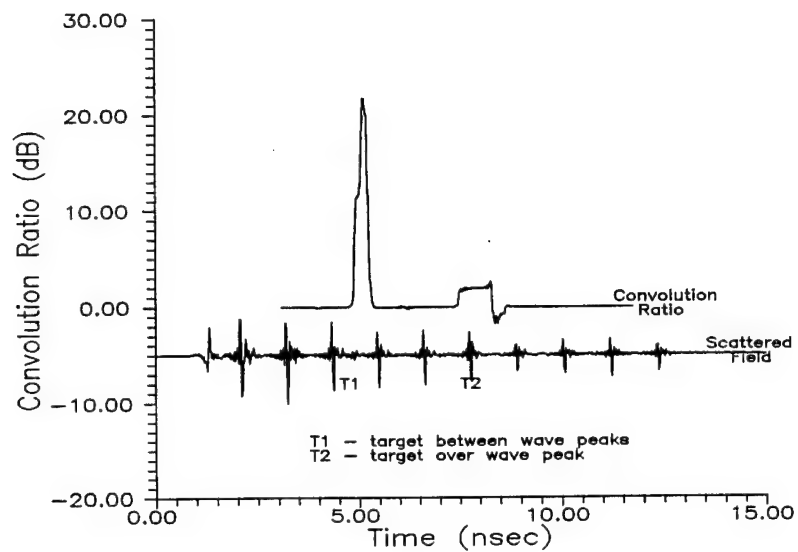


**Figure 7.** Convolution Energy Ratio for Stokes Surface

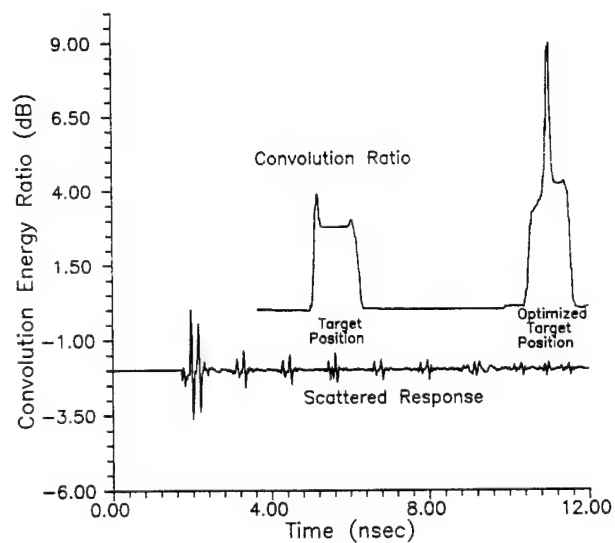


**Figure 8.** Convolution Energy Ratio for Double Sinusoid

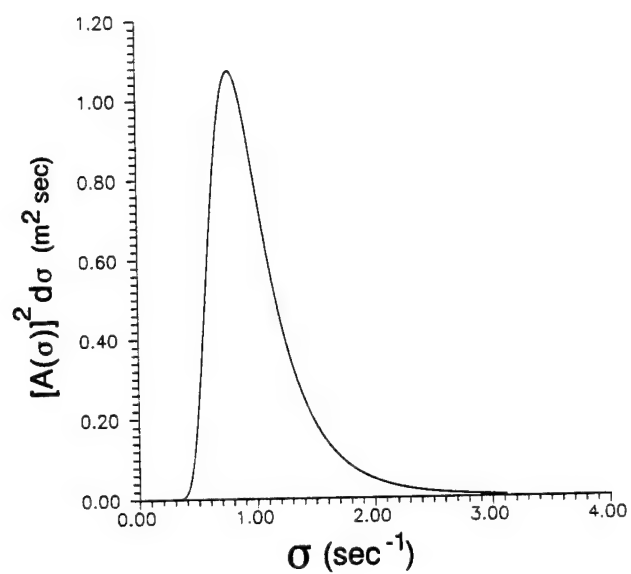


**Figure 9.** Neumann Spatial Frequency Spectrum

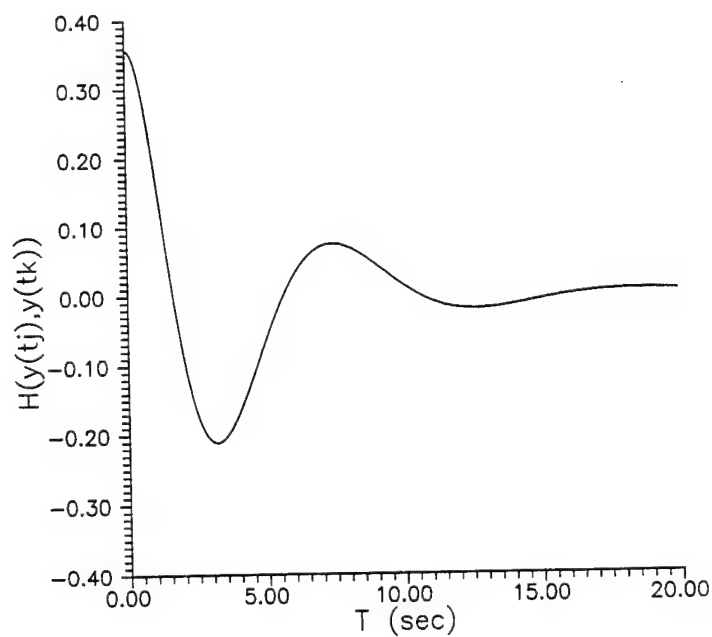


**Figure 10.** Covariance distribution generated using Neumann frequency spectrum with 20 knot winds

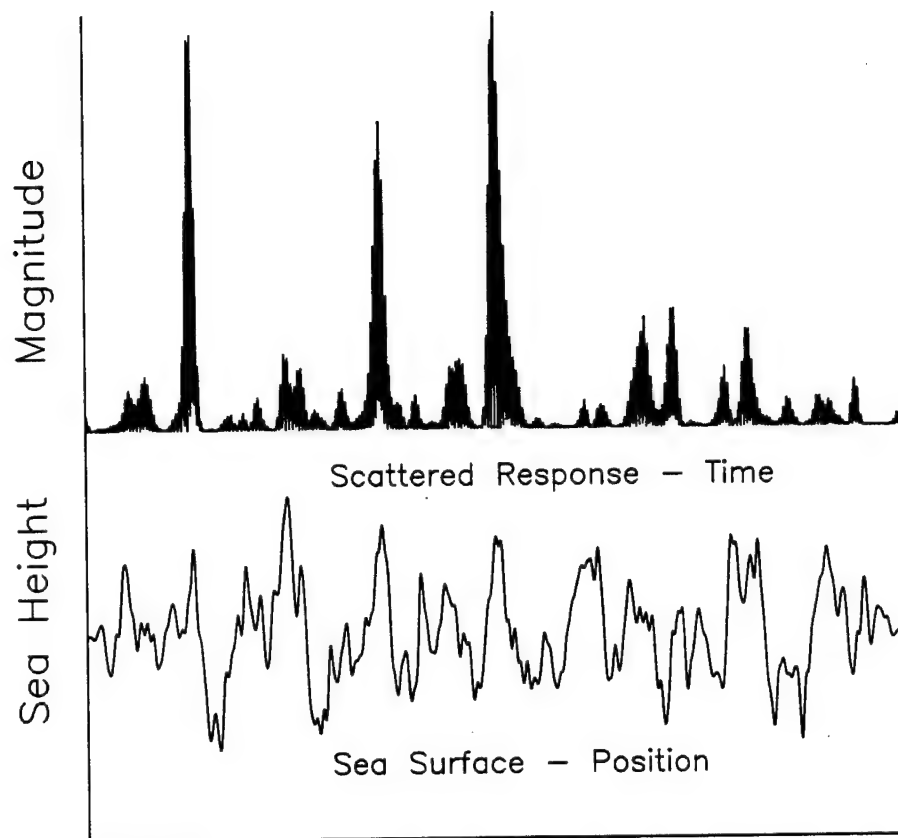


**Figure 11.** Absolute value of typical band-limited sea clutter return from stochastically-generated sea surface



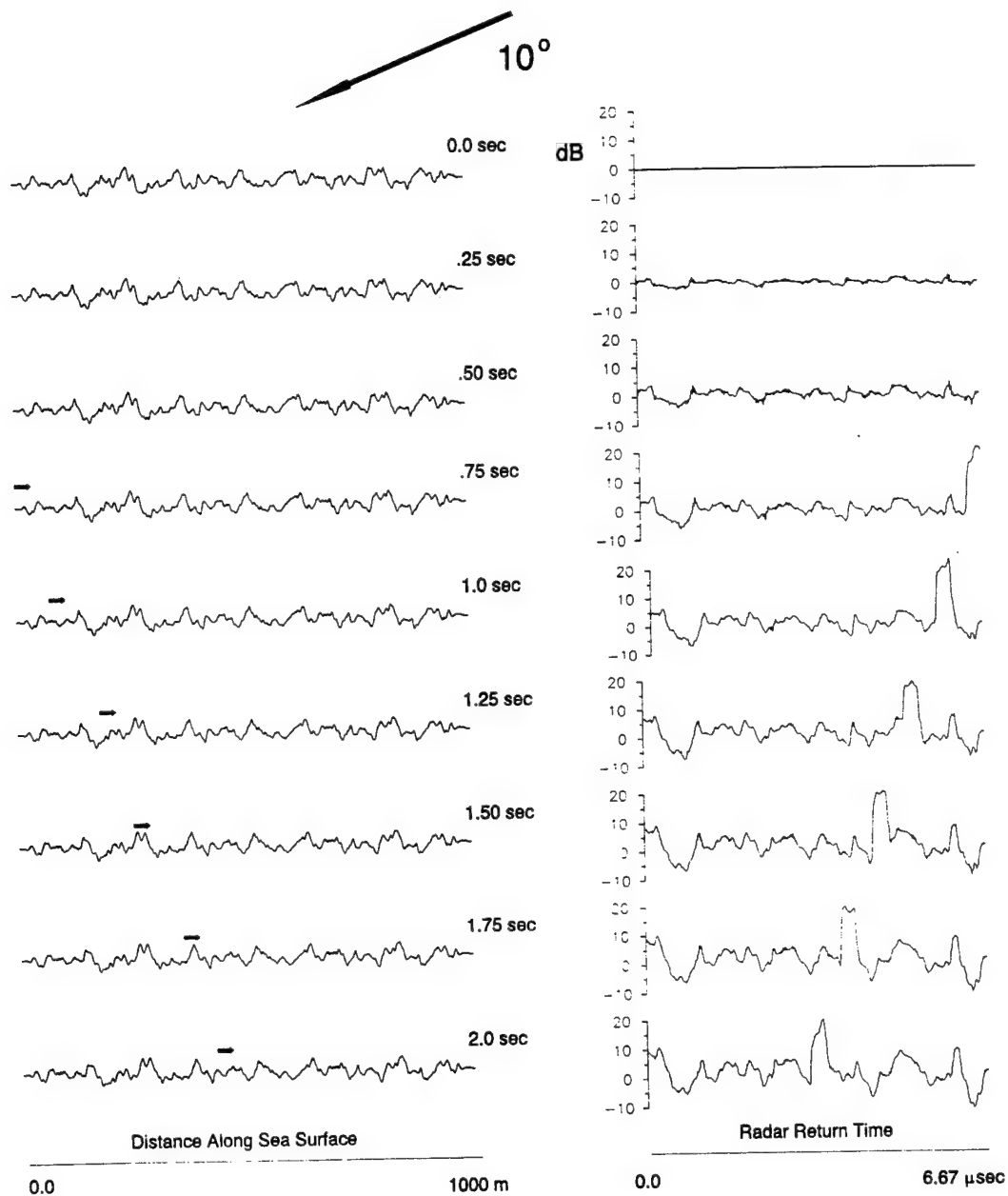


**Figure 12.** Profiles for an evolving stochastically-generated sea surface, and computed energy ratios for Phoenix missile/clutter combination. Arrow indicates spatial position of the missile.

## References

1. K.M. Chen, E. Rothwell, D.P. Nyquist, J. Ross, P. Ilavarasan, R. Bebermeyer, Q. Li, C.Y. Tsai and A. Norman, Radar identification and detection using ultra-wideband/short-pulse radaars, in: *Ultra-Wideband, Short-Pulse Electromagnetics 2*, Lawrence Carin and Leopold B. Felsen, ed., Plenum Press, New York (1995).
2. E. Rothwell, K.M. Chen, D.P. Nyquist, P. Ilavarasan, J.E. Ross, R. Bebermeyer, and Q. Li, A general E-pulse scheme arising from the dual early-time/late-time behavior of radar scatters, *IEEE Trans. Ant. Propagat.*, 42:1336 (1994).
3. Blair Kinsman, *Wind Waves: Their Generation and Propagation on the Ocean Surface*, Chap. 5, Prentice-Hall, Englewood Cliffs, N.J., 1965.
4. Blair Kinsman, *Wind Waves: Their Generation and Propagation on the Ocean Surface*, Chap. 8, Prentice-Hall, Englewood Cliffs, N.J., 1965.

## Appendix 4

### A General E-pulse Scheme Arising from the Dual Early-Time/Late-Time Behavior of Radar Scatterers

Edward J. Rothwell, *Senior Member, IEEE*, Kun-Mu Chen, *Fellow, IEEE*,  
Dennis P. Nyquist, *Senior Member, IEEE*, Ponniah Ilavarasan,  
*Member, IEEE*, John E. Ross, *Member, IEEE*,  
Robert Bebermeyer, *Student Member, IEEE*, and Qing Li

**Abstract**—A duality between the temporal late-time response and the spectral early-time response of a radar target is used to form the basis for a general E-pulse technique. Examples, using the ultrawide-band measurements of an aircraft model, reveal that E-pulse cancellation is possible both in the time domain for the late-time component and in the frequency domain for the early-time component. Applications to radar target discrimination and clutter cancellation are described, and the aspect dependence of early-time discrimination is investigated.

#### I. INTRODUCTION

The E-pulse radar target discrimination scheme is a resonance cancellation technique grounded in the late-time behavior of the transient scattered field [1]–[5]. It is based on the target natural frequencies, which form a global description of the scatterer, and is inherently aspect-independent. Unfortunately, this approach ignores the early-time behavior, which is dominated by localized specular reflections from target scattering centers. In this communication we will demonstrate a duality between the temporal behavior of the late-time component of the transient response and the spectral

Manuscript received July 26, 1993; revised January 6, 1994. This work was supported by the Office of Naval Research under Grant N00014-93-1-1272.

The authors are with the Department of Electrical Engineering, Michigan State University, East Lansing, MI 48824-1226 USA.

IEEE, Log Number 9404561.

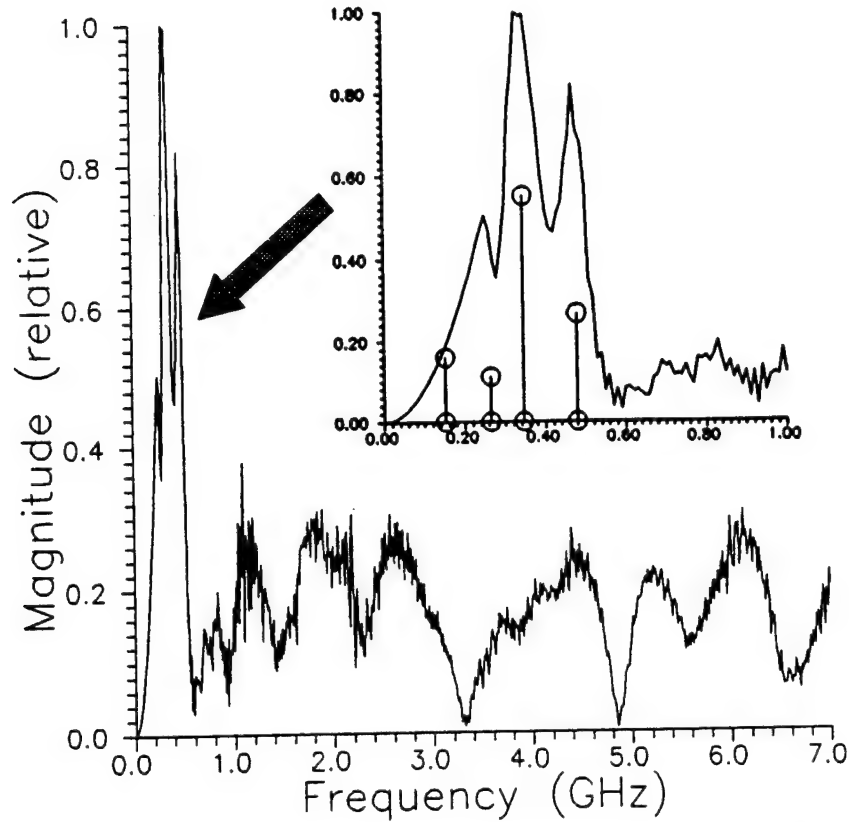


Fig. 1. Frequency domain scattered-field response of B-58 aircraft model measured at nose-on incidence. Inset shows low frequency behavior, with extracted resonant frequencies indicated by circles.

behavior of the early-time component. Because of this duality, it is possible to devise a general E-pulse technique that can be applied to both the early- and late-time components. For the early time, this amounts to a cancellation of the frequency-domain sinusoidal functions arising from the aspect-dependent temporal positions of the specular reflections.

## II. MODELING OF EARLY- AND LATE-TIME TRANSIENT SCATTERING

Assume a time-limited interrogating pulse is incident on a radar target and its scattered-field transient response is measured. Baum [6] has proposed a model of the late-time response using the aspect-independent natural resonance frequencies of the target  $\{s_n = \sigma_n + j\omega_n\}$ :

$$r_L(t) = \sum_{n=-N}^N A_n e^{s_n t} \quad t > T_L. \quad (1)$$

Here  $T_L$  designates the beginning of the late-time period,  $N$  modes are assumed excited by the incident pulse, and the aspect-dependent complex amplitudes  $\{A_n\}$ , along with the natural frequencies, occur in complex-conjugate pairs (i.e.,  $s_{-n} = s_n^*$ ). This model has formed the basis for the aspect-independent late-time E-pulse technique.

Altes [7] has proposed a simple model for the early-time response

$$r_E(t) = \sum_{m=1}^M f_m(t - T_m) u(t - T_m). \quad (2)$$

Here,  $f_m$  is the localized pulse response originating at the  $m$ th scattering center at time  $T_m$ ,  $u(t)$  is the unit step function, and  $M$  is the number of scattering centers considered. In the frequency domain,

this response becomes

$$R_E(\omega) = \mathcal{F}\{r_E(t)\} = \sum_{m=1}^M F_m(\omega) e^{-j\omega T_m}. \quad (3)$$

In general, the spectral response of the  $m$ th scattering center can be represented as a series of  $K_m$  real exponentials

$$F_m(\omega) = \sum_{k=1}^{K_m} b_{m,k} e^{\alpha_{m,k} \omega} \quad (4)$$

where  $\{b_{m,k}\}$  are complex amplitudes. Hurst and Mittra [8] suggest that the number of terms in the series (4) should not be too large for reasonable scattering shapes. Substituting (4) into (3) and redefining the summation index gives

$$R_E(\omega) = \sum_i B_i e^{\tau_i \omega} \quad (5)$$

where  $\tau_i = \alpha_i - jT_i$  are complex times associated with the scattering center impulse responses. Note that this is essentially the model used by Carriere and Moses [9] in their Prony-method analysis of target scattering centers.

It is readily seen that there is a duality between the temporal late-time response (1) and the spectral early-time response (5). This duality allows the direct application of E-pulse cancellation to spectral early-time data.

## III. E-PULSE TECHNIQUE FOR GENERAL EXPONENTIAL SIGNALS

Consider an exponential signal of the form

$$f(x) = \sum_{k=1}^K C_k e^{Q_k x} \quad X_1 < x < X_2 \quad (6)$$

where  $\{C_k\}$  and  $\{Q_k\}$  are complex constants,  $\{X_1, X_2\}$  represents the domain of the signal measurement, and  $x$  can represent frequency in the case of an early-time response and time in the case of a late-time response. An E-pulse  $e(x)$  is a real waveform of finite extent  $X_E$  that upon convolution with  $f(x)$  eliminates a preselected component of the exponential series. In particular, the entire series can be eliminated, resulting in

$$\begin{aligned} c(x) &= e(x) * f(x) = \int_0^{X_E} f(x') e(x - x') dx' \\ &= 0 \quad X_1 + X_E < x < X_2. \end{aligned} \quad (7)$$

The conditions for synthesizing such an E-pulse can be given in the context of resonance cancellation as [3]

$$E(s = Q_k) = 0 \quad 1 \leq k \leq K \quad (8)$$

where  $E(s)$  is the Laplace spectrum of  $e(x)$ . If the complex numbers  $\{Q_k\}$  are known, the E-pulse can be constructed by expanding  $e(x)$  in a set of basis functions (often rectangular pulses) and using (7) to obtain the basis function amplitudes. If  $\{Q_k\}$  are unknown, the E-pulse mode extraction technique [3], [10]–[12] can be used to find the basis function amplitudes, and  $\{Q_k\}$  can then be found from (8).

#### IV. DEMONSTRATION OF E-PULSE CANCELLATION USING EARLY- AND LATE-TIME TARGET RESPONSES

The ultrawide-band measurement of a 1:48 scale B-58 aircraft model can be used to demonstrate E-pulse cancellation of both early and late-time scattered-field responses. Fig. 1 shows the magnitude of the scattered-field response of the B-58 measured at nose-on incidence in the Michigan State University free-field scattering range within the frequency band 0.2–7 GHz. (For more information about the measurement process, see [13]). The scattering is slightly bistatic, with the incident electric field polarized in the plane of the aircraft wings. An HP 8720B network analyzer was used to obtain the data, and the system response was removed using the theoretical response of a 14-in diameter calibration sphere. To reduce the effect of windowing, the magnitude of the response was quadratically interpolated to zero amplitude at zero frequency, and the phase was linearly interpolated.

The spectral response of the B-58 is seen to be composed of two distinct regions. The lower frequencies clearly display a resonance behavior with several sharp peaks below 0.5 GHz. (The inset is an expansion of the region 0–1 GHz). A very rough approximation gives the fundamental resonance of a thin body of length  $L$  at  $f_0 \approx c/2L$ . Using this, the first fuselage resonance is at roughly 0.23 GHz and the first wing resonance is at 0.42 GHz; the first and third peaks in the figure match these values fairly well, while the second may be a coupled wing-body resonance. Above 0.5 GHz the spectrum displays the typical interfering-sinusoid type pattern due to time-shifted specular reflections. Thus, low frequencies correspond to late time while higher frequencies are more involved in the early time.

The transient response of the B-58 has been obtained by weighting the spectrum with a Gaussian function and then inverse transforming using the FFT. The result is shown in Fig. 2. Temporally, there is a clear demarcation between an early-time period dominated by specular reflections, during which the incident pulse crosses the aircraft, and a late-time period during which the target oscillates freely. In this synthesized situation, the equivalent incident pulse is the inverse transform of the Gaussian weighting function, as shown in Fig. 2; its width is roughly 0.3 ns—about 1/7 the one-way transit time of the B-58. The beginning of the late-time period occurs after the pulse has traversed the target and the information has returned to

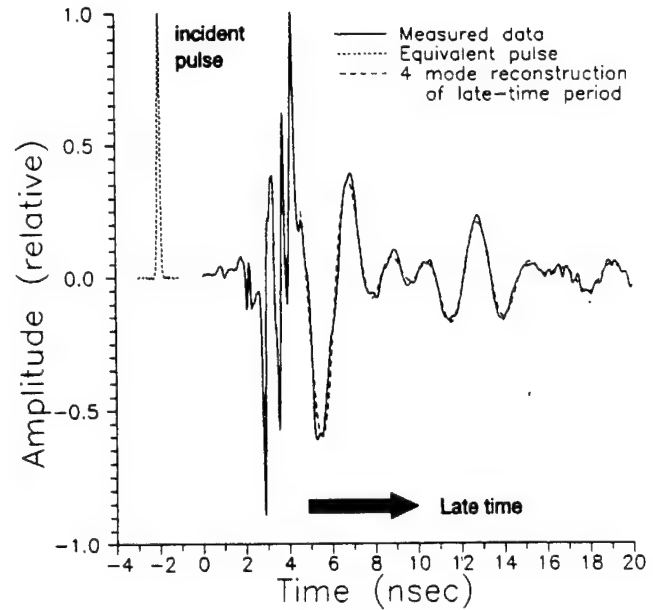


Fig. 2. Transient response of B-58 aircraft model. Region  $t < 0$  displays equivalent incident pulse. Dotted line indicates reconstruction of late-time period using extracted resonant frequencies.

the receiver (approximately the two-way transit time of the target), at about 4.9 ns in Fig. 2.

The late-time portion of the response can be canceled by constructing an E-pulse based on the natural resonant frequencies, as described by (8). Since these frequencies are unknown, they are determined using the E-pulse mode extraction technique [11]. Four modes were extracted from the late-time signal. The imaginary parts of the resonant frequencies and the modal amplitudes are indicated by the positions and heights of the circles in Fig. 1. The frequencies are seen to match well with the peaks in the spectrum of the total response. The lowest mode at about 0.15 GHz is probably an anomaly due to a discontinuity introduced by the interpolation of the spectrum to zero frequency. A reconstruction of the late-time response using all four extracted modes is shown in Fig. 2 and is found to match the measured data quite well. The E-pulse constructed from these frequencies is shown in Fig. 3, and the convolution with the total response is shown in Fig. 4. It is seen that the E-pulse has annihilated the modal portion of the B-58 response so that the portion of the convolution at times greater than the beginning of late time plus the E-pulse duration ( $t > 14$  ns) is null. Note that a forced dc-canceling E-pulse was used to eliminate a spurious dc level introduced by the inverse transform. This requires ten pulse basis functions to cancel four modes.

The spectrum of the early-time portion of the response can be canceled by constructing an E-pulse based on the complex times determined by the specular points on the B-58. Extraction of thirteen complex times from the B-58 spectrum reveals the imaginary parts (corresponding to the temporal positions of the scattering centers) shown by the circles in Fig. 5; the amplitude of the exponential is indicated by the circle height. Also shown in this figure is an illustration of the B-58, scaled so that its length corresponds to the two-way transit time of the aircraft, and the early-time portion of the B-58 response. The extracted times are seen to correspond with important scattering events on the aircraft, with particularly large events occurring at the junctions of the engine mounts and the wing. Fig. 6 shows the real part of the spectrum of the early time and its reconstruction using the extracted complex times. The match is seen to be excellent.

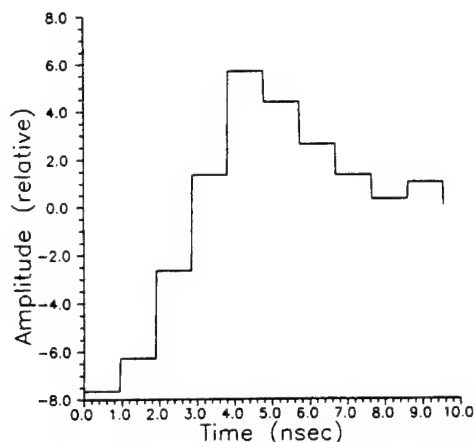


Fig. 3. E-pulse constructed to cancel late-time portion of temporal B-58 response.

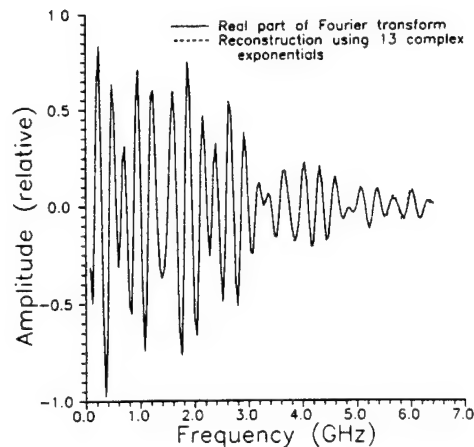


Fig. 6. Real part of spectrum of early-time portion of B-58 response. Dotted line is reconstruction using a 13-term exponential series.

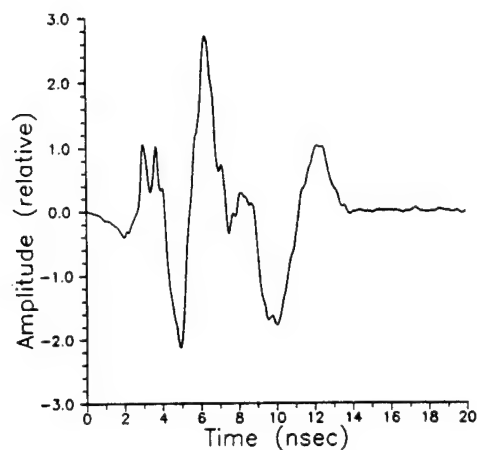


Fig. 4. Convolution of late-time E-pulse with temporal B-58 response indicating cancellation of late time.

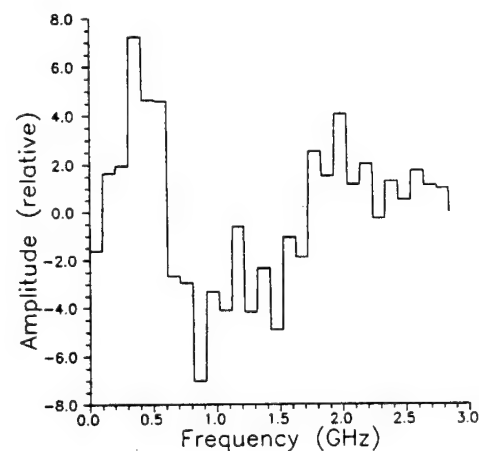


Fig. 7. E-pulse constructed to cancel spectrum of early-time B-58 response.

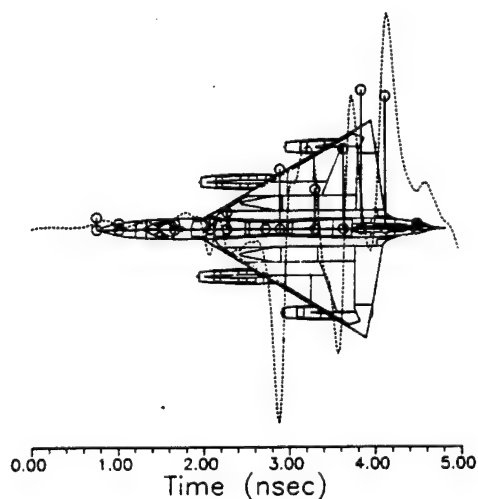


Fig. 5. Early-time response of B-58. Imaginary parts of extracted times, indicated by circles, describe temporal positions of scattering centers.

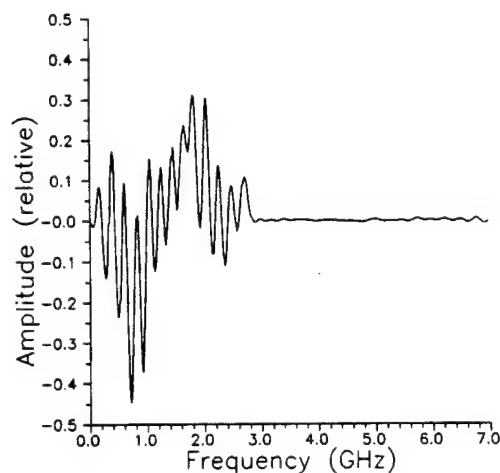


Fig. 8. Convolution of early-time E-pulse with spectrum of early-time B-58 response.

The E-pulse constructed from the extracted complex times is shown in Fig. 7; again, a forced dc-canceling E-pulse has been used. Note that now the horizontal axis is frequency since this E-pulse

will cancel the frequency-domain sinusoids arising from the early time. Convolution of this E-pulse with the real part of the early-time spectrum is shown in Fig. 8, revealing a null response in the frequency range greater than the E-pulse duration ( $f > 3$  GHz).

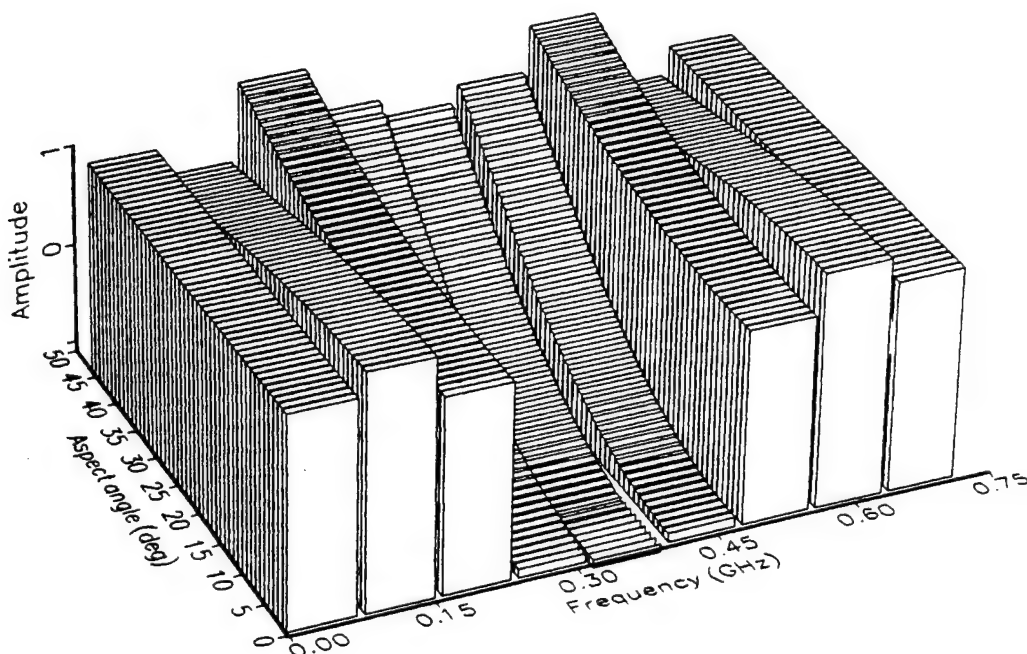


Fig. 9. E-pulses for Y-wire aircraft model.

#### V. APPLICATIONS OF E-PULSE RESONANCE CANCELLATION

The late-time E-pulse technique has formed the basis for a successful automated target discrimination scheme [5]. An E-pulse library is created for a set of targets and convolved with the measured response of an unknown target. The convolved response with the minimum late-time signal is then associated with the unknown target providing an identification. Since the E-pulses are based on target natural frequencies, they form an aspect-independent classifier.

A similar technique is possible using the early-time signal. However, since the specular response of a target is aspect dependent (because of the changing temporal positions and scattering characteristics of the scattering centers with aspect angle) each target requires a set of E-pulses for different aspect angles. Identification is then accomplished by convolving the global set of E-pulses with the spectrum of an unknown response. Thus, it is necessary to determine the number of E-pulses that must be retained for each target, i.e., the level of discretization of aspect angle required for accurate identification.

A preliminary investigation into the aspect dependence of the early-time E-pulse technique is most easily accomplished using a simple set of targets, such as wire-stick aircraft models. To make the results easily verifiable, the elementary physical optics (PO) scattered field response of a wire segment will be employed. If a plane wave with electric field of the form  $\vec{E}(\vec{r}) = \vec{E}_0 e^{-j\vec{k} \cdot \vec{r}}$  is incident on a thin, straight wire segment of radius  $a$  and length  $2d$  oriented along a unit vector  $\hat{u}$ , the physical optics current induced along its axis is given by

$$I(u) = \frac{2\pi a}{n\eta_0} \hat{u} \cdot \vec{E}^i(u) \quad (9)$$

where  $n$  is the length of the vector normal to the wire surface in the plane of the incident wave vector  $\vec{k}^i$ ,  $\vec{n} = \hat{u} \times (\hat{u} \times \vec{k}^i)$ . Substituting (9) into the standard formula for the far-zone electric field gives the scattered field

$$\vec{E}(\vec{r}) = -\frac{ad}{2r} \frac{\hat{u} \cdot \vec{E}_0}{n} \frac{e^{j\omega(T_1 - T_0)}}{T_1} - \frac{e^{-j\omega(T_1 + T_0)}}{T_1} \vec{\Omega}(\theta, \phi) \quad (10)$$

where  $T_0 = [\vec{r} - (\vec{r} - \vec{k}^i) \cdot \vec{r}_c]/c$ ,  $T_1 = [(\vec{r} - \vec{k}^i) \cdot \hat{u}d]/c$ ,  $\vec{\Omega}(\theta, \phi) = \hat{\theta}(\hat{\theta} \cdot \hat{u}) + \hat{\phi}(\hat{\phi} \cdot \hat{u})$ ,  $r$  is the distance from the origin to the observation point, and  $\vec{r}_c$  is a vector from the origin to the center of the wire segment. Since PO scattering is purely specular, the scattered field (10) is seen to be composed of two undamped sinusoids, representing specular reflections from the wire ends. This is more easily seen if the inverse Fourier transform of (10) is taken, giving

$$\vec{E}(\vec{r}, t) = -\frac{ad}{2r} \frac{\hat{u} \cdot \vec{E}_0}{n} \frac{\delta(t - [T_0 - T_1]) - \delta(t - [T_0 + T_1])}{T_1} \vec{\Omega}(\theta, \phi) \quad (11)$$

The two simple wire-aircraft models shown in Fig. 10 will be used to test the aspect dependence of the early-time E-pulse technique. Responses for aspect angles of  $1^\circ$  increment have been created using superpositions of (10) for each wire segment, with the origin of coordinates shown in Fig. 10 as a solid circle, for the frequency range 1–7 GHz. Note that the choice of  $r$  establishes a time reference that determines the E-pulse shape and that must be found in practice by detecting a certain temporal event (generally the largest portion of the response). Here, a distance of  $r = 1$  m is chosen. Forced E-pulses of duration 0.72 GHz were then created for each response. Since there are four distinct scattering centers, nine pulses are required in each E-pulse expansion; dc E-pulses are not needed since the responses are computed exactly, and no spurious dc level is present. The E-pulses for the range of aspect angles  $0 \leq \alpha \leq 45^\circ$  for the Y-wire model are shown in Fig. 9. The variation of the E-pulses with aspect angle is seen to be quite smooth, since the transit times to each scattering center are smoothly varying with aspect angle.

To simulate a discrimination scenario, the frequency-domain response of the Y-wire at  $15^\circ$  is assumed to arise from an unknown target, and the E-pulses for both the Y-wire and T-wire models are convolved with the response. Fig. 10 shows the results, plotting the energy in the convolved response divided by the E-pulse energy (with the largest energy ratio normalized to unity.) Obviously, convolution with the  $15^\circ$  Y-wire E-pulse gives zero energy, but convolution

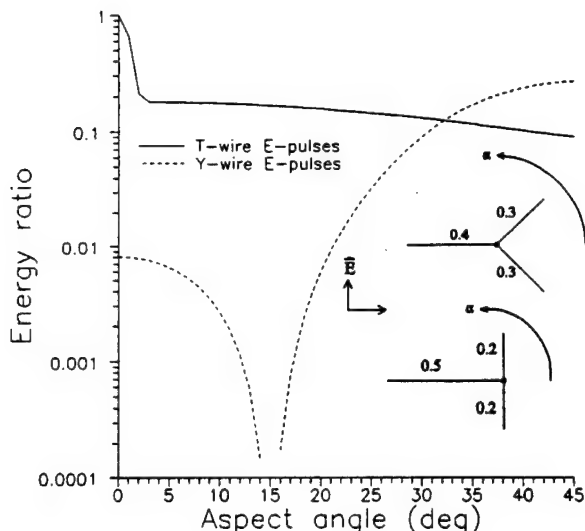


Fig. 10. Energy in convolutions of T-wire and Y-wire E-pulses with 15° Y-wire response. Dimensions on T-wire and Y-wire are in meters.

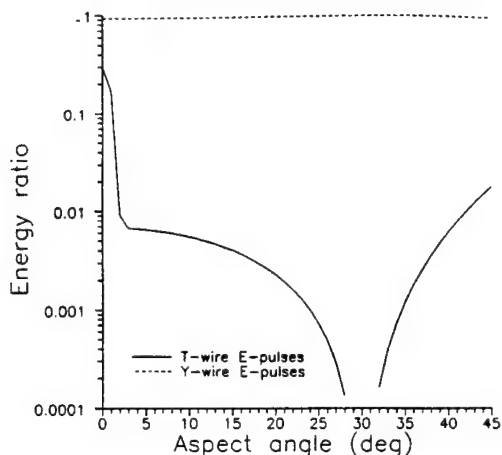


Fig. 11. Energy in convolutions of T-wire and Y-wire E-pulses with 30° T-wire response.

with E-pulses for angles near 15° also gives a small result. In contrast, convolution with any of the E-pulses for the T-wire gives a significantly larger result. Similar results are shown in Fig. 11 when the 30° T-wire response is assumed to arise from an unknown target. This suggests that the E-pulse technique may not be severely aspect dependent, and a relatively small number of E-pulses may be required to characterize a target over a wide range of aspect angles. Whether this observation holds for more complicated targets and under severe noise conditions must be tested.

It must also be investigated whether the E-pulse technique gives an advantage over more standard waveform correlation approaches [14]. There is certainly a reduction of storage with the E-pulse technique, since only the amplitudes of a few pulses must be stored at each aspect, rather than the entire waveform. However, more advanced storage schemes using wavelets [15] or scattering center information [16] may also reduce the memory requirements. Another possible advantage of the E-pulse techniques lies in the combination of both early and late-time information into a more robust scheme. For example, the late-time response could be used to narrow the possible target choices followed by the early-time technique to provide a positive identification. Or, the information from both the early and late times could be combined into a single discrimination quantifier.

Cancellation of frequency-domain sinusoids is possible for any response that is specular in nature. Thus, the general E-pulse technique is also applicable to the cancellation of transient clutter signals arising from the deterministic scattering from specular objects such as the sea surface. This cancellation would enhance target detection as long as the specular reflections from the target are not temporally aligned with those from the clutter.

These applications will be addressed in future publications.

#### REFERENCES

- [1] E. J. Rothwell, D. P. Nyquist, K. M. Chen, and B. Drachman, "Radar target discrimination using the extinction-pulse technique," *IEEE Trans. Antennas Propagat.*, vol. AP-33, pp. 929–937, Sept. 1985.
- [2] K. M. Chen, D. P. Nyquist, E. J. Rothwell, L. Webb, and B. Drachman, "Radar target discrimination by convolution of radar return with extinction-pulse and single-mode extraction signals," *IEEE Trans. Antennas Propagat.*, vol. AP-34, pp. 896–904, July 1986.
- [3] C. E. Baum, E. J. Rothwell, K. M. Chen, and D. P. Nyquist, "The singularity expansion method and its application to target identification," *Proc. IEEE*, vol. 79, pp. 1481–1492, Oct. 1991.
- [4] K. M. Chen, D. P. Nyquist, E. J. Rothwell, and W. M. Sun, "New progress on E/S pulse techniques for noncooperative target recognition," *IEEE Trans. Antennas Propagat.*, vol. 40, pp. 829–833, July 1992.
- [5] P. Ilavarasan, J. E. Ross, E. J. Rothwell, K. M. Chen, and D. P. Nyquist, "Performance of an automated radar target discrimination scheme using E-pulses and S-pulses," *IEEE Trans. Antennas Propagat.*, vol. 41, no. 5, pp. 582–588, May 1993.
- [6] C. E. Baum, "Emerging technology for transient and broad-band analysis and synthesis of antennas and scatterers," *Proc. IEEE*, vol. 64, pp. 1598–1616, Nov. 1976.
- [7] R. A. Altes, "Sonar for generalized target description and its similarity to animal echolocation systems," *J. Acoust. Soc. Amer.*, vol. 59, pp. 97–105, Jan. 1976.
- [8] M. P. Hurst and R. Mittra, "Scattering center analysis via Prony's method," *IEEE Trans. Antennas Propagat.*, vol. AP-35, pp. 986–988, Aug. 1987.
- [9] R. Carriere and R. L. Moses, "High resolution radar target modeling using a modified Prony estimator," *IEEE Trans. Antennas Propagat.*, vol. 40, pp. 13–18, Jan. 1992.
- [10] E. Rothwell, K. M. Chen, and D. P. Nyquist, "Extraction of the natural frequencies of a radar target from a measured response using E-pulse techniques," *IEEE Trans. Antennas Propagat.*, vol. AP-35, pp. 715–720, June 1987.
- [11] E. J. Rothwell and K. M. Chen, "A hybrid E-pulse/least squares technique for natural resonance extraction," *Proc. IEEE*, pp. 296–298, Mar. 1988.
- [12] P. Ilavarasan, E. J. Rothwell, K. M. Chen, and D. P. Nyquist, "Natural resonance extraction from multiple data sets using physical constraints," *Radio Sci.*, vol. 29, no. 1, pp. 1–7, Jan.–Feb. 1994.
- [13] J. E. Ross, "Application of transient electromagnetic fields to radar target discrimination," Ph.D. dissertation, Michigan State Univ., 1992.
- [14] H. J. Li and S. H. Yang, "Using range profiles as feature vectors to identify aerospace objects," *IEEE Trans. Antennas Propagat.*, vol. 41, pp. 261–268, Mar. 1993.
- [15] E. J. Rothwell, K. M. Chen, D. P. Nyquist, J. E. Ross, and R. Bebermeyer, "A radar target discrimination scheme using the discrete wavelet transform for reduced data storage," *IEEE Trans. Antennas Propagat.*, vol. 42, no. 7, pp. 1033–1037, July 1994.
- [16] Q. Li *et al.*, "Data storage techniques for use in correlation-based early-time radar target discrimination," *1994 IEEE AP-S Int. Symp. and URSI Radio Science Meeting*.



## Appendix 5

### A Radar Target Discrimination Scheme Using the Discrete Wavelet Transform for Reduced Data Storage

E. J. Rothwell, *Senior Member, IEEE*, K. M. Chen, *Fellow, IEEE*,  
D. P. Nyquist, *Senior Member, IEEE*, J. E. Ross, *Member, IEEE*,  
and R. Bebermeyer, *Student Member, IEEE*

**Abstract**—A correlative radar target discrimination scheme using the transient scattered-field response is proposed. This scheme uses a one-dimensional discrete wavelet transform on the temporal response to reduce the amount of data that must be stored for each anticipated aspect angle. Experimental results show that a reduction in stored data of sixteen to one still allows accurate discrimination in adverse noise situations with signal-to-noise ratios as low as -5 dB.

#### I. INTRODUCTION

A fascinating variety of radar target discrimination schemes have been proposed in the past several years. Each of these techniques must deal with the complicated dependence of scattered

Manuscript received August 23, 1993; revised January 31, 1994. This work was supported by the ThermoTrex Corporation under Purchase Order 22068, and in part by the Northeast Consortium for Engineering Education under Purchase Order NCEE/A303/23-93 and the Office of Naval Research under Grant N00014-93-1-1272.

The authors are with the Department of Electrical Engineering, Michigan State University, East Lansing, MI 48824 USA.

IEEE Log Number 9402826.

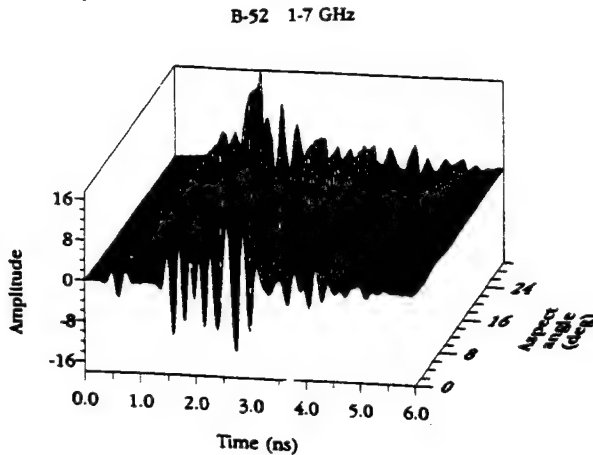


Fig. 1. Scattered field response of B-52 aircraft model as a function of aspect angle.

field on aspect angle, frequency and polarization. Time-domain techniques often reduce the complexity by concentrating on either the late-time resonant response of the target, or the early-time specular response. If the discrimination algorithm is based on the target resonant frequencies, aspect-independent late-time schemes can be devised [1]–[6] which eliminate the need for storage of aspect-dependent information (since target natural frequencies are aspect-independent). When bandwidth restrictions preclude the use of low-frequency resonant information, the early-time portion of the transient response must be used. Since the early-time response is highly aspect-dependent, a large amount of information about the target signature must be stored. This communication describes how the discrete wavelet transform (DWT) can be used to reduce the amount of stored data required for accurate discrimination.

## II. A CORRELATIVE DISCRIMINATION SCHEME

Several methods have been proposed for using the early-time information in a radar target discrimination scheme. Fig. 1 shows the experimental early-time response of a 1:72 scale B-52 aircraft model as a function of aspect angle, measured from nose-on. The response was measured in the frequency band 1–7 GHz using an HP 8720B network analyzer, calibrated, and inverse Fourier transformed into the time domain. (For more information regarding the experiment, see [7]). It is readily seen that the specular response of the target is highly aspect-dependent. If discrimination schemes are based on the actual transient return, a large amount of information must be stored. Several techniques, such as the neural network approach [8], [9] and the early-time E-pulse method [10], seek to reduce the storage requirements through indirect methods.

It has been suggested [8], [12] that direct correlation of target waveforms with their stored counterparts provides a simple, robust, time-shift-insensitive method for discrimination. Unfortunately, storing complete waveforms for each target at many aspect angles requires extensive computer resources. Combining the DWT with correlative processing results in a robust technique requiring minimal computer resources.

The DWT provides a linear transformation of a discretized signal into the “wavelet domain” much in the same manner as the discrete Fourier transform (DFT) [13], [16]. The signal is represented as a linear combination of wavelet basis functions (analogous to sinusoids

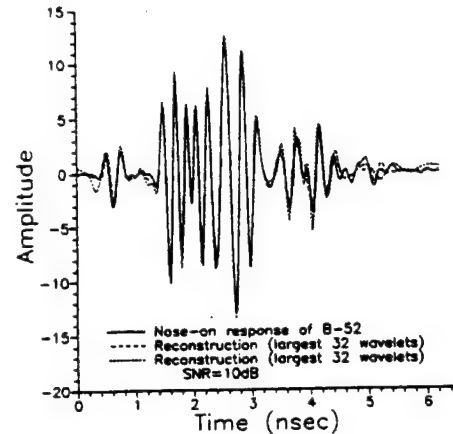


Fig. 2. Nose-on ( $0^\circ$ ) response of B-52 aircraft model and 32 wavelet reconstruction.

for the Fourier transform) and can thus be reconstructed by

$$s_i = \sum_{j=1}^N a_j w_{ij} \quad 1 \leq i \leq N. \quad (1)$$

Here  $s_i$  is the signal sampled at time  $t_i$ ,  $a_j$  is the amplitude of the  $j^{\text{th}}$  wavelet basis function,  $w_{ij}$  is the  $j^{\text{th}}$  wavelet basis function sampled at time  $t_i$ , and  $N$  is the length of the signal (usually a power of 2). Wavelet basis functions are constructed so that the wavelet coefficient vector  $\{a_i\}$  is sparse for a certain class of waveforms (polynomials of a chosen degree). Because of this sparseness, the DWT can be used to compress the signal. References [14], [15] give a good overview of wavelet transforms, while [17]–[19] demonstrate ways in which wavelets can be used for data compression.

To perform target discrimination, the correlation of a received signal from an unknown target is performed with each of the stored target responses. This correlation is most efficiently computed using the fast Fourier transform (FFT). Let  $\{r_i\}$  represent the sampled received signal and  $\{R_i\}$  the DFT of the signal. Then the correlation  $\{c_i\}$  is given by the inverse DFT as

$$c_i = \text{DFT}^{-1}\{SR^*\}, \quad 1 \leq i \leq N \quad (2)$$

where  $\{S_i\}$  is the DFT of  $\{s_i\}$ . Using (1),  $\{S_i\}$  can be written as

$$S_i = \sum_{j=1}^N a_j W_{ij} \quad 1 \leq i \leq N \quad (3)$$

where  $\{W_{ij}\}$  is a matrix containing the DFT's of the wavelet basis functions. Thus, storage of a single wavelet transformation matrix  $\{W_{ij}\}$  along with some significant subset of the wavelet coefficients  $\{a_i\}$  for each target is required for this scheme. Experimentation using measured target responses has shown that the number of wavelet coefficients required for successful discrimination can be reduced to a small fraction of  $N$ .

## III. DEMONSTRATION OF STORAGE REDUCTION

To demonstrate the validity of storage reduction using the DWT, consider the nose-on ( $0^\circ$ ) response of the B-52 sampled at 256 time points, as shown in Fig. 2. Fig. 3 shows the wavelet spec-

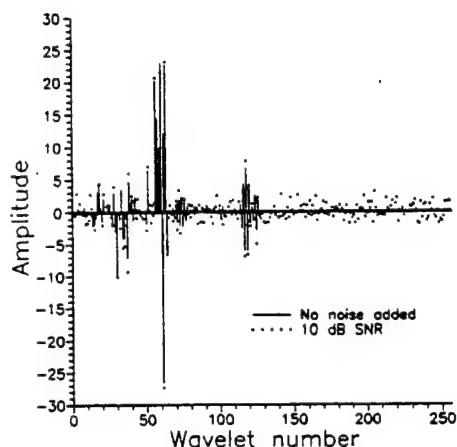


Fig. 3. Wavelet spectrum of nose-on (0°) response of B-52 aircraft model.

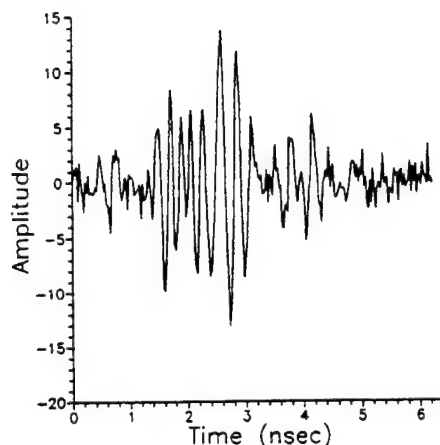


Fig. 4. Nose-on (0°) response of B-52 aircraft model with zero-mean white Gaussian noise added: SNR=10 dB.

trum  $\{a_i\}$  computed using a 256-point Lemarie DWT [13]. It is readily seen that only a small subset of the wavelet coefficients are significant. Note that the small values of coefficients  $a_{129}$  through  $a_{256}$  is due to an oversampling of the data by a factor of about 2. The DWT thus automatically compensates for frequency oversampling.

Fig. 2 also shows the B-52 response reconstructed using only the 32 largest wavelet coefficients. As expected, the reconstruction is not perfect, since some information has been omitted. However, each of the major scattering events is reproduced. Similar results are shown in Fig. 5 where only the largest eight wavelet coefficients are retained (representing a data reduction ratio of 32 to 1). In this case some of the smaller events, such as the initial reflection from the nose of the aircraft, are lost, but the largest events are retained.

To see the effects of random noise on the wavelet reconstruction of data, zero-mean white Gaussian noise has been added to the nose-on response of the B-52; the resulting waveform, with a signal-to-noise ratio (SNR) of 10 dB, is shown in Fig. 4. Here, the SNR for a sampled transient waveform is defined by

$$SNR = 10 \log_{10} \left[ \frac{\sum_{i=1}^N s_i^2}{\sum_{i=1}^N n_i^2} \right] \text{ dB.} \quad (4)$$

Fig. 3 shows the wavelet spectrum of the noisy response. Although there is a perturbation of each of the wavelet coefficients, the values of the larger coefficients are changed only slightly. Thus, when only a few coefficients are retained in reconstructing the response, the result is a much more faithful representation than the original noisy waveform. In other words, much of the noise is represented by perturbation of very small wavelet coefficients which are neglected (effectively filtered out) in the reconstruction. This is seen in Figs. 2 and 5.

#### IV. TARGET DISCRIMINATION USING WAVELET-REDUCED DATA

To demonstrate target discrimination using wavelet-reduced data, the transient responses of a 1:72 scale model B-52 aircraft, a 1:48 B-58 model, a 1:48 TR-1 model, a 1:48 F-14 model and a 1:48 Mig-29 model have been constructed from measurements within the frequency band 1–7 GHz. Each model was measured at 68 aspect angles between 0 and 30.15°, in 0.45° increments. Because of the size of the models, no significant natural resonances were excited, and thus the data represents the specular early-time response. The

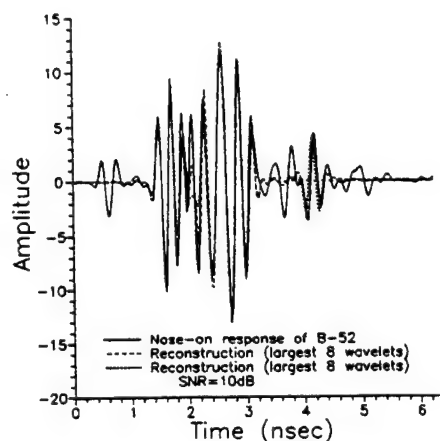


Fig. 5. Nose-on (0°) response of B-52 aircraft model and 8 wavelet reconstruction.

wavelet coefficients of each of the 68 responses of the five aircraft models were found using a 256-point Lemarie transform and the largest 32 coefficients were then stored in a computer file to act as a waveform data base. One of the waveforms was assumed to arise from an unknown aircraft, and was reconstructed from its largest 32 coefficients. Identification of the unknown target is then accomplished by correlating the unknown aircraft response with the response of each target in the data base, reconstructed from its largest 32 wavelet coefficients. Note that the original measured data could also be used as the unknown target signal, as long as enough wavelet coefficients have been used to accurately reconstruct the stored waveforms. However, if only a few coefficients are used, the reconstructed data will not correlate well with the measured signal.

It is convenient to normalize the correlation (2) using

$$\bar{C}_i = \frac{c_i^2}{\sum_{j=1}^N s_j^2 \sum_{j=1}^N r_j^2}. \quad (5)$$

Then, a maximum value of unity is achieved only when the correlated waveforms are identical to within a constant.

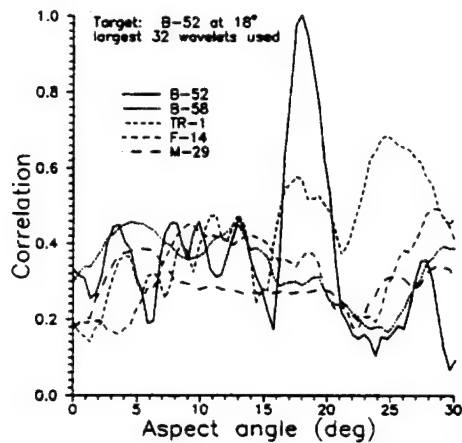


Fig. 6. Maximum correlation of 18° B-52 response with responses from all targets. Target waveforms represented using 32 wavelets.

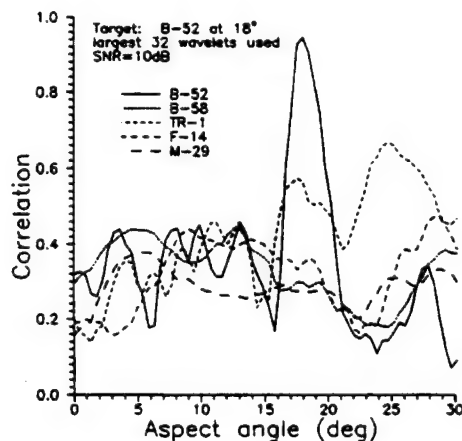


Fig. 7. Maximum correlation of 18° B-52 response with noisy responses from all targets. Target waveforms represented using 32 wavelets. SNR = 10 dB.

Fig. 6 shows the maximal normalized correlation as a function of aspect angle when the unknown aircraft is the B-52 at 18°. As expected, correlation with the 18° B-52 response gives an exact match (unity correlation) while other responses give a smaller result. Note that the B-52 can be discriminated from the other targets over a range of aspect angles from about 17° to 20°. When noise is added to the unknown target response, performance degrades, as shown in Fig. 7, and the range of aspects over which the target can be discriminated is reduced. However, with a SNR of 10 dB the degradation is slight, since only the largest wavelet coefficients are used.

A measure of the quality of the discrimination decision is given by the relative distance between the peak correlation and the next largest value. That is, in Fig. 7 the maximum correlation is about 0.94 for the B-52, while the TR-1 produces a maximal correlation of 0.69. Thus, a "discrimination ratio" can be defined as the ratio of these two values, or 1.36. The larger the ratio, the better the discrimination. If this number is close to unity, discrimination will not be reliable. Fig. 8 shows this ratio calculated as a function of added Gaussian noise level. One response from each target was in turn associated with an unknown aircraft. Each curve was generated by performing 20 correlations, using 20 different noise waveforms,

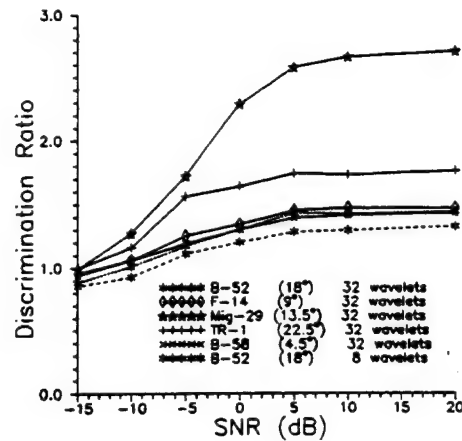


Fig. 8. Discrimination of various aircraft targets as a function of noise level.

and the results averaged. Since the correct response is known a priori, the numerator in the discrimination ratio is always taken to be that of the correct target. Thus, when the discrimination ratio is less than unity, an incorrect decision is made. From this plot it is seen that while the level of discrimination varies significantly from response to response, each unknown aircraft can be correctly identified in adverse noise conditions of up to -5 dB SNR. In fact, identification at this level is possible using even fewer wavelet coefficients. Fig. 8 also shows the discrimination ratio for the 18° B-52 response when only eight wavelet coefficients are retained. As expected, the performance degrades, since less information about smaller specular reflections is retained, but correct identification is still possible up to a -5 dB SNR.

## V. CONCLUSION

It has been shown that a significant reduction in the storage requirements for correlative discrimination of radar targets using transient responses is possible using the discrete wavelet transform. Experimental results demonstrate that a reduction of 16 to 1 (with no oversampling) is possible while still maintaining discrimination capabilities at SNR levels as low as -5 dB. Computation involves a reconstruction of waveforms using linear operations, and an inverse Fourier transform using the FFT. These calculations can be performed rapidly, providing a robust, efficient means of target discrimination.

## REFERENCES

- [1] P. Ilavarasan, J. E. Ross, E. J. Rothwell, K. M. Chen, and D. P. Nyquist, "Performance of an automated radar target discrimination scheme using E pulses and S pulses," *IEEE Trans. Antennas Propagat.*, vol. 41, pp. 582-588, May 1993.
- [2] M. C. Lin and Y. W. Kiang, "Target discrimination using multiple-frequency amplitude returns," *IEEE Trans. Antennas Propagat.*, vol. 38, pp. 1885-1889, Nov. 1990.
- [3] M. C. Lin, Y. W. Kiang, and H. J. Li, "Experimental discrimination of wire stick targets using multiple-frequency amplitude returns," *IEEE Trans. Antennas Propagat.*, vol. 40, pp. 1036-1040, Sept. 1992.
- [4] F. Y. S. Fok, "K-pulse estimation for a right-angled bent wire using more than one impulse response," *IEEE Trans. Antennas Propagat.*, vol. 38, pp. 1092-1098, July 1990.
- [5] J. P. Bayard and D. H. Schaubert, "Target identification using optimization techniques," *IEEE Trans. Antennas Propagat.*, vol. 38, pp. 450-456, Apr. 1990.
- [6] M. A. Morgan, "Scatterer discrimination based upon natural resonance annihilation," *J. Electromag. Waves Appl.*, vol. 2, no. 5/6, pp. 481-502, 1988.

- [7] J. E. Ross, "Application of Transient Electromagnetic Fields to Radar Target Discrimination." Ph. D. dissertation, Michigan State Univ., 1992.
- [8] H. J. Li and V. Chiou, "Aerospace target identification—Comparison between the matching score approach and the neural network approach," *J. Electromag. Waves Appl.*, vol. 7, no. 6, pp. 873–893, 1993.
- [9] R. G. Atkins, R. T. Shin, and J. A. Kong, "A neural network method for high range resolution target classification," in *Progress in Electromagnetics Research*. New York: Elsevier, 1991, pp. 255–292.
- [10] E. J. Rothwell, K. M. Chen, D. P. Nyquist, P. Ilavarasan, J. E. Ross, R. Bebermeyer, and Q. Li, "A general E-pulse scheme arising from the dual early-time/late-time behavior of radar scatterers," *IEEE Trans. Antennas Propagat.*, to be published.
- [11] C. Y. Tsai, R. Bebermeyer, E. Rothwell, K. M. Chen, and D. Nyquist, "Radar target discrimination using neural networks and the discrete wavelet transform," in *Proc. URSI Radio Science Meeting (Ann Arbor, MI)*, June 28–July 2, 1993, p. 219.
- [12] H. J. Li and S. H. Yang, "Using range profiles as feature vectors to identify aerospace objects," *IEEE Trans. Antennas Propagat.*, vol. 41, pp. 261–268, Mar. 1993.
- [13] W. H. Press, S. A. Teukolsky, W. T. Vetterling, and B. P. Flannery, *Numerical Recipes in FORTRAN*, 2nd ed. Cambridge, U.K.: Cambridge University Press, 1992, ch. 13.
- [14] O. Rioul and M. Vetterli, "Wavelets and signal processing," *IEEE Signal Processing Mag.*, vol. 8, pp. 14–38, Oct. 1991.
- [15] I. Daubechies, "The wavelet transform, time-frequency localization and signal analysis," *IEEE Trans. Inform. Theory*, vol. 36, pp. 961–1005, Sept. 1990.
- [16] O. Rioul and P. Duhamel, "Fast algorithms for discrete and continuous wavelet transforms," *IEEE Trans. Inform. Theory*, vol. 38, pp. 569–586, Mar. 1992.
- [17] R. A. DeVore, B. Jawerth and B. J. Lucier, "Image compression through wavelet transform coding," *IEEE Trans. Inform. Theory*, vol. 38, pp. 719–746, Mar. 1992.
- [18] S. G. Mallat, "Multifrequency channel decomposition of images and wavelet models," *IEEE Trans. Acoust., Speech, Signal Processing*, vol. 37, pp. 2091–2110, Dec. 1989.
- [19] —, "A theory for multiresolution signal decomposition: the wavelet transform," *IEEE Trans. Pattern Anal. Machine Intell.*, vol. 11, pp. 674–693, July 1989.

# Scattering Center Analysis of Radar Targets Using Fitting Scheme and Genetic Algorithm

Qing Li, Edward J. Rothwell, *Senior Member, IEEE*, Kun-Mu Chen, *Fellow, IEEE*,  
and Dennis P. Nyquist, *Senior Member, IEEE*

**Abstract**—Development of successful radar target discrimination schemes using ultrawideband signatures hinges on an accurate understanding of the scattering behavior of complex radar targets. Since it is very difficult to calculate the scattered field of complex targets theoretically, a mathematical model (Altes model) representing scattering center impulse response has been developed to describe the scattered field. The extraction of temporal positions, pulse responses, and transfer functions of target scattering centers is demonstrated using artificially created and measured responses. Two different scale aircraft models (B-58 and B-52) are utilized. The fitting scheme based on the least squares method is quite satisfactory but its accuracy deteriorates when the overlapping of scattering-center pulse responses is severe. To overcome this problem a genetic algorithm is used to improve the results. While the genetic algorithm gives much better accuracy, it consumes much more computer time due to its global nature and lack of derivative information. The purpose of this analysis is to provide a method to reduce data storage for ultrawideband signatures in target discrimination.

## I. INTRODUCTION

DEVELOPMENT of successful radar target discrimination schemes using ultrawideband signatures hinges on an accurate understanding of the scattering behavior of complex radar targets. In the time domain, a target response consists of an early-time component, which is localized and specular in nature, followed by a late-time component. The temporal shape of specular responses depends on the localized geometry of the target. Many radar targets can be well approximated as consisting of a set of discrete scattering centers.

One common approach to estimate a time-domain target scattering profile and to locate and characterize the discrete scattering centers is a parametric scattering model, such as the Prony model [1]–[3]. Although Prony's method is simple to use, it is extremely sensitive to random noise and the selection of the number of scattering centers present in the measured response waveform. The most important drawback is that the scattering center temporal positions determined by the above model do not correspond to the actual ones for a band-limited measurement system. These papers did not

present pulse responses and transfer functions of individual scattering centers on the target.

This paper introduces a model suggested by Altes [4], which presents a more fundamental study of scattering properties of radar targets. The pulse responses and transfer functions of individual scattering centers have been identified using the early-time responses with temporally separated "hot spots." By understanding how these centers process the transmitted waveform, scattering center information is stored instead of the response. Thus, the data storage is reduced markedly. A correlation-based radar target discrimination scheme has been developed based on the scattering center information and will be presented in a future paper.

The results of scattering center transfer functions obtained using the least squares method are quite satisfactory when scattering centers are widely separated, but the accuracy of the method deteriorates when the overlapping of scattering-center pulse responses is severe. To solve this problem, a genetic algorithm [5] which is based on the mechanics of natural selection and natural genetics is introduced.

The outline of this paper is as follows—in Section II, we describe a scattering model (Altes model) and present the fitting scheme based on the least squares method and the genetic algorithm to determine scattering center temporal positions and amplitudes. In Section III, we test the Altes model using artificial pulse responses and determine the range of parameter values by comparing a theoretical result based on physics optics (PO) with that using Altes model. Two scale aircraft models of B-58 and B-52 are utilized in Section IV to illustrate the scheme performance for complex targets.

## II. SCATTERING MODEL

### A. Fitting Scheme

Altes [4] suggests that the early-time scattered field response,  $s_0(t)$ , consists of distinct specular reflections arising from scattering centers on the target. The response is assumed to be sampled at time  $t_i$ ,  $i = 1, 2, \dots, I$ . If  $h_m(t)$  represents impulse response of the  $m$ th scattering center at some aspect angle, then the early-time scattered field pulse response is modeled as

$$s_0(t) \approx p(t) * \sum_m h_m(t) = \sum_m f_m(t) \quad (1)$$

Manuscript received November 14, 1994; revised August 21, 1995. This work was supported by Thermo Trex Corporation under Purchase Order 22068 and the office of Naval Research under Grant N00014-93-1271.

The authors are with the Department of Electrical Engineering, Michigan State University, East Lansing, MI 48824 USA.

Publisher Item Identifier S 0018-926X(96)01203-3.



where  $p(t)$  is the transmitted pulse waveform, and  $f_m(t)$  is pulse response of the  $m$ th scattering center given by

$$f_m(t) = p(t) * h_m(t). \quad (2)$$

If the model (2) is taken to be an accurate physical description of early-time scattering, only the impulse response  $h_m(t)$  needs to be determined to specify the scattered field response. If the scattering centers are purely specular, each impulse response will take the form of a delta function.

Without loss of generality, the impulse response of the  $m$ th scattering center located at temporal position  $T_m$  can be expanded as [4]

$$h_m(t) = \sum_{n=-\infty}^{\infty} a_{mn} \delta^{(n)}(t - T_m). \quad (3)$$

Here, a negative value of  $n$  refers to the  $n$ th integral of the delta function while a positive value of  $n$  refers to the  $n$ th derivative of the delta function. The case of  $n = 0$  represents the delta function itself. This is equivalent to representing the transfer function of the  $m$ th scattering center as a polynomial function of  $\omega$ . Using the time shifting and differential theorem for Fourier transforms gives

$$H_m(\omega) = \mathcal{F}\{h_m(t)\} = \sum_n a_{mn} e^{-j\omega T_m} (j\omega)^n. \quad (4)$$

Unfortunately, it is not possible to measure  $H_m(\omega)$  since only a finite portion of the spectrum can be covered in any measurement. Thus, it is necessary to deal with the band-limited pulse response of the scattering centers. Let  $F_m(\omega)$  represent the band-limited frequency domain response of the  $m$ th scattering center

$$F_m(\omega) = \mathcal{F}\{f_m(t)\} = \sum_n a_{mn} G_{mn}(\omega) \quad (5)$$

where

$$G_{mn}(\omega) = P(\omega) e^{-jT_m \omega} (j\omega)^n. \quad (6)$$

Thus, the pulse response of the  $m$ th scattering center can be written as

$$f_m(t) = \sum_n a_{mn} g_{mn}(t) \quad (7)$$

where

$$g_{mn}(t) = \mathcal{F}^{-1}\{G_{mn}(\omega)\}. \quad (8)$$

When the response of a target is measured in the frequency domain, the scattering center transfer functions cannot be separated. However, if the frequency band is wide enough, the pulse responses found by windowing and inverse transforming the frequency domain target response will be temporally separated. Thus, computation of the scattering center transfer functions must be done in the time domain, by calculating the unknown amplitudes  $a_{mn}$ . These then give the transfer functions through (4).

The procedure for computing the amplitudes  $a_{mn}$  is as follows. The measured frequency domain scattered field response of a particular target is windowed with the incident

pulse spectrum  $P(\omega)$  (to reduce unwanted truncation-induced oscillations) and inverse transformed into time domain using the fast Fourier transform (FFT). The early-time portion of the time-domain pulse response will consist of events representing the pulse responses of the scattering centers. If the equivalent pulse  $p(t)$  is wide, some of the pulse responses will overlap, and it is extremely difficult to separate scattering centers. However, if the pulse is narrow, the events will be temporally separated and can be easily analyzed using the least squares method. First, the first scattering-center pulse response  $f_1(t)$  calculated from (7) is fit to the measured pulse response  $s_0(t)$  with the amplitudes,  $a_{1n}$ , determined to provide a minimum error best fit. This best fit will match the scattering center with the largest energy. After the scattering-center pulse response has been determined, a signal,  $r_2(t)$ , is formed by subtracting off  $f_1(t)$  from  $s_0(t)$  (providing a signal with one less scattering center). Then a waveform  $f_2(t)$  is fit to  $r_2(t)$ , determining the pulse response of the scattering center with the second highest energy. This response is then subtracted off to form a signal  $r_3(t)$  and the process is repeated until all of the dominant scattering-center pulse responses have been determined. This process is called the "fitting scheme."

In the process of determining the scattering-center pulse responses, it is necessary to find  $T_m$ , the  $m$ th temporal position of the scattering center. This is done by the least squares method during the minimization process which determines the amplitudes  $a_{mn}$ . Define the error function to be minimized as

$$\begin{aligned} \epsilon(T_m) &= \sum_i \left[ s_0(t_i) - \sum_{k=1}^m \sum_n a_{kn} g_{kn}(t_i) \right]^2 \\ &= \sum_i \left[ r_m(t_i) - \sum_n a_{mn} g_{mn}(t_i) \right]^2 \end{aligned} \quad (9)$$

where

$$\begin{aligned} r_m(t) &= s_0(t) - \sum_{k=1}^{m-1} \sum_n a_{kn} g_{kn}(t) \quad m > 1 \\ r_m(t) &= s_0(t) \quad m = 1. \end{aligned} \quad (10)$$

In essence, the scattering-center pulse response is "placed" over the pulse response at  $T_m$ ; and  $a_{mn}$  are determined to minimize the error for that choice of  $T_m$ . The proper  $T_m$  which describes the temporal position of the scattering center is that which produces the least minimized error. To determine the minimum, the entire early-time range of possible values of  $T_m$  is searched.

Note that the error is minimized when

$$\frac{\partial \epsilon(T_m)}{\partial a_{mk}} = -2 \sum_i \left[ r_m(t_i) - \sum_n a_{mn} g_{mn}(t_i) \right] g_{mk}(t_i) = 0 \quad k = 1, 2, \dots, N \quad (11)$$

where  $N$  is the total number of  $n$  used in (4). The above equation can be written in linear equation form as

$$\sum_n a_{mn} A_{nk} = b_k \quad k = 1, 2, \dots, N \quad (12)$$

where

$$\begin{aligned} A_{nk} &= \sum_i g_{mn}(t_i) g_{mk}(t_i) \\ b_k &= \sum_i r_m(t_i) g_{mk}(t_i) \end{aligned} \quad (13)$$

### B. Genetic Algorithm

Genetic algorithms are different from other methods in four ways [5]:

- 1) Genetic algorithms work with a coding of the parameter set, not the parameters themselves.
- 2) Genetic algorithms search from a population of points, not a single point.
- 3) Genetic algorithms use objective function information, not derivatives or other auxiliary knowledge.
- 4) Genetic algorithms use probabilistic rules, not deterministic rules.

A simple genetic algorithm is composed of three operations: selection, crossover, and mutation.

Consider the sampled early-time response  $r(t_i)$  created or measured at time  $t_i$ . The scattering-center pulse response amplitudes  $\{a_{mn}\}$  can be found by minimizing the residual

$$R(T_m, a_{mn}) = \sum_i \frac{1}{\epsilon} [r(t_i) - s_0(t_i)]^2 \quad (14)$$

where  $s_0(t)$  is fitting function given by (1). Here,  $\epsilon$  is the energy in the response.

Once the time positions  $T_m$  are found by minimizing (14), the scattering center amplitudes,  $a_{mn}$ , are determined for given  $\{T_m\}$  using the least squares method. Then the  $m$ th scattering center transfer function can be reconstructed using (4).

In the standard implementation of genetic algorithms [5], only a function maximization is defined. Thus, to minimize (14) we must maximize a fitness function defined as

$$F(T_m) = C - R(T_m) \quad (15)$$

where  $F(T_m)$  must be greater than zero. The constant  $C$  is given by the user and can be updated to reduce  $\max[F(T_m)]$  toward zero.

$F(T_m)$  is maximized by a repeated three-step process: selection, crossover, and mutation. The genetic algorithm mimics biological natural selection by encoding the parameters as binary strings, and then crossbreeding and mutating the strings using a survival rule. Let  $T_m$  be defined on  $[T_m^{\min}, T_m^{\max}]$  and be coded by

$$T_m = T_m^{\min} + \frac{T_m^{\max} - T_m^{\min}}{2^L - 1} \sum_{l=1}^L b_{m,l} 2^{l-1} \quad (16)$$

where  $L$  is length of a bit string and  $b_{m,l}$  is the bit pattern. The bit strings are then concatenated to form a single string  $B$  of length  $ML$  which represents all the variables.  $M$  is the total number of scattering centers assumed. There are many ways to choose offspring with appropriate bias toward the best [5]. One way is that breeding begins by using "stochastic

remainder sampling without replacement" to create a "pool" (population) of  $K$  ( $K$  is even) bit strings. Let

$$F_k = F(T(B_k)) \quad (17)$$

$$P_k = \frac{F_k}{\sum_k F_k} \quad (18)$$

and

$$e_k = KP_k \quad (19)$$

where  $T$  includes  $T_1, T_2, \dots, T_M$ ,  $P_k$  is the probability of the  $k$ th bit string,  $B_k$  is a bit string consisting of the concatenation of all the variable bit strings, and  $e_k$  is the "expected" allocation of members to the pool. By applying a rule of survival, we place the integer part of  $e_k$  copies of  $B_k$  into the pool; and fill the remainder of pool by selecting at random from  $\{B_k\}$  with probability

$$p_k = e_k - (e_k) \quad (20)$$

where  $(e_k)$  is integer part of  $e_k$ .

After the pool is filled,  $K/2$  pairs of bit strings from the pool are selected at random. Pairs are bred with probability  $P_c$  (selected by the user, typically  $P_c = 0.5$  to  $0.6$ ), a crossover point is chosen at random and bit string information is "swapped". After the population has been completely bred, one bit in  $B_k$  is chosen at random and is replaced with probability  $P_m$  by Not (bit) to mimic mutation. The probability  $P_m$  is selected by the user, but is generally chosen as

$$P_m \approx \frac{1}{K} \quad (21)$$

To improve results, the three steps are repeated many times by creating a new population from the old one. Thus, more "fit" bit strings pass on their information with the greatest probability and, on the average, produce a larger value of the objective function. The process is terminated when the population becomes stable.

We should regulate the level of competition among members of the population to achieve the performance we desire. At the start of the genetic algorithm, it is common to have a few extraordinary individuals in the population and, using the normal selection rule, these individuals would take over a significant proportion of the finite population in a single generation. This undesirable feature may be overcome using "fitness scaling." The scaling method used here is linear scaling

$$F^* = aF + b \quad (22)$$

where  $F$  is the raw-fitness function and  $F^*$  is a scaled-fitness function.

We choose the average scaled fitness  $F_{\text{avg}}^*$  to be equal to the average raw fitness  $F_{\text{avg}}$ , because subsequent use of the selection procedure will insure that each average population number contributes one expected offspring to the next generation. To control the number of offspring given to the population member with maximum raw fitness, the maximum scaled fitness,  $F_{\text{max}}^*$ , is taken as

$$F_{\text{max}}^* = c_{\text{mult}} F_{\text{avg}} \quad (23)$$



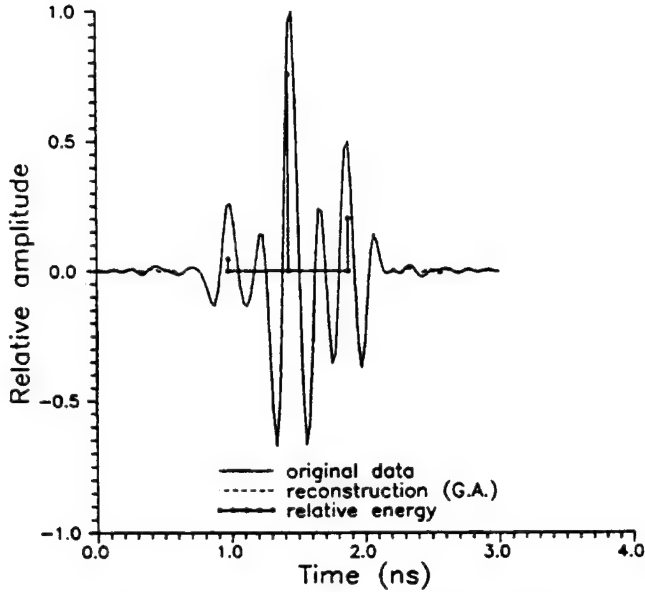


Fig. 1. Artificial response and reconstructed response using genetic algorithm, three scattering centers,  $n = -2, -1, \dots, 2$ , and  $K = 200$ ,  $L = 40$ ,  $P_c = 0.6$ ,  $P_m = 0.03$ , and 25 generations.

where  $c_{\text{mult}}$  is the scaling factor desired for the best population member, and is typically taken between 1.2 and 2. From the above two conditions,  $a$  and  $b$  are given by

$$\begin{aligned} a &= (c_{\text{mult}} - 1) \frac{F_{\text{avg}}}{F_{\text{max}} - F_{\text{avg}}} \\ b &= (1 - a)F_{\text{avg}} \end{aligned} \quad (24)$$

So, a few extraordinary individuals get scaled down and lower members of the population get scaled up. When some bad strings are far below the population average and maximum, using the above linear scaling may force lower fitness values to be negative. In this case, we still let the raw and scaled fitness average be the same, but map the minimum raw fitness  $F_{\text{min}}$  to the scaled fitness  $F_{\text{min}}^* = 0$ . Then  $a$  and  $b$  are expressed as

$$\begin{aligned} a &= \frac{F_{\text{avg}}}{F_{\text{avg}} - F_{\text{min}}} \\ b &= -aF_{\text{min}} \end{aligned} \quad (25)$$

Generally the genetic algorithm is not likely to get stuck at a local minimum, since its random nature forces it to investigate a dense range of parameters simultaneously. However, there is no guarantee that the global maximum will be reached due to this random nature.

Two methods to solve this problem are to increase the numbers  $L$  and  $K$  and improve the fitness scaling. The global nature of the algorithm and the lack of derivative information causes the genetic algorithm to converge very slowly compared to other nonglobal methods. However, these other methods might not converge at all.

### III. SIMPLE TESTS OF ALTES MODEL

To test the Altes model, we created an artificial response with three scattering centers. If the scattering centers are

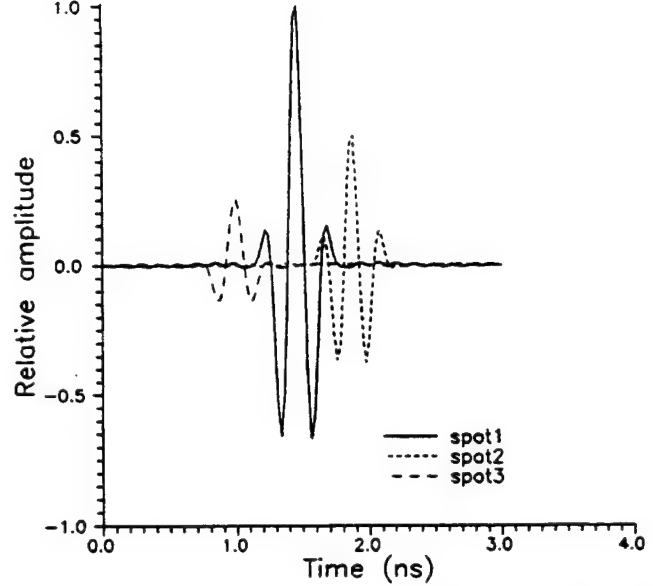


Fig. 2. Pulse responses of three specular points obtained using the genetic algorithm.

temporally separated, the transfer functions can be determined accurately using both the fitting scheme and the genetic algorithm. When the pulse response overlapping due to relatively narrow bandwidth used in our measurement system is considerable, the transfer functions cannot be determined accurately using the fitting scheme. A genetic algorithm must then be utilized to extract scattering center information since the genetic algorithm considers all specular responses simultaneously. The genetic algorithm should provide better performance. Fig. 1 shows the artificially created pulse response which has considerable overlapping. Each scattering center impulse response is represented by an integral of a delta function, a delta function, and a derivative of a delta function, which have the amplitudes of 0.25, 1.0, and 0.5, respectively. They are created in the frequency band 1–7 GHz, windowed using a Gaussian modulated cosine (GMC) function centered at 4 GHz and inverse transformed with a 4096 point FFT [6]. Also shown in Fig. 1 is the reconstructed response found using the genetic algorithm. Here,  $K = 200$ ,  $L = 40$ , and 25 generations were used, and  $n = -2, -1, \dots, 2$  for a better fit. The agreement is very good. The heights and positions of the stars (\*) represent the relative energy in each response and the temporal positions of the three scattering centers. The pulse responses of the three scattering centers calculated using (2) are shown in Fig. 2. The scattering center transfer functions, calculated using (4) are shown in Fig. 3. As expected, the first, second, and third scattering centers are dominated by a constant,  $\omega$ , and  $1/\omega$ , respectively. Note that to get the true transfer function, the spectrum of the pulse  $P(\omega)$  has been divided out.

The genetic algorithm has many variables to consider. The accuracy of the results is highly dependent on both the initial population size  $K$  and the bit string length  $L$ . More bits give greater accuracy but slower convergence. A larger population provides a better sampling of the solution space

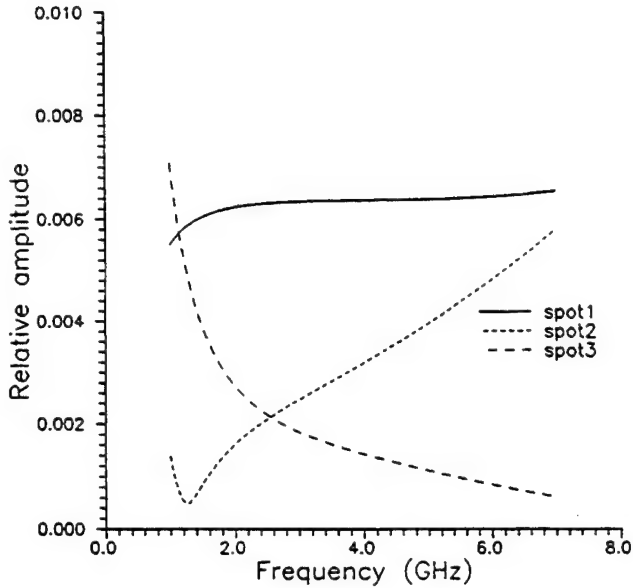


Fig. 3. Transfer functions of three specular points obtained using genetic algorithm.

but slower convergence too. Note that mutation guards against the algorithm getting stuck in a local minimum but results in slower convergence. The main impact of the options is on convergence speed.

The drawback of the genetic algorithm is that it consumes far more computer time (about 30–40 times) than the fitting scheme. It takes about 10 min. using the fitting scheme while five hours are required using the genetic algorithm in the above example for a 486 DX-66 personal computer. If overlapping is not considerable, we prefer the fitting scheme to the genetic algorithm.

The pulse response of a cylinder illuminated from the end was used as a test of the sensitivity of pulse-response reconstruction to the number of terms used in the polynomial expansion of the transfer function using the fitting scheme.

Consider the excitation field incident on the end of a finite cylinder as shown in Fig. 4. The electric field in the far zone is given by [7], [8]

$$\vec{E} = -j2\pi E_0 \frac{e^{-jk r}}{k r} \frac{1}{\lambda^2} [e_{0x} \gamma \hat{x} + e_{0y} \gamma \hat{y} - (\alpha e_{0x} + \beta e_{0y}) \hat{z}] V \quad (26)$$

where

$$V = 2a^2 \int_{-\pi/2}^{\pi/2} \cos^2 t \operatorname{sinc} \left[ \frac{2a(\alpha + \alpha_0) \cos t}{\lambda} \right] \times \exp[jka(\beta + \beta_0) \sin t] dt \quad (27)$$

and the direction cosines  $\alpha_0, \beta_0, \gamma_0, \alpha, \beta, \gamma$  are given in terms of incident and reflection aspect angles  $\theta_0, \phi_0$  and  $\theta, \phi$ . The incident field vector  $\hat{e}_0$  can be written as

$$\begin{aligned} \hat{e}_0 &= e_{0x} \hat{x} + e_{0y} \hat{y} + e_{0z} \hat{z} \\ &= e_{0x} \hat{x} + e_{0y} \hat{y} - \left( \frac{\alpha_0}{\gamma_0} e_{0x} + \frac{\beta_0}{\gamma_0} e_{0y} \right) \hat{z}. \end{aligned} \quad (28)$$

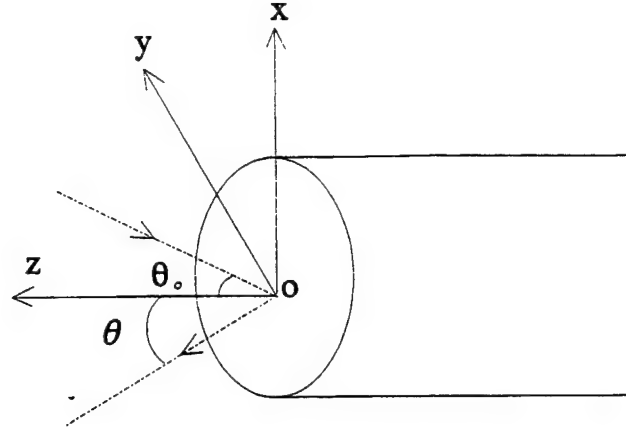


Fig. 4. Excitation geometry for scattering from the end of a thick cylinder.

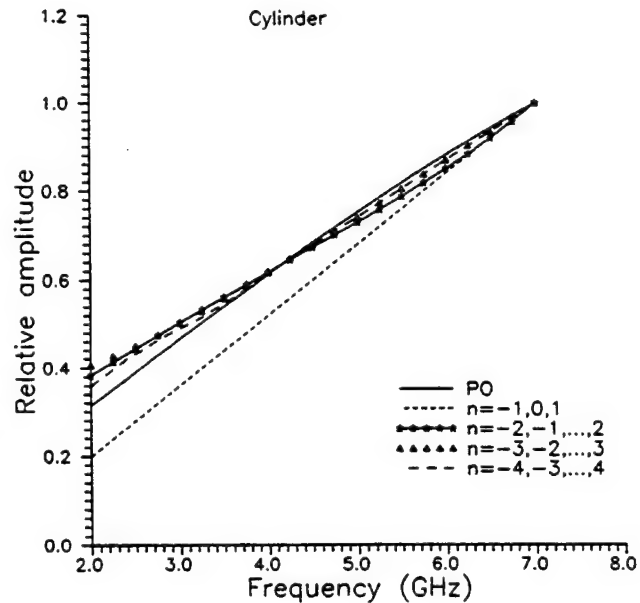


Fig. 5. Transfer function of single scattering center for cylinder with end-incident excitation determined using various numbers of terms in the polynomial expansion.

The transfer function is defined by

$$H(\omega) = \frac{\vec{E} \cdot \hat{e}_r}{E_0} = \frac{\vec{H} \cdot \hat{h}_r}{H_0} \quad (29)$$

where  $\hat{e}_r$  and  $\hat{h}_r$  are the receiver polarization unit vectors.

Fig. 5 shows the transfer function of the cylinder (4" in diameter and 12" in length) scattering center found using the fitting scheme and various number of terms. The circular cylinder is measured in the frequency band 1–7 GHz, windowed using a GMC function centered at 4 GHz and inverse transformed with a 4096 point FFT. For  $n = -1, 0, 1$  the result is quite poor. As the number of terms increases, the agreement with PO improves. Note that incident and reflected aspect angles are taken as  $\theta_0 \approx \theta \approx 3^\circ, \phi_0 \approx 45^\circ, \phi \approx 225^\circ$  due to a slightly bistatic setup in our measurement system. When the number of terms is increased too much, it will cost

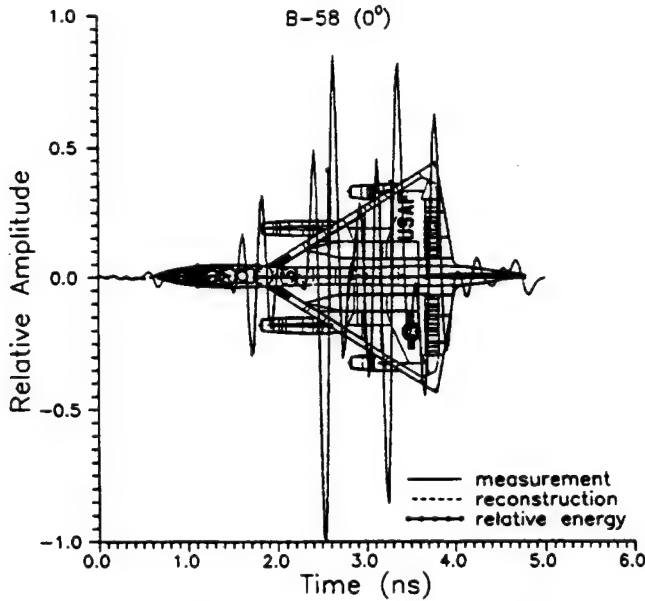


Fig. 6. Response of  $0^\circ$  B-58 measured in the band 1–7 GHz, and reconstructed response using genetic algorithm, and  $n = -2, -1, \dots, 2$ , and  $K = 600, L = 80$ , and 30 generations.

more computer effort. In general,  $n$  is taken as  $-2, -1, \dots, 2$  or  $-3, -2, \dots, 3$  according to our experience.

#### IV. PERFORMANCE OF THE FITTING SCHEME AND GENETIC ALGORITHM USING MEASURED DATA OF B-58 AND B-52 AIRCRAFT

Fig. 6 shows the nose-on pulse response of a B-58 measured in the frequency band 1–7 GHz, windowed using a GMC function centered at 4 GHz and inverse transformed with a 4096 point FFT as before. Since the bandwidth is limited, some pulse responses overlap. If accurate estimation of the number of scattering centers is not possible, we first use a lesser scattering center number and observe the scattering-center pulse responses and transfer functions. Second, if the reconstructed waveform does not match well, we then increase the estimation number until a better fit and reasonable larger responses are observed. Also shown in Fig. 6, are the temporal positions of six scattering centers found using the genetic algorithm outlined before. The transfer functions of these scattering centers have been found using  $n = -2, -1, \dots, 2$ . The height of the stars shown in Fig. 6 represents the relative energy in each pulse response. Obviously, the dominant specular reflection comes from the first engine mount and the next largest reflection comes from the second engine mount. Note that each specular reflection matches quite well with a physical feature on the target, including the front stabilizer, and the inlets of the first and second engine.

Once the scattering-center pulse responses have been determined, the overall early-time pulse response of the target can be reconstructed using (1). This is shown in Fig. 6 as the dotted line. The reconstructed response matches extremely well.

Fig. 7 shows the scattering center transfer functions found using (4). These waveforms are different from each other, indi-

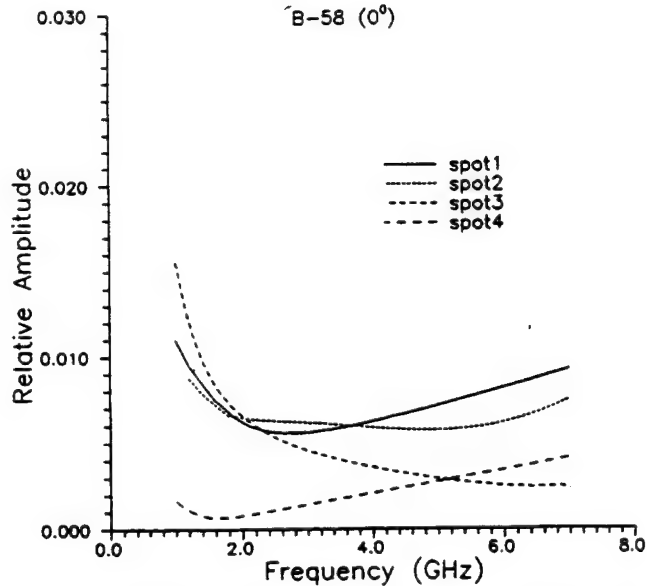


Fig. 7. Transfer functions of first, second, and third specular points obtained using genetic algorithm.

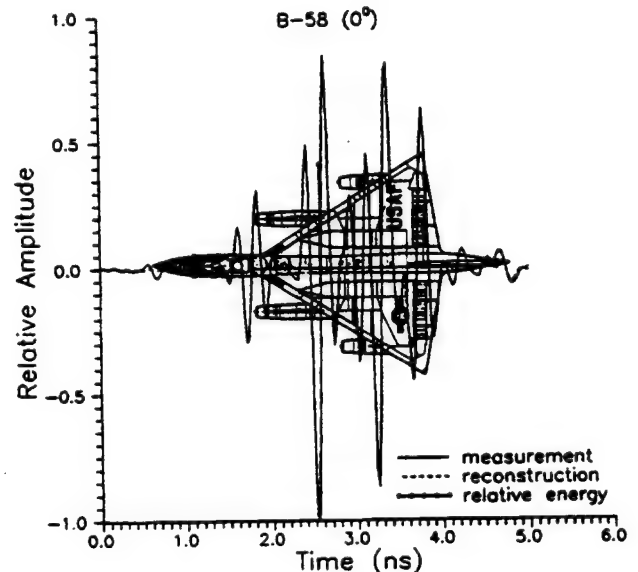


Fig. 8. Response of B-58 at  $0^\circ$  aspect angle measured in band 1–7 GHz, and reconstructed response using the fitting scheme, six scattering centers,  $n = -2, -1, \dots, 2$ , and GMC window with  $\tau = 0.3$  ns,  $f_c = 4$  GHz.

cating that different scattering centers lead to different transfer functions. The responses of the first and second scattering centers are dominated by a relatively flat shape, indicating a primarily impulsive response, and the third scattering center is dominated by the first integral of the equivalent pulse.

As a comparison, the fitting scheme is applied to the early-time transient response shown in Fig. 6. Fig. 8 shows the reconstructed response of B-58 at the nose-on incidence. We notice that the temporal positions of the third, fifth, and sixth scattering centers are shifted somewhat due to pulse response overlapping. Consequently, the responses are not as good as

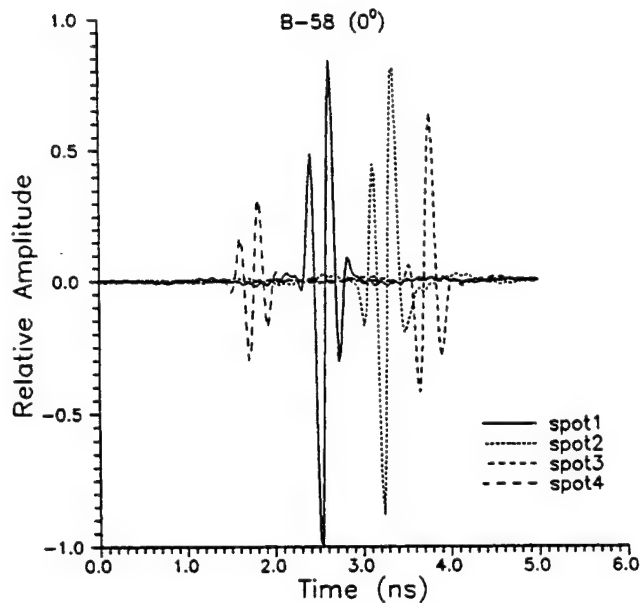


Fig. 9. Pulse response of the four largest specular points obtained using the fitting scheme.

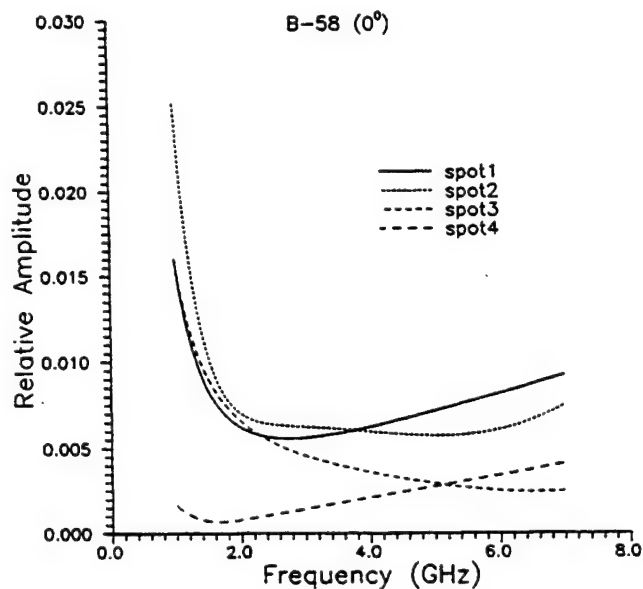


Fig. 10. Transfer functions of the four largest specular points obtained using the fitting scheme.

those shown before, especially in the lower frequency region. These can be observed in Figs. 9 and 10.

To test the effect of aspect angle on the performance, the pulse response of the B-58 model at  $10^\circ$  measured at 601 points in the frequency band 1–7 GHz, with six scattering centers and  $n = -2, -1, \dots, 2$ , is shown in Fig. 11. At this aspect angle, the second inner engine inlet and first outer engine mount, the second inner engine mount, and second outer engine inlet are at almost at the same down range point. In Fig. 11, we see that the dominant specular reflection comes from the first inner engine mount and the next largest reflection comes from the second inner engine mount. The

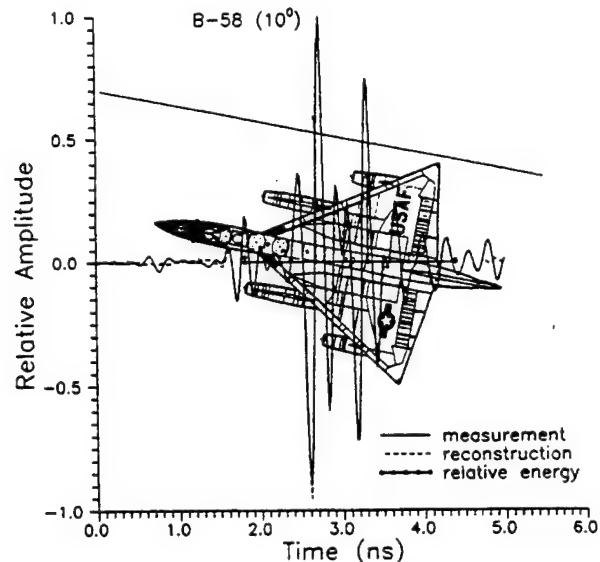


Fig. 11. Response of B-58 at  $10^\circ$  aspect measured in band 1–7 GHz, and reconstructed response using six scattering centers, 4096 pt FFT,  $n = -2, -1, \dots, 2$ , and GMC window with  $\tau = 0.3$  ns,  $f_c = 4$  GHz.

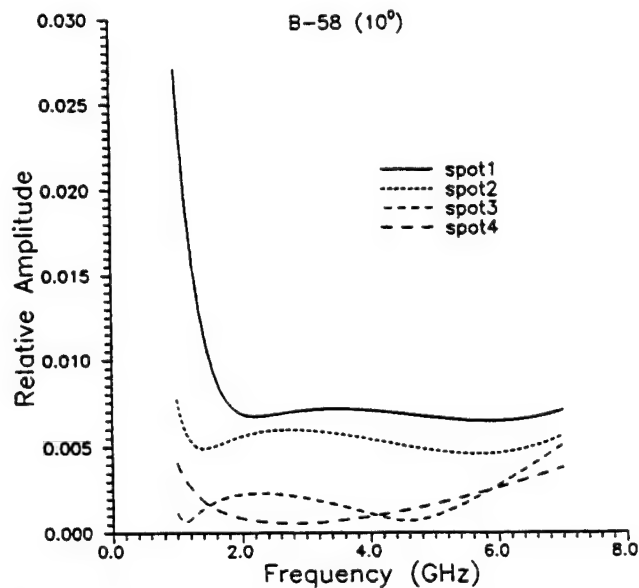


Fig. 12. Transfer functions of first, second, third, and fourth specular points.

front stabilizer and first inner engine inlet are also located at the expected place. Because of aspect angle variation, the transfer functions of associated scattering centers show some difference, as illustrated in Fig. 12.

As another example, Fig. 13 shows the nose-on pulse response of a B-52 and the reconstructed waveform using nine scattering centers, and  $n = -2, -1, \dots, 2$  using the fitting scheme. The dominant specular reflection comes from the first engine mount (which coincides with the second engine inlet) and the next largest reflection comes from the second engine mount. Note that each specular reflection again matches quite well with a physical feature on the target, including the wing joint, trailing edges of the wing and rear stabilizer (rear

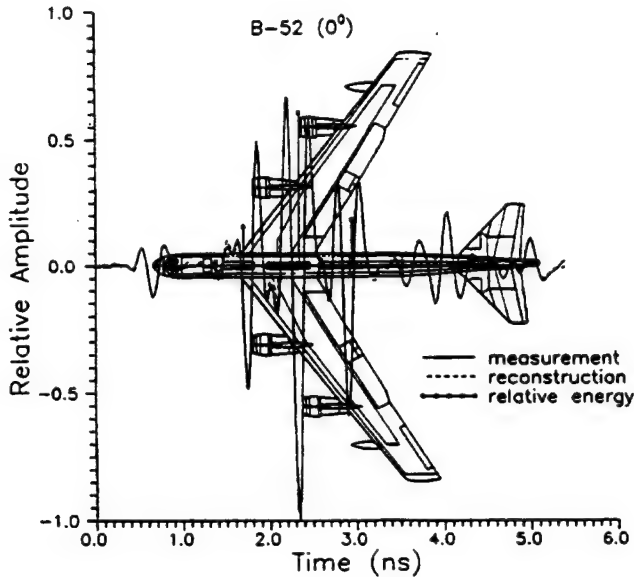


Fig. 13. Response of B-52 at  $0^\circ$  aspect angle measured in band 1–7 GHz, and reconstructed response using the fitting scheme, nine scattering centers,  $n = -2, -1, \dots, 2$  and GMC window with  $\tau = 0.3$  ns,  $f_c = 4$  GHz.

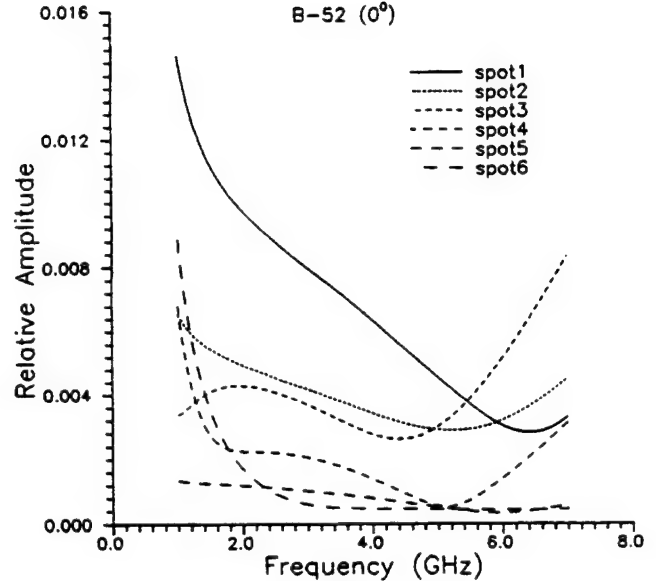


Fig. 14. Transfer functions of the six largest specular points obtained using the fitting scheme.

wing). It is also interesting to see that in terms of relative energy, the reflection from the nose of the aircraft is quite small. The first scattering center transfer function is dominated by a downward slope, indicating a  $1/\omega$  or integral impulse response. The other responses are relatively flat, indicating a primarily impulsive response as shown in Fig. 14. Note that the nose response is quite close to a delta function over the measurement band. Again, each scattering center has different transfer function waveforms. We also notice from Figs. 6 and 14 that the transfer function of a particular scattering center is also highly dependent on the physical properties of the surface at the specular point.

To test the effects of random noise on the scheme, zero-mean white Gaussian noise is added. SNR for a sampled transient waveform is defined by [9]

$$\text{SNR} = 10.0 \log_{10} \left\{ \frac{\int_W v^2(t) dt}{W \psi_0} \right\} \quad (30)$$

where  $v(t)$  is the noise-free signal,  $\psi_0$  is the mean-square value of the noise voltage, and  $W$  is chosen as the minimum duration window that contains 99% of the total energy in the noise-free data.

Fig. 15 shows the pulse response of the  $0^\circ$  B-52 scale aircraft model with zero-mean white Gaussian noise added with SNR = 10 dB. We notice that the response is slightly distorted due to this random noise. Fig. 16 shows the noise-free B-52 response, and the reconstructed waveforms from the noisy data found using nine scattering centers and  $n = -2, -1, \dots, 2$ . The five largest dominated scattering center temporal positions can be extracted, and their three largest scattering center transfer functions match quite well with the noise-free results as shown in Fig. 17. The smallest scattering

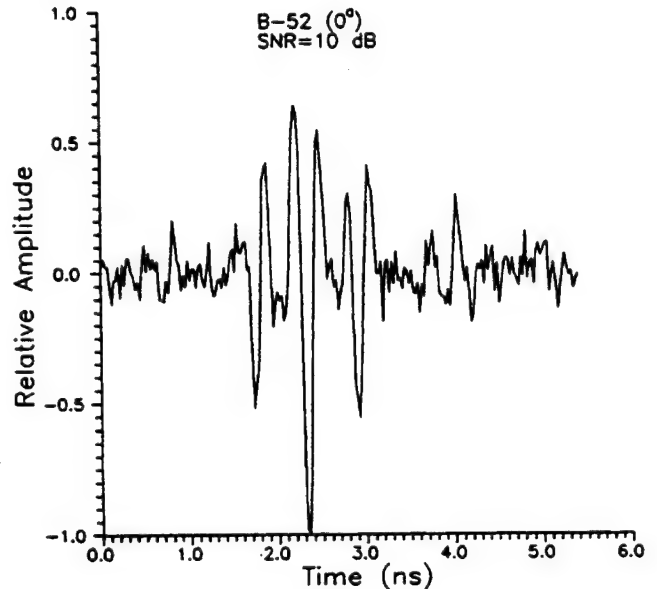


Fig. 15. Response of B-52 aircraft model at nose-on incidence with zero-mean white Gaussian noise added. SNR = 10 dB.

centers do not represent physical features on the target, but correspond to noise realizations.

Fig. 18 shows the reconstructed response of the noisy  $0^\circ$  B-52 measured in the frequency band 1–7 GHz with SNR = -5 dB, using six scattering centers, and  $n = -1, 0, 1$ . It is interesting to note that the locations of first engine mount, the second engine mount, the wing joint and trailing edge of wings scattering centers match quite well. The reconstructed response is a much better representation than the original noisy waveform. We conclude that the determination of scattering center temporal positions is much less sensitive to noise than the transfer functions.

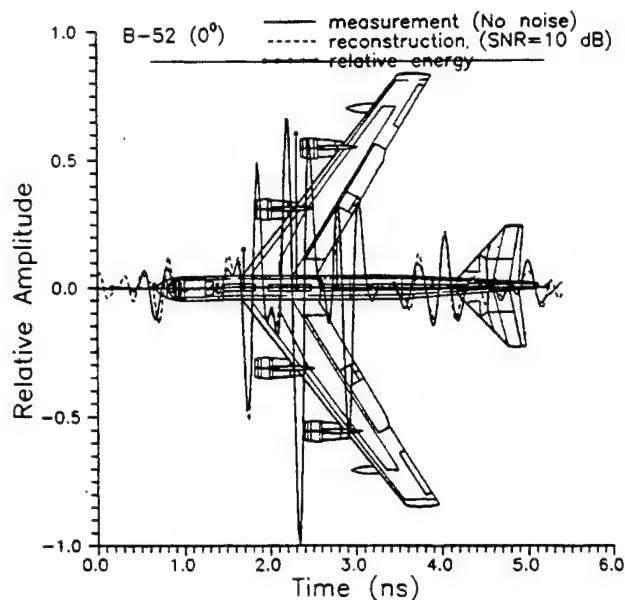


Fig. 16. Response of B-52 at  $0^\circ$  aspect measured in band 1–7 GHz, and reconstructed response using 9 scattering centers with SNR = 10 dB,  $n = -2, -1, \dots, 2$ , and GMC window with  $\tau = 0.3$  ns,  $f_c = 4$  GHz.

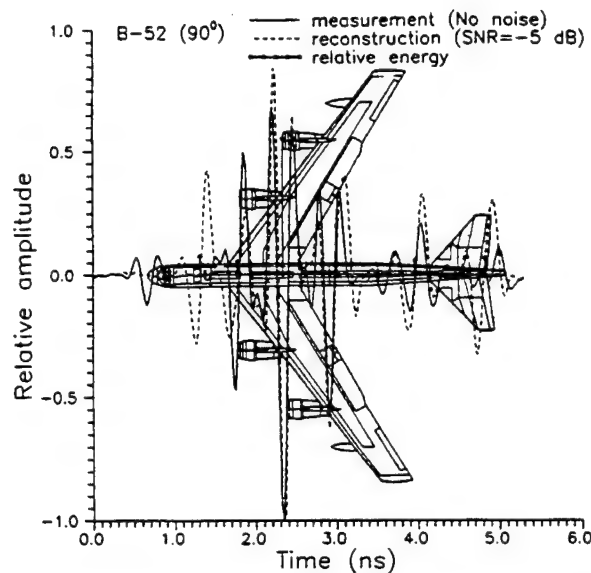


Fig. 18. Response of B-52 at  $90^\circ$  aspect angle measured in band 1–7 GHz, and reconstructed response using 6 scattering centers with SNR = -5 dB,  $n = -1, 0, 1$ , and GMC window with  $\tau = 0.3$  ns,  $f_c = 4$  GHz.

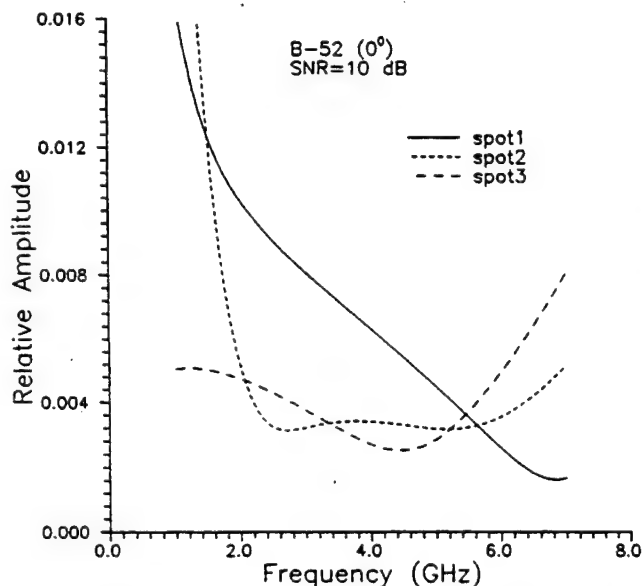


Fig. 17. Transfer functions of first, second, and third specular points. SNR = 10 dB.

## V. CONCLUSION

The Altes model describing the transient early-time response is evaluated using both artificial data and measured data. The fitting scheme is good in the determination of scattering center temporal positions, pulse responses, and transfer functions with respect to the different targets if the overlapping of scattering-center pulse responses is not considerable. The range of powers on  $\omega$  is always chosen as  $-2, -1, \dots, 2$  or  $-3, -2, \dots, 3$  to obtain reasonable accuracy. A genetic algorithm provides better results, although it consumes far more computer time. There are many parameters to control

and trade-offs to consider in using the genetic algorithm, such as population size, bit string length, etc. The transfer function of a particular scattering center is highly dependent on the physical properties of the surface at the specular point. When the signals are contaminated with noise the performance of the scheme is degraded, but the largest dominant scattering centers can be reproduced quite well with noise level as high as SNR = 10 dB, while the temporal positions of these scattering centers can still be extracted well with a noise level as high as SNR = -5 dB. We also show that varying the incident aspect angle by  $10^\circ$  for the B-58 leads to smooth and predictable changes in the reproduction of scattering centers.

## REFERENCES

- [1] M. P. Hurst and R. Mittra, "Scattering center analysis via Prony's method," *IEEE Trans. Antennas Propagat.*, vol. AP-35, pp. 986–988, Aug. 1987.
- [2] R. Carriere and R. L. Moses, "High resolution radar target modeling using a modified Prony estimator," *IEEE Trans. Antennas Propagat.*, vol. 40, pp. 13–18, Jan. 1992.
- [3] E. J. Rothwell, K. M. Chen, D. P. Nyquist, P. Ilavarasan, J. E. Ross, R. Bebermeyer, and Q. Li, "A general  $E$ -pulse scheme arising from the dual early-time/late-time behavior of radar scatterers," *IEEE Trans. Antennas Propagat.*, vol. 42, pp. 1336–1341, Sept. 1994.
- [4] R. A. Altes, "Sonar for generalized target description and its similarity to animal echolocation systems," *J. Acoust. Soc. Amer.*, vol. 59, pp. 97–105, Jan. 1976.
- [5] D. E. Goldberg, *Genetic Algorithms*. New York: Addison-Wesley, ch. 1–4, 1989.
- [6] J. E. Ross, "Application of transient electromagnetic fields to radar target discrimination," Ph.D. dissertation, Michigan State Univ., East Lansing, 1992.
- [7] R. H. Clarke and J. Brown, *Diffraction Theory and Antenna*. New York: Wiley, 1980.
- [8] Q. Li, "High frequency scattering and reduced scale computation of targets coated with a lossy dielectric," M.S. thesis, Univ. Electron. Sci. Technol. China, Chengdu, P. R. China, 1991.
- [9] P. Ilavarasan, J. E. Ross, E. J. Rothwell, K. M. Chen, and D. P. Nyquist, "Performance of an automated radar target discrimination scheme using  $E$ -pulses and  $S$ -pulses," *IEEE Trans. Antennas Propagat.*, vol. 41, no. 5, pp. 582–588, May 1993.



**Qing Li** was born September 16, 1965 in Chengdu, P. R. China. She received the B.S. and M.S. degrees in electrical engineering from the University of Electronic Science and Technology of China, Chengdu, in 1986 and 1991, respectively, and the Ph.D. degree in electrical engineering from Michigan State University, East Lansing, in 1995.

She is currently an Electrical Design Engineer at Component General, Inc., FL. Her research interests include electromagnetic scattering and radiation, component and antennas design, RCS measurement and calculation, and radar signal processing.



**Edward J. Rothwell** (S'84-M'85-SM'92) was born in Grand Rapids, MI, on September 8, 1957. He received the B.S. degree in electrical engineering from Michigan Technological University, Houghton, in 1979, the M.S. degree in electrical engineering and the degree of Electrical Engineer from Stanford University, Stanford, CA, in 1980 and 1982, respectively, and the Ph.D. degree in electrical engineering from Michigan State University, East Lansing.

He worked for Raytheon Co., Microwave and Power Tube Division, Waltham, MA, from 1979–1982, on low power traveling wave tubes, and for MIT Lincoln Laboratory, Lexington, MA, in 1985. He has been at Michigan State University, from 1985–1990, as an Assistant Professor of electrical engineering, and from 1990, as an Associate Professor.

Dr. Rothwell held the Dean's Distinguished Fellowship at Michigan State University, in 1985. He received the first John D. Withrow award for teaching excellence from the College of Engineering at Michigan State University in 1991. He is a member of Phi Kappa Phi, Sigma Xi, and Commission B of URSI.



**Kun-Mu Chen** (SM'64-F'76) was born in Taipei, Taiwan on February 3, 1933. He received the B.S. degree in electrical engineering from National Taiwan University, Taipei, in 1955, and the M.S. and Ph.D. degrees in applied physics from Harvard University, Cambridge, MA, in 1958 and 1960, respectively.

From 1960–1964 he was associated with the Radiation Laboratory, The University of Michigan, Ann Arbor, where he was engaged in the studies of electromagnetics and plasma. Since 1964, he has been with Michigan State University, East Lansing, first as an Associate Professor, and from 1967–1995, as a Professor of Electrical Engineering. In 1995, he became a Richard M. Hong Professor of Electrical Engineering. From 1968–1973, he was the Director of Electrical Engineering program of the Department of Electrical Engineering and Systems Science. He was a Visiting Professor with Chao-Tung University, Taiwan, in 1962, with National Taiwan University, Taiwan, in 1989, and with Tohoku University, Japan, in 1989. He has published many papers on electromagnetic radiation and scattering, radar target discrimination and detection, plasma, and bioelectromagnetics.

Dr. Chen is a Fellow AAAS. He received the Distinguished Faculty Award from Michigan State University, in 1976, the Withrow Distinguished Scholar Award from the College of Engineering, Michigan State University, in 1993, and the Outstanding Achievement Award from Taiwanese American Foundation, in 1984.



**Dennis P. Nyquist** (S'63-M'67-SM'92) was born in Detroit, MI, on August 18, 1939. He received the B.S.E.E. and M.S.E.E. degrees in 1961 and 1964, respectively, and the Ph.D. degree in electrical engineering from Michigan State University, East Lansing, MI, in 1966.

In 1966 he joined the Michigan State University faculty and in 1979, became a Professor. His current research interests include electromagnetic interactions in integrated electronics, electromagnetic characterization of materials, and transient

electromagnetics.

Dr. Nyquist maintains membership in Commission B of URSI, Sigma Xi, Tau Beta Pi, and Phi Kappa Phi. He was the recipient of the Michigan State University Teacher-Scholar Award in 1969.



### **Target discrimination using neural networks with time domain or spectrum magnitude response**

C. Y. Tsai, E. J. Rothwell, and K. M. Chen

Department of Electrical Engineering  
Michigan State University  
East Lansing, MI 48824, USA

**Abstract**—Several different memory-based neural networks are used to discriminate radar targets based on their early-time, aspect-dependent response. The beginning of the response is difficult to locate in practice, so we use only the magnitude of the time response's DFT Spectrum as input to the neural network, thus eliminating time-shift uncertainty. Especially promising is the Recurrent Correlation Accumulation Adaptive Memory-Generalized Inverse (RCAAM-GI) cascade neural network. From the simulation results, the network demonstrates a decision strategy which is flexible, parallel adaptive, computation space efficient, and highly noise tolerant. Performances of the networks presented in this paper are compared with those of existing networks.

#### **I. INTRODUCTION**

Many interesting schemes have been proposed for radar target discrimination [1-16]. Particularly fascinating are those which use the transient response of the target. These include methods based on the aspect-independent late-time response [1-9], time domain imaging techniques [10-12], correlation [13-15] and wavelet transforms [16]. Many of these schemes use only the early-time specular target response, or the late-time resonant portion. Of those techniques that use the entire waveform, problems arise in the amount of computer storage required and the time needed to process the measured response of an unknown target. Recently, neural networks have been used to perform target discrimination with reasonable storage requirements and rapid processing times [17,18]. Much of this effort was based on simple back-propagation networks. This paper will examine more sophisticated networks and demonstrate that target discrimination can be accomplished in a high-noise environment with great reliability.

The transient scattered field response of a radar target is aspect sensitive, but for an interrogating pulse of a given bandwidth, a discretization of aspect angle can be found for which changes are gradual from angle to angle. Therefore, we can store some specified aspect responses as the reference patterns for each target, design a neural network to memorize the association among reference patterns and expect the network will correctly converge to some reference pattern when it is triggered at the input by a pattern that is sufficiently close to one of the reference patterns.



In the Michigan State University anechoic chamber, a HP-8720B network analyzer is used to perform stepped frequency measurements of four scale aircraft models, B-52 (1:72), B58 (1:48), F14 (1:48) and TR1 (1:48). The targets are measured from  $0^\circ$  to  $28.8^\circ$  with an azimuthal aspect increment of  $0.9^\circ$ , resulting in 33 aspect measurements for each target. The frequency response spectra are calibrated using a 14" sphere as in [19] and taken into the time domain using the inverse fast Fourier Transform (IFFT). We then select 17 time-domain responses from  $0^\circ$  to  $28.8^\circ$  with aspect increment  $1.8^\circ$  for each target as training/stored patterns, and 16 responses as untrained/unstored network generality test patterns from  $0.9^\circ$  to  $27.9^\circ$  with the same increment. Therefore, every untrained/unstored test pattern resides at the middle of two training/stored patterns. Figure 1 shows all 68 patterns used for network training for four targets.

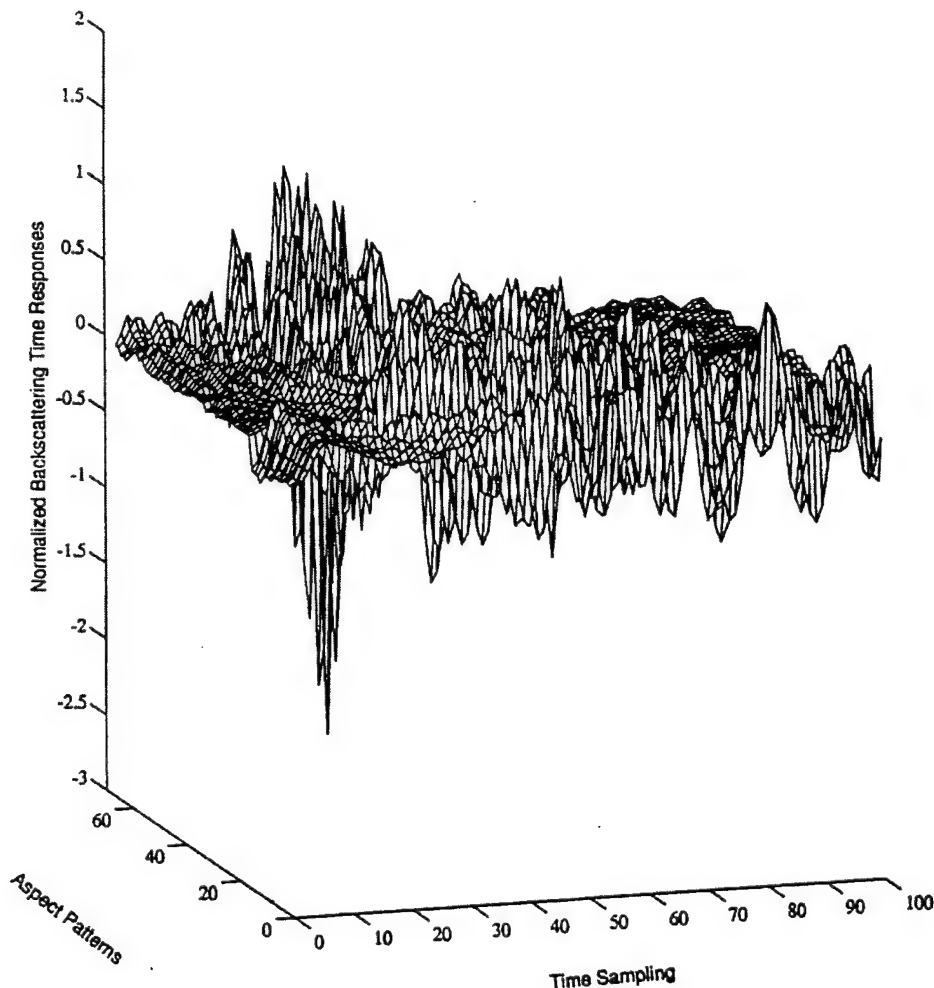


**Figure 1.** 68 aspect time response truncated patterns used for time process network trainings/storage. Time process networks simulate 4 targets, each target has 17 trained/stored aspect time response patterns. Pattern 1-17 are B52, 18-34 are B58, 35-51 are F14 and 52-68 are TR1.

We have used both time response patterns and Discrete Fourier Transform (DFT) spectrum magnitude patterns to simulate target discrimination for each neural network. In time response processing, the beginning response time has been assumed known, and we extract the next 100 response points as the aspect prototype from the assumed beginning point. Based on this assumed segment, noise is later added to test network noise tolerances. The difficulty of locating the beginning response point in practice prompts the use of DFT frequency spectrum magnitudes as aspect process patterns since a time shift is implicated in the phase of the spectrum.

In binomial input simulations, we quantize each time response using 7 numerical levels and encode these 7 levels using 3 bits, while we quantize each DFT spectrum by 5 levels and encode these 5 levels by using 3 bits. More levels are used for the time responses, since they exhibit a much wider oscillation range than the spectral magnitudes.

In section II through IV we present the theory for several different neural networks for target discrimination. In section II, the Generalized Inverse (GI) algorithm and its iterative network learning procedure are presented. In section III, we discuss Recurrent Correlation Associative Memories (RCAM), and analyze the High Order Recurrent Correlation Associative Memory (HCAM) and Exponential Correlation Associative Memory (ECAM). In section IV, we propose a new network structure, Recurrent Correlation Accumulation Adaptive Memory (RCAAM), which uses a dynamic memory structure to accumulate correlations and allows spurious states to either stay as unknown or converge to one of the stored patterns. We may call it a real-time adaptive learning network. The RCAAM performs discrimination equally well to the ECAM, always outperforms the HCAM, and requires much less processing space than the ECAM. In section V, we implement the backscattering time response process neural networks and DFT spectrum magnitude process neural networks, and then analyze the simulation results for different network architectures. A modified process is constructed for analog spectrum process networks. In section VI, we briefly summarize and compare neural networks used in this paper to some popular ones, and also compare the spectrum magnitude network performances with different quantization levels (one for 5 levels and the other for 7 levels). We discuss implementation complexities and conclude in the section VII.

## II. GENERALIZED INVERSE NETWORK

Assume we have  $p$  aspect patterns to be stored in memory,  $\mathbf{X} = \{\mathbf{X}^1, \mathbf{X}^2, \dots, \mathbf{X}^p\}$ , where  $\mathbf{X}^i$  is an  $m$ -dimension column vector, i.e.  $\mathbf{X}^i = [\mathbf{X}_1^i \ \mathbf{X}_2^i \ \dots \ \mathbf{X}_m^i]^T$ , and assume  $\mathbf{Y} = \{\mathbf{Y}^1, \mathbf{Y}^2, \dots, \mathbf{Y}^p\}$  are the associative code patterns corresponding to  $\mathbf{X}$ , where  $\mathbf{Y}^i$  is an  $n$ -dimension column vector, i.e.  $\mathbf{Y}^i = [\mathbf{Y}_1^i \ \mathbf{Y}_2^i \ \dots \ \mathbf{Y}_n^i]^T$ . Then we can write an equation representing the above associations as

$$\mathbf{W}\mathbf{X} = \mathbf{Y} \quad (1)$$

where  $\mathbf{W}$  is an  $n$  by  $m$  matrix. For our application,  $\mathbf{Y}^i$  is the target associated to the stored aspect pattern  $\mathbf{X}^i$ . Typically,  $\mathbf{X}$  is not a square matrix and  $m > p$

is assumed. Thus a direct Generalized Inverse matrix computation can be used to solve the interconnection weight matrix  $\mathbf{W}$  [22, 23, 30] as

$$\mathbf{W} = \mathbf{Y}(\mathbf{X}^T \mathbf{X})^{-1} \mathbf{X}^T = \mathbf{Y} \mathbf{X}^+ \quad (2)$$

where  $\mathbf{X}^+$  is the generalized (or pseudo) inverse of  $\mathbf{X}$ . The generalized inverse  $\mathbf{X}^+$  exists only if  $\mathbf{m} > \mathbf{P}$ , but the direct computation of the generalized inverse becomes difficult or impractical if the dimension of  $\mathbf{m}$  or  $\mathbf{P}$  is too large. In addition, problems may occur when two adjacent aspect angle target responses are close enough to have very close or the same quantized sequence codes, causing the generalized inverse computation to become instable or singular. Therefore, instead of direct computation of the generalized inverse, we can use iterative training based on the gradient descent algorithm to solve for the interconnection matrix  $\mathbf{W}$ . We iteratively train the network  $\mathbf{W}$  and expect the network output to each trained pattern  $\mathbf{X}^i$ ,  $\mathbf{W}\mathbf{X}^i$ , will retrieve its associative pattern  $\mathbf{Y}^i$ . First, we can construct a cost (error) function  $\mathbf{J}(\mathbf{W})$  as

$$J(\mathbf{W}) = \|\mathbf{Y} - \mathbf{W}\mathbf{X}\|^2 = \sum_{i=1}^P \sum_{j=1}^n [Y_j^i - (\mathbf{W}\mathbf{X}^i)_j]^2 \quad (3)$$

where  $\|\cdot\|$  denotes the Euclidian  $L_2$  norm. To minimize the error function  $\mathbf{J}(\mathbf{W})$ , the gradient descent learning rule [22, 23, 27, 30] can be used

$$\mathbf{W}[k+1] = \mathbf{W}[k] - \frac{1}{2} \eta \frac{\partial J(\mathbf{W}[k])}{\partial \mathbf{W}[k]} = \mathbf{W}[k] + \eta(\mathbf{Y} - \mathbf{W}[k]\mathbf{X})\mathbf{X}^T \quad (4)$$

where  $\mathbf{W}[\mathbf{k}]$  is network weight matrix at learning iteration  $\mathbf{k}$ , and  $\eta$  is the "learning rate" with  $0 < \eta < 1$ .

The above training algorithm is a batch mode learning by which each learning pattern adjusts the interconnection weights  $\mathbf{W}$  without considering the adjustments done by the other learning patterns at the same learning iteration. The learning algorithm can be modified to asynchronously update for each training pattern,  $\mathbf{X}^i$ , and its associative pattern components,  $\mathbf{Y}_j^i$ . Therefore, a current training pattern adjusts the  $\mathbf{W}$  updated by the previous learning pattern. The asynchronous update rule gives

$$\mathbf{W}_j[k+1] = \mathbf{W}_j[k] + \eta(\mathbf{Y}_j^{(i)} - \mathbf{W}_j[k]\mathbf{X}^{(i)})\mathbf{X}^{(i)T} \quad (5)$$

where  $\mathbf{W}_j[\mathbf{k}]$  denotes the  $j^{\text{th}}$  row of  $\mathbf{W}$  at update iteration  $\mathbf{k}$  and  $\mathbf{Y}_j^{(i)}$  is the  $j^{\text{th}}$  component of the desired pattern  $\mathbf{Y}^i$  associated with  $\mathbf{X}^i$ . To train each pattern and component fairly, and avoid being trapped in a local minimum, the training pattern  $i$  and output component  $j$  are randomly selected.

The binomial form can be introduced to the output stage to increase the noise tolerance, and therefore a nonlinear threshold function can be added to the network. Then we have

$$G_\beta(\mathbf{W}\mathbf{X}) = \mathbf{Y} \quad (6)$$

where

$$G_\beta(\nu) = \frac{2}{1 + \exp(-\beta\nu)} - 1 \quad (7)$$

and then

$$G(\nu)'_{\beta} = \frac{\beta}{2}(1 + G_{\beta}(\nu))(1 - G_{\beta}(\nu)) \quad (8)$$

The asynchronous update rule for pattern  $\mathbf{X}^i$  and its associative pattern component  $\mathbf{Y}_j^i$  is then

$$W_j[k+1] = W_j[k] + \eta G(\nu)'_{\beta} |_{W_j[k]X^{(i)}} (Y_j^{(i)} - W_j[k]X^{(i)})X^{(i)T} \quad (9)$$

The equations related to each row of  $\mathbf{W}$  indicate  $P$  associative equations and each has  $m$  variables. Therefore, for  $m > P$ , there are multiple exact solutions. If  $\mathbf{W}$  is randomly initialized, then  $\mathbf{W}$  may converge to some specific solution that has noise tolerance for some trained patterns, but low noise tolerance for others. To avoid the solutions being biased by some learning patterns and also to speed up trainings, we may initiate the weight matrix by  $\mathbf{W} = \mathbf{YX}^T$ . That is, we use the correlation recording matrix or Hopfield memory with nonzero diagonals. Therefore, the **GI** network is a multi-layer Feedforward and Error-Backpropagation network without a hidden layer, if the network  $\mathbf{W}$  is not initialized by the correlation recording matrix  $\mathbf{YX}^T$ . Thus the **GI** network can be considered as a hybrid network composed of an initial architecture of correlation associative memory and later learning-based backpropagation network. We may also say the **GI** network is a single layer net with initial weight matrix  $\mathbf{W} = \mathbf{YX}^T$ .

### III. RECURRENT CORRELATION ASSOCIATIVE MEMORIES

Assume we want  $p$  associative pattern pairs  $\{(\mathbf{x}^i, \mathbf{y}^i) \mid i = 1, 2, \dots, P\}$  stored in memory, where  $\mathbf{x}^i$  is an  $m$ -dimension column vector, and  $\mathbf{y}^i$  is an  $n$ -dimension column vector associated to  $\mathbf{x}^i$ , so that  $\mathbf{X} = \{\mathbf{x}^1, \mathbf{x}^2, \dots, \mathbf{x}^P\}$  and  $\mathbf{Y} = \{\mathbf{y}^1, \mathbf{y}^2, \dots, \mathbf{y}^P\}$ . The recurrent correlation associative memories (RCAM)[20-29] are designed to recall the associative pattern  $\mathbf{y}^i$  using recurrent correlation operations, for a given input  $u$  which is sufficiently close to  $\mathbf{x}^i$ . This type of neural network has application in pattern discrimination. If  $\mathbf{y}^i = \mathbf{x}^i, i = 1, \dots, P$ , then the RCAM is called an autoassociative memory. In this section, we discuss this type of RCAM. Since the correlation of two normalized or bipolar signals is one measure of how close two signals are, RCAM can discriminate patterns based on this property.

If  $\mathbf{x}^i$  has binomial (binary or bipolar) components and  $s$  is an input or the current state with dimension  $m$ , then an RCAM has the evolutionary behavior [24,25]

$$s' = G\left\{\left(\sum_{i=1}^P f_i(x^{(i)T} s)x^{(i)}\right)\right\} \quad (10)$$

where  $s'$  is the next network state,  $f_i$  is a weighting function and  $G$  is a threshold (or activation) function. In bipolar processing, the Signum (**Sign**) function,

$$\text{Sign}(\nu) = \begin{cases} 1 & , \nu > 0 \\ -1 & , \nu < 0 \end{cases} \quad (11)$$

is used for the threshold function  $G$ . We see that the Hopfield network is a special case of the RCAM with weighting function  $f(c)=c$  and degenerated diagonals. The

network first computes the correlations between the given state  $s$  and each stored pattern, then processes each correlation by weighting function  $f$  to obtain the weighted correlation gain, and then multiplies each stored pattern by its weighted correlation gain. Finally, the network adds every amplified pattern together, and then manipulates the sum by the **Sign** threshold function to achieve the network output (next state). Since the correlation between two binomial vectors can be regarded as one similarity measurement, we could classify a given input to its stored prototype by appropriately using correlation gains. Generally, the larger a correlation value two vectors have, the closer they are. So the weighting function should be strictly increasing to assure the viability of the correlation-based retrieve algorithm.

In the Hopfield net [20, 21, 25] with nonzero diagonals,

$$s' = \text{Sign} \left\{ \sum_{i=1}^P (x^{(i)T} s) x^{(i)} \right\} \quad (12)$$

The network only considers a 1-dimension relationship between the given state and the stored vector  $\mathbf{x}^i$ . Since the next state is generated by the sum of each amplified pattern, a pattern with a slightly larger correlation gain may be distorted by the sum of the others. Therefore, it wouldn't dominate the next state after the addition of all amplified patterns. If we compare the relationship between  $\mathbf{x}_j^i \mathbf{x}_k^i$  and  $s_j s_k$ , where  $j = 1, \dots, m$ , and  $k = 1, \dots, m$ , then we can use more information to emphasize the correlation between these two vectors  $\mathbf{x}^i$  and  $s$  before adding them to provide the next state. The one-dimension model (Hopfield net) compares two vector strings bit by bit to compute the number of identical bits, while the two-dimension model constructs the individual auto correlation planes for each stored pattern and the given input, i.e.  $\mathbf{x}^i (\mathbf{x}^i)^T$  and  $s(s)^T$ , and then compares the input autocorrelation 2-d plane to each stored pattern 2-d plane to find the closest autocorrelation plane structure among all stored patterns. So it's clear that the 2-d model uses  $m$  times the information of the 1-d model to discriminate patterns.

The use of a high dimensional autocorrelation hyperplane is called the High Order Correlation Associative Memory (HCAM). An HCAM [24,25] has the weighting function

$$f(c) = (c + T_{os})^r \quad (13)$$

where  $r > 1$ .  $T_{os}$  is some offset value designed to avoid amplifying negative correlation gains for even  $r$ . If  $(c + T_{os})$  is positive or  $r$  is a positive odd integer, the weighting function  $f$  is strictly increasing, as required for correct retrieves.

Another RCAM used for our target discrimination simulations is the Exponential Correlation Associative Memory (ECAM) [24,25] which has the weighting function

$$f(c) = b^c \quad (14)$$

where  $b > 1$ . Again, this weighting function  $f$  is strictly increasing. RCAM's with a continuous and strictly increasing weighting function  $f$  are asymptotically stable in both synchronous and asynchronous update [25]. This means that

network recurrent operations will drive a given input state to some stable state, therefore ensuring that there is no oscillation cycle during the recurrent convergent iterations. Thus the RCAM will converge to either one of the stored patterns or some spurious (unknown) state when triggered at the input by a given pattern.

The HCAM requires a predetermined fixed order  $r$  to proceed. A network with low order  $r$  can't retrieve correct associative patterns, while a high order  $r$  wastes computation space. When the ECAM exponentially amplifies the correlation gains, producing excellent discrimination resolution, it also exponentially expands the network computation space. It is not possible to physically realize an ECAM processing large dimension patterns. For example, in our simulations each bipolar stored pattern has 300 bits, so the maximum weighted correlation gain is  $2^{300}$  for the ECAM with the weighting function  $f(c) = 2^c$ , i.e.  $b = 2$ . Therefore, a huge processing space is required to fulfill the hardware realization in chip design scale.

#### IV. RECURRENT CORRELATION ACCUMULATION ADAPTIVE MEMORY

When the recurrent update of RCAM amplifies individual correlations between the initial given input and stored patterns, it also introduces noisy crosscorrelation terms between any two stored patterns  $i$  and  $j$  with  $i \neq j$ . For example, given an initial input  $s$ , the HCAM of order  $r$  has output state  $s''$  after two synchronous updates

$$s'' = \text{Sign} \left\{ \sum_{j=1}^P [x^{(j)T} \text{Sign} \left( \sum_{i=1}^P (x^{(i)T} s)^r x^{(i)} \right)]^r x^{(j)} \right\} \quad (15)$$

Therefore it did not purely amplify the correlations between the initial given input and stored patterns, and the nonlinear threshold function **Sign** prohibits the recurrent iterations from linearly accumulating the respective pattern correlation gains,  $[(x^{(i)T} s)^r]$ , produced by the last iteration. The recurrent feedbacks introduce noisy crosscorrelation terms. If the network can release the nonlinear interferences caused by the threshold function **Sign** and accumulate the previous respective correlation gains for each stored pattern, then the network will function efficiently and stably. No nonlinear interference means there will be linear amplifications on respective (cross) correlation terms generated during the last iteration, and the accumulations of previous recurrent iterations will speed up the order of correlations.

For HCAM, we need to guess for what order the network can discriminate well among all possible inputs before processing the input. Some inputs may be easily discriminated, while some may be more difficult. If a network can use flexible and sufficient orders of correlation to reach the same performance, then it will be a better choice. Thus we wish to use a dynamic order, dependent on the input, to discriminate among the stored patterns.

We propose an Recurrent Correlation Accumulation Adaptive Memory (RCAAM) which uses dynamic memory structure to accumulate the correlation information between the input( $s$ ) and all stored patterns. Then the network dis-

crimination resolution (ability) to an input will increase as the recurrent iterations increase. Compared to the ECAM and HCAM, the RCAAM uses recurrent accumulative and dynamic structures to gradually converge a given input to some (semi-)stable state(s). We may regard this network as a real time learning network. The network adjusts its real-time learning structure to converge the given input to the nearest stable state associated to the stored patterns as long as the recurrent operations continue. And, unlike Multi-layer Feedforward Error-Backpropagation learning it can avoid being trapped in local minimum states. Suppose the stored associative pattern pairs are  $\{(\xi^i, \zeta^i) | i = 1, \dots, P\}$ , where  $\xi^i$  is a column vector with length  $m$  and  $\zeta^i$  is a column vector with length  $n$ . We intend to implement a neural network that can recall  $\xi^i$  if given an input sufficiently close to  $\zeta^i$ . If  $U$  is an  $n$ -dimensional column vector input and **init** is a positive initial order, then we can construct the initial RCAAM,  $M_o$ , as follows:

$$M_o = \sum_{i=1}^P \xi^{(i)} [(\zeta^{(i)T} U)^{\text{init}} \zeta^{(i)}]^T = \sum_{i=1}^P \xi^{(i)} (w_o^{(i)} \zeta^{(i)})^T \quad (16)$$

where  $w_o^{(i)}$  is the dynamic weighting for the  $i^{\text{th}}$  stored pattern at time 0. If **init** = 0, then  $M_o$  will degrade to the Hopfield memory with nonzero diagonal. Suppose the stored patterns  $\xi^i$  have bipolar form, then, with this initial memory matrix, the network output is given by

$$V_o = \text{Sign} \{M_o U\} = \text{Sign} \left\{ \sum_{i=1}^P [w_o^{(i)} \zeta^{(i)}]^T U \xi^{(i)} \right\} \quad (17)$$

We have three versions of the RCAAM based on the recurrent updatings. The first version is RCAAM with fixed input (RCAAM/fi). Version 2 is RCAAM with dynamic input connected to output (RCAAM/di). Version 3 is RCAAM with analog input/digital output (RCAAM/ad). Therefore, RCAAM/fi and RCAAM/di have binomial  $\zeta^i$  and  $\xi^i$ , while RCAAM/ad has analog  $\zeta^i$  but binomial  $\xi^i$ . Suppose  $U_k$  denotes the network input at time  $k$  and  $V_k$  denotes the network output at time  $k$  corresponding to the input  $U_k$ . Then, the dynamic memory has  $U_k = U$  for RCAAM/fi and RCAAM/ad, and has  $U_k = V_{k-1}$  for RCAAM/di. The dynamic memory and the network output at time 1 are given by

$$M_1 = \sum_{i=1}^P \xi^{(i)} \{[(w_o^{(i)} \zeta^{(i)})^T U] \zeta^{(i)T}\} = \sum_{i=1}^P \xi^{(i)} (w_1^{(i)} \zeta^{(i)})^T \quad (18)$$

$$V_1 = \text{Sign} \{M_1 U_1\} = \text{Sign} \left\{ \sum_{i=1}^P [w_1^{(i)} \zeta^{(i)}]^T U_1 \xi^{(i)} \right\}$$

where the dynamic weighting for stored pattern  $\zeta^i$  at time 1 has  $w_1^{(i)} = (w_o^{(i)} \zeta^i)^T U$ . Then the dynamic memory and network output at time  $k$  are given



by

$$M_k = \sum_{i=1}^P \xi^{(i)} \{ [(w_{k-1}^{(i)} \zeta^{(i)})^T U_{k-1}] \zeta^{(i)T} \} = \sum_{i=1}^P \xi^{(i)} (w_k^{(i)} \zeta^{(i)})^T \quad (19)$$

$$V_k = \text{Sign} \{ M_k U_k \} = \text{Sign} \left\{ \sum_{i=1}^P [w_k^{(i)} \zeta^{(i)}]^T U_k \xi^{(i)} \right\}$$

where  $U_k = U$  for RCAAM/fi and RCAAM/ad,  $U_k = V_{k-1}$  for RCAAM/di, and  $w_k^{(i)} = (w_{k-1}^{(i)} \zeta^{(i)})^T U_{k-1}$  is the weighting matrix for the stored pattern  $\zeta^{(i)}$  at time  $k$ . The algorithm shows the RCAAM has stored patterns weighted by  $w_k^{(i)}$  at time  $k$ , and each pattern weighting indicates the correlation accumulation through iterations between the network recurrent input states and the stored pattern itself. Therefore, the weightings of those stored patterns that are closer to the given input will become larger than the others, as long as the recurrent iterations increase. It is equivalent to say that by real-time adjustment of the individual pattern weightings of the dynamic memory, the recurrent outputs will gradually adapt to the closest stored pattern. Since the pattern weighting adjustments are parallel in each stored pattern vector direction at each iteration, there is no local minimum trap phenomenon in RCAAM. With its dynamical matrix structure, the dynamic accumulation will eliminate the oscillation phenomenon which occurs in recurrent Hopfield nets. Although it may have semi-stable states at which the network stays for a finite number of iterations, its dynamic accumulative memory will quickly function to leave those states. Therefore, the network updatings won't be trapped in an oscillation cycle.

For RCAAM/fi and RCAAM/ad, the pattern weighting iteration  $w_k^{(i)} = (w_{k-1}^{(i)} \zeta^{(i)})^T U$  doesn't introduce nonlinear threshold function **Sign**, and thus crosscorrelation interference terms are no more a problem to the networks. Therefore, the correlation accumulation becomes linear. This useful processing structure is possible for RCAAM/fi and RCAAM/ad, but not for the RCAM's. And this advantage still benefits from the dynamically accumulative memory structure. Compared to [29] which trains the associative memory off-line by Linear Programming or Sequential Multiple Training to guarantee the recall of stored patterns, the RCAAM learns on-line and adjusts the stored pattern weightings to converge the given input to the closest stored pattern. The RCAAM doesn't have predetermined order or a fixed memory matrix, so the network is quite flexible and applicable to any kind of distorted stored inputs. The network only takes a few recurrent iterations to recognize a slightly distorted stored pattern, and requires more recurrent iterations to discriminate a more ambiguous input.

## V. IMPLEMENTATIONS AND SIMULATIONS

### A. Using Backscattering Time Responses as Network Process Patterns

In this subsection, we use the sampled backscattering time responses of various aircraft models as the network processing information. For each target we select



17 aspect responses as the training/stored patterns from  $0^\circ$  to  $28.8^\circ$  with aspect angle spacing  $1.8^\circ$ , giving a total of 68 training/stored patterns. We pick the first 100 sample points as the aspect pattern, starting from the assumed target beginning time. Often the backscattering time responses are dominated by a few large specular reflections at a few specific aspect angles. If we normalize the responses to the largest value over all aspect angles, the small aspect responses will approach zero. Therefore the discrimination will concentrate on a few extremely large peaks and ignore the rest of the responses. This very biased concentration on a few extremely large peaks and ignore the rest of the responses. This very biased concentration will reduce the resolution and make the aspect differentiations of a target more inconsistent. Thus a normalization as described later for spectral signals is inappropriate. This will be especially true when a time shift is taken into consideration. Since we use the prior measured data patterns as the network stored patterns, we have prior knowledge to set a threshold for the targets which the network is designed to recognize. To balance those aspect responses that have large localized peaks, we set a maximum threshold value equal to the sum of all response amplitudes multiplied by 0.06, and then smooth the peak if a response peak amplitude is larger than the threshold value. Then, we allow an extra one fifth of the threshold value to smooth the excessive part, and normalize each balanced aspect pattern to unity energy.

For binomial (binary or bipolar) processing, we quantize each time response sample by using 7 numerical levels and then use 3 bits to encode these 7 numerical intervals. Therefore, each binomial aspect pattern has 300 bits as a processing pattern. To test the network noise tolerances, we add Gaussian noise to the same training/stored processing segment, then normalize the noisy response and encode it to a 300-bit processing pattern. The Gaussian noise used in the simulations was generated using the Matlab software package with zero mean and variances corresponding to simulation SNR's. To test network generality performance, we use 16 unstored (or untrained) patterns, whose aspect angles reside halfway between the two stored patterns, as test patterns for each target.

The code for 7 levels coded with 3 bits is not exactly a linear code so that two close levels don't really result in two similar codes. But if we assign the code-to-level mapping as shown in the table below, the codes have a linear characteristic for the adjacent levels. This means that if the noise contamination range is smaller than  $\pm 1.5$  level intervals, then the code linearity still functions statistically. Therefore the network discrimination won't be affected by the coding scheme. If the noise contamination is severe, then the linearity may not work for every response level. Under heavy noise conditions, some wrong or unrecognized discriminations may probably result from this nonlinear coding scheme.

For example, if the true response is in level 3 (represented by 1 -1 1), and contamination is in  $\pm 1.5$  level intervals, then the contaminated signal will be in either level 2 (represented by -1 -1 1) or level 4 (represented by 1 -1 -1), and these two codes (-1 -1 1 and 1 -1 -1) still are the most similar codes to the true one (1 -1 1). If the number of quantization levels is fixed, then the resolution will be the same quantization. The more digits we use, the more linearity the code mapping

has, but also the more process space is required. Therefore it becomes a trade-off problem, either save process space with less code bits, then process quickly but badly under heavy noises or expend more memory with more code bits, then process slowly but well under severe contamination. This problem can be solved by processing the analog (numerical) valued responses instead of binomial codes for digital computer simulation. But the problem will still remain the same for hardware realization.

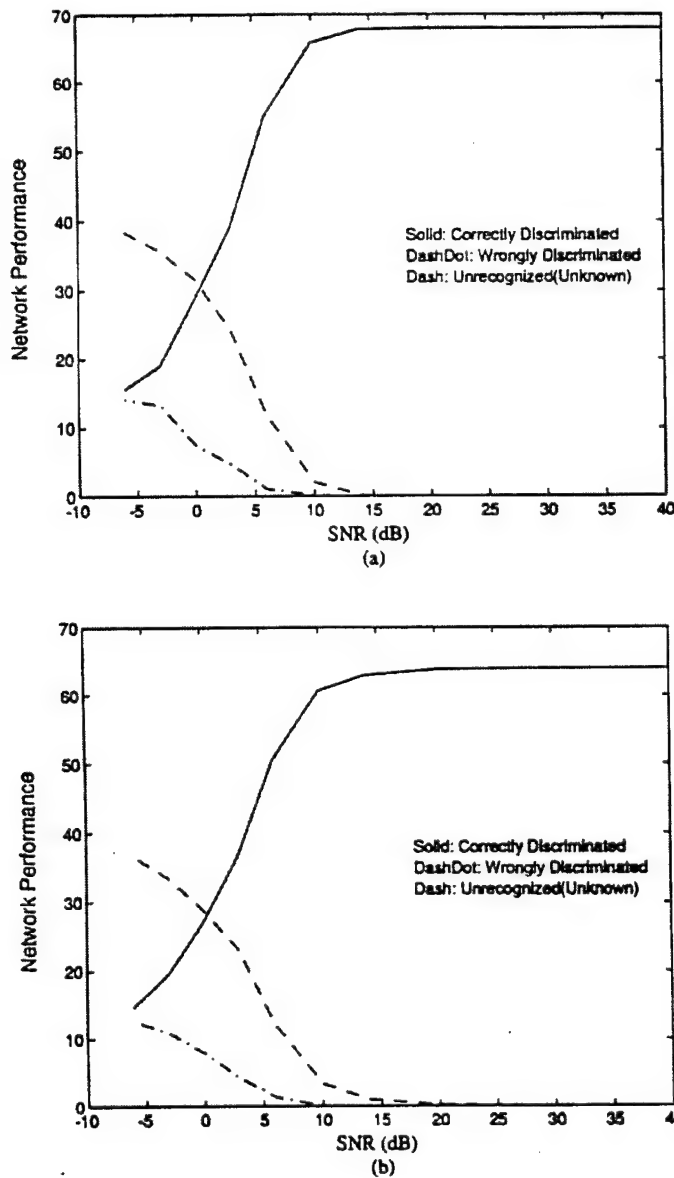
Bit1Bit2	-1 -1	-1 1	1 1	1 -1
Bit3				
-1	1	6	5	4
1	2	7		3

**Table 1.** Code assignment of 7 quantization levels coded by three bipolar bits.

In the **GI** network simulation with bipolar processing, we initiate the weight matrix **W** with  $\mathbf{YX}^T$  divided by a sufficiently large scale factor to ensure that **W** won't lead to rough network outputs,  $\mathbf{WX}^i$ , deeply into the saturation region of the threshold function. For example, we use  $\beta = 2$  for the nonlinear threshold function  $G_\beta$  where  $G_2(1.5) = 0.9526$  and  $G_2(v)'|_{v=1.5} = 0.0926$ . Therefore the learning (or adjusting) becomes nearly zero for a rough output (i.e. input to  $G_2(v)$ ) larger than 1.5. After the trainings converge to zero error, we continue training the network to let those marginally convergent patterns move deeply into the saturation region of the threshold (activation) function. Therefore, the network noise tolerance will be increased.

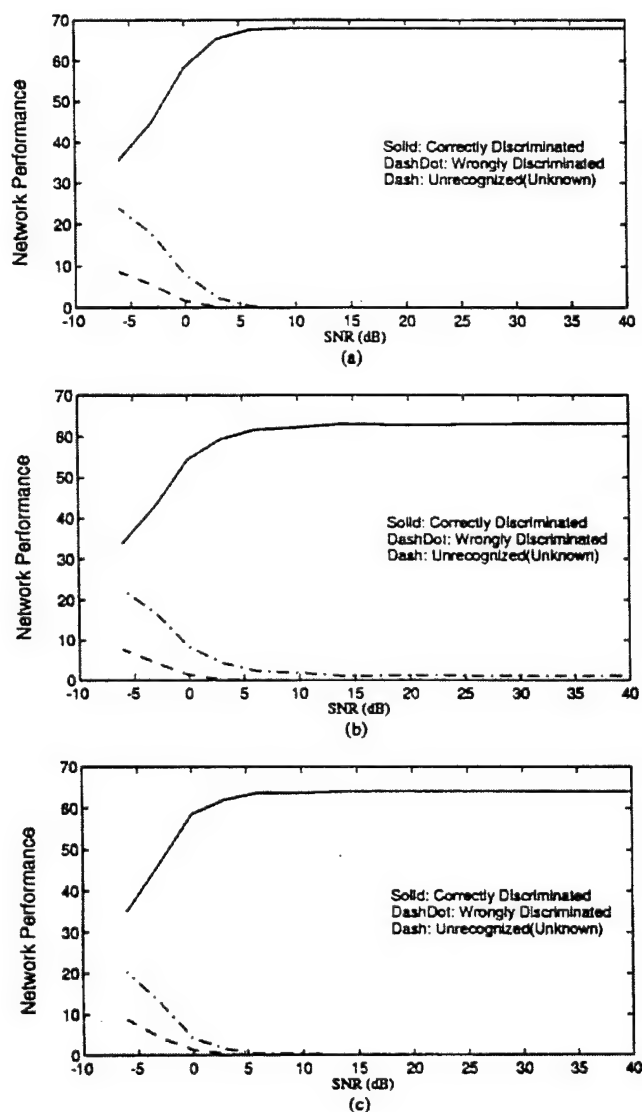
Figure 2(a) shows the Generalized Inverse (GI) network performances for 68 trained aspect patterns from the four target models described in section I, while figure 2(b) presents the GI network generality performances using 64 untrained patterns. Note that the GI network prefers to characterize an ambiguous pattern as unknown rather than wrong. This indicates that the GI network records many of spurious states (patterns) which will be retrieved as none or multiple stored patterns. The noise tolerance is not very high compared to the correlation-based associative memories described later, since the GI network usually regards a distorted pattern as a linear combination of multiple stored patterns. This ambiguous resolution can be improved by recurrent correlation processing, so recurrent correlation-based memories have a greater discrimination resolution for a contaminated pattern.

Since the GI network prefers to leave heavily distorted states unknown rather than wrongly discriminated, we use it as a decoder cascaded to the correlation-based associative memories. The RCAM or RCAAM network first converges a given input to a stable state, then passes this stable state to the GI network to associate the final target code to the given aspect pattern input. Therefore, the stored bipolar patterns  $\xi^i$  of the RCAM and RCAAM are the same as the trained input patterns of the GI network.



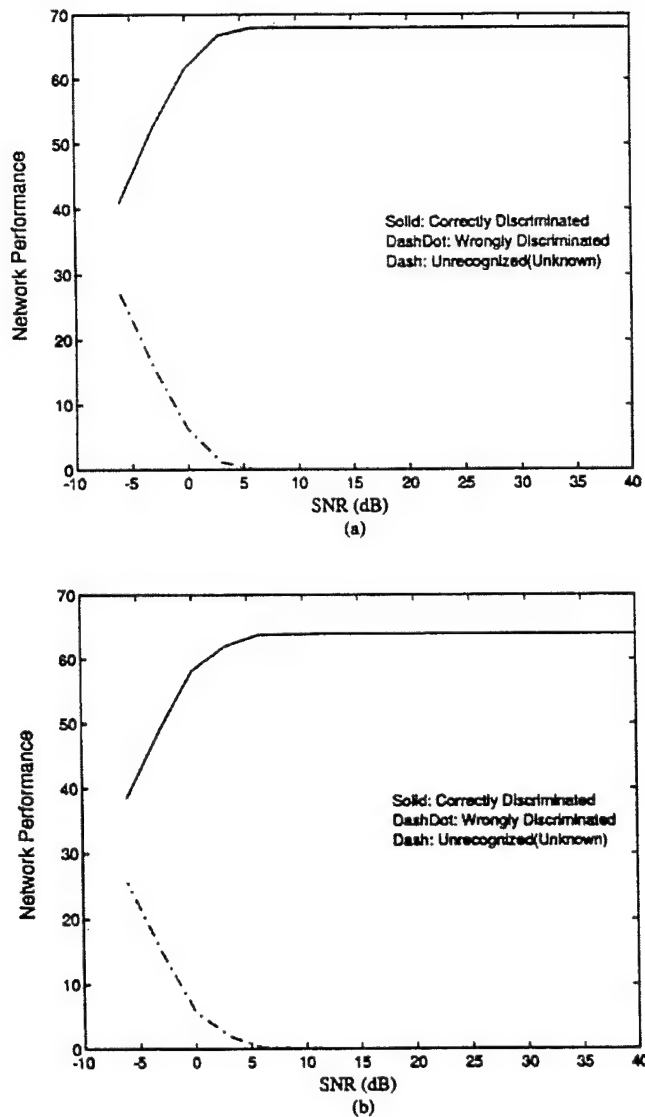
**Figure 2.** Generalized Inverse (GI) network performances vs. SNR for time domain inputs. (a) GI network performance for the 68 trained patterns, (b) GI network generality performance for 64 untrained patterns.

Figure 3(a) shows the HCAM (order 3)-GI cascade network performances for the 68 stored aspect patterns, and Figure 3(b) presents the network generality performances by testing 64 unstored aspect patterns. Figure 3(c) shows that for SNR greater than 10 db, the HCAM (order 5)-GI cascade network correctly discriminates all unstored testing patterns, while the HCAM (order 3)-GI cascade network still wrongly discriminates one unstored testing pattern. This shows that the predetermined order will affect the HCAM performances.



**Figure 3.** HCAM - GI cascade network performances vs. SNR for time domain inputs. (a) HCAM (order 3)-GI cascade network performance for the 68 stored patterns, (b) HCAM (order 3)-GI cascade network generality performance for the 64 untrained patterns. (c) HCAM (order 5)-GI network generality performance for 64 unstored patterns.

This simulation implicitly proves two typical deficiencies of the RCAM's analyzed in section III. First, the recurrent nonlinear threshold feedback has interfered with correlation gain amplifications between the given input and stored patterns by nonlinearly introducing crosscorrelation terms. Second, the network doesn't effectively accumulate the correlation gains generated by previous recurrent processes. This deficiency becomes apparent when the HCAM uses an insufficient order. Figure 4(a) shows the ECAM - GI cascade network performances for the 68 stored aspect patterns, and Figure 4(b) presents the network generality performances by testing 64 unstored aspect patterns.



**Figure 4.** ECAM-GI cascade network performances vs. SNR for time domain inputs. (a) ECAM-GI cascade network performance for the 68 stored patterns, (b) ECAM-GI network generality performance for 64 unstored patterns.

The ECAM - GI cascade network shows the best performance among the three networks considered. This is expected, since the ECAM has exponentially expanded the distance between any two stored patterns. Because of the asymptotically stable characteristic of RCAM with continuous and strictly increasing weighting function, the HCAM and ECAM will converge to an unique stable state if the network is activated. Therefore, as soon as  $\mathbf{V}_k = \mathbf{V}_{k-1}$ ,  $\mathbf{V}_k$  is the final state and won't change even recurrent updates continue.

For easy implementation, the RCAAM can be further realized, then the initial memory  $\mathbf{M}_0$  is

$$\begin{aligned} M_0 &= \sum_{i=1}^P \xi^{(i)} [(\zeta^{(i)T} U)^{init} \zeta^{(i)}]^T \\ &= \sum_{i=1}^P \xi^{(i)} (w_o^{(i)} \zeta^{(i)})^T \\ &= \xi \cdot \{Diag[\zeta^T \cdot U] \cdot \zeta^T\} \\ &= \xi \cdot [Diag(W_o)] \cdot \zeta^T \end{aligned} \quad (20)$$

where

$$\begin{aligned} \zeta &= [\zeta^{(1)} \zeta^{(2)} \dots \zeta^{(P)}] \\ \xi &= [\xi^{(1)} \xi^{(2)} \dots \xi^{(P)}] \\ W_o &\equiv [w_o^1 w_o^2 \dots w_o^P] \\ A.^q &\equiv [A_1^q A_2^q \dots A_P^q]^T \end{aligned}$$

and

$$Diag(A) \equiv \begin{bmatrix} A_1 & 0 & \dots & 0 \\ 0 & A_2 & 0 & \dots \\ \vdots & \vdots & \ddots & \vdots \\ 0 & \dots & 0 & A_P \end{bmatrix}$$

if  $\mathbf{A} = [\mathbf{A}_1 \mathbf{A}_2 \dots \mathbf{A}_P]$ . Then the network output is

$$\begin{aligned} V_o &= Sign \{M_o U\} = Sign \left\{ \sum_{i=1}^P [w_o^{(i)} \zeta^{(i)T} U] \xi^{(i)} \right\} \\ &= \xi \cdot \{[Diag(W_o)] \cdot (\zeta^T U)\} \end{aligned} \quad (21)$$

Then the dynamic memory at recurrent time  $k$  is

$$\begin{aligned} M_k &= \sum_{i=1}^P \xi^{(i)} \{[(w_{k-1}^{(i)} \zeta^{(i)T} U_{k-1}) \zeta^{(i)T}]^T\} \\ &= \xi \cdot [Diag(W_{k-1}) \cdot Diag(\zeta^T U_{k-1})] \cdot \zeta^T \\ &= \sum_{i=1}^P \xi^{(i)} (w_k^{(i)} \zeta^{(i)})^T \\ &= \xi \cdot [Diag(W_k)] \cdot \zeta^T \end{aligned} \quad (22)$$

where

$$\mathbf{W}_k \equiv [\mathbf{w}_k^1 \mathbf{w}_k^2 \dots \mathbf{w}_k^P]$$

and

$$\mathbf{w}^{(i)} = \mathbf{w}_{k-1}^{(i)} (\zeta^{(i)T} \mathbf{U}_{k-1}),$$

and the output is

$$\begin{aligned} V_k &= \text{Sign} \{M_k U_k\} = \text{Sign} \left\{ \sum_{i=1}^P [w_k^{(i)} \zeta^{(i)T} U_k] \xi^{(i)} \right\} \\ &= \xi \cdot \{[\text{Diag}(W_k) \zeta^T] \cdot U_k\} \\ &= \xi \cdot \{[\text{Diag}(W_k)] \cdot (\zeta^T U_k)\} \end{aligned} \quad (23)$$

Again, RCAAM/fi and RCAAM/ad have  $\mathbf{U}_k = \mathbf{U}$ , while RCAAM/di has  $\mathbf{U}_k = \mathbf{V}_{k-1}$ . Therefore the dynamic memories  $\mathbf{M}_k$  and the evolution outputs  $\mathbf{V}_k$  for RCAAM/fi and RCAAM/ad can be further simplified as

$$\begin{aligned} M_k &= \sum_{i=1}^P \xi^{(i)} \{[(w_{k-1}^{(i)} \zeta^{(i)T} U) \zeta^{(i)T}] \} \\ &= \xi \cdot [\text{Diag}(W_{k-1}) \cdot \text{Diag}(\zeta^T U)] \cdot \zeta^T \\ &= \xi \cdot \{[\text{Diag}[(\zeta^T U) \cdot \wedge (init + k)]]\} \cdot \zeta^T \\ V_k &= \text{Sign} \{M_k U\} = \text{Sign} \left\{ \sum_{i=1}^P [(w_k^{(i)} \zeta^{(i)T} U) \xi^{(i)}] \right\} \\ &= \xi \cdot [\text{Diag}(W_k) \cdot (\zeta^T \cdot U)] \\ &= \xi \cdot [(\zeta^T U) \cdot \wedge (init + k + 1)] \end{aligned} \quad (24)$$

For heteroassociative memory ( $\zeta^i$  is not equal to  $\xi^i$ ), we have 68 stored aspect response patterns belonging to four different targets, so  $\zeta$  has 68 columns. Suppose the B52 is encoded by  $[1 \ -1 \ -1 \ -1]$ , the B58 by  $[-1 \ 1 \ -1 \ -1]$ , the F14 by  $[-1 \ -1 \ 1 \ -1]$  and the TRI by  $[-1 \ -1 \ -1 \ 1]$ , then  $\xi^1 \sim \xi^{17} = [1 \ -1 \ -1 \ -1]^T$ ,  $\xi^{18} \sim \xi^{34} = [-1 \ 1 \ -1 \ -1]^T$ ,  $\xi^{35} \sim \xi^{51} = [-1 \ -1 \ 1 \ -1]^T$  and  $\xi^{52} \sim \xi^{68} = [-1 \ -1 \ -1 \ 1]^T$ . From the above realization algorithms, the network only requires storing memories for  $P = 68$  dynamically weighted stored patterns, 4 target group codes, one current input pattern and one output. Since RCAAM has a dynamic memory structure, there may be semi-stable states at which the network stays until the correlation accumulation is high enough to escape the temporary spurious state and move toward other states. We define the stable criterion *sc* by  $\mathbf{V}_k = \mathbf{V}_{k-1} = \dots = \mathbf{V}_{k-\text{sc}}$ . Therefore, we regard the state  $\mathbf{V}_k$ , which satisfies  $\mathbf{V}_k = \mathbf{V}_{k-1} = \dots = \mathbf{V}_{k-\text{sc}}$ , as the network discrimination pattern, if the stable criterion *sc* is adopted. This indicates the RCAAM has a flexible decision strategy for an ambiguous input, allowing us to either leave it unknown or force it to one of the stored patterns. To leave those spurious states as unknown the stable criterion can be set to a low value (eg., 1 or 2). The stable criterion can be set to a high value (eg., larger than 2) if a definite discrimination is required.

This allows convergence to one of the stored patterns. The RCAAM needs only the minimum computation scale space which the RCAM can possibly offer to discriminate an arbitrarily given input. Thus the RCAAM not only needs less processing space than the RCAM, but will perform the same or better.

Figure 5(a) shows the RCAAM/fi-GI cascade network performance with stable criterion  $sc = 2$  for the 68 stored patterns, while Figure 5(b) presents the network generality performance by testing 64 unstored aspect patterns. Both performances are similar to the ECAM-GI cascade network performances, except for the unknown and wrong discriminations. Using the above analysis, the unknowns can be eliminated by setting the stable criterion high, forcing them to be interpreted as a correct or incorrect decision.

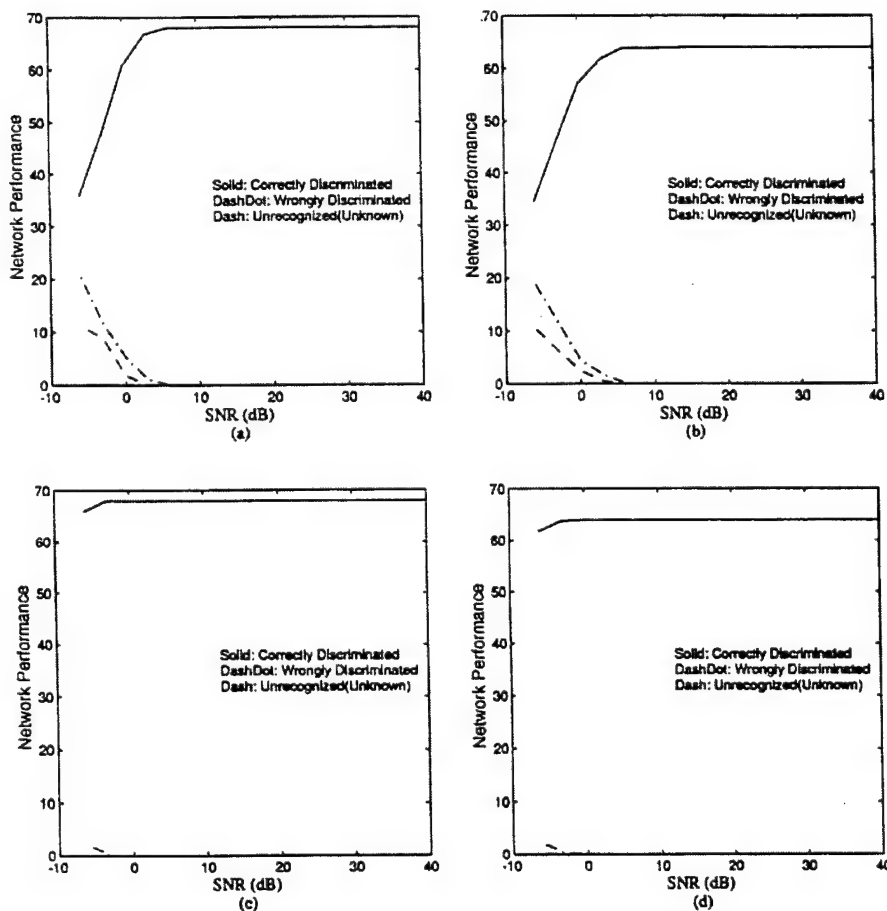


**Figure 5.** RCAAM - GI cascade network performances vs. SNR for time domain inputs. (a) RCAAM/fi-GI cascade network performance for the 68 stored patterns, (b) RCAAM/fi-GI network generality performance for 64 unstored patterns, (c) RCAAM/ad-GI cascade network performance for the 68 stored patterns, (d) RCAAM/ad-GI network generality performance for 64 unstored patterns.



Since the discrete quantization to analog response may lose the resolution required for ambiguous pattern discrimination, an analog process model is tried. We simulate the analog processing network using RCAAM/ad. The RCAAM/ad has an analog input dimension of 100 and a bipolar output dimension of 300, while the immediately following GI network has a bipolar input dimension of 300 and a bipolar output dimension of 4. Thus the RCAAM/ad is a heteroassociative analog-digital hybrid memory. Figure 5(c) shows the RCAAM/ad-GI cascade network performance with a stable criterion  $sc = 2$  for the 68 stored patterns, and Figure 5(d) presents the network generality performance by testing 64 unstored patterns. Both performances demonstrate excellent noise tolerances for SNR as low as -3dB.

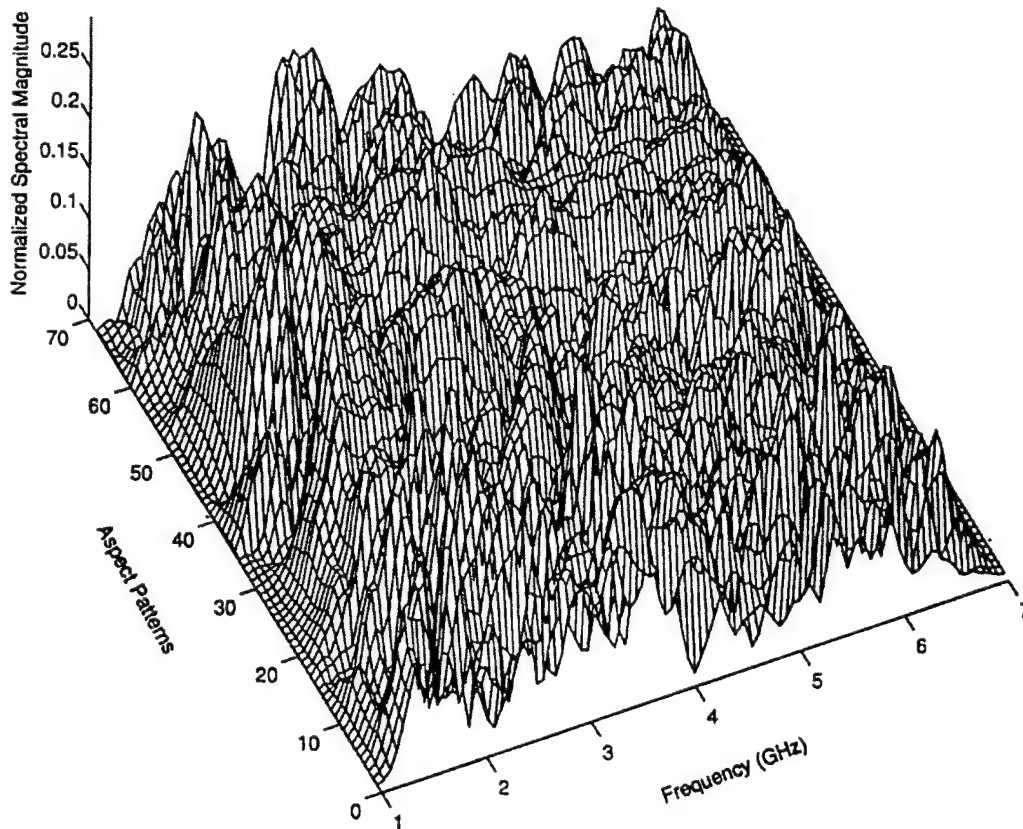
### B. Using FFT Spectrum Magnitude as Network Process Patterns

In the previous subsection, we used the sampled backscatter time response as the network process information. In a practical noise-limited situation, finding the same beginning response time used in training is very difficult. Therefore the network must also store or train several time-shift neighborhoods of the time segment pattern for each aspect angle, to increase tolerance for time-shifted patterns. This is impractical, since it dramatically reduces the network capacity. In this subsection we use the spectral magnitude, which is time-shift invariant, as the network process information. Unfortunately, we use less information here than the time domain process since the phase is ignored. Also, the sharp specular peaks characteristic of a typical backscatter time response doesn't occur in the corresponding frequency spectrum.

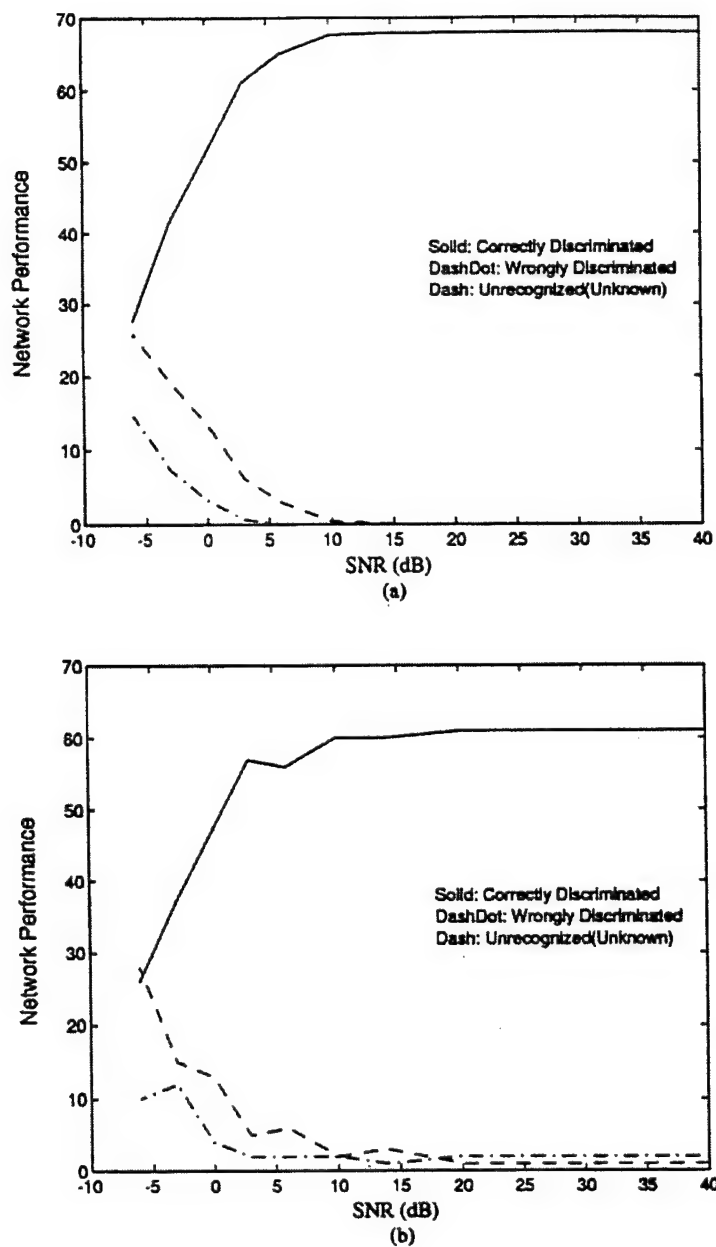
To simulate an actual situation, we measure the frequency responses of 4 targets in the frequency band 1-7 GHz, and then use a 8192 point inverse FFT to create scattering time responses. Then we regard these time responses as measured by a time-domain radar system. Therefore, we time-gate the responses to eliminate any spurious reflections within the measurement chamber, and use the DFT to transform the time responses back into the frequency domain. The spectral magnitudes then become the network processing patterns with each aspect frequency spectrum magnitude to energy 1. Figure 6 shows the 68 training/stored spectral magnitude patterns obtained from the 68 aspect time responses where sample point 1 corresponds to 1 GHz and point 100 to 7 GHz. Since the dynamical range of spectral magnitudes is much smaller than the time domain one, we can use 5 numerical intervals to quantize each pattern for binomial processing. Then we use 3 bits to binomially encode the 5 numerical intervals, so each binomial pattern has 300 bits.

Target discrimination simulation proceeds as follows. First, Gaussian noise is added to the time responses reproduced by the inverse FFT from the measured frequency responses, and then transferred back to the frequency domain. Second, 100 samples are obtained within the band 1-7 GHz, and normalized to the maximum value. Lastly the spectra are encoded to 300 bits and presented at the network input.

Figure 7(a) shows the GI network performances for the 68 trained patterns, while Figure 7(b) presents the network generality performances from testing 64 untrained aspect patterns. The GI network still prefers to categorize a response as unknown rather than wrong under severe noise conditions.

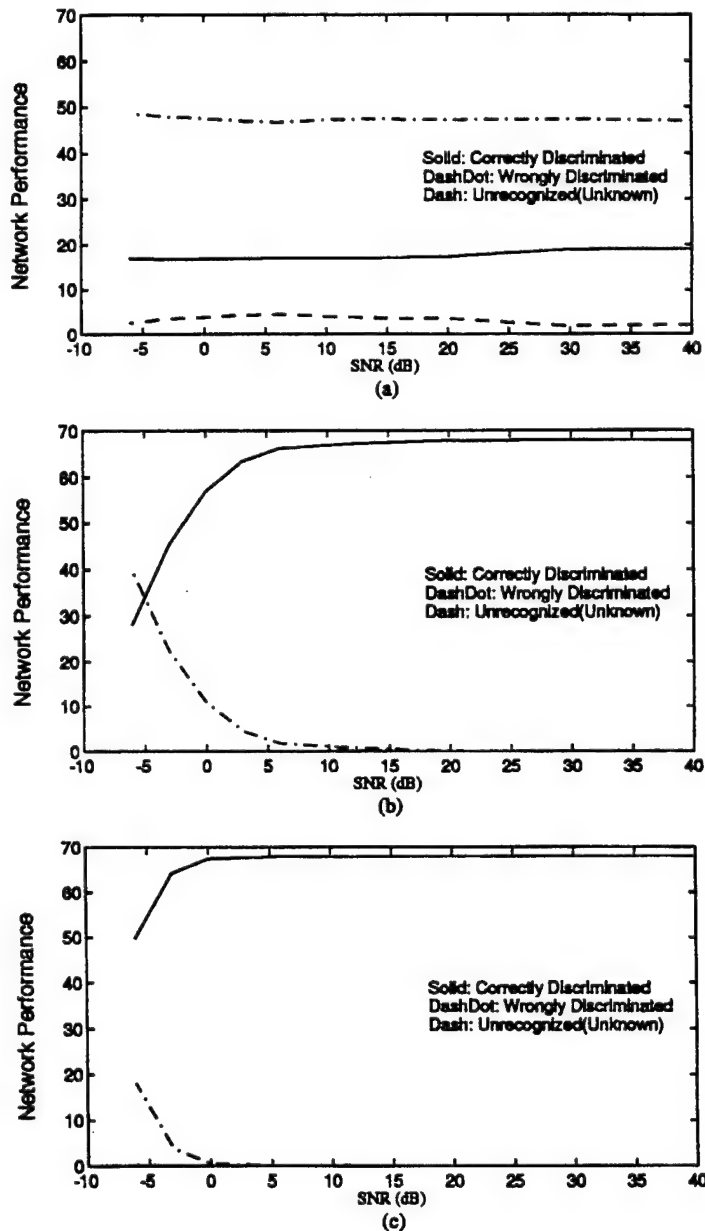


**Figure 6.** 68 Aspect FFT spectrum response magnitude patterns used for spectrum process network trainings/storage. Spectrum process networks simulate 4 targets, each target has 17 trained/stored aspect spectrum patterns. The truncation frequency band is 1-7 GHz.

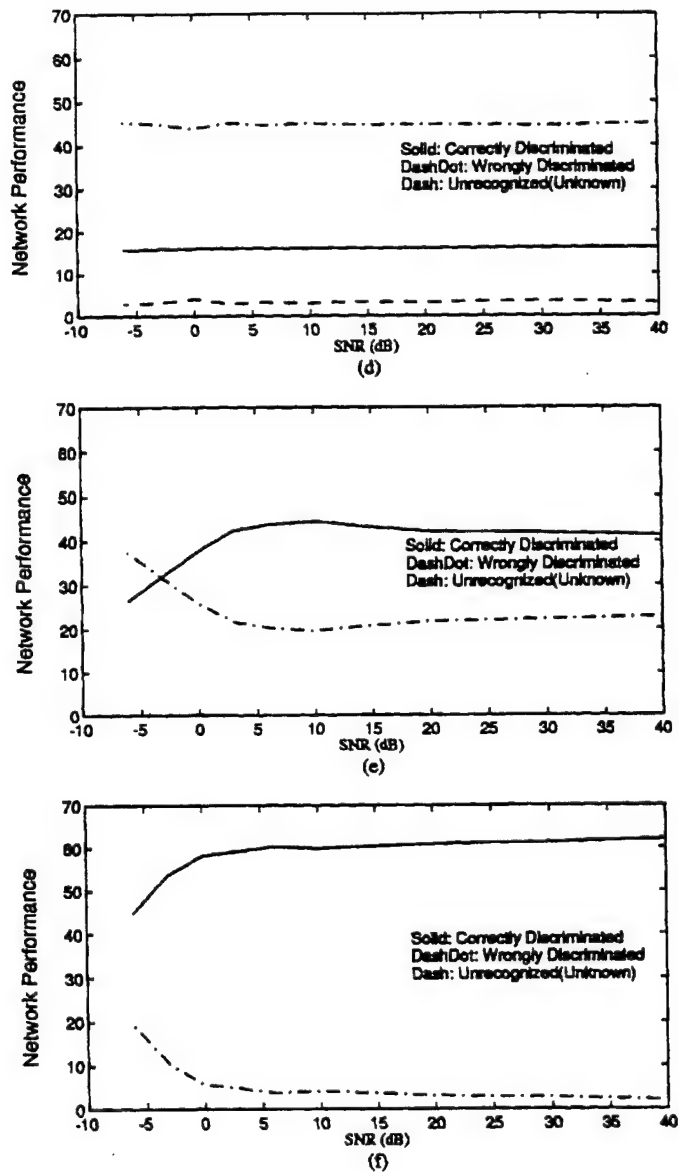


**Figure 7.** Spectrum process Generalized Inverse (GI) network performances vs. SNR. (a) GI network performance for the 68 trained patterns, (b) GI network generality performance for 64 untrained patterns.

Figure 8(a), (b) and (c) respectively show the HCAM (orders 3, 5 and 7)-GI cascade network performances for the 68 stored patterns, while Figure 8(d), (e) and (f) respectively present the network generality performances with HCAM orders of 3, 5, and 7 from testing 64 unstored aspect patterns. Compared to the GI network, a low order HCAM produces much worse results. Again, the predetermined order of HCAM greatly affects the network performance.

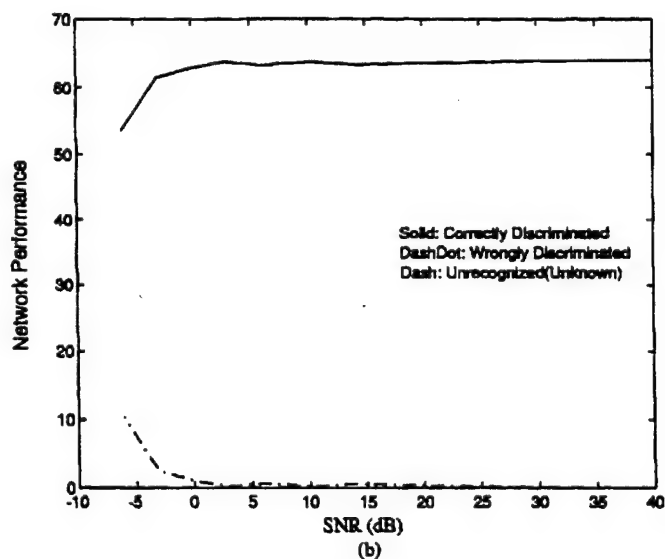
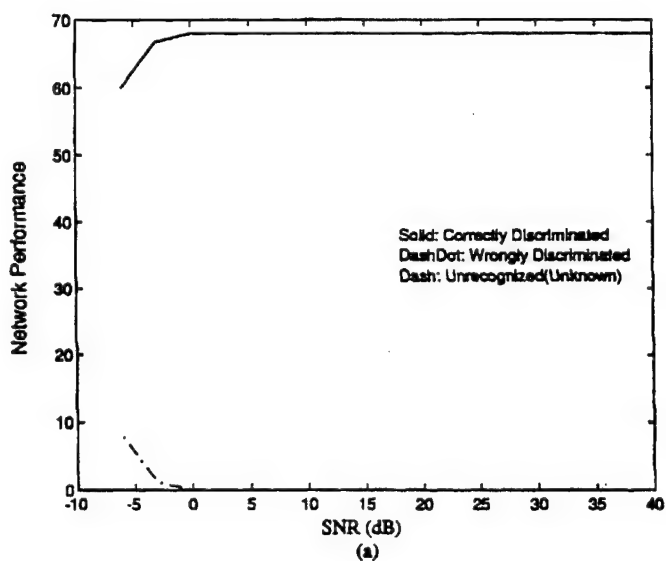


**Figure 8.** Spectrum process HCAM-GI cascade network performances vs. SNR. (a) HCAM (order 3)-GI cascade network performance, (b) HCAM (order 5)-GI cascade network performance, and (c) HCAM (order 7)-GI cascade network performance respectively for 68 stored patterns.



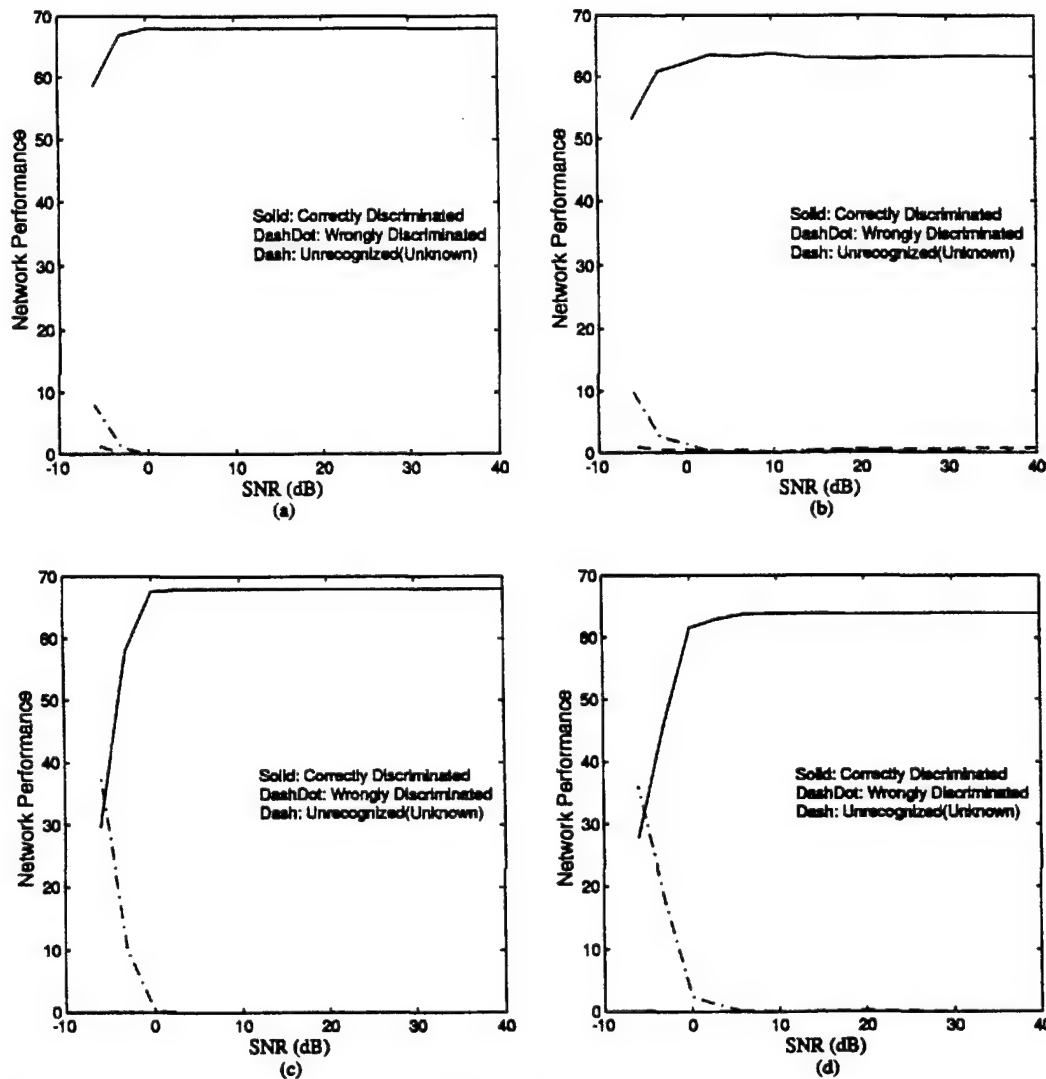
**Figure 8.(cont)** Spectrum process HCAM-GI cascade network generality performances vs. SNR. (d) HCAM (order 3)-GI network generality performance, (e) HCAM (order 5)-GI network generality performance, and (f) HCAM (order 7)-GI network generality performance respectively for 64 unstored patterns.

Figure 9(a) shows the ECAM-GI cascade network performances for the 68 stored patterns, and Figure 9(b) presents the network generality performances from testing 64 unstored aspect patterns. The ECAM-GI cascade network still has the best performance among the three networks. Since the ECAM exponentially amplifies the correlation gains, there are no spurious (or unknown) states left.



**Figure 9.** Spectrum process ECAM-GI cascade network performances vs. SNR. (a) ECAM-GI cascade network performance for the 68 stored patterns, (b) ECAM-GI network generality performance for 64 unstored patterns.

Figure 10(a) shows the RCAAM/fi-GI cascade network performances with fixed input,  $\text{init} = 1$ , and stable criterion  $\text{sc} = 2$  for the 68 stored patterns, and Figure 10(b) presents the network generality performances from testing 64 unstored patterns. Both performances are very similar to those from ECAM-GI. Again, a previously unknown pattern can be associated with one of the stored patterns by setting the stable criterion high.



**Figure 10.** Spectrum process RCAAM-GI cascade network performances vs. SNR. (a) RCAAM/fi-GI cascade network performance for the 68 stored patterns, (b) RCAAM/fi-GI network generality performance for 64 unstored patterns, (c) RCAAM/ad-GI cascade network performance for the 68 stored patterns, (d) RCAAM/ad-GI network generality performance for 64 unstored patterns.

There are some problems with analog spectrum process networks, since the spectral magnitude carries less information than the time response signal. In the time responses, the location of specular peaks is a good measurement for discrimi-

nation. In contrast, the spectral magnitude doesn't oscillate around its mean value nor have a lot of sharp peaks. Apparently, the frequency magnitude changes much slower than the time signal, and its variance is much less than its corresponding time response. Therefore, the spectral magnitude distribution is more uniform and discrimination among these spectrums becomes harder. Since the spectrum magnitude is positive, the correlation between any two stored spectrum patterns is always a positive value. If the network spectrum process patterns has analog form, a special normalization is required to satisfy the following two conditions:

- (1). Every stored pattern must be normalized to 0 mean value.
- (2). The energy of each pattern must be normalized to some uniform value.

The above condition (1) makes recurrent correlation process with a nonlinear threshold function more efficient, while condition (2) enhances the linearity of the correlation operation.

Suppose  $\{\mathbf{A}(i)|i = 1, \dots, n\}$  is a stored spectral magnitude pattern with energy 1. Then

$$\sum_{i=1}^n A(i)^2 = 1 \quad (25)$$

Letting  $\underline{a}$  denote mean of  $\mathbf{A}$ , i.e.,

$$\underline{a} = \frac{1}{n} \sum_{i=1}^n A(i) \quad (26)$$

and  $\mathbf{E}\{\mathbf{A}(i) - \underline{a}\} = 0$ , then we have two processes by which to produce the normalized pattern  $\underline{\mathbf{A}}$

(1). Prior Process

For condition (2), we have

$$\sum_{i=1}^n [C \cdot (A(i) - \underline{a})]^2 = 1 \quad (27)$$

so that

$$C = \sqrt{\frac{1}{1 - n\underline{a}^2}} \quad (28)$$

and

$$\underline{\mathbf{A}}(i) = C \cdot (A(i) - \underline{a})$$

If  $\mathbf{A}_M(i) = \mathbf{A}(i) - \underline{a}$  has been calculated, then we use

(2). Posterior Process

Condition (2) gives

$$\underline{A}(i) = \frac{A_M(i)}{\sqrt{\sum_{i=1}^n A_M(i)^2}} = D \cdot A_M(i) \quad (29)$$



where

$$D = \sqrt{\frac{1}{\sum_{i=1}^n A_M(i)^2}} \quad (30)$$

Since we have assumed  $\mathbf{A}$  has energy 1

$$\sum_{i=1}^n A_M(i)^2 = 1 - n\bar{a}^2 \quad (31)$$

and thus  $\mathbf{C} = \mathbf{D}$ .

Thus, we now have the normalized spectrum magnitude pattern  $\underline{\mathbf{A}}$  satisfying both conditions (1) and (2)

$$E\{\underline{\mathbf{A}}(i)\} = 0 \quad (32)$$

$$\sum_{i=1}^n \underline{\mathbf{A}}(i)^2 = 1 \quad (33)$$

Although we have normalized the spectral magnitude to overcome the deficiency caused by disregarding phase, the analog correlation processing algorithm still requires further improvement. As analyzed previously, the frequency spectra are more similar to each other than the time responses, and thus the crosscorrelations between any two stored spectral patterns almost always have positive values, even after the above normalization. Therefore, we need an offset to further compensate.

We statistically evaluate the crosscorrelations of all the stored spectral patterns to find out the average and the minimum, and then design the **offset**. Since the spectral patterns have been normalized, the maximum correlation gain, (i.e. autocorrelation), among all stored patterns is 1, provided the input is equal to some stored pattern. Let  $C_{\min}$  denote the minimum of crosscorrelations among all stored patterns. If a recurrent correlation associative network is to converge to the expected stored pattern, it needs to satisfy at least

$$1 - \text{Offset} > -(C_{\min} - \text{Offset}) \quad (34)$$

and thus

$$\text{Offset} < \frac{1 + C_{\min}}{2} \quad (35)$$

Typically,  $C_{\min}$  has a negative value. If  $-(C_{\min} - \text{Offset}) > 1 - \text{Offset}$  exists, there exists an input and one stored pattern that have negative normalized correlation gain and the gain scale is larger than the normalized input autocorrelation. Therefore, the stored pattern with minimum correlation gain will overcome the others when the recurrent iterations are even. If we use the value of **Offset** just satisfying the above inequality margin, then the network may not converge or may converge very slowly. We evaluate the mean of all crosscorrelations, then statistically and experimentally find that 2/3 of the mean is good choice for the **Offset**. Therefore, the network processing algorithm for RCAAM/ad requires some modification to process the analog frequency spectrum magnitude.

Suppose  $\{(\xi^i, \zeta^i) | i = 1, \dots, P\}$  are the associative pattern pairs stored in RCAAM/ad, where  $\xi^i$  is a bipolar column vector of length  $m$  and  $\zeta^i$  is a normalized analog spectral magnitude vector of length  $n$ , given by  $\xi = [\xi^1, \xi^2, \dots, \xi^P]$  and  $\zeta = [\zeta^1, \zeta^2, \dots, \zeta^P]$ , and let the offset vector  $\mathbf{F}_{\text{offset}}$  be a column vector of length  $P$  with each component value equal to the **Offset**. If  $U$  is an  $n$ -dimensional normalized analog spectral magnitude input, then we can construct the initial Analog-Digital RCAAM as follows:

$$M_o = \xi \cdot \{ \text{Diag} [(\zeta^T \cdot U - F_{\text{offset}}) \cdot \wedge (\text{init})] \cdot \zeta^T \} \quad (36)$$

$$OS_o = \xi \cdot \{ \text{Diag} [(\zeta^T U - F_{\text{offset}}) \cdot \wedge (\text{init})] \cdot F_{\text{offset}} \} \quad (37)$$

where  $\mathbf{OS}_o$  is an  $m$  by 1 column vector.

Then the current dynamic memory output is

$$V_o = \text{Sign} (M_o \cdot U - OS_o) \quad (38)$$

The initial order **init** is usually set to 0. Since the input has analog form (the same as  $\zeta^i$ ), and the output has binomial form (the same as  $\xi^i$ ), we have fixed input ( $\mathbf{U}_k = U$ ), for this analog-digital hybrid memory. Then the dynamic memory  $\mathbf{M}_k$ , the dynamic **Offset** vector  $\mathbf{OS}_k$  and the evolution outputs  $\mathbf{V}_k$  at the recurrent iteration time  $k$  have

$$M_k = \xi \cdot \{ \text{Diag} [(\zeta^T U - F_{\text{offset}}) \cdot \wedge (\text{init} + k)] \cdot \zeta^T \} \quad (39)$$

$$OS_k = \xi \cdot \{ \text{Diag} [(\zeta^T U - F_{\text{offset}}) \cdot \wedge (\text{init} + k)] \cdot F_{\text{offset}} \} \quad (40)$$

$$V_k = \text{Sign} (M_k \cdot U - OS_k) \quad (41)$$

Figure 10(c) shows the analog RCAAM/ad performances with **init** = 0 and the stable criterion **sc** = 2 for the 68 stored patterns, while Figure 10(d) presents the network generality performances from testing 64 unstored patterns. Although this analog RCAAM/ad requires several complex preprocesses, its performance is apparently better than any of the bipolar networks examined. However, the spectrum processing RCAAM/ad performs worse than the time process version analyzed previously.

We can summarize the architectures of the recurrent correlation associative networks used in Table 2. The computation space for RCAAM's is iteratively adaptive. For lightly contaminated patterns, the computation space required for discrimination is small due to few iterations, while a larger space is required for highly distorted patterns. Row 5 presents the available knowledge observed from the network operations about contamination or similarity between input and the final stable output. The ECAM converges most distorted inputs to some stable states within 3 iterations since it greatly expands the discrimination space. Therefore, we are unable to determine contamination from the ECAM. The HCAM's with small order are usually trapped in some spurious stable states, while the RCAAM typically avoids that with its accumulatively dynamic memory and the adjustment of **sc**. The decisions are deterministic for both HCAM and ECAM, when their outputs don't change for one iteration, since their memories are fixed.

Network	HCAM	ECAM	RCAAAM
Input form	Binomial	Binomial	Binomial or Analog
Process structure/ Recurrent operation	Fixed memory/ Adaptive	Fixed memory/ Adaptive	Dynamic memory/ Accumulatively adaptive
Computation Space	Small for small orders	Extremely huge	Fit for discrimination
Observability about contamination or similarity between input and the final output	High for small orders; low for high orders	Very little	High
Possibility trapped in unknown stable states	Very high for small orders	Very little	Adjustable
Decision strategy	Deterministic	Deterministic	Flexible
Hardware Realization	Capable for fair orders	Nearly incapable	Capable

**Table 2.** Architecture summary of the current correlation associative networks used.

## VI. NETWORK COMPARISONS

Several bipolar/binary networks, the Hopfield recurrent net and BAM's, have been simulated to act as comparisons. ART(Adaptive Resonance Theory) [31, 32] nets also use binomial data, but they are not suitable for our application. The ARTs' architecture uses two layers, a bottom or input layer and a top or classification layer, totally interconnected to competitively learn and classify inputs. These kinds of networks are suitable for unsupervised self-organization or classification. They may be used for supervised learning, but require clear clusters so that the patterns belonging to same cluster will be closer (or more similar) to each other than ones belonging to any other cluster. For our applications, this is usually not true. For example, two responses of different targets with the same azimuthal aspect are usually more similar than two responses of a single target at different aspects. Therefore, if ART's are used, the unsupervised competitive learning will result in a wrong clustering and the ART's might become an azimuthal aspect discrimination net instead of a target discrimination net. If the supervised ART's are used, then the learnings might get confused from the ambiguous grouping and require careful manipulation of the vigilance parameter and learning rate. It is possible that the ART's will categorize a lot of groups, and then require another network to complete the target classification.

To demonstrate the RCAAM's advantages over other popular networks, the following neural networks have been simulated : Hopfield recurrent network, Bidirectional Associative Memories (BAM) and Multi-Layer feedforward and error-BackPropagation (ML/BP) networks. Their architectures and performances are summarized in Table 3 for time domain process, in Table 4 for spectrum magni-

tude process with 5 quantization levels coded by 3 bits and in Table 5 for spectrum magnitude process with 7 quantization levels coded by 3 bits. All the networks listed in the tables have been simulated 10 times and each stored/trained or untrained/untrained pattern is tested under 10 different SNR levels, [40, 30, 20, 14, 10, 6, 3, 0, -3, -6] dB, in each simulation, and then the average results are given in three tables.

Network	Input/ Output Form	Memory Size	Training Epoch/Error	Recog. Iterations	Min. dB w/ 95% Correct Recog.	% of Correct Recog. at 40/0 dB	Max. Integer Comput. Scale
				Trained; Untrained	Trained; Untrained	Trained; Untrained	
Hopfield Net	Bip/Bip	300x300	X	9.68; 9.71	None; None	0/0; 0/0	300 <sup>2</sup>
BAM	Bip/Bip	300x7	X	4.28; 4.27	None; None	36.2/8.7; 6.4/4.7	300 <sup>2</sup>
BAM using group code	Bip/Bip	300x7	X	4.28; 4.25	20 dB; None	96.0/63.6; 78.1/54.8	300 <sup>2</sup>
ML/BP w/o hidden layer	Analog/Bip	100x4	164+1012/0	X	10 dB; 14 dB	100/59.3; 98.0/56.6	Not Integer
ML/BP w/ 1 hidden layer	Analog/Bip	100x25 +25x4	624+414/0	X	14 dB; 14 dB	100/56.6; 99.5/54.2	Not Integer
GI Net	Bip/Bip	300x4	3+120/0	X	10 dB; 14 dB	100/42.4; 100/42.3	Not Integer
HCAM w/ Order of 3	Bip/Bip	68x300	X	5.02; 6.07	None; None	80.6/52.5; 63/47.2	300 <sup>Order</sup>
ECAM-GI	Bip/Bip	68x300	X	3.01; 3.03	3 dB; 3 dB	100/90.7; 100/90.9	2 <sup>300</sup>
RCAAAM/di -GI	Bip/Bip	68x300	X	4.38; 5.12	3 dB; 3 dB	100/90.9; 100/91.7	Adaptive
RCAAAM/fi -GI	Bip/Bip	68x300	X	5.99; 7.27	3 dB; 3 dB	100/89.6; 100/89.4	Adaptive
RCAAAM/da -GI	Analog/Bip	68x100 +68x300	X	6.99; 8.16	-6 dB; -6 dB	100/100; 100/100	Adaptive

**Table 3.** Network architectures and performances summary for time domain target discrimination with 7 quantization levels coded by bits.

Network	Input/ Output Form	Memory Size	Training Epoch/Error	Recog. Iterations  Trained; Untrained	Min. dB w/ 95% Correct Recog.  Trained; Untrained	% of Correct Recog. at 40/0 dB  Trained; Untrained	Max. Integer Comput. Scale
Hopfield Net	Bip/Bip	300x300	X	5.40; 5.29	None; None	0/0; 0/0	300 <sup>2</sup>
BAM	Bip/Bip	300x7	X	4.74; 4.73	None; None	8.8/4.9; 0/0.47	300 <sup>2</sup>
BAM using group code	Bip/Bip	300x7	X	4.73; 4.71	None; None	55.9/48.1; 44.4/40.6	300 <sup>2</sup>
ML/BP w/o hidden layer	Analog/Bip	100x4	1981+864/0	X	14 dB; None	100/65.2; 87.5/64.4	Not Integer
ML/BP w/ 1 hidden layer	Analog/Bip	100x25 +25x4	1337+678/0	X	10 dB; None	100/62.5; 90.6/60.2	Not Integer
GI Net	Bip/Bip	300x4	10+120/0	X	6 dB; 20 dB	100/75.3; 95.3/73.4	Not Integer
HCAM w/ Order of 3  Order of 5	Bip/Bip	68x300	X	6.56; 6.22 4.51; 7.71	None; None None; None	2.79/0; 0/0; 94.9/57.2; 32.5/28	300 <sup>3</sup>  300 <sup>5</sup>
ECAM-GI	Bip/Bip	68x300	X	2.95; 3.05	-3 dB; -3 dB	100/100; 100/98.3	2 <sup>300</sup>
RCAAAM/di -GI	Bip/Bip	68x300	X	7.12; 9.42	3 dB; None	100/88.1; 87.5/79.2	Adaptive
RCAAAM/fi -GI	Bip/Bip	68x300	X	5.24; 8.21	-3 dB; -3 dB	100/100; 98.9/97.2	Adaptive
RCAAAM/da -GI	Analog/Bip	68x100 +68x300	X	12.31; 15.93	0 dB; 3 dB	100/99.3; 98.8/94.5	Adaptive

Table 4. Network architectures and performances summary for spectrum magnitude target discrimination with 5 quantization levels coded by 3 bits.

Network	Input/ Output Form	Memory Size	Training Epoch/Error	Recog. Iterations	Min. dB w/ 95% Correct Recog.	% of Correct Recog. at 40/0 dB	Max. Integer Comput. Scale
				Trained; Untrained	Trained; Untrained	Trained; Untrained	
Hopfield Net	Bip/Bip	300x300	X	6.37; 6.19	None; None	0/0; 0/0	300 <sup>2</sup>
BAM	Bip/Bip	300x7	X	4.17; 4.13	None; None	22.5/11.2; 0/1.72	300 <sup>2</sup>
BAM using group code	Bip/Bip	300x7	X	4.17; 4.13	None; None	83.4/70; 77.7/59.5	300 <sup>2</sup>
ML/BP w/o hidden layer	Analog/Bip	100x4	1981+864/0	X	14 dB; None	100/65.2; 87.5/64.4	Not Integer
ML/BP w/ 1 hidden layer	Analog/Bip	100x25 +25x4	1337+678/0	X	10 dB; None	100/62.5; 90.6/60.2	Not Integer
GI Net	Bip/Bip	300x4	10+156/0	X	10 dB; None	100/66.3; 89.5/63.4	Not Integer
HCAM w/ Order of 3	Bip/Bip	68x300	X	5.18; 9.38	40 dB; None	96.5/59.9; 48.6/33.1	300 <sup>3</sup>
ECAM-GI	Bip/Bip	68x300	X	2.96; 3.05	0 dB; 0 dB	100/99.9; 97.5/95.3	2 <sup>300</sup>
RCAAAM/di -GI	Bip/Bip	68x300	X	4.06; 5.83	0 dB; 14 dB	100/99.6; 95.6/90.3	Adaptive
RCAAAM/fi -GI	Bip/Bip	68x300	X	4.09; 6.10	0 dB; 0 dB	100/99.7; 98.4/95.2	Adaptive
RCAAAM/da -GI	Analog/Bip	68x100 +68x300	X	12.3; 16.45	0 dB; 3 dB	100/99.3; 100/94.8	Adaptive

**Table 5.** Network architectures and performances summary for spectrum magnitude target discrimination with 7 quantization levels coded by 3 bits

Column 4 in each table presents the training epochs and final errors for ML/BPs and GI networks. The first number in this column presents the training epochs with which network trainings converge to 0 error, while the second number denotes the extra training cycles made to ensure all training pattern outputs deeply enter the saturation regions of the sigmoid function. Theoretically, this will increase noise tolerances and decrease the biased learnings. Column 5 presents the average iterations which the recurrent networks require to reach the stable state adopted for target discrimination. The upper number in every row corresponding to 'Trained' means the result obtained by testing the trained/stored patterns, while the lower number corresponding to 'Untrained' indicates the result obtained

by testing the untrained/unstored patterns. Column 6 presents the minimum SNR in dB at which the network still performs 95 % correct discrimination. Column 7 shows the correct discrimination rates in percentage respectively at 40 and 0 dB. Finally, column 8 presents the maximum integer computation scale required for processing one stored pattern.

The autoassociative Hopfield net always goes to some undefined states and leaves nothing discriminated. The BAM also has bad performances and always converges to the wrong heteroassociative partners. We have altered the BAM process strategy by using target group code in its heteroassociative partners, and then we only discriminate the target group code portion of the final stable state and ignore the rest of the code. This effort has greatly improved its correct recognition rate and also reduced the wrong rate in simulations. In our simulations, we design a set of 7-bit heteroassociative codes corresponding to the 68 300-bit stored patterns. The first two bits are designed as a target group code for four different targets, i.e. [-1 -1] for B52, [-1 1] for B58, [1 -1] for F14 and [1 1] for TR1, and then the next five bits are coded to represent 17 azimuthal responses of each target. Therefore, this altered BAM will discriminate an input as a correct target or wrong target, and leave none unknown. For example, the BAM using group code has 36.2 % and 8.7 % correct discriminations respectively at 40 and 0 dB; therefore the remaining 63.8 % and 91.3 % all contribute to wrong discriminations.

High resolution and linearity are the most important advantages gained from using analog networks. The high resolution will expand the differences between any two trained/stored patterns and then increase the discrimination accuracy, while the linearity between an input and the stored patterns can greatly increase the confidence in network performances. But analog data are hard to use in a recurrent associative update, therefore the analog networks can't iteratively adapt to the final stable state. So it may be difficult to determine the contamination or the similarity between an input and the network output. Also an analog network can't be cascaded to a high performance and high dimension recurrent autoassociative network as a group decoder. Unless an analog network is capable of hardware realization, it can't take advantage of today's digital computer technologies. Binomial data only have two states by which an artificial neuron model emulates the bi-state, activated and inactive, of a biological neuron. Therefore, the binomial data format is well qualified for use in recurrent and cascade operations, like complicated biological neural nets. Binomial data use much less space than continuous data in a digital computer process, and it can be more further compressed. Quantizing continuous data by finite discrete levels can also result in a tolerance of light contamination in a way. And the binary data are easy and safe to store for long periods of time.

We also simulate two ML/BPs, one without a hidden layer and another with one hidden layer containing 25 neurons, to compare their performances to the networks we used. We use the uncoded 100 analog responses as training inputs for each training pattern, and use the same output target set used by the GI net. Therefore, they have analog inputs and bipolar outputs. The initial weights are



randomly initiated, and a momentum has been used to reduce being trapped in local minima. Compared to the GI net, ML/BPs require more training epochs and manipulations to converge all training patterns to their desired targets with zero error. Although a momentum has been used, the trainings still get trapped in local minima a number of times. The ML/BP nets have a similar performance phenomenon to the GI net. As expected, they prefer to leave ambiguous inputs unknown rather than discriminate wrongly. The HCAM's with small order have a low correct discrimination rate in the generality performance, but, compared to the BAM's discussed above, they converge to undefined states instead of wrong stored patterns.

We have used two different numbers of discrete levels to quantize an analog spectrum magnitude, 5 levels and 7 levels. The codes generated by coding 5 levels with 3 bits are more linear than the codes generated by coding 7 levels, explained in section V, subsection A. Less quantization levels give not only higher linearity but also lower noise sensitivity, although they may lose resolution. In a badly noisy condition, the coding's linearity and noise tolerance will become important. From the Figure 1 and 6, it is easy to see that the time responses oscillate with a much larger range than the frequency spectral magnitudes. Therefore 7 levels are used in the time responses for accurately representing its large oscillation range. Different factors prevail in different networks.

The noise tolerance and linearity factors prevail in training-based convergent networks, i.e. the GI net, while the resolution factor prevails in correlation-based recurrent memories under fair noise conditions. If a GI net, trained with patterns of few quantization levels, can converge with zero error, then well trained GI net can discriminate all the training patterns under this low resolution. When a GI net trained with high resolution patterns suffers from noise sensitivity, a GI net trained with low resolution patterns may still work very well. This issue can be proved by comparing the GI net's performances in table 4 (using 5 quantization levels) and table 5 (using 7 quantization levels). For correlation-based recurrent memories, more quantization levels will slightly affect the correlation gain of two similar patterns but greatly reduce the gain of two unlike patterns. This two-side effect greatly increases the discrimination resolution, so the recurrent network performance will increase. As discussed in section V, subsection A, the linearity still exists within  $\pm 1.5$  quantization levels for the 7-level coding scheme we use, so the nonlinearity may bother the recurrent memories only if the noise amplitude is larger than 1.5 quantization levels. This resolution prevalence can be seen by comparing the recurrent memories in table 4 to those in table 5, especially the BAM's and HCAM's. Since the BAM's only converge to correct or wrong patterns, increasing the correct rate will reduce the wrong rate. The average number of recognition iterations decrease when the pattern resolution becomes high. Another apparent change is that the minimum SNR with 95% correct recognition increases, as expected, since the larger the number of quantization levels, the lower the noise tolerance. The ML/BP nets use continuous data, and are listed there only for comparison.



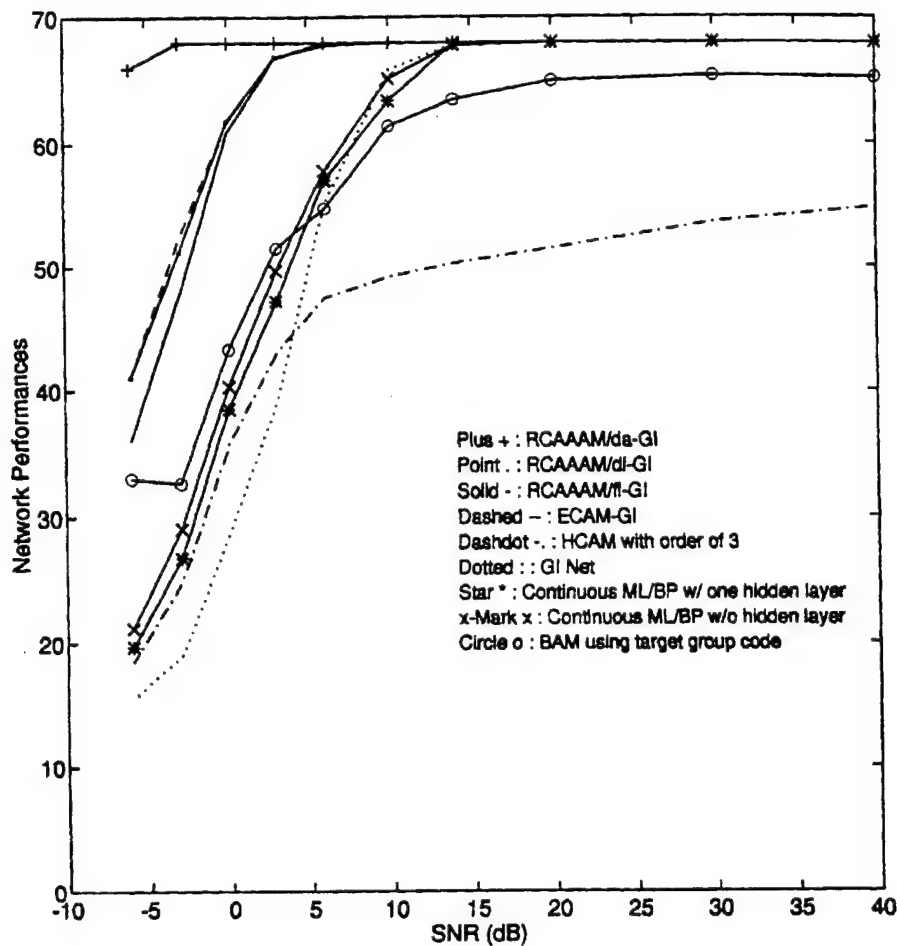


**Figure 11.** Correct discriminations of different time domain process networks vs. SNR for 68 trained/stored patterns.

To illustrate in detail 9 different network performances under 10 different SNR levels, six figures are plotted. Figure 11 shows the time domain network correct discrimination performances, while Figure 12 presents the time domain network generality performances of correct discrimination. Figure 13 shows the spectrum magnitude network correct discrimination performances with 5 quantization levels coded by 3 bits, and Figure 14 presents their generality performances. Figure 15 shows the spectrum magnitude network correct discrimination performances with 7 quantization levels coded by 3 bits, while Figure 16 presents their generality performances of correct discrimination.

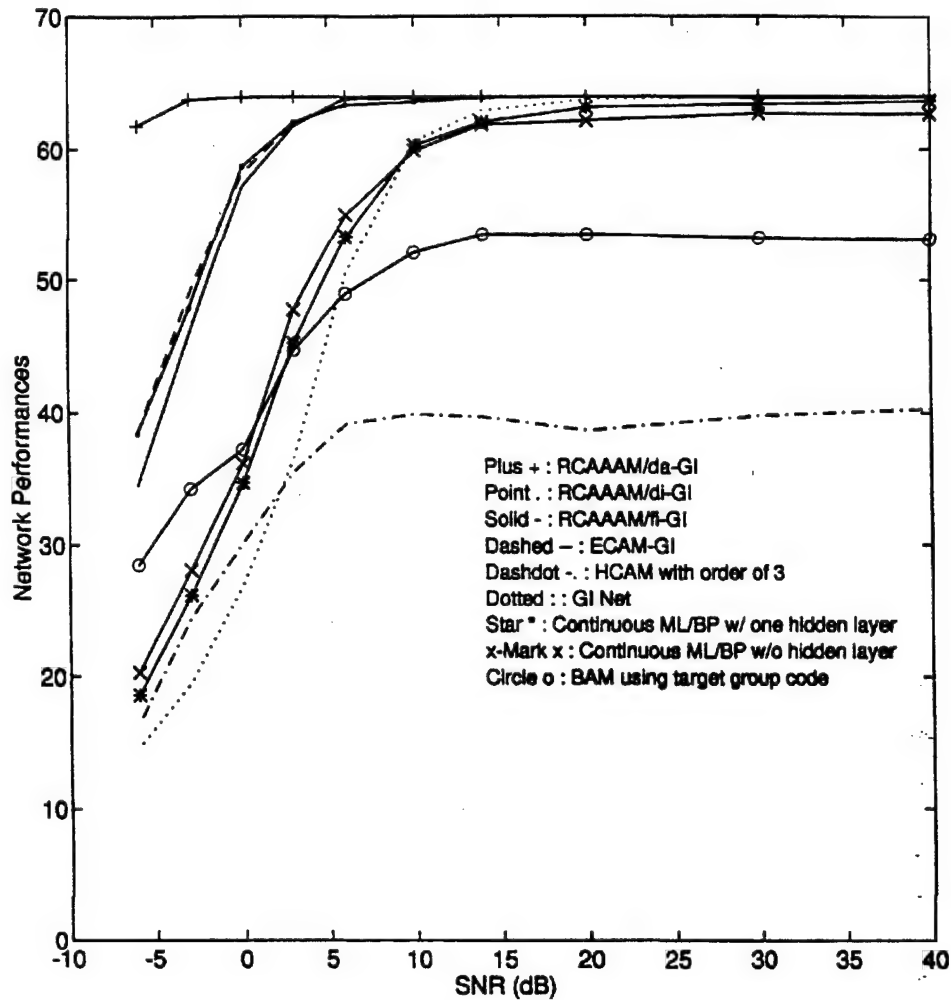


Figure 12. Correct discriminations of different time domain process networks vs. SNR for 64 untrained/unstored patterns.

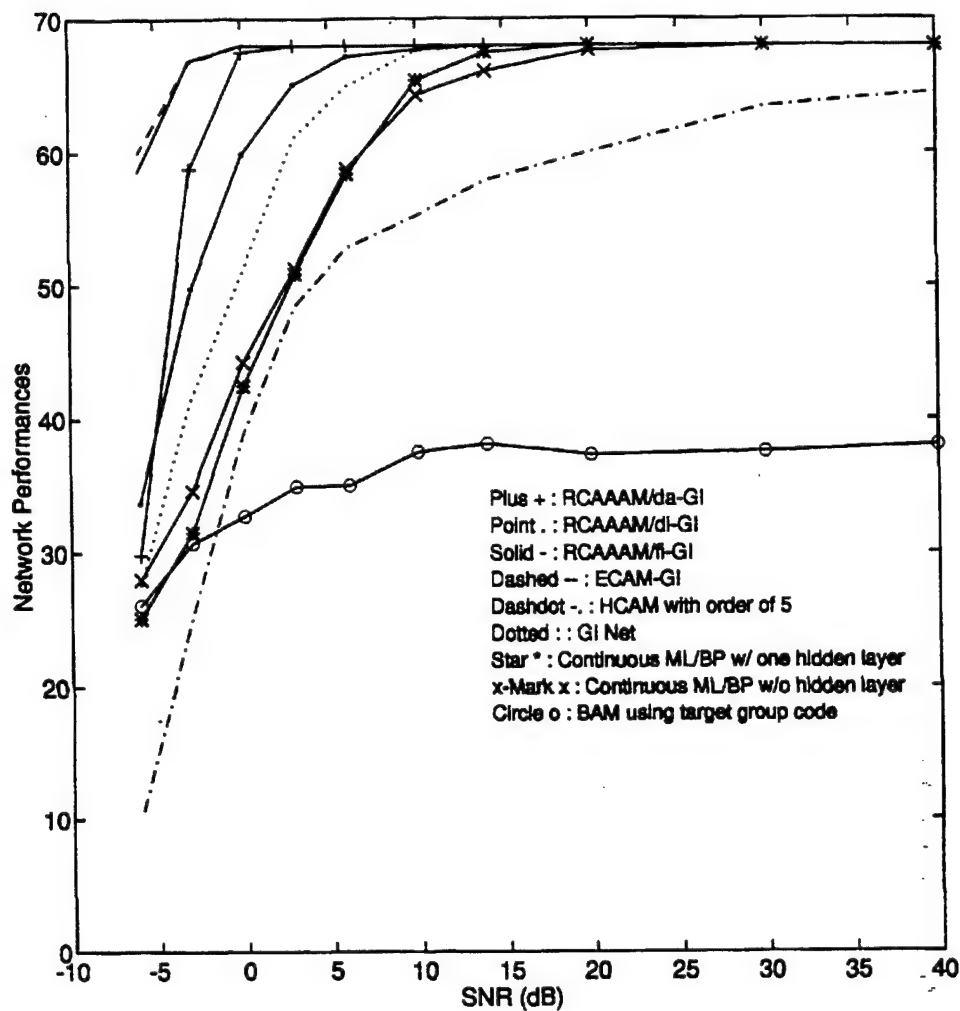


Figure 13. Correct discriminations of different spectrum magnitude process networks with 5 quantization levels coded by 3 bits vs. SNR for 68 trained/stored patterns.

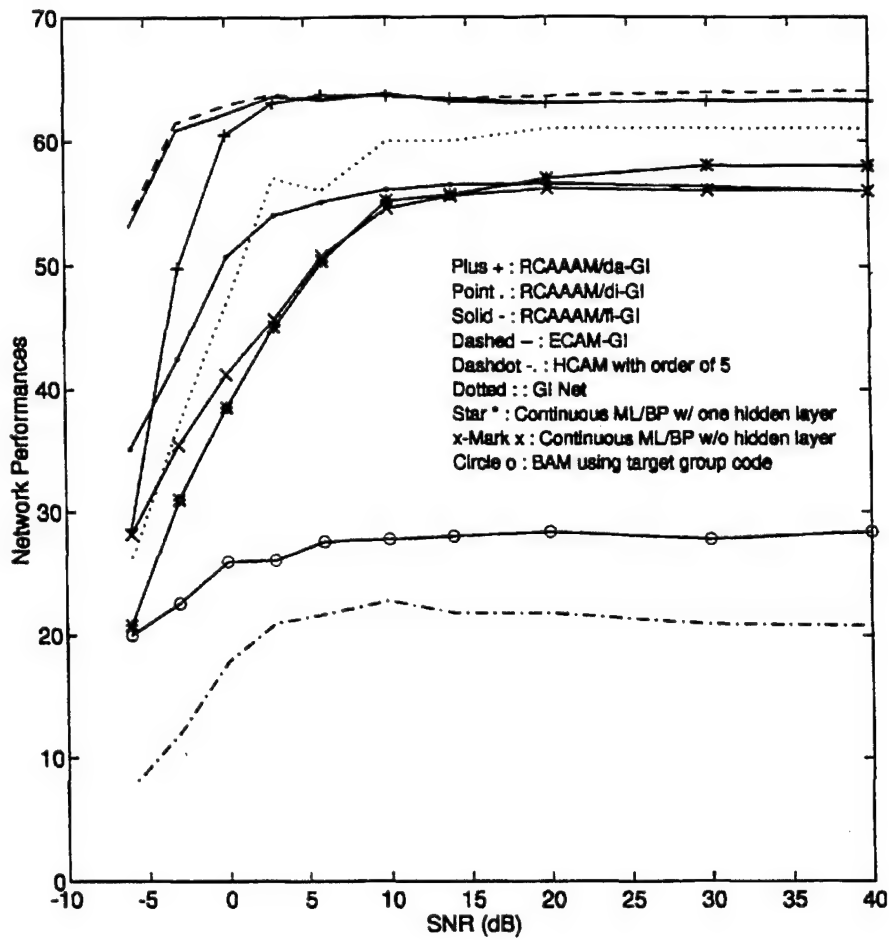
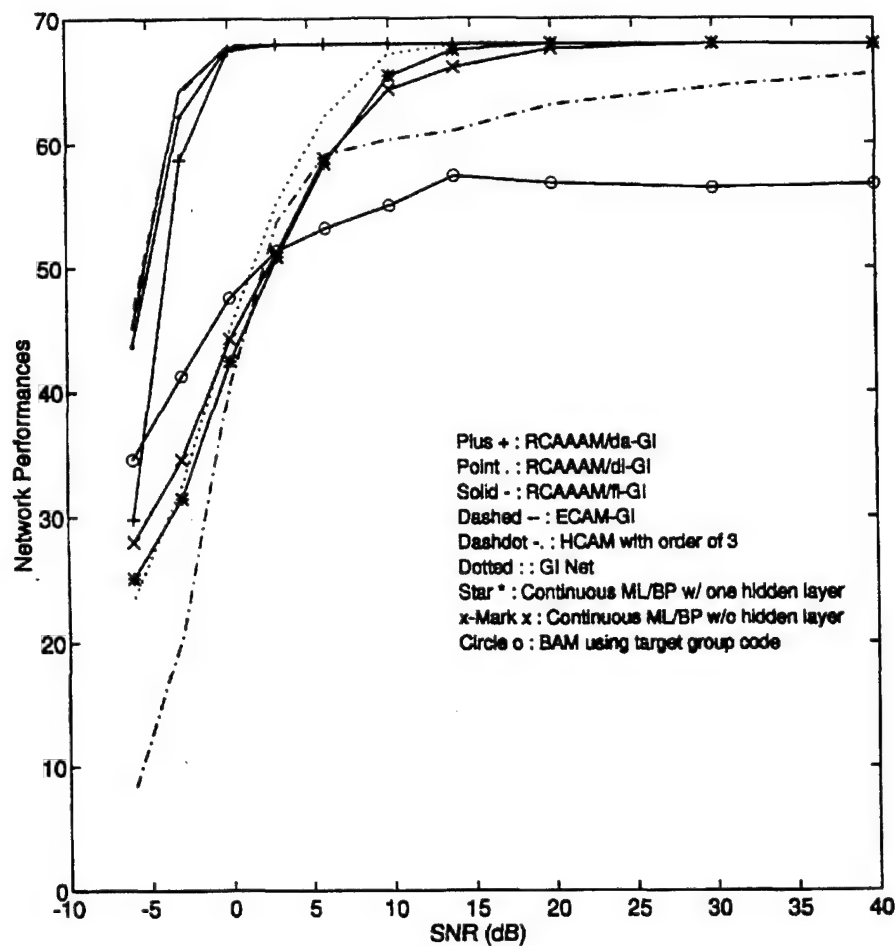
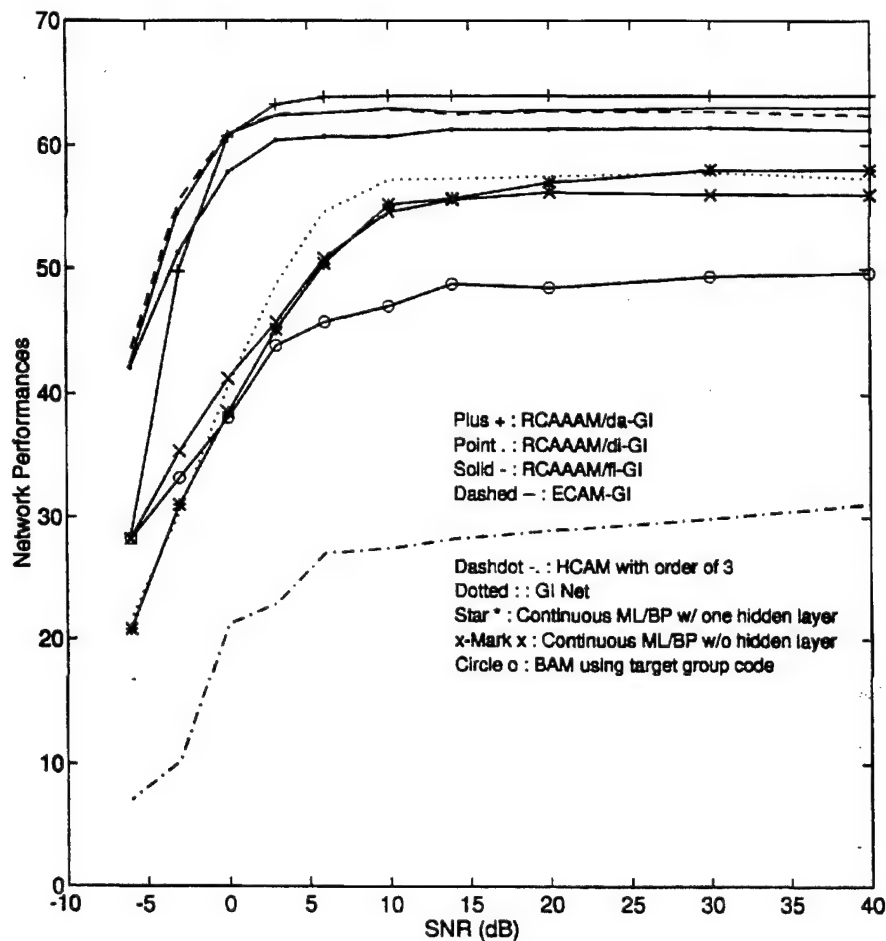


Figure 14. Correct discriminations of different spectrum magnitude process networks with 5 quantization levels coded by 3 bits vs. SNR for 64 untrained/unstored patterns.



**Figure 15.** Correct discriminations of different spectrum magnitude process networks with 7 quantization levels coded by 3 bits vs. SNR for 68 trained/stored patterns



**Figure 16.** Correct discriminations of different spectrum magnitude process networks with 7 quantization levels coded by 3 bite vs. SNR for 64 untrained/unstored patterns.

## VII. CONCLUSION

We have used several different neural network architectures to discriminate among radar targets at a wide variety of aspect angles. From the simulations, it appears that correlation-based neural networks have powerful and effective problem solving abilities. Comparing the GI network to the recurrent correlation-based associative memories, we find the GI network has a smaller stored pattern attraction region within which the GI net can correctly converge from an input to its associative stored pattern. Therefore, the GI network noise tolerance is inferior to the correlation-based associative memories. Typical RCAM's have off-line predetermined fixed memory, limiting the network flexibility and adaptability. Therefore, some RCAM networks may need a large computation space to operate, and some may not work well if used with insufficient predetermined order.

We have proposed a flexible and highly adaptive real-time learning network, RCAAM, which has dynamic memory to allow the given input to parallel adapt to all stored patterns, and an adjustable stabel criterion to observe those semi-stable states. The network may have several semi-stable states corresponding to various inputs if the criterion is set low. The spurious (unknown) semi-stable states will be transferred to one of the stored patterns if the criterion is set high. Thus, the discrimination decision strategy is flexible : 3 phases, correct/wrong/unknown, or 2 phases, correct/wrong. We have simplified the RCAAM iteration to an easily realizable implementation form, which speeds up the dynamic memory computations.

We have also used the spectral magnitudes as the network processing patterns. The simulations reveal excellent results for ECAM-GI, HCAM-GI with order higher than 5, and RCAAM-GI. After some modifications for analog application, the spectrum process RCAAM/ad-GI has a performance almost competitive to that using time responses. The RCAAM has the same or better performances, but much great space saving compared to the ECAM and the implementation complexity similar to the HCAM.

#### ACKNOWLEDGEMENT

This work was supported by the Thermo Trek Corporation under purchase order 22068, and in part by the Northeast Consortium for Engineering Education under purchase order NCEE/A303/23-93 and the office of Naval Research under Grant N00014-93-1-1271.

#### REFERENCES

- 1 Ilavarasan, P., J. E. Ross, J. Rothwell, K. M. Chen, and D. P. Nyquist, "Performance of an automated radar target discrimination scheme using E pulses and S pulses," *IEEE Trans. Antennas Propagat.*, Vol. 41, 582-588, May 1993.
- 2 Baum, C. E., E. J. Rothwell, K. M. Chen, and D. P. Nyquist, "The singularity expansion method and its applications to target identification," *Proc. IEEE*, Vol. 79, No. 10, 1481-1492, October 1991.
- 3 Rothwell, E. J., K. M. Chen, D. P. Nyquist, and W. M. Sun, "Frequency domain E-pulse synthesis and target discrimination," *IEEE Trans. Antennas Propagat.*, Vol. AP-35, 426-434, April 1987.
- 4 Kennaugh, E. M., "The K-pulse concept," *IEEE Trans. Antennas Propagat.*, Vol. AP-29, No. 2, 329-331, March 1981.
- 5 Fok, F. Y. S., "K-pulse estimation for a right-angle bent wire using more than one impulse response," *IEEE Trans. Antennas Propagat.* Vol. 38, 1092-1098, July 1990.
- 6 Bayard, J. P., and D. H. Schaubert, "Target identification using optimization techniques," *IEEE Trans. Antennas Propagat.*, Vol. 38, 450-456, April 1990.
- 7 Moran, M. A., "Scatterer discrimination based upon natural resonance annihilation," *J. Electromagnetic Waves Appl.*, Vol. 2, No. 5/6, 481-502, 1988.
- 8 Dudley, D. G., and D. M. Goodman, "Transient identification and target classification," *Time Domain Measurements in Electromagnetics*, 456-497, E. K. Miller, Ed., New York, Van Nostrnad-Reinhold, 1986.
- 9 Chuang, C. W., and D. L. Moffatt, "Natural resonances of radar targets via Prony's method and target discrimination," *IEEE Trans. Aerosp. Electron. Syst.*, Vol. AES-12, 583-589, Sept. 1986.

- 10 Rothwell, E. J., K. M. Chen, D. P. Nyquist, and J. E. Ross, "Time-domain imaging of airborne targets using ultra-wideband or short-pulse radar," *IEEE Trans. Antennas Propagat.*, Vol. 43, No. 3, March 1995.
- 11 Bennet, C. L., "Time-domain inverse scattering," *IEEE Trans. Antennas Propagat.*, Vol. AP-29, No. 2 213-219, March 1981.
- 12 Young, J. D., "Radar imaging from ramp response signatures," *IEEE Trans. Antennas Propagat.*, Vol. AP-24, 276-282, May 1976.
- 13 Lin, M. C., and Y. W. Kiang, "Target discrimination using multiple-frequency amplitude returns," *IEEE Trans. Antennas Propagat.*, Vol. 38, 1885-1889, Nov. 1990.
- 14 Lin, M. C., and Y. W. Kiang, and H. J. Li, "Experimental discrimination of wire stick targets using multiple frequency amplitude returns," *IEEE Trans. Antennas Propagat.*, Vol. 40, 1036-1040, Sept. 1992.
- 15 Li, H. J., and S. H. Yang, "Using range profiles as feature vectors to identify aerospace objects," *IEEE Trans. Antennas Propagat.*, Vol. 41, 261-268, March 1993.
- 16 Rothwell, E. J., K. M. Chen, D. P. Nyquist, J. E. Ross, and R. Bebermeyer, "A radar target discrimination scheme using the discrete wavelet transform for reduced data storage," *IEEE Trans. Antennas Propagat.*, Vol. 42, No. 7, 1033-1037, July 1994.
- 17 Atkins, R. G., R. T. Shin, and J. A. Kong, "Chapter 7 : A neural network method for high range resolution target classification," *Progress in Electromagnetics Research* 4, J. A. Kong, Ed., Elsevier, New York, 1991.
- 18 Li, H. J., and V. Chiou, "Aerospace target identification-comparison between the matching score approach and the neural network approach," *Journal of Electromagnetic Waves and Applications*, Vol. 7, No. 6, 87-893, 1993.
- 19 John Edwin Ross III, "Chapter 5 transient measurements," Ph.D. Thesis : Application of Transient Electromagnetic Fields to Radar Target Discrimination, 1992.
- 20 Hopfield, J. J., "Neural network and physical systems with emergent collective computational," *Proc. Nat. Acad. Sci. U.S.* Vol. 81, 2554-2558, 1982
- 21 Hopfield, J. J., "Neurons with graded response have collective computational properties like those of two-state neurons," *Proc. Nat. Acad. Sci. U.S.* Vol. 81, 3088-3092, 1984.
- 22 Kamp, Y., and M. Hasler, "Recursive neural networks for associative memory," (John Willy & Sons Ltd.) 1990.
- 23 Hassoun, M. H., "Dynamic associative memories" *Artificial neural networks and stochastic pattern recognition, old and new connections*, 195-218, 1991.
- 24 Chiueh, T. D., and R. M. Goodman, "High-Capacity Exponential Associative Memory" *IEEE Int. Conf. Neural Networks (San Diego, CA)*, Vol. 1 153-160, 1988.
- 25 Chiueh, T. D., and R. M. Goodman, "Recurrent correlation associative memories" *IEEE Trans. on Neural Networks*, Vol. 2 No. 2 275-283, 1991.
- 26 Hertz, J., A. Krogh, and R. G. Palmer, *Introduction to the Theory of Neural Computation*, Addison-Wesley, 1991.
- 27 Kohonen, T., *Self-Organization and Associative Memory*, Springer Verlag, Berlin, 1989.
- 28 Kosko, B., "Bidirectional associative memories," *IEEE Trans. Sys. Man Cybern.*, SMC-18, 49-60, 1988.
- 29 Wang, Y. F., J. B. Cruz, Jr., and J. H. Mulligan, Jr., "Guaranteed recall of all training pairs for bidirectional associative memory" *IEEE Trans. on Neural Networks*, Vol. 2 No. 6 559-567, 1991.
- 30 Schalkoff, R., *Pattern Recognition : Statistical, Structural and Neural Approaches*, John Wiley & Sons, Inc. 1992.
- 31 Carpenter, G., and S. Grossberg, "A massively parallel architecture for a self-organizing neutral pattern recognition machine," *Computer Vision, Graphics, and Image Processing*, Vol. 37, 54-115, 1987.
- 32 Carpenter, G., and S. Grossberg, "ART2 : Self-organization of stable category recognition codes for analog input patterns," *Applied Optics*, Vol. 26, No. 3 4919-4930.



**C. Y. Tsai** was born in Ping-Tung, Taiwan. He received the B.S. degree in Electrical Engineering from the National Central University in Taiwan in 1988, and the M.S. degree in Electrical Engineering from Florida Atlantic University in Boca Raton, Florida, in 1990. In 1992 he came to Michigan State university where he is currently working toward a Ph.D. in Electrical Engineering.

**Edward J. Rothwell** was born in Grand Rapids, MI. He received the B.S. degree in Electrical Engineering from Michigan Technological University in 1979, the M.S. degree in Electrical Engineering and the degree of Electrical Engineer from Stanford University in 1980 and 1982, respectively, and the Ph.D. degree in Electrical Engineering from Michigan State University in 1985, where he held the Dean's Distinguished Fellowship. He worked for Raytheon Co. from 1979-1982, and for MIT Lincoln Laboratory in 1985. He has been at Michigan State University since 1985 first as an Assistant Professor of Electrical Engineering and now as an Associate Professor. He received the first John. D. Withrow award for teaching excellence from the College of Engineering at Michigan State University in 1991. Dr. Rothwell is a Senior Member of the IEEE, and a member of Phi Kappa Phi, Sigma Xi, and Commission B of URSI.

**Kun-Mu Chen** was born in Taipei, Taiwan. He received the B.S. degree in Electrical Engineering from National Taiwan University in 1955, and the M.S. and Ph.D. degrees in Applied Physics from Harvard University in 1958 and 1960, respectively. From 1960 to 1964 he was associated with the Radiation Laboratory at the University of Michigan. In 1964 he joined the faculty of Michigan State University as an Associate Professor, and since 1967 has been a Professor of Electrical Engineering. Dr. Chen is a fellow of IEEE and AAAS. He is the recipient of the Distinguished Faculty Award and Withrow Distinguished Scholar Award from Michigan State University and the Outstanding Achievement Award from the Taiwanese American Foundation.

## Appendix 8

### Time-Domain Imaging of Airborne Targets using Ultra-Wideband or Short-Pulse Radar

E. J. Rothwell, K. M. Chen, D. P. Nyquist, and J. E. Ross

**Abstract**—A time-domain physical optics inverse scattering identity is derived for real-time use in ultra-wideband radar systems. It is shown that using the band-limited impulse response of a radar target provides an edge-enhanced image. A simulation based on stepped-frequency, multi-aspect measurements of aircraft models produces clear images with highly-defined edges.

#### I. INTRODUCTION

Microwave imaging of airborne radar targets has received considerable interest in recent years. Most attention has focused on the use of inverse synthetic aperture radar (ISAR) [1], [2] where the target is modeled as a collection of scattering centers, and the image is constructed from an inverse Fourier transform of multi-aspect, frequency-domain data. The advent of viable ultra-wideband, time-domain radars with a baseband spectrum extending well into the microwave regime [3] precipitates the need of an imaging identity which can be used directly in the time-domain. Several time-domain techniques have been proposed including those using ramp illumination [4], [5] to determine projected area and chirp-FM [6] to determine the target characteristic function. This communication presents a simple time-domain inverse scattering identity, easily derivable from Bojarski's physical optics (PO) technique [7], which provides the target thickness function.

#### II. TIME-DOMAIN IDENTITY

Consider a plane wave of constant amplitude  $E_0$  and polarization  $\hat{e}$  incident upon a perfectly conducting scatterer along an incident wave vector  $\vec{k}^i$ . If  $\vec{E}^s(\vec{k}^i, r)$  is the back-scattered field (monostatic case)

Manuscript received June 2, 1994; revised November 2, 1994. This work was supported in part by the ThermoTrex Corporation, and in part by the Northeast Consortium for Engineering Education, and the Office of Naval Research Grant N00014-93-1-1272.

The authors are with the Department of Electrical Engineering, Michigan State University, East Lansing, MI 48824 USA.

IEEE Log Number 9408998.

at a distance  $r$  in the far zone of the target, then Bojarski [7] shows that the characteristic function of the target is given by

$$\gamma(\vec{r}') = 2\text{Re} \left\{ \frac{1}{(2\pi)^3} \int \int \int_{-\infty}^{\infty} E^s(\vec{K}') e^{j\vec{K}' \cdot \vec{r}'} \frac{d^3 K'}{K^2} \right\} \quad (1)$$

where  $\vec{K}' = 2\vec{k}'$ ,  $K = |\vec{K}'| = 2\omega/c$ , and  $E^s$  is the transmit-polarization component of the phase and range normalized scattered field

$$E^s(\vec{K}') = \hat{e} \cdot \vec{E}^s(\vec{k}', r) \left/ \left[ \frac{E_0}{4\pi} \frac{e^{-jk'r}}{r} \right] \right. \quad (2)$$

Because the characteristic function is unity for all points  $\vec{r}'$  within the domain of the scatterer and zero without,  $\gamma(\vec{r}')$  reproduces the scatterer geometry.

For measurements made in a sectional plane, the thickness of the scatterer in a direction normal to the plane is given by

$$T(\vec{\rho}') = 2\text{Re} \left\{ \frac{1}{(2\pi)^2} \int \int_{-\infty}^{\infty} E^s(K'_x, K'_y, 0) e^{j\vec{K}' \cdot \vec{\rho}'} \frac{d^2 K'}{K^2} \right\} \quad (3)$$

where  $\vec{\rho}'$  is the position vector in the sectional ( $u, v$ ) plane. To convert this identity into time-domain form, a polar-coordinate representation is used (analogous to the projection-slice theorem of tomographic reconstruction [8])

$$T(\vec{\rho}') = 2\text{Re} \left\{ \frac{1}{(2\pi)^2} \int_{\phi_i=0}^{2\pi} \int_{k=0}^{\infty} E^s(k, \phi_i) e^{-j2k\rho' \cos(\phi' - \phi_i)} \frac{dk}{k} d\phi_i \right\} \quad (4)$$

where  $\phi_i$  is the incidence angle in the sectional plane, and  $(\rho', \phi')$  is the position of a point in polar coordinates in the sectional plane. Substituting for  $E^s$  from (2) gives

$$T(\vec{\rho}') = \frac{2}{\pi} \int_{\phi_i=0}^{2\pi} \text{Re} \left\{ \int_0^{\infty} F(\omega) e^{j\omega\tau} d\omega \right\} d\phi_i \quad (5)$$

where

$$F(\omega) = \rho \frac{\hat{e} \cdot \vec{E}^s}{\omega E_0} \quad (6)$$

and

$$\tau = \frac{\rho}{c} - 2 \frac{\rho'}{c} \cos(\phi' - \phi_i). \quad (7)$$

Since the thickness function must be real, the inner integral is recognized as a temporal Fourier transform [9] and thus the thickness function can be written as

$$T(\rho') = \int_0^{2\pi} f\{[\rho - 2\rho' \cos(\phi' - \phi_i)]/c\} d\phi_i \quad (8)$$

where  $f(t)$  is the inverse Fourier transform of  $F(\omega)$ .

The thickness function (8) is seen to be a superposition over incidence angle of values of the waveform  $f(t)$ . Because of the  $\omega$  in the denominator of  $F(\omega)$ , the appropriate waveform to use for reconstructing the target thickness is the step response (or a related function). The time at which the waveform is evaluated is the two-way transit time to the point  $(\rho', \phi')$  along the angle  $\phi_i$ , and is thus consistent with the scattering-center interpretation used in ISAR.

Note that an identity equivalent to (8) can be obtained directly in the time domain by beginning with the formula for the projected area [4] as a function of aspect angle, and using the inverse radon transform [11] and the physical-optics approximation.

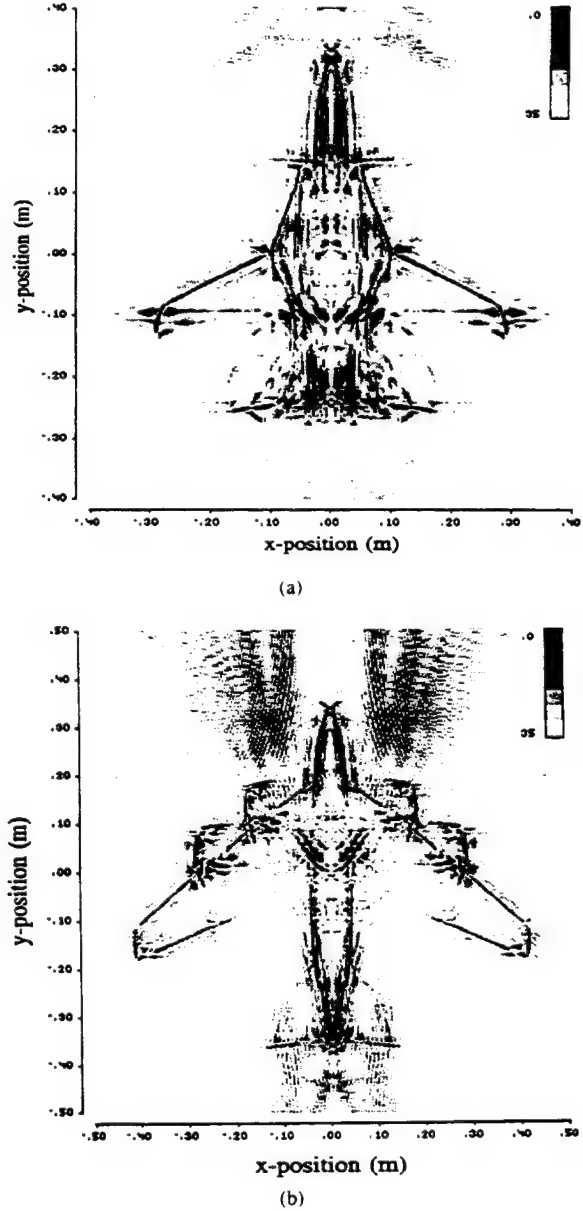


Fig. 1. Images of aircraft models created from measured data using the time-domain physical optics inverse scattering identity. (a) 1 : 32 scale F-14. (b) 1 : 72 scale B-52.

### III. IMAGING SIMULATION

The time-domain identity (8) can be used in real time to construct an image from ultra-wideband radar measurements. A simulation of time-domain imaging is carried out using data measured in the Michigan State University free-field scattering range. The field scattered from several aircraft models was measured in the plane of the aircraft wings in the frequency band 2–18 GHz at 200 aspect angles from 0 degrees (nose-on) to 180 degrees, using an HP 8720B network analyzer. The data from the nonilluminated side was provided through symmetry. Each scattered field response was deconvolved using a 14-inch diameter sphere as a reference target and inverse transformed into the time domain using the FFT to provide a band-limited impulse response [10]. Rather than forming the step response, the measured impulse response data was used directly in (8). This is equivalent to using a derivative of the step response, and thus a sharpening of the target edges is provided—a technique common to image processing [8].

Fig. 1 shows the images of a 1 : 32 scale model F-14 aircraft and a 1 : 72 scale model B-52 aircraft. The edges of the aircraft are clearly visible, with the fuselage and vertical stabilizers producing the largest thickness values, as expected. There is some distortion in the aircraft shapes due to a slightly bistatic antenna arrangement and an inaccurate estimate of target range. Note that the PO approximation used to derive (8) does not include information about shadowing, and thus shadowed edges, such as the rear of the F-14 wing and the inner sides of the B-52 engines, are not clearly visible. Note also that images can be obtained using data from a restricted range of aspect angles (e.g., 0–90°), albeit of reduced fidelity.

## REFERENCES

- [1] M. Soumekh, *Fourier Array Imaging*. Englewood Cliffs, NJ: Prentice-Hall, 1994.
- [2] G. Dural and D. L. Moffatt, "ISAR imaging to identify basic scattering mechanisms," *IEEE Trans. Antennas Propagat.*, vol. 42, no. 1, pp. 99–110, Jan. 1994.
- [3] C. Phillips, P. Johnson, K. Garner, G. Smith, A. Shek, R. C. Chou, and S. Leong, "Ultra-high-resolution radar development and test," in *Second Int. Conf. Ultra-Wideband, Short-Pulse Electromagn.*, New York, Apr. 5–7, 1994.
- [4] C. L. Bennett, "Time domain inverse scattering," *IEEE Trans. Antennas Propagat.*, vol. AP-29, no. 2, pp. 213–219, Mar. 1981.
- [5] W.-M. Boerner, C.-M. Ho, and B.-Y. Foo, "Use of Radon's projection theory in electromagnetic inverse scattering," *IEEE Trans. Antennas Propagat.*, vol. AP-29, no. 2, pp. 336–341, Mar. 1981.
- [6] C. K. Chan and N. H. Farhat, "Frequency swept tomographic imaging of three-dimensional perfectly conducting objects," *IEEE Trans. Antennas Propagat.*, vol. AP-29, no. 2, pp. 312–319, Mar. 1981.
- [7] N. N. Bojarski, "A survey of the physical optics inverse scattering identity," *IEEE Trans. Antennas Propagat.*, vol. AP-30, no. 5, pp. 980–989, 1982.
- [8] J. S. Lim, *Two-Dimensional Signal and Image Processing*. Englewood Cliffs, NJ: Prentice-Hall, 1990.
- [9] A. Papoulis, *The Fourier Integral and Its Applications*. New York: McGraw-Hill, 1962.
- [10] J. E. Ross, "Application of transient electromagnetic fields to radar target discrimination," Ph.D. dissertation, Michigan State Univ., E. Lansing, MI, 1992.
- [11] Y. Das and W.-M. Boerner, "On radar target shape estimation using algorithm for reconstruction from projections," *IEEE Trans. Antennas Propagat.*, vol. AP-26, no. 2, pp. 274–279, Feb. 1982.

## Appendix 9

# Time-Domain Imaging of Radar Targets Using Short Pulse Radars and Algorithms for Reconstruction from Projections

Y. Dai, E.J. Rothwell, *senior Member, IEEE*,  
K.M. Chen, *Fellow, IEEE*, D.P. Nyquist, *Senior Member, IEEE*

**Abstract**-A time-domain bistatic inverse scattering identity based on the Radon transform and the space-time magnetic integral equation is derived for real-time use in short pulse radar systems. It is shown that using a Sine-Modulated Exponential Pulse (SMEP) and algorithms for reconstruction from projections provides an edge-enhanced image. A simulation based on stepped-frequency, multi-aspect measurements of aircraft models produces clear images with highly-defined edges. Images using data from a restricted range of aspect angles are also demonstrated.

---

The authors are with the Department of Electrical Engineering, Michigan state University, East Lansing, MI 48824 USA.

This work was supported by the Office of Naval Research under Grant N00014-93-1271.

## I. Introduction

Target imaging and identification using electromagnetic responses in the time and frequency domains has attracted increasing interests, with most methods carried out in the frequency domain. The use of time domain techniques was first discussed by Kennaugh and Cosgroff in 1957 [1]. Since then many researchers have developed approaches to the inverse scattering problem [2-7]. They have shown that the target impulse, step, and ramp responses are related to the target geometry based on physical optics principles. Under the physical optics approximation Bojarski has established a Fourier transform relationship between the conducting scatterer and a form of the scattering cross section [9]. Since this approach is based on the physical optics approximation, it is valid only in the limit of high frequency. When the size of the scatterer is comparable to the incident pulsewidth, the physical optics solution is inadequate for this scattering problem. Furthermore, the impulse, step, or ramp response of the target is hard to obtain in practice.

In this paper we start from the space-time magnetic field integral equation, and by using a Sine-Modulated Exponential Pulse (SMEP) waveform as the incident field, an exact two-dimensional time-domain bistatic inverse scattering identity can be obtained based on the inverse Radon transform. The details are carried out in section III. In section IV, the reconstruction algorithm is developed and discussed. Numerical verification is carried out for a test sphere in section V. Experimental results and some images of aircraft models are shown in section VI.

## II. The Radon Transform

The Radon transform of a function at a given hyperplane is defined as the integral of the function over that hyperplane [6-8]. For a hyperplane in  $n$ -dimensional Euclidean space defined by

$$\hat{\xi} \cdot \bar{x} = p \quad (1)$$

where  $\bar{x}$  is the spatial position vector,  $\hat{\xi}$  is a unit vector orthogonal to the hyperplane, and  $p$  is the Euclidean distance from the origin, the Radon transform  $F(\hat{\xi}, p)$  of a function  $f(\bar{x})$  over the hyperplane is given by

$$F(\hat{\xi}, p) = \int_{\hat{\xi} \cdot \bar{x} = p} f(\bar{x}) ds \quad (2)$$

The above equation may be expressed more conveniently in the following form by using the Dirac delta function  $\delta$ :

$$F(\hat{\xi}, p) = \int f(\bar{x}) \delta(p - \hat{\xi} \cdot \bar{x}) d\bar{x} \quad (3)$$

The inversion of the Radon transform consists of expressing  $f(\bar{x})$  in terms of its integrals  $F(\hat{\xi}, p)$  over the hyperplanes. The inversion formula for odd dimension in  $n$  is

$$f(\bar{x}) = \frac{1}{2(2\pi j)^{n-1}} \int_{|\hat{\xi}|=1} F_p^{(n-1)}(\hat{\xi}, \hat{\xi} \cdot \bar{x}) d\hat{\xi} \quad (4)$$

where  $F_p^{(n-1)}$  is the  $(n-1)$ th derivative of  $F$  with respect to  $p$ . For even  $n$ , the inversion formula is

$$f(\bar{x}) = \frac{j}{2(2\pi j)^{n-1}} \int_{|\hat{\xi}|=1} H F_p^{(n-1)}(\hat{\xi}, \hat{\xi} \cdot \bar{x}) d\hat{\xi} \quad (5)$$

where  $H$  denotes Hilbert transform.

Radon transform theory has become a very important mathematical operation and its applications are well known. They include computerized tomography (CT) applications in, for example, diagnostic medicine, radio astronomy, electron microscopy, optical interferometry, and geophysical exploration. These well-established concepts can be extended and applied to the radar inverse scattering problem.

### III. Derivation of Space-time Integral Equations and Inverse Scattering Identity

When an electromagnetic field is incident upon an object, currents and charges are induced on and in the object. The induced currents and charges will then maintain a scattered electromagnetic field. Once the induced currents flowing on the conducting scatterer surface and the scatterer geometry are given, the scattered field can be calculated directly.

The expression for the surface currents is derived from an expression for the total field at an arbitrary point in space [4]. This arbitrary point is specialized to a point on the scatterer surface, and the appropriate boundary conditions are applied. This yields an equation for the surface current  $\vec{J}$  at the point  $\vec{r}$  on the scatterer surface and at the time  $t$  as

$$\vec{J}(\vec{r}, t) = \begin{cases} 2\hat{n} \times \vec{h}^i(\vec{r}, t) + \vec{J}_c(\vec{r}, t) & \hat{n} \cdot \vec{q} > 0 \\ \vec{J}_c(\vec{r}, t) & \hat{n} \cdot \vec{q} < 0 \end{cases} \quad (6)$$

where

$$\vec{J}_c(\vec{r}, t) = \frac{1}{2\pi} \int_s \hat{n} \times \left\{ \left[ \frac{1}{R^2} + \frac{1}{R} \frac{\partial}{\partial \tau} \right] \vec{J}(\vec{r}', \tau) \times \hat{a}_R \right\} ds \quad (7)$$

where  $\vec{h}^i(\vec{r}, t)$  is the incident magnetic field,  $\hat{n}$  is the unit vector normal to the scatterer surface,



$\vec{r}$  is the position vector to the observation point,  $\vec{r}'$  is the position vector to the integration point,  $R = |\vec{r} - \vec{r}'|$ ,  $\hat{a}_R = (\vec{r} - \vec{r}')/R$ ,  $\hat{q}$  is the unit vector to the transmitting antenna, and  $t$  denotes normalized time in meters.

From equation (6), we can see that the first term of the right-hand side represents the direct influence of the incident field on the current at the observation point. When applied to the illuminated side of the scatterer, it yields the familiar physical optics approximation for the surface current. The second term on the right-hand side of (6) represents the influence of currents at other surface points on the current at the observation point.

Once the surface current density has been obtained, the far scattered field of the scatterer shown in Figure 1 can be calculated by the expression

$$\vec{h}^s(\vec{r}_s, t) = \frac{1}{4\pi} \left[ \nabla \times \int_S \frac{\vec{J}(\vec{r}', \tau')}{R_s} ds' \right] \quad (8)$$

Where

$$R_s = |\vec{r}_s - \vec{r}'|, \text{ and } \tau' = t - R_s$$

Assuming that the observation point  $\vec{r}_s$  is not on S, the curl operator may be carried inside the integral. Using the far-field approximations and standard vector identities, we have

$$\begin{aligned} \vec{h}^s(\vec{r}_s, t) &= \frac{1}{4\pi} \int_S \left[ \frac{\partial \vec{J}(\vec{r}', \tau')}{\partial \tau'} \times \frac{\vec{R}_s}{R_s^2} + \vec{J}(\vec{r}', \tau') \times \frac{\vec{R}_s}{R_s^3} \right] ds' \\ &\approx -\frac{1}{4\pi R_s} \int_S \hat{R}_s \times \frac{\partial \vec{J}(\vec{r}', \tau')}{\partial \tau'} ds' \end{aligned} \quad (9)$$

where

$$\hat{R}_s = (\vec{r}_s - \vec{r}')/|\vec{r}_s - \vec{r}'|$$

In the far zone, we can use the approximations  $R_s \approx r_s - \hat{r}_s \cdot \bar{r}'$  for the phase term and

$R_s \approx r_s$  and  $\hat{R}_s \approx \hat{r}_s$  for the amplitude term. Then (9) becomes

$$\bar{h}^s(\bar{r}_s, t) = -\frac{1}{4\pi r_s} \int_s \hat{r}_s \times \frac{\partial \bar{J}(\bar{r}', \tau')}{\partial \tau'} ds' \quad (10)$$

Now, we define the aperture function

$$A(\hat{r}_i, \hat{n}) = \begin{cases} 1 & \hat{r}_i \cdot \hat{n}(\bar{r}') > 0 \\ 0 & \hat{r}_i \cdot \hat{n}(\bar{r}') < 0 \end{cases} \quad (11)$$

which is unity on the illuminated region of scatterer surface, and zero on the shadow region.

Substituting (6) into (10), we have

$$\bar{h}^s(\bar{r}_s, t) = -\frac{1}{2\pi r_s} \int_s \hat{r}_s \times \hat{n}' \times \frac{\partial \bar{h}^i(\bar{r}', \tau)}{\partial \tau} A(\hat{r}_i, \hat{n}) ds' - \frac{1}{4\pi r_s} \int_s \hat{r}_s \times \frac{\partial \bar{J}_c(\bar{r}', \tau')}{\partial \tau'} ds' \quad (12)$$

where  $\tau = t - R_i - R_s \approx t - r_i - r_s + (\hat{r}_i + \hat{r}_s) \cdot \bar{r}'$ ,  $\tau' = t - R_s \approx t - r_s + \hat{r}_s \cdot \bar{r}'$

Using the vector identity

$$\hat{r}_s \times (\hat{n}' \times \hat{h}^i) = \hat{n}' (\hat{r}_s \cdot \hat{h}^i) - \hat{h}^i (\hat{r}_s \cdot \hat{n}') \quad (13)$$

and letting  $h^s(\bar{r}_s, t) = \hat{h}^i \cdot \bar{h}^s(\bar{r}_s, t)$ , then

$$\begin{aligned} \hat{h}^i \cdot (\hat{r}_s \times \hat{n}' \times \hat{h}^i) &= \hat{n}' \cdot [(\hat{r}_s \cdot \hat{h}^i) \hat{h}^i - \hat{r}_s] \\ &= -\hat{n}' \cdot \bar{K} \end{aligned} \quad (14)$$

where

$$\bar{K} = \hat{r}_s - (\hat{r}_s \cdot \hat{h}^i) \hat{h}^i$$

Then (12) can be written as

$$h^s(\vec{r}_s, t) = \frac{1}{2\pi r_s} \int_s \hat{n}' \cdot \vec{K} \frac{\partial h^i(\vec{r}', \tau)}{\partial \tau} A(\hat{r}_i, \hat{n}) ds' - \frac{1}{4\pi r_s} \left[ \int_s \hat{r}_s \times \frac{\partial \vec{J}_c(\vec{r}', \tau')}{\partial \tau'} ds' \right] \cdot \hat{h}^i \quad (15)$$

Now, letting the same incident pulse illuminate the shadow region of the scatterer, we have

$$h_2^s(\vec{r}_s, t) = \frac{1}{2\pi r_s} \int_s \hat{n}' \cdot \vec{K} \frac{\partial h^i(\vec{r}', \tau)}{\partial \tau} A_2(\hat{r}_i, \hat{n}) ds' - \frac{1}{4\pi r_s} \left[ \int_s \hat{r}_s \times \frac{\partial \vec{J}_{c2}(\vec{r}', \tau')}{\partial \tau'} ds' \right] \cdot \hat{h}^i \quad (16)$$

Combining (15) and (16) yields

$$\begin{aligned} h^s(\vec{r}_s, t) + h_2^s(\vec{r}_s, t) &= \frac{1}{2\pi r_s} \int_s \hat{n}' \cdot \vec{K} \frac{\partial h^i(\vec{r}', \tau)}{\partial \tau} [A(\hat{r}_i, \hat{n}) + A_2(\hat{r}_i, \hat{n})] ds' - h_{c1}^s(\vec{r}_s, t) - h_{c2}^s(\vec{r}_s, t) \\ &= \frac{1}{2\pi r_s} \int_s \hat{n}' \cdot \vec{K} \frac{\partial h^i(\vec{r}', \tau)}{\partial \tau} ds' - h_{c1}^s(\vec{r}_s, t) - h_{c2}^s(\vec{r}_s, t) \end{aligned} \quad (17)$$

where

$$\begin{aligned} h_{c1}^s(\vec{r}_s, t) &= \frac{1}{4\pi r_s} \left[ \int_s \hat{r}_s \times \frac{\partial \vec{J}_c(\vec{r}', \tau')}{\partial \tau'} ds' \right] \cdot \hat{h}^i \\ h_{c2}^s(\vec{r}_s, t) &= \frac{1}{4\pi r_s} \left[ \int_s \hat{r}_s \times \frac{\partial \vec{J}_{c2}(\vec{r}', \tau')}{\partial \tau'} ds' \right] \cdot \hat{h}^i \end{aligned} \quad (18)$$

Using Gauss' law, (17) becomes

$$\begin{aligned} h^s(\vec{r}_s, t) + h_2^s(\vec{r}_s, t) &= \frac{1}{2\pi r_s} \int_V \nabla' \cdot \left[ \vec{K} \frac{\partial h^i(\vec{r}', \tau)}{\partial \tau} \right] dv' - h_{c1}^s(\vec{r}_s, t) - h_{c2}^s(\vec{r}_s, t) \\ &= \frac{1}{2\pi r_s} \int_V \vec{K} \cdot \frac{\partial}{\partial \tau} \nabla' h^i(\vec{r}', t - r_i - r_s + (\hat{r}_i + \hat{r}_s) \cdot \vec{r}') dv' - h_{c1}^s(\vec{r}_s, t) - h_{c2}^s(\vec{r}_s, t) \\ &= \frac{1}{\pi r_s} \int_V (\vec{K} \cdot \hat{r}) \cos \frac{\beta}{2} \frac{\partial^2 h^i(\vec{r}, \tau)}{\partial^2 \tau} dv' - h_{c1}^s(\vec{r}_s, t) - h_{c2}^s(\vec{r}_s, t) \end{aligned} \quad (19)$$

where

$$\hat{r}_i + \hat{r}_s = 2 \cos \frac{\beta}{2} \hat{r}. \quad \beta \text{ is the bistatic angle}$$

Assuming the incident magnetic field is a SMEP defined by

$$h^i(t) = \sin(\omega_c t) e^{-\alpha t} U(t) \quad (20)$$

the derivative of  $h(t)$  is

$$\frac{\partial h^i(t)}{\partial t} = [\omega_c \cos(\omega_c t) - \alpha \sin(\omega_c t)] e^{-\alpha t} U(t) \quad (21)$$

and the second derivative of  $h(t)$  is

$$\frac{d^2 h^i(t)}{d^2 t} = [(\alpha^2 - \omega_c^2) \sin(\omega_c t) - 2\alpha \omega_c \cos(\omega_c t)] e^{-\alpha t} U(t) + \omega_c \delta(t) \quad (22)$$

Now, let's write equation (19) in the forms

$$\int_V \frac{\partial^2 h^i(\vec{r}', \tau)}{\partial \tau^2} dV' = \frac{\pi r_s}{(\vec{K} \cdot \vec{r}) \cos(\beta/2)} [h^s(\vec{r}_s, t) + h_2^s(\vec{r}_s, t) + h_{c1}^s(\vec{r}_s, t) + h_{c2}^s(\vec{r}_s, t)] = \frac{\pi r_s}{(\vec{K} \cdot \vec{r}) \cos(\beta/2)} H^s(\vec{r}_s, t) \quad (23)$$

where

$$H^s(\vec{r}_s, t) = h^s(\vec{r}_s, t) + h_2^s(\vec{r}_s, t) + h_{c1}^s(\vec{r}_s, t) + h_{c2}^s(\vec{r}_s, t)$$

The left hand side of equation (23) can be written as

$$\int_V \frac{\partial^2 h^i(\vec{r}', \tau)}{\partial \tau^2} dV' = \frac{\partial}{\partial t} \int_V \frac{\partial h^i(\vec{r}', \tau)}{\partial \tau} dV' = \frac{\partial^2}{\partial t^2} \int_V h^i(\vec{r}', \tau) dV' \quad (24)$$

Then, we can obtain two equations from (23) and (24):

$$\begin{aligned} \int_V \frac{\partial h^i(\vec{r}', \tau)}{\partial \tau} dV' &= \frac{\pi r_s}{(\vec{K} \cdot \vec{r}) \cos(\beta/2)} \int_0^t H^s(\vec{r}_s, t) dt + \left[ \int_V \frac{\partial h^i(\vec{r}', \tau)}{\partial \tau} dV' \right]_{t=0} \\ &= \frac{\pi r_s}{(\vec{K} \cdot \vec{r}) \cos(\beta/2)} \int_0^t H^s(\vec{r}_s, t) dt \end{aligned} \quad (25)$$

and

$$\begin{aligned}\int_V h'(\bar{r}', \tau) dv' &= \frac{\pi r_s}{(\bar{K} \cdot \bar{r}) \cos(\beta/2)} \int_0^t \int_0^t H^s(\bar{r}_s, t) dt^2 + \int_0^t \left[ \int_V \frac{\partial h'(\bar{r}', \tau)}{\partial \tau} dv' \right]_{t=0} dt + \left[ \int_V h'(\bar{r}', \tau) dv' \right]_{t=0} \\ &= \frac{\pi r_s}{(\bar{K} \cdot \bar{r}) \cos(\beta/2)} \int_0^t \int_0^t H^s(\bar{r}_s, t) dt^2\end{aligned}\quad (26)$$

Substituting (20) into (26), we have

$$\int_V \sin(\omega_c \tau) e^{-\alpha \tau} U(\tau) dv' = \frac{\pi r_s}{(\bar{K} \cdot \bar{r}) \cos(\beta/2)} \int_0^t \int_0^t H^s(\bar{r}_s, t) dt^2 \quad (27)$$

Substituting (21) into (25), we have

$$\int_V [\omega_c \cos(\omega_c \tau) - \alpha \sin(\omega_c \tau)] e^{-\alpha \tau} U(\tau) dv' = \frac{\pi r_s}{(\bar{K} \cdot \bar{r}) \cos(\beta/2)} \int_0^t H^s(\bar{r}_s, t) dt \quad (28)$$

Substituting (22) into (23), we get

$$\int_V \delta(\tau) dv' = \frac{\pi r_s}{(\bar{K} \cdot \bar{r}) \omega_c \cos(\beta/2)} H^s(\bar{r}_s, t) - \int_V \frac{1}{\omega_c} [(\alpha^2 - \omega_c^2) \sin \omega_c \tau - 2\alpha \omega_c \cos \omega_c \tau] e^{-\alpha \tau} U(\tau) dv' \quad (29)$$

Combining (27) and (28) then yields

$$\int_V \omega_c \cos(\omega_c \tau) e^{-\alpha \tau} U(\tau) dv' = \frac{\pi r_s}{(\bar{K} \cdot \bar{r}) \cos(\beta/2)} \left[ \int_0^t H^s(\bar{r}_s, t) dt + \alpha \int_0^t \int_0^t H^s(\bar{r}_s, t) dt^2 \right] \quad (30)$$

Substituting (27) and (30) into (29), we have

$$\int_V \delta(\tau) dv' = \frac{\pi r_s}{(\bar{K} \cdot \bar{r}) \cos(\beta/2) \omega_c} \left[ H^s(\bar{r}_s, t) + 2\alpha \int_0^t H^s(\bar{r}_s, t) dt + (\omega_c^2 + \alpha^2) \int_0^t \int_0^t H^s(\bar{r}_s, t) dt^2 \right] \quad (31)$$

Now, define the characteristic function

$$\gamma(\bar{r}') = \begin{cases} 1 & \bar{r}' \in V \\ 0 & \bar{r}' \notin V \end{cases} \quad (32)$$

Then (31) becomes

$$\int_{-\infty}^{\infty} \int_{-\infty}^{\infty} \gamma(\vec{r}') \delta(t - r_i - r_s - 2\cos(\frac{\beta}{2}) \hat{r} \cdot \vec{r}') dv' = \frac{\pi r_s}{\vec{K} \cdot \hat{r} \cos(\beta/2) \omega_c} \left[ H^s(\vec{r}_s, t) - 2\alpha \int_0^t H^s(\vec{r}_s, t) dt + (\omega_c^2 - \alpha^2) \int_0^t \int_0^t H^s(\vec{r}_s, t) dt^2 \right] \quad (33)$$

Using the properties of the Delta function

$$\begin{aligned} \delta(\tau) &= \delta(-\tau) \\ \delta(2\cos(\frac{\beta}{2})\tau) &= \frac{1}{2\cos(\beta/2)} \delta(\tau) \end{aligned} \quad (34)$$

(33) becomes

$$\int_{-\infty}^{\infty} \int_{-\infty}^{\infty} \gamma(\vec{r}') \delta(t_s - \hat{r} \cdot \vec{r}') dv' = \frac{2\pi r_s}{\vec{K} \cdot \hat{r} \omega_c} \left[ H^s(\vec{r}_s, t) + 2\alpha \int_0^t H^s(\vec{r}_s, t) dt + (\omega_c^2 + \alpha^2) \int_0^t \int_0^t H^s(\vec{r}_s, t) dt^2 \right] \quad (35)$$

Where

$$t_s = \frac{r_i + r_s - t}{2\cos(\beta/2)}$$

It can be seen from equation (35) and Figure 2 that the right hand side of (35) is the Radon transform of  $\gamma(\vec{r}')$  [6], [7], [8]. It denotes the projected area function at the plane

$$t_s = \hat{r} \cdot \vec{r}'$$

$$A(\hat{r}, t_s) = \int_{-\infty}^{\infty} \int_{-\infty}^{\infty} \gamma(\vec{r}') \delta(t_s - \hat{r} \cdot \vec{r}') dv' \quad (36)$$

Here  $A(\hat{r}, t_s)$  is the projected area onto  $t_s$  for the particular aspect direction  $\hat{r}$  along  $t_s$ .

Note that the cross sectional area  $A(\hat{r}, t_s)$  is formed with a time scale such that the cutting plane  $t_s = \hat{r} \cdot \vec{r}'$  used to determine  $A(\hat{r}, t_s)$  moves with  $1/(2\cos(\beta/2))$  (one half for the monostatic case) the velocity of the incident SMEP.

If the view angles are available only in the  $x-y$  plane ( $\theta' = \pi/2$ ,  $0 \leq \phi' \leq 2\pi$ ), then the body geometry can be related to the cross-sectional areas  $A(\hat{r}, t_s)$  through

$$A(\hat{r}, t_s) = \int_{-\infty}^{\infty} \int_{-\infty}^{\infty} \gamma(x', y', z') \delta(t_s - (x' \cos \phi' + y' \sin \phi')) dx' dy' dz' \quad (37)$$

Integrating with respect to  $z$ , (37) becomes

$$A(\hat{r}, t_s) = \int_{-\infty}^{\infty} \int_{-\infty}^{\infty} \Gamma(x', y') \delta(t_s - (x' \cos \phi' + y' \sin \phi')) dx' dy' \quad (38)$$

Where  $\Gamma(x, y) = \int_{-\infty}^{\infty} \gamma(x, y, z) dz$  is the "thickness function" of the target in the  $z$  direction.

Taking the two-dimensional inverse Radon transform of equation (38), we can get the thickness function [6-8].

$$\begin{aligned} \Gamma(\bar{\rho}') &= -\frac{1}{4\pi^2} \int_0^{2\pi} \int_{-\infty}^{\infty} \frac{\partial A(\hat{r}, t_s)}{\partial t_s} \frac{dt_s d\phi}{t_s - \rho' \cos(\phi' - \phi)} \\ &= -\frac{1}{4\pi^2} \int_0^{2\pi} \left[ \frac{A(\hat{r}, t_s)}{t_s - \rho' \cos(\phi' - \phi)} \right]_{-\infty}^{\infty} + \int_{-\infty}^{\infty} \frac{A(\hat{r}, t_s)}{(t_s - \rho' \cos(\phi' - \phi))^2} dt_s \Big] d\phi \\ &= -\frac{1}{2\pi^2} \int_0^{\pi} \int_{-\infty}^{\infty} \frac{A(\hat{r}, t_s)}{(t_s - \rho' \cos(\phi' - \phi))^2} dt_s d\phi \\ &= -\frac{1}{\pi^2} \int_0^{\pi} \int_{-\infty}^{\infty} \frac{\cos(\beta/2) A(\hat{r}, t_s)}{(t - \rho_{is} + 2\rho' \cos(\beta/2) \cos(\phi' - \phi))^2} dt d\phi \end{aligned} \quad (39)$$

where  $\bar{\rho}' = x' \hat{x} + y' \hat{y} = \rho' \cos \phi' \hat{x} + \rho' \sin \phi' \hat{y}$ ,  $\rho_{is} = \rho_i + \rho_s$

Substituting (35) into (39), we have

$$\Gamma(\bar{\rho}) = -\frac{2\rho_s \cos(\beta/2)}{(\bar{K} \cdot \hat{\rho}) \pi \omega_c} \int_0^\pi \int_{-\infty}^\infty \frac{H^s(\bar{\rho}_s, t) - 2\alpha \int_0^t H^s(\bar{\rho}_s, t) dt + (\omega_c^2 + \alpha^2) \int_0^t \int_0^t H^s(\bar{\rho}_s, t) dt^2}{[t - \rho_{is} - 2\rho' \cos(\beta/2) \cos(\phi' - \phi)]^2} dt d\phi \quad (40)$$

From equation (40), we know  $\phi$  depends on  $\phi'$ ,  $\phi^s$  and  $\beta$ . Here we only consider the special case when both transmitting and receiving antennas are fixed and the target rotating or the scatterer is static and the transmitting and receiving antennas are moving around the scatterer with bistatic angle  $\phi' - \phi^s = \text{constant } \beta$ . Then

$$\begin{aligned} 2\cos\left(\frac{\beta}{2}\right) \hat{\rho} \cdot \bar{\rho}' &= 2\rho' \cos\left(\frac{\beta}{2}\right) \cos(\phi' - \phi) \\ &= 2\rho' \cos\left(\frac{\beta}{2}\right) \cos(\phi' - \phi' + \frac{\beta}{2}) \end{aligned} \quad (41)$$

and from (40), we have

$$\begin{aligned} \Gamma(\bar{\rho}') &= -\frac{2\rho_s \cos(\beta/2)}{(\bar{K} \cdot \hat{\rho}) \pi \omega_c} \int_{\beta/2}^{\pi - \beta/2} \int_{-\infty}^\infty \frac{H^s(\bar{\rho}_s', t) + 2\alpha \int_0^t H^s(\bar{\rho}_s', t) dt + (\omega_c^2 + \alpha^2) \int_0^t \int_0^t H^s(\bar{\rho}_s', t) dt^2}{[t - \rho_{is} + 2\rho' \cos(\beta/2) \cos(\phi' - \phi' + \beta/2)]^2} dt d\phi' \\ &= -\frac{2\rho_s \cos(\beta/2)}{(\bar{K} \cdot \hat{\rho}) \pi \omega_c} \int_0^\pi \int_{-\infty}^\infty \frac{H^s(\bar{\rho}_s', t) + 2\alpha \int_0^t H^s(\bar{\rho}_s', t) dt + (\omega_c^2 + \alpha^2) \int_0^t \int_0^t H^s(\bar{\rho}_s', t) dt^2}{[t - \rho_{is} + 2\rho' \cos(\beta/2) \cos(\phi' - \phi' + \beta/2)]^2} dt d\phi' \end{aligned} \quad (42)$$

This is the complete solution to the two-dimensional bistatic problem of recovering a body from its scattered field: it needs the reflected fields and the correction term from all possible directions in the x-y plane. The next step is to solve equation (42). We can use an iterative approach to get the 2-dimensional target geometry [4]. First, neglect the correction terms  $h_{c1}^s(\bar{\rho}', t)$  and  $h_{c2}^s(\bar{\rho}', t)$  in equation (42). This is the time domain physical optics inverse problem. We can thus obtain an initial estimate of  $\Gamma_1(\bar{\rho})$ , and the correction terms,  $h_{c1}^s(\bar{\rho}', t)$  and  $h_{c2}^s(\bar{\rho}', t)$ , in (42)



can be obtained by solving  $\bar{J}_c(\bar{r}, t)$ ,  $\bar{J}_{c2}(\bar{r}, t)$  in (6) using the marching on in time method, and then used in (18). Then the correction terms can be used in (42) to obtain a new estimate of  $\Gamma_2(\bar{\rho})$ . Then  $\Gamma_1(\bar{\rho})$  and  $\Gamma_2(\bar{\rho})$  can be compared to see if the change is less than some small number, and the procedure continued until this convergence criterion is satisfied. The numerical results for a sphere of 14 inch radius using those procedures will be shown in section V.

Note that from (23) we can see when the incident magnetic field is a ramp, use physical optics approximation by dropping the correction terms, and using  $\beta=0$ ,  $\bar{K} \cdot \hat{r}=1$  for the monostatic case, then the backscattered ramp response is proportional to the cross-sectional area of the target as a function of the distance along the line of incident direction [10]. This is the same result which Kennaugh, Cosgriff, and Moffatt had obtained [1], [2]. Das and Boerner [7] have shown that the size and shape of an object can be obtained from its area functions, and the problem can be reduced to the classical Radon problem.

#### IV. Reconstruction algorithm

The basic idea of reconstruction of an image from a series of its projections appears to have been first discussed by Radon [11]. The techniques that exist for reconstruction fall into two directions. The whole operation can be done in frequency space directly, or the equivalent of these expressions can be transformed in the spatial domain. Whether implemented in the spatial domain or in the frequency domain, the reconstruction algorithms can be conveniently interpreted

by means of a straightforward and interesting theorem, which is the projection-slice theorem. This theorem states that the Fourier transform of a projection is a center-cross-section of the Fourier transform of the projected object. Most of the modern tomographic systems are based on this theorem.

The algorithm that is currently being used in almost all applications of straight ray tomography is the filtered backprojection algorithm. It has been shown to be extremely accurate and amenable to fast implementation. We will extend this approach to our radar inversion problems.

Let's start with the thickness function  $\Gamma(\bar{\rho}')$ . It can be written as

$$\Gamma(\bar{\rho}') = -\frac{1}{2\pi^2} \int_0^\pi \int_{-\infty}^\infty \frac{f(\bar{\rho}', t) dt d\phi^i}{[t - \rho_{is} + 2\rho' \cos(\beta/2) \cos(\phi' - \phi^i + \beta/2)]^2} \quad (43)$$

where

$$f(\bar{\rho}', t) = \frac{4\rho_s \cos(\beta/2)}{(\bar{K} \cdot \bar{\rho}) \omega_c} \left[ H^s(\bar{\rho}', t) + 2\alpha \int_0^t H^s(\bar{\rho}', t) dt + (\omega_c^2 + \alpha^2) \int_0^t \int_0^t H^s(\bar{\rho}', t) dt^2 \right] \quad (44)$$

From equation (43), we know that the inner integral is the convolution of  $f(\rho_{is} - 2\rho' \cos(\beta/2) \cos(\phi' - \phi^i + \beta/2))$  and  $1/[\rho_{is} - 2\rho' \cos(\beta/2) \cos(\phi' - \phi^i + \beta/2)]^2$ . Equation (43) thus can be written as

$$\Gamma(\bar{\rho}') = \int_0^\pi \int_{-\infty}^\infty \frac{1}{2\pi} |\omega| F(\omega) \exp[j\omega(\rho_{is} - 2\rho' \cos(\frac{\beta}{2}) \cos(\phi' - \phi^i + \frac{\beta}{2}))] d\omega d\phi^i \quad (45)$$

Since the Fourier transform of  $1/[\rho_{is} - 2\rho' \cos(\beta/2) \cos(\phi' - \phi^i + \beta/2)]^2$  is  $-\pi |\omega|$ , and the

Fourier transform of  $f(\rho_{is} - \rho' \cos(\beta/2) \cos(\phi' - \phi^i + \beta/2))$  is  $F(\omega)$ , and the convolution is the Fourier transform of a product. We can see from equation (45) that the inner integral represents a filtering operation, where the frequency response of the filter is given by  $|\omega|$ . Therefore the inner integral part is called a "filtered projection". The resulting projections for different angles are then added to form the estimate of  $\Gamma(\bar{\rho}')$ .

When the projections are bandlimited by the highest frequency  $B$ , the projection data are collected at the Nyquist frequency, with a sampling interval of  $a = 1/(2B)$ . Equation (45) may be expressed as

$$\Gamma(\bar{\rho}') = \int_0^\pi \int_{-\infty}^{\infty} Q(\omega) F(\omega) \exp[j\omega(\rho_{is} - 2\rho' \cos(\beta/2) \cos(\phi' - \phi^i + \beta/2))] d\omega d\phi^i \quad (46)$$

where

$$Q(\omega) = \frac{1}{2\pi} |\omega| \text{rect}(\omega) \quad (47)$$

and

$$\text{rect}(\omega) = \begin{cases} 1 & |\omega| < 2\pi B \\ 0 & \text{otherwise} \end{cases} \quad (48)$$

$Q(\omega)$ , shown in Figure 3, represents the transfer function of a filter with which the projections must be processed. The impulse response,  $q(t)$ , of this filter is given by the inverse Fourier transform of  $Q(\omega)$  and is

$$\begin{aligned} q(t) &= \frac{1}{2\pi} \int_{-\infty}^{\infty} \frac{1}{2\pi} |\omega| \text{rect}(\omega) \exp(j\omega t) d\omega \\ &= 2B^2 \text{sinc}(2\pi Bt) - B^2 \text{sinc}^2(\pi Bt) \end{aligned} \quad (49)$$

This function is shown in Figure 4. Since the projection data are measured with a

sampling interval of  $1/(2B)$ , for digital processing the impulse response needs only be known with the same sampling interval. The samples,  $q(n)$ , of  $q(t)$  are given by

$$q(n) = \begin{cases} \frac{1}{4a^2} & n=0 \\ 0 & n=even \\ -\frac{1}{\pi^2 n^2 a^2} & n=odd \end{cases} \quad (50)$$

This filter was first discussed by Ramachandran and Lakshminarayanan [12]. We can replace integrals in (43) by sums and obtain the approximate reconstruction formula given by

$$\Gamma(x,y) = \frac{a}{2N} \sum_{l=0}^{N-1} \sum_{k=-\infty}^{\infty} f(\phi^l, t_k) q(t_k - \rho_{is} + 2\rho' \cos(\beta/2) \cos(\phi' - \phi^l + \beta/2)) \quad (51)$$

where there are  $N$  angles  $\phi^l$  for which the scattered fields are known

## V. Numerical Results and Images for Metal Sphere

A metal sphere is the simplest target which can be used to validate the formulas developed in the previous sections. We use SMEP as the incident magnetic field pulse. Figure 5 shows the theoretical SMEP generated by taking  $\alpha=8 \times 10^9$  and  $f_c=10GHz$  in (20) and the synthesized SMEP using the frequency band 4-16GHz. Both figures have been moved to right by 1 ns. The spectrum of the synthesized SMEP is shown in Figure 6. Figure 7 shows far-zone scattered field of a 14 inch sphere computed by using the Mie series and the marching on in time method, respectively. The cross-sectional areas obtained using equation (35) is shown in Figure

8. Note in Figure 8 that the cross-sectional area  $A(\hat{r}, t_s)$  is plotted with a time scale such that the cutting plane  $t_s = \hat{r} \cdot \vec{r}'$  used to determine  $A(\hat{r}, t_s)$  moves with  $1/(2\cos(\beta/2))$  (one half for the monostatic case) the velocity of the incident SMEP. Figure 9 shows the images of the sphere using the time domain identity (51) with the PO approximation. Figure 10 shows the image of the same sphere when the correction terms are considered. We can see that the correction term provides only a small contribution to the reconstruction.

## VI. Experimental Results and Images for Aircraft

The time-domain identity (51) can be used in real time to construct an image from short pulse radar measurements. A simulation of time-domain imaging is carried out using data measured in the Michigan State University free-field scattering range. The field scattered from several aircraft models was measured in the plane of the aircraft wings in the frequency band 4-16GHz at 200 aspect angles from 0° (nose-on) to 180°, using an HP8720B network analyzer. The bistatic angle is  $\beta=10^\circ$ . The data from the non-illuminated side was provided through symmetry. Each scattered field response was first calibrated using a 14 inch diameter sphere as a reference target, multiplied by the SMEP window, and then inverse transformed into the time-domain using the FFT to provide a SMEP response. The data we used are the derivative of the measured SMEP response data, and thus a sharpening of the target edges is provided.

Two different frequency truncated SMEPs haven been used in our radar target imaging. Figures 11, 12 and 13 show the images of a 1:48 scale model TR-1 aircraft, a 1:32 scale model

F-14 aircraft and a 1:72 scale model B-52 aircraft, respectively, using the synthesized SMEP shown in Figure 5. The edges of the aircraft are clearly visible, with the fuselage and vertical stabilizers producing the largest thickness values, as expected. There is some distortion in the aircraft shapes due to the use of PO approximation and an inaccurate estimate of target range. The image obtained using data from the restricted range of aspect angles  $0-90^\circ$  is shown in figure 14. It can be seen that the shadowed edges of the target are invisible due to the limited view-angles and use of the physical optics approximation. Figure 15 shows another theoretical SMEP generated by taking  $\alpha=4\times 10^9$  and  $f_c=10GHz$  in (20) and the synthesized SMEP for the frequency band 7-13GHz. Again, both figures have been moved to right by 1 ns. Figure 16 shows the spectrum of the synthesized SMEP. Figure 17 shows the image of the same 1:72 scale model B-52 aircraft by using the second SMEP. We can see that the edges of the aircraft are not as clear as in Figure 13 because the pulsewidth is bigger than that of the first SMEP. We can improve the quality of the picture by adding a proper window to the SMEP response data in time-domain. This window is formed by two steps. First, the biggest points in each SMEP response data are found by comparing the values of the data; these biggest points actually are the responses from the scattering centers of the target. Then the values in a small range around the biggest point are set to unity and to 0.5 within the two next biggest point ranges. Note that different data sets have different windows. Figure 18 is a SMEP response data before windowing, the window produced based on Figure 18 is shown in figure 19. Figure 20 is the SMEP response data after windowing. The image of the same B52 aircraft model by using windowed data is shown in figure 21. By using windowing we have increased the resolution of the SMEP and obtained clear images with highly-defined edges.

## VII. Conclusions

A time-domain approach to the inverse scattering problem has been provided and demonstrated. In this approach, starting with the exact space-time magnetic integral equation, and by using Radon's theory and a SMEP as the incident pulse, we obtained the complete inverse scattering identity which considers both illuminated and shadowed range contributions. The reconstruction algorithm based on the projection theory and the inverse scattering identity was developed. By using SMEP response data and the reconstruction algorithm, we have obtained very good images of several aircraft models. This approach is more practical than methods using impulse, step, or ramp responses of the target since the SMEP can be directly transmitted in time-domain. Ways to obtain quality images using limited viewing aperture and frequency bandwidth data will be investigated in the future.

## References

- [1] E. M. Kennaugh and R. L. Cosgriff, "The use of impulse response in electromagnetic scattering problem," *IRE National Convention Record*, part I, PP 72-77, 1958.
- [2] E. M. Kennaugh and D. L. Moffatt, "Transient and impulse response approximations", *Proc. IEEE*, vol. 53, pp.893-901, Aug. 1965.
- [3] J. D. Young, "Radar imaging from ramp response signatures", *IEEE Trans. Antennas Propagat.* vol AP-24 no. 3, pp.276-282, May 1976.
- [4] C. L. Bennett, "Time domain inverse scattering", *IEEE Trans. Antennas propagat.* vol. AP-29, no. 2, pp.213-219, Mar. 1981.
- [5] E. J. Rothwell, K. M. Chen, D. P. Nyquist, J. E. Ross, "Time domain imaging of airborne targets using ultra-wideband or short-pulse radar", *IEEE Trans. Antennas propagat.* vol. AP-43, no. 3, pp.327-329, Mar. 1995.
- [6] D. Ludwig, "The Radon transform on Euclidean spaces", *Comm. Pure and Applied Math.*, vol. XIX, pp.49-81, 1966.
- [7] Y. Das and W. M. Boerner, "On radar target shape estimation using algorithm for reconstruction from projections", *IEEE Trans. Antennas Propagat.*, vol AP-26, no. 2, pp.274-279, Feb. 1978.
- [8] S. R. Deans, *The Radon transform and some of its applications*. John Wiley & Sons, 1983.
- [9] N. N. Bojarski, "A survey of the physical optics inverse scattering identity", *IEEE Trans. Antennas Propagation*, vol. AP-30, No. 5, September 1982.
- [10] Y. Dai, E.J. Rothwell, D.P. Nyquist and K.M. Chen, "Time-domain imaging of radar targets using ultra-wideband or short pulse radars", *IEEE AP-S International Symposium and URSI Radio Science Meeting*, 1995.
- [11] J. Radon, "On the Determination of Function from their Integrals Along certain Manifolds", *Ber. Saechs. Akad. Wiss. Leipzig, Math. Physics Kl.*, vol. 69, pp. 262-277, 1917.
- [12] G. N. Ramachandran and A. V. lakshminarayanan, "Three dimensional reconstruction from radiographic and electron micrographic application of convolutions instead of Fourier transforms," *Proc. Nat.Acad. Sci. U.S.*, vol.68, pp. 21-24,1974.



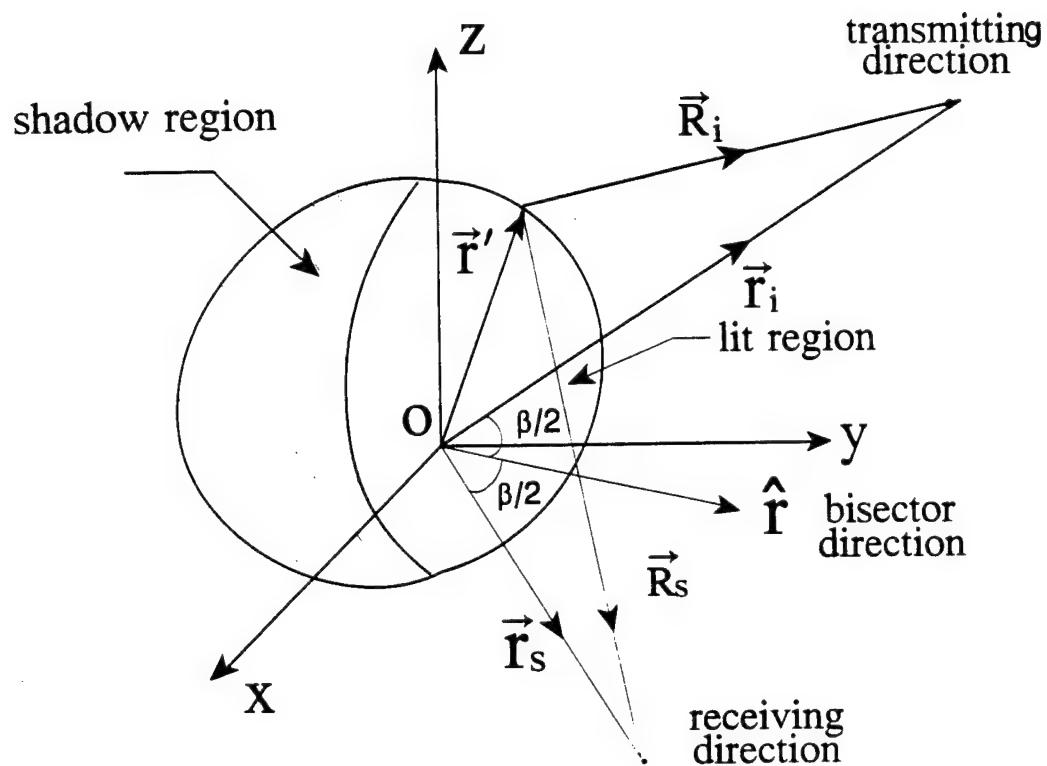


**Figure 1** Geometry of the scatterer and graphic view of space parameters.

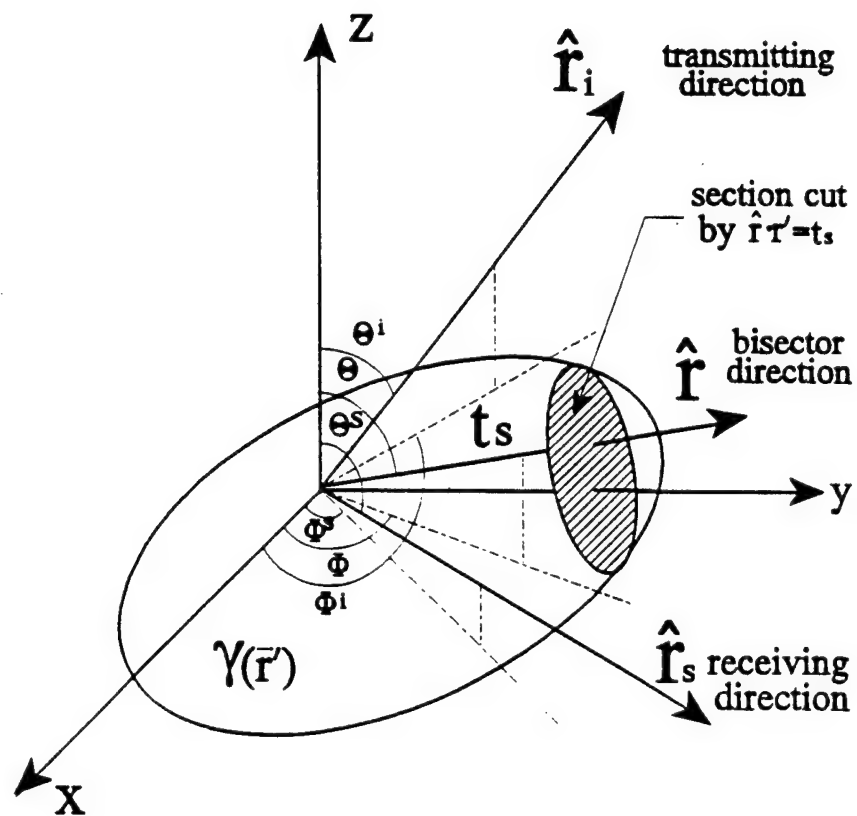


**Figure 2** Geometry of 3-D body reconstruction problem

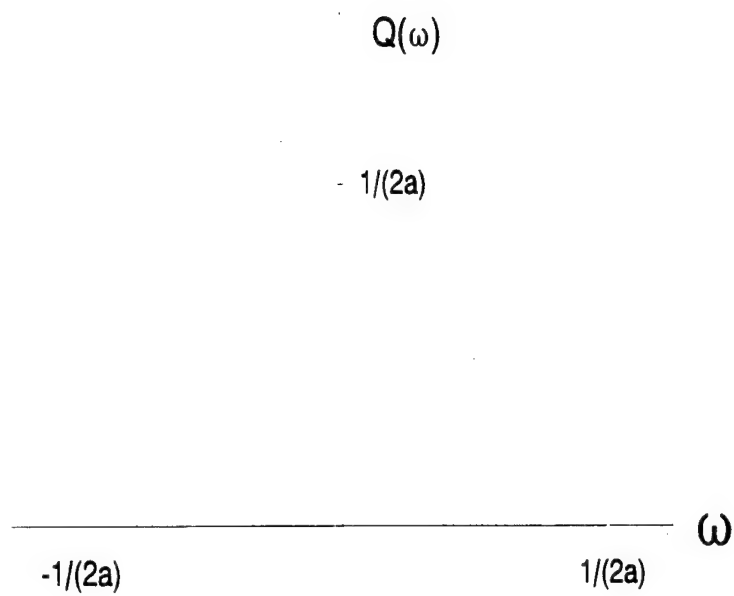


**Figure 3** The filter response for the filtered backprojection algorithm. It has been bandlimited to  $1/2a$ .

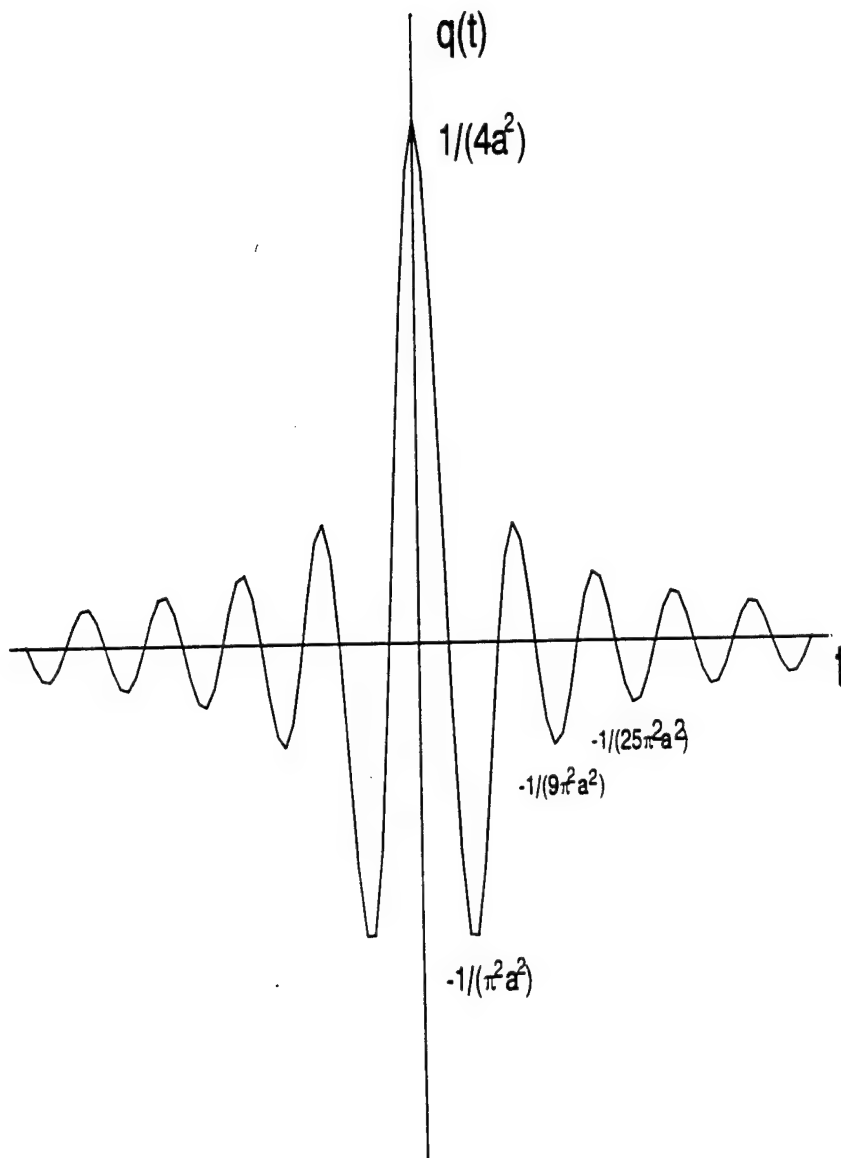


**Figure 4** The impulse response of the filter shown in Figure 3.

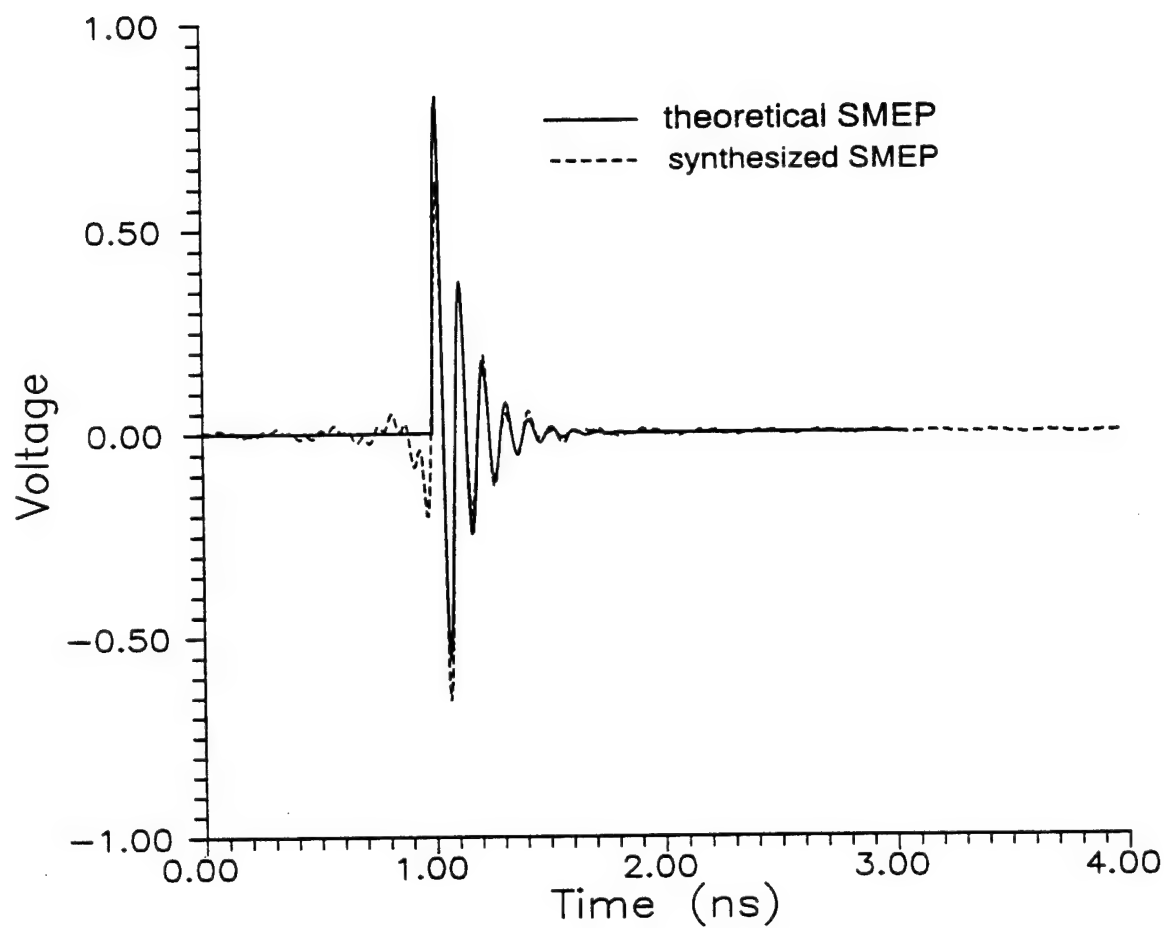


**Figure 5** Comparison of theoretical ( $\alpha=8 \times 10^9$ ,  $f_c=10\text{GHz}$  in (20)) and synthesized (4-16GHz) SMEP. Both figures have been moved to the right by 1 ns.

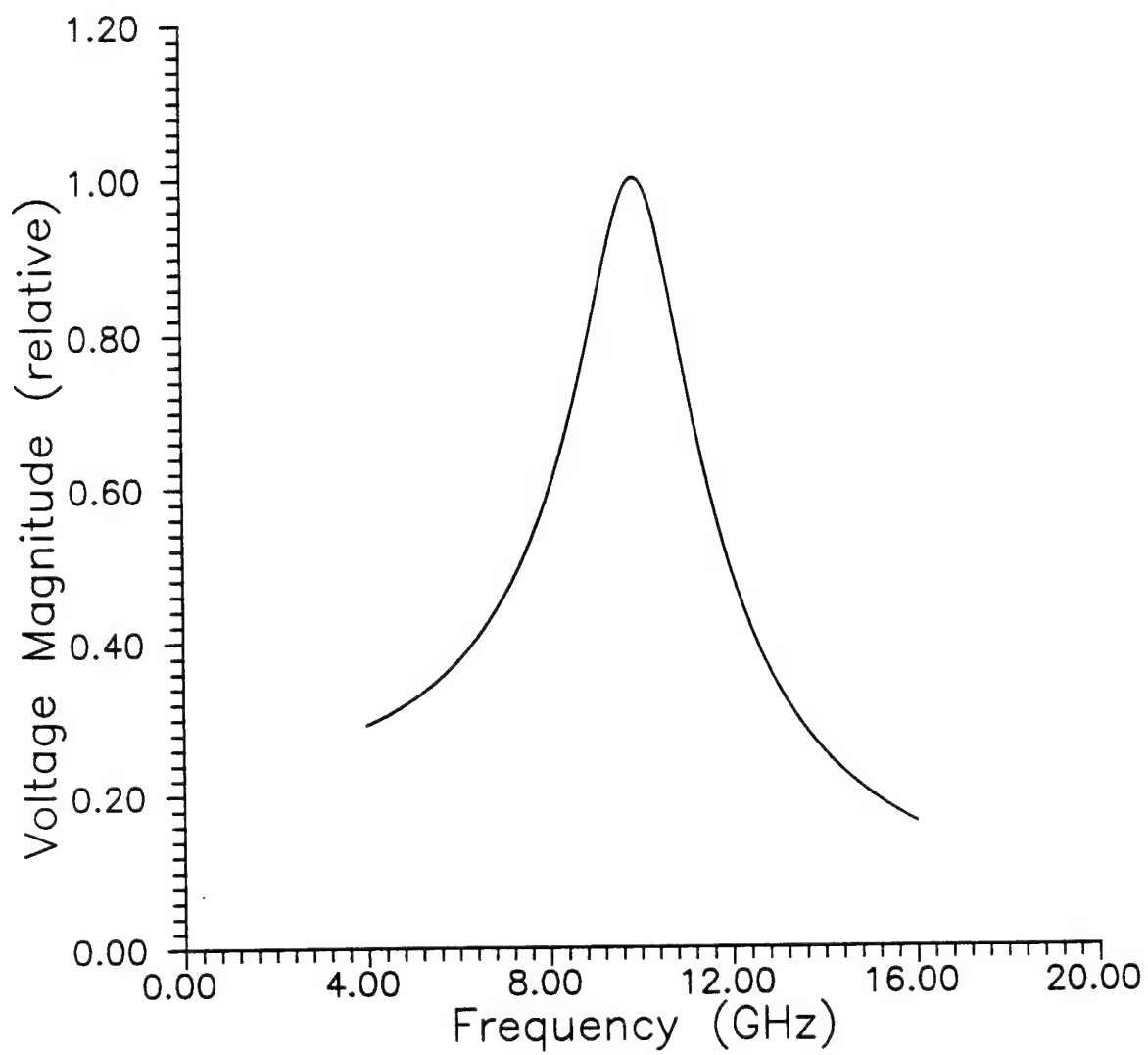


**Figure 6** Synthesized SMEP spectrum.

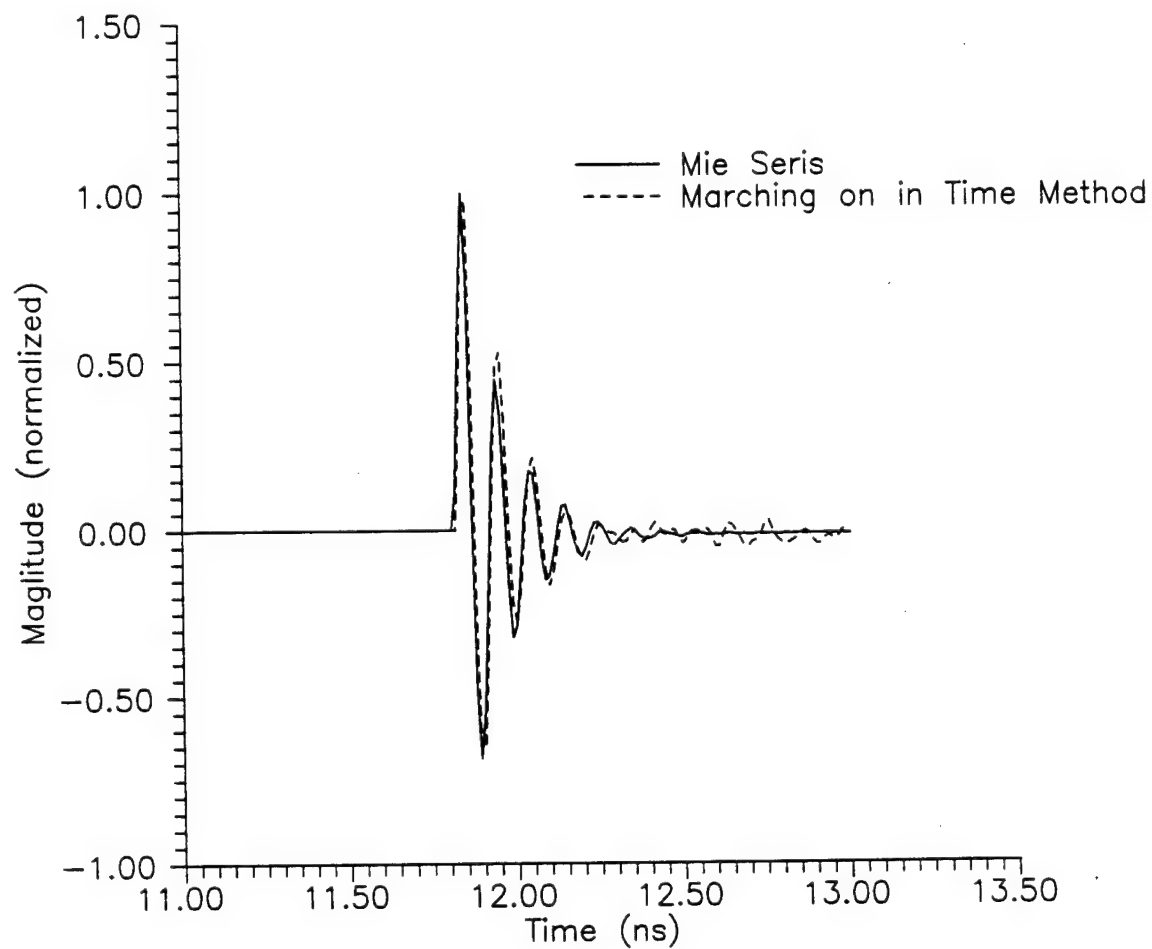


**Figure 7** Far-zone SMEP scatter field of a 14 inch sphere

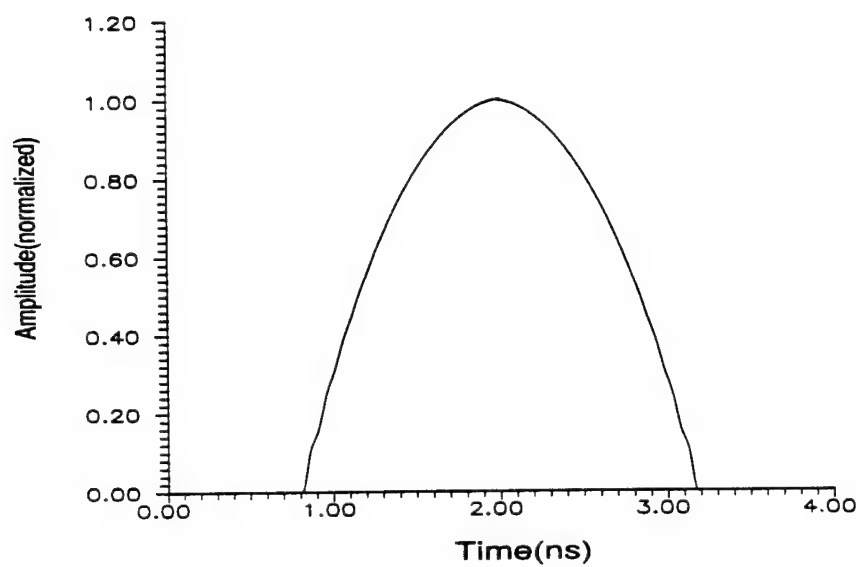


**Figure 8** Cross-sectional area function of a sphere 14 inches in diameter



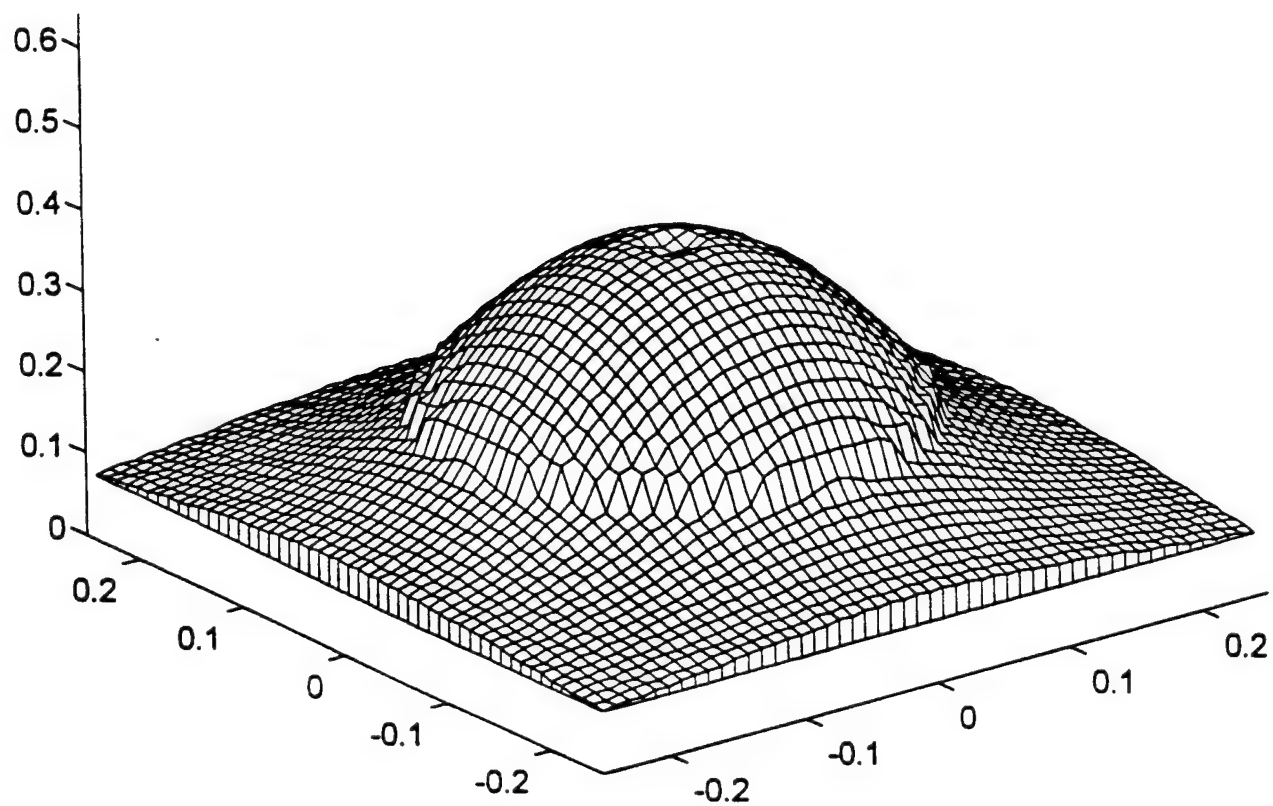


**Figure 9**      Upper surface image of the 14 inch diameter sphere using PO approximation.

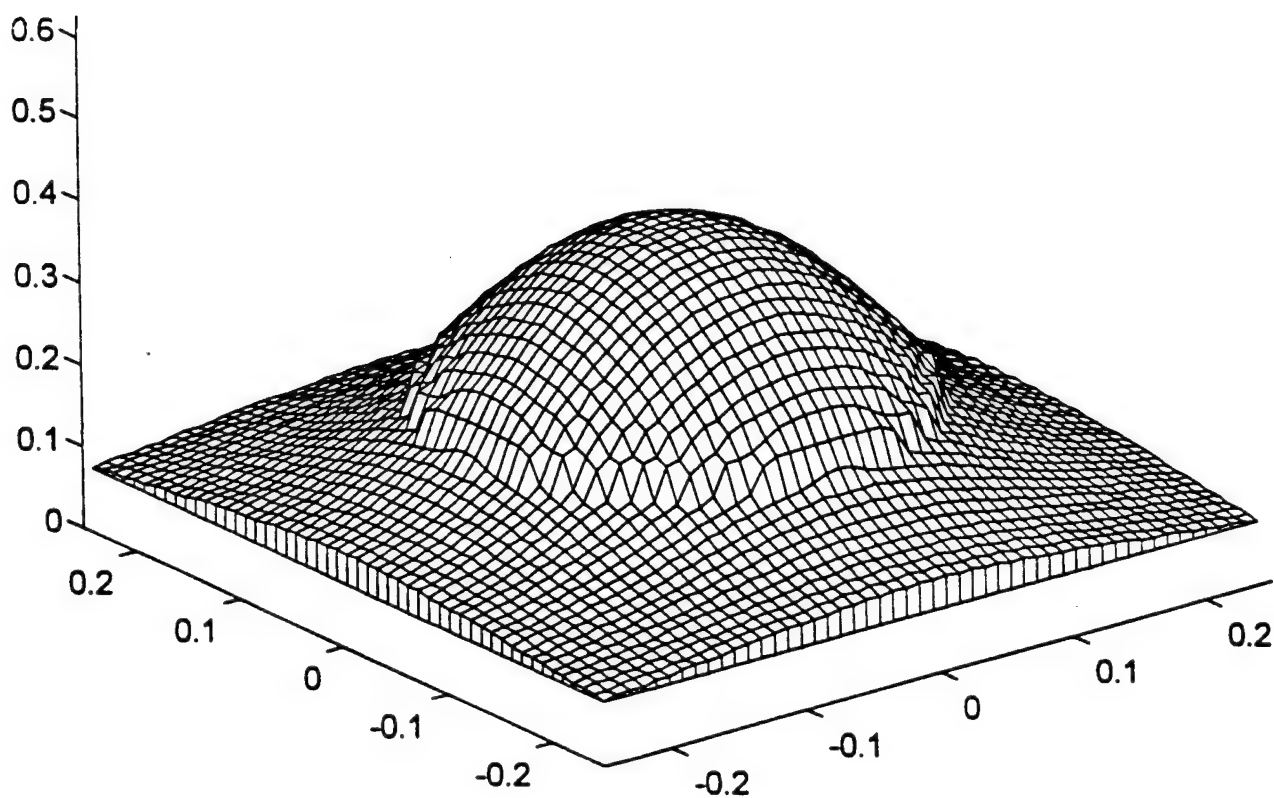


**Figure 10**      Upper surface image of the 14 inch diameter sphere considering the correction terms.

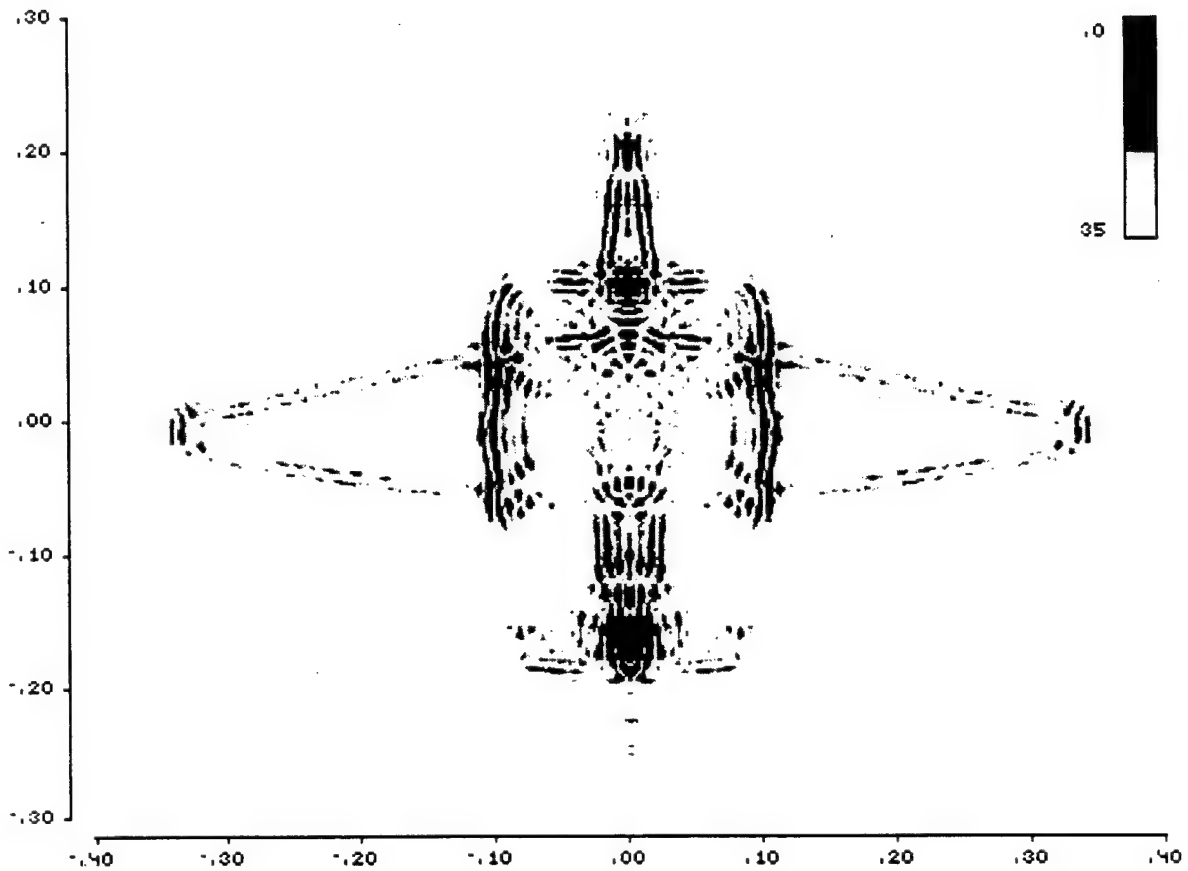


**Figure 11** Image of TR-1 from 0°-180° data in band 4-16 GHz

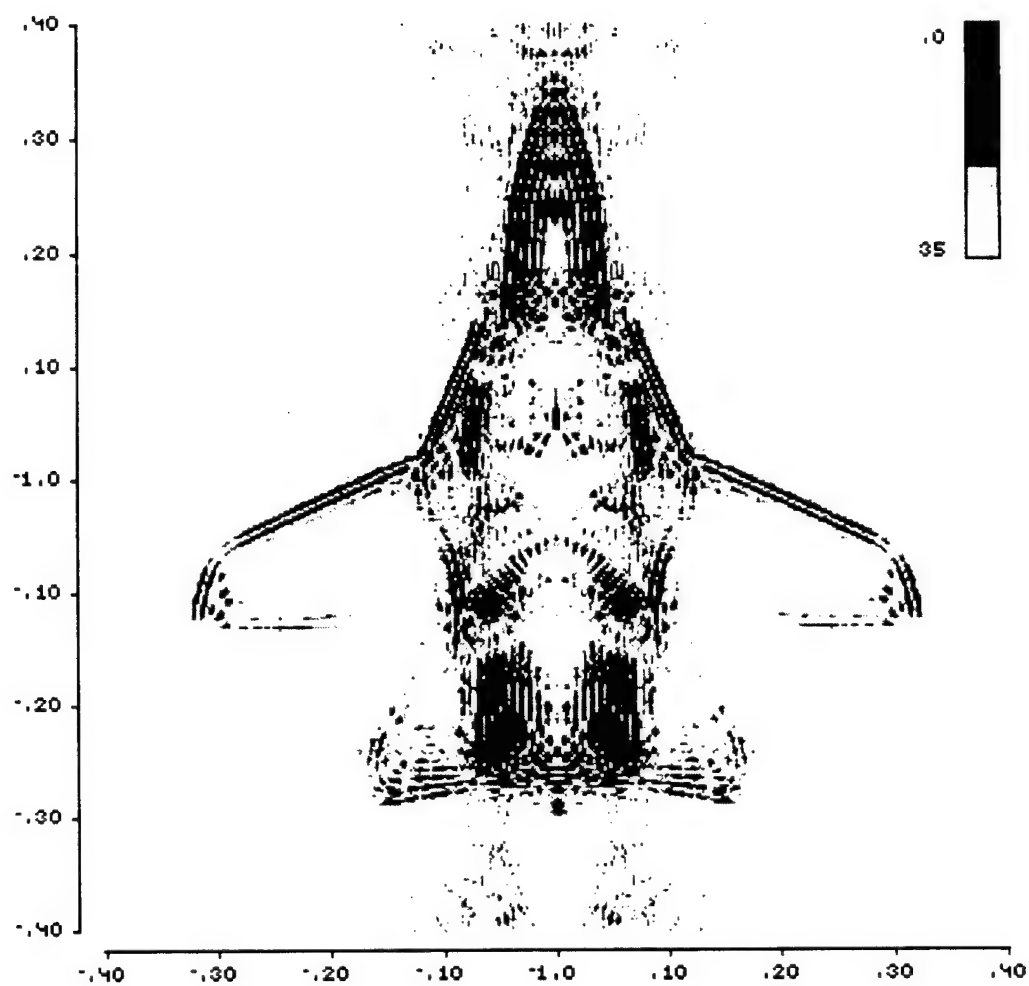


**Figure 12** Image of F-14 from 0°-180° data in band 4-16 GHz.

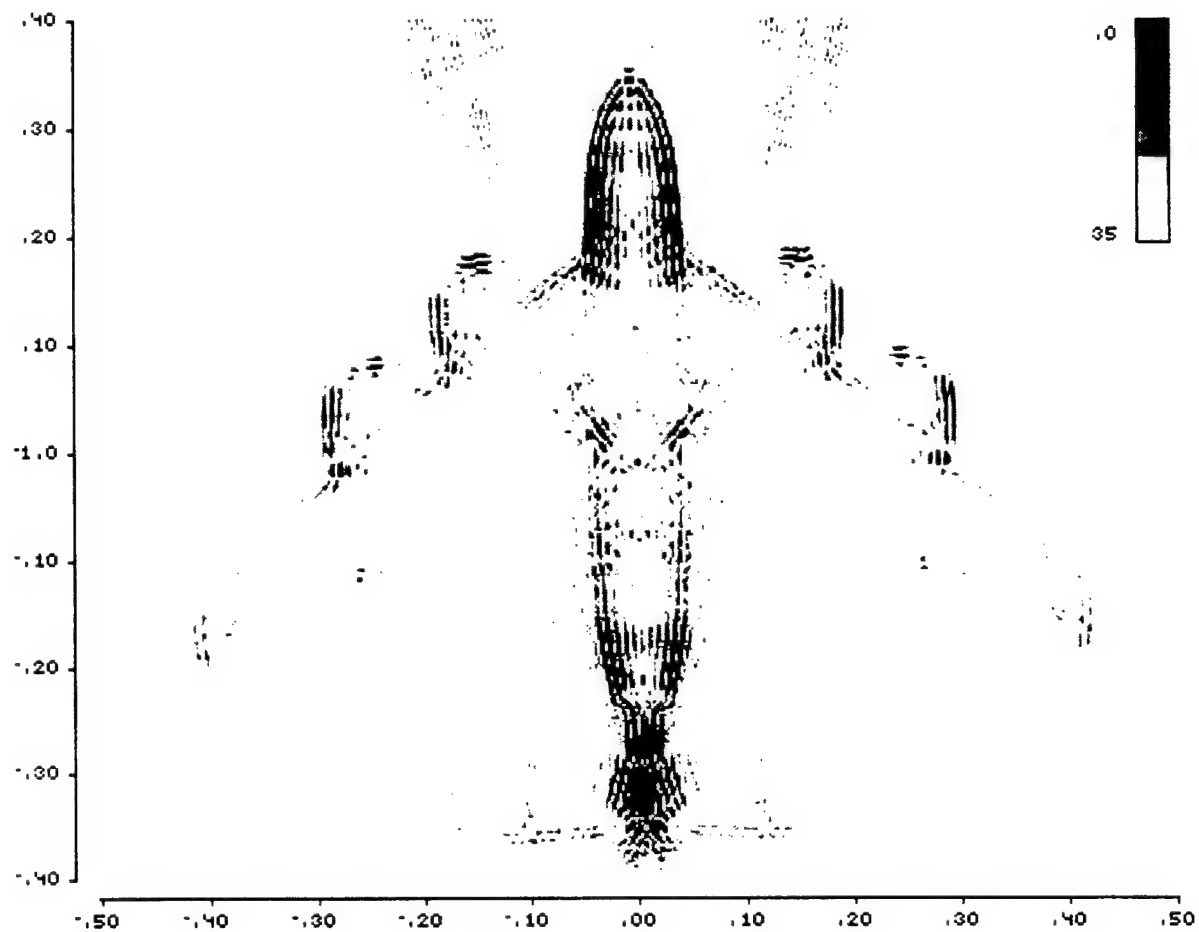
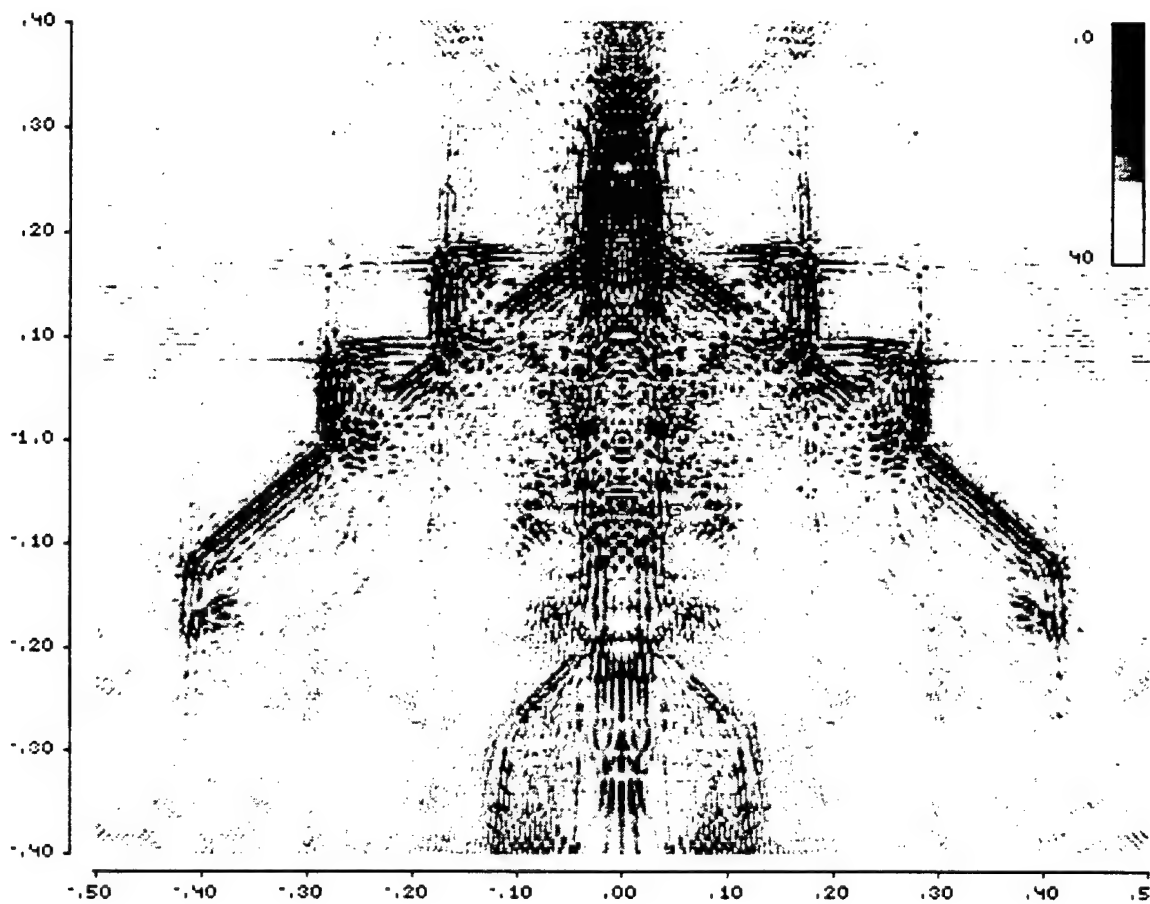
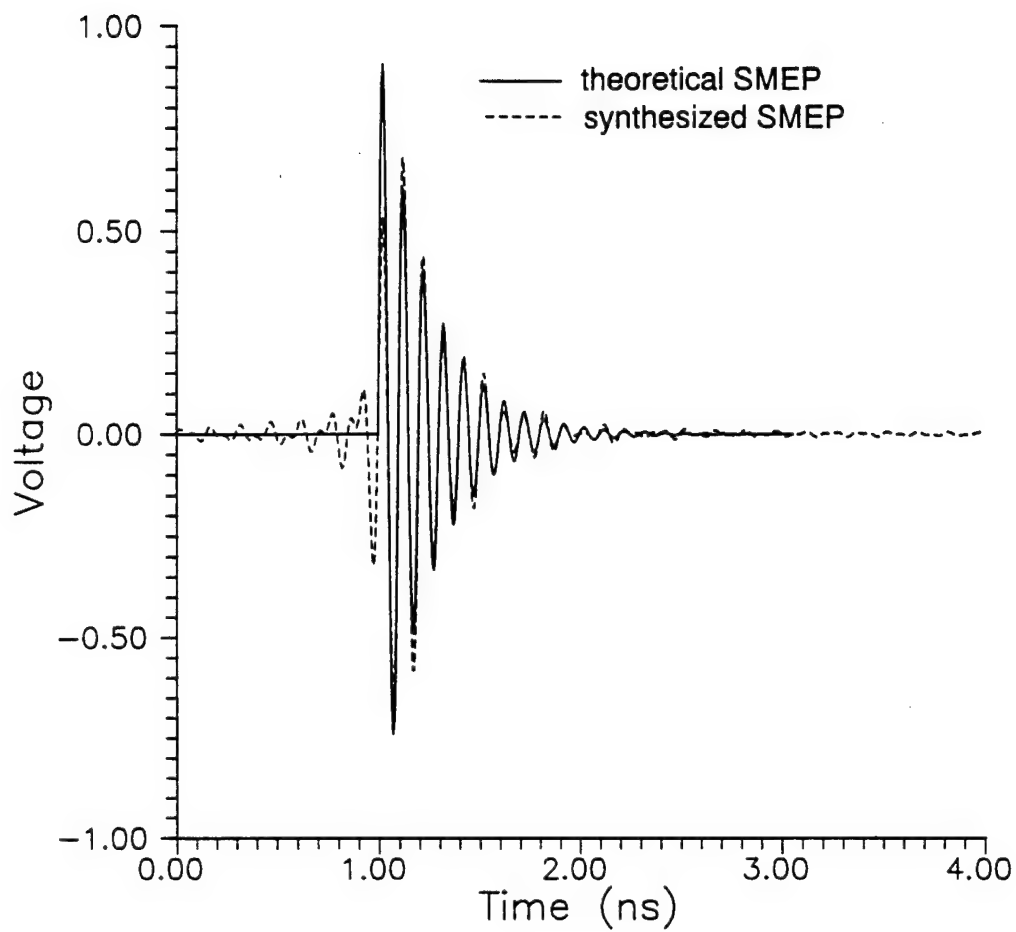


Figure 13. Image of B-52 from 0°-180° data in band 4-16 GHz.



**Figure 14.** Image of B-52 from 0°-90° data in band 4-16 GHz.



**Figure 15** Comparison of theoretical ( $\alpha=4 \times 10^9$ ,  $f_c=10\text{GHz}$  in (20)) and synthesized (7-13GHz) SMEP. Both figures have been moved to the right by 1 ns.

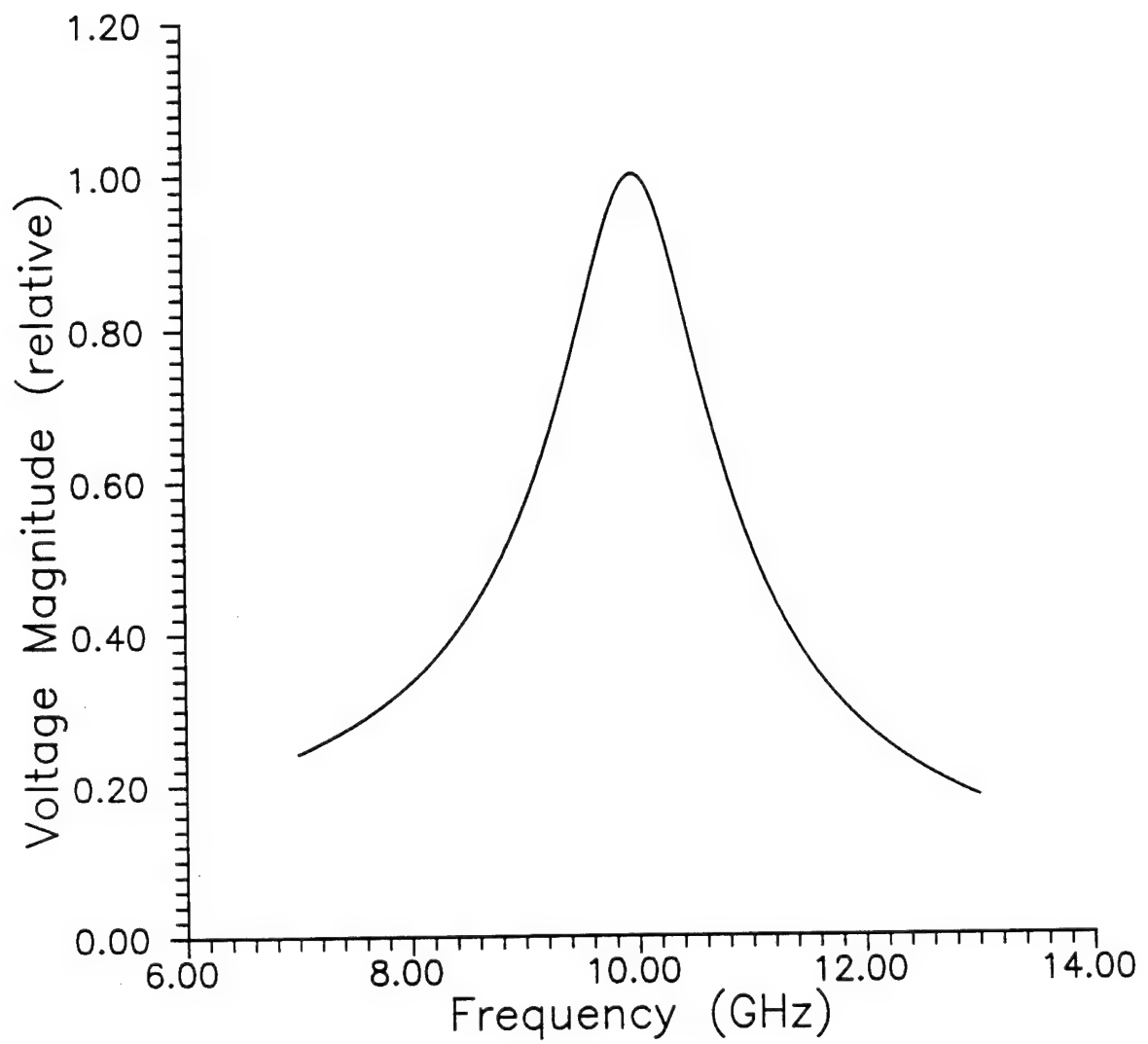


**Figure 16** The spectrum of the synthesized SMEP.



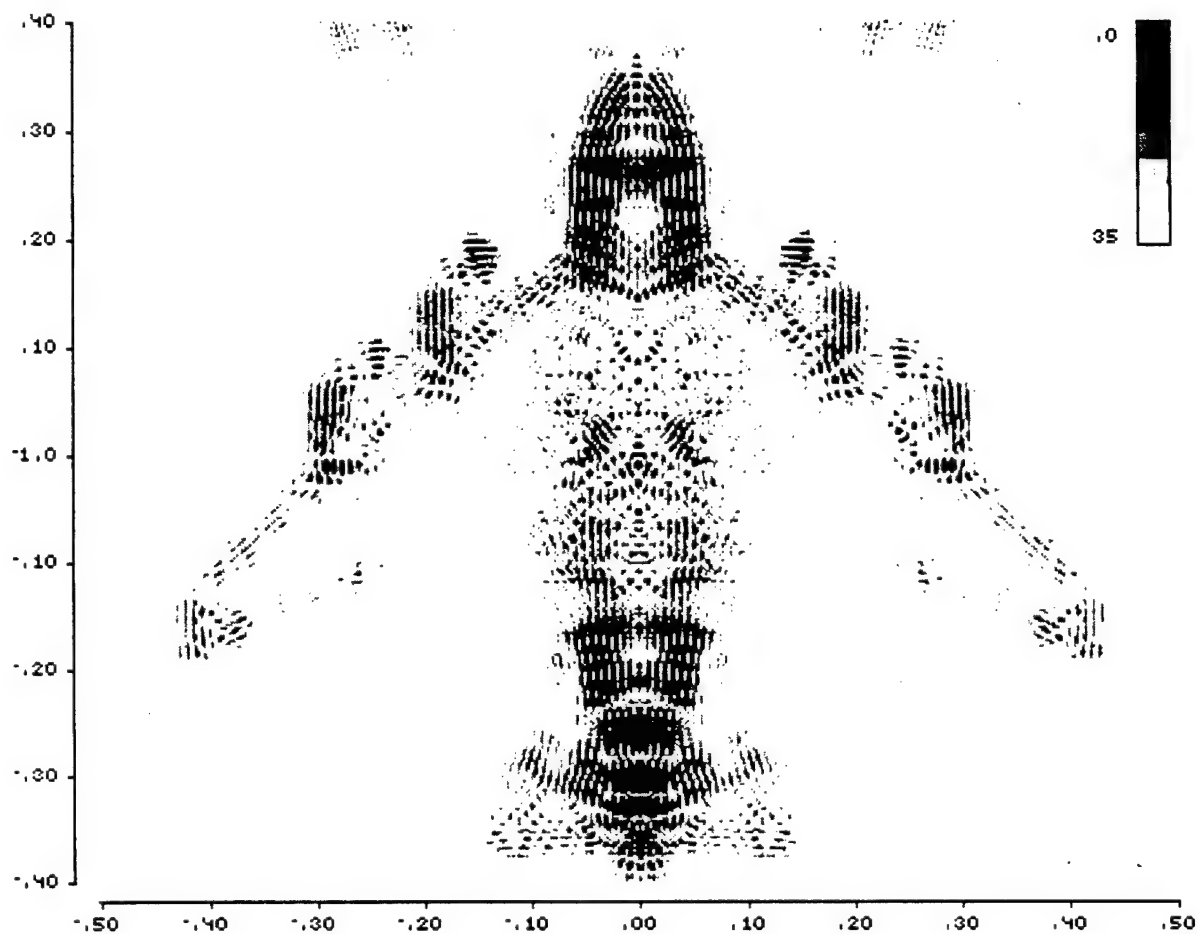


**Figure 17.** Image of B-52 from  $0^{\circ}$ - $180^{\circ}$  data in band 7-13 GHz (before windowing).

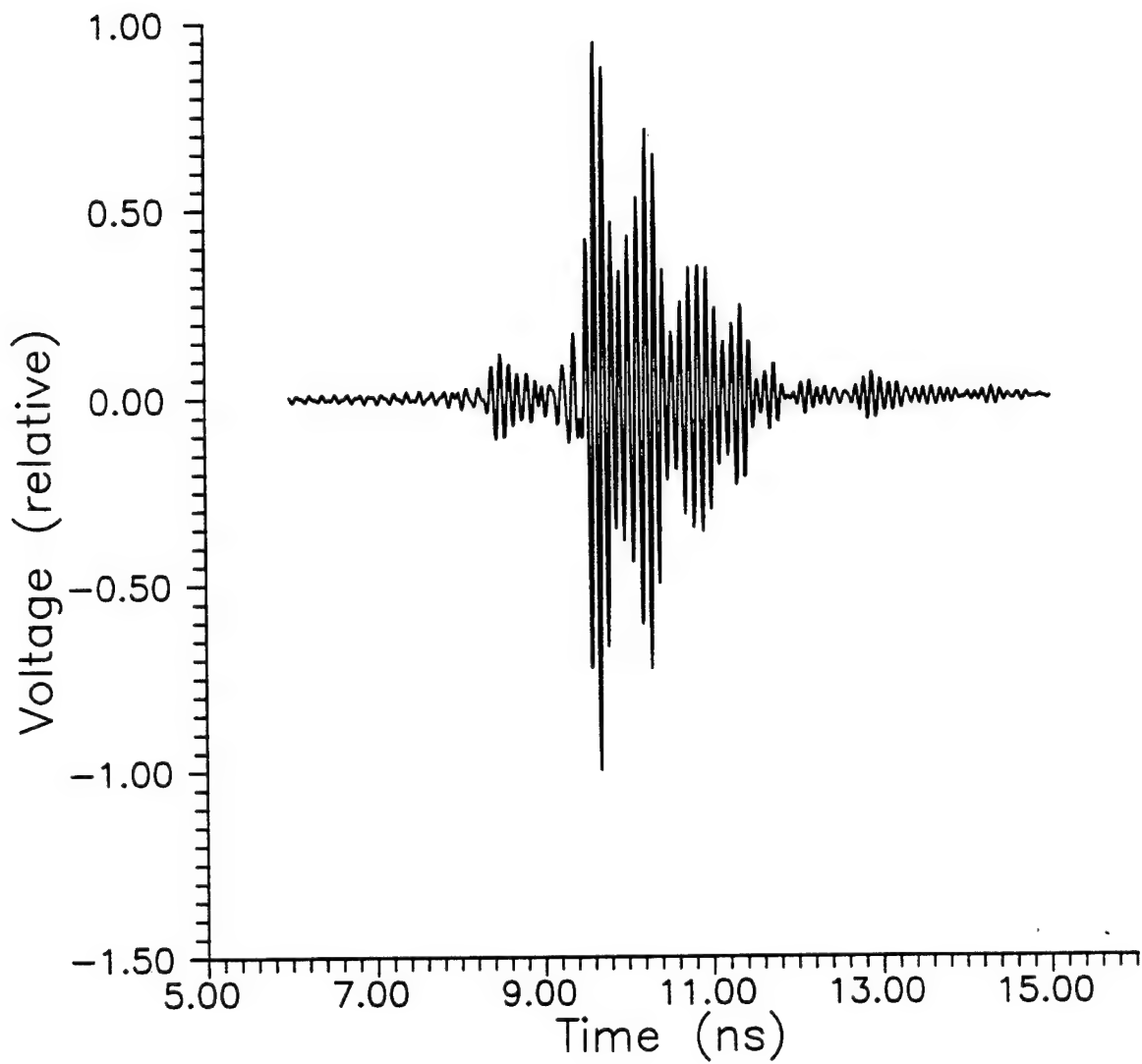


**Figure 18.** B-52 SMEP response (nose-on) before windowing.

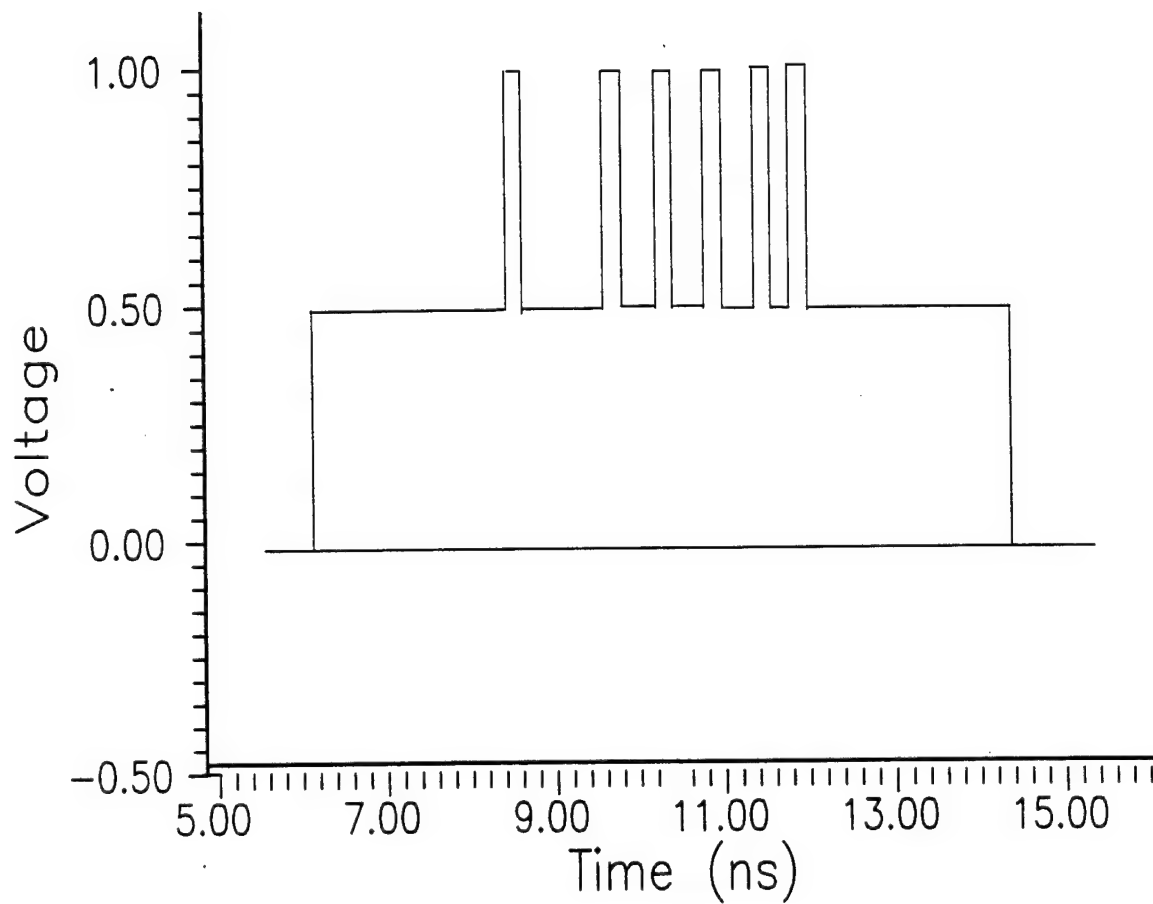


**Figure 19.** Window produced based on Figure 18.

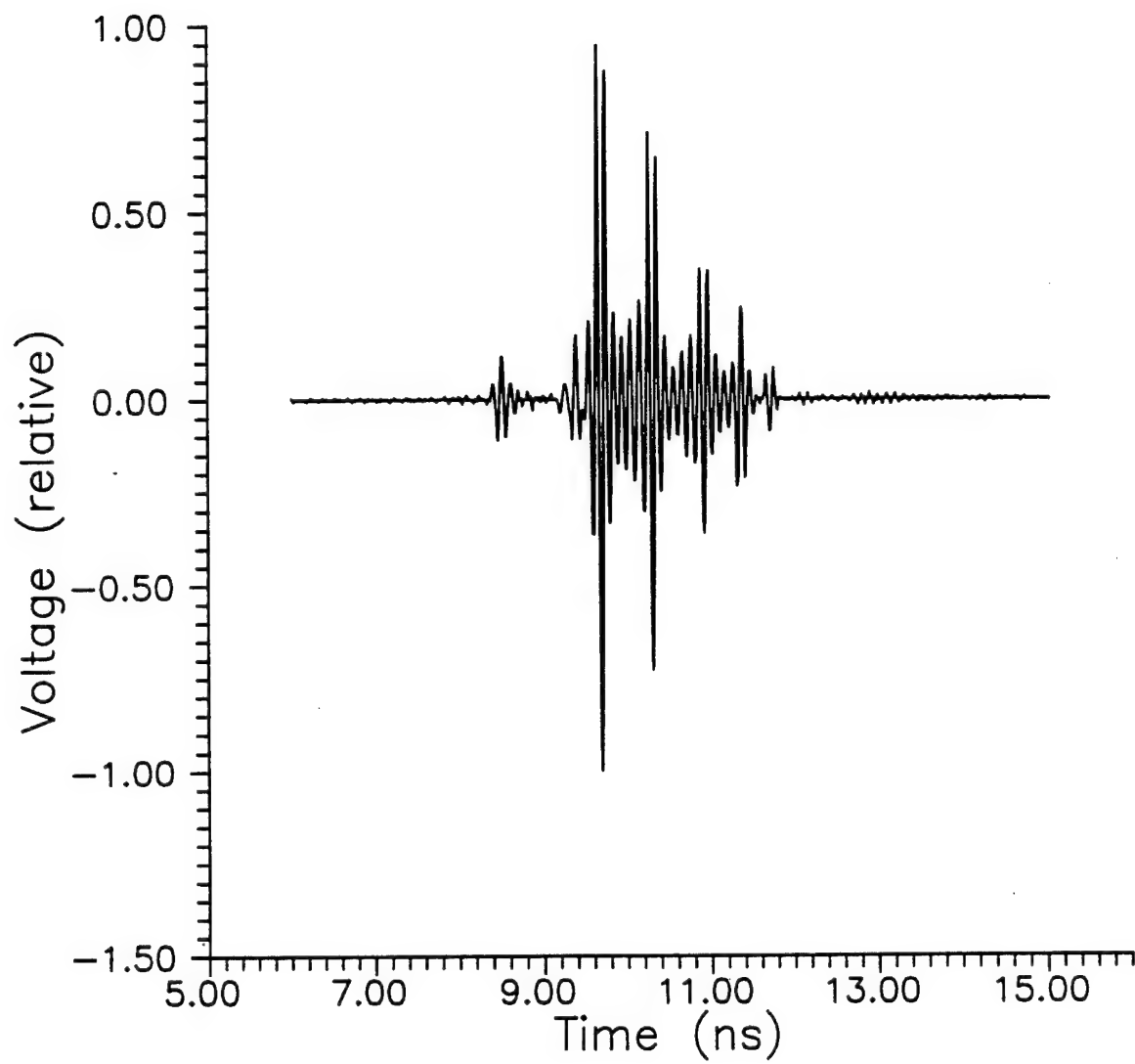


**Figure 20.** B-52 SMEP response (nose-on) after windowing.

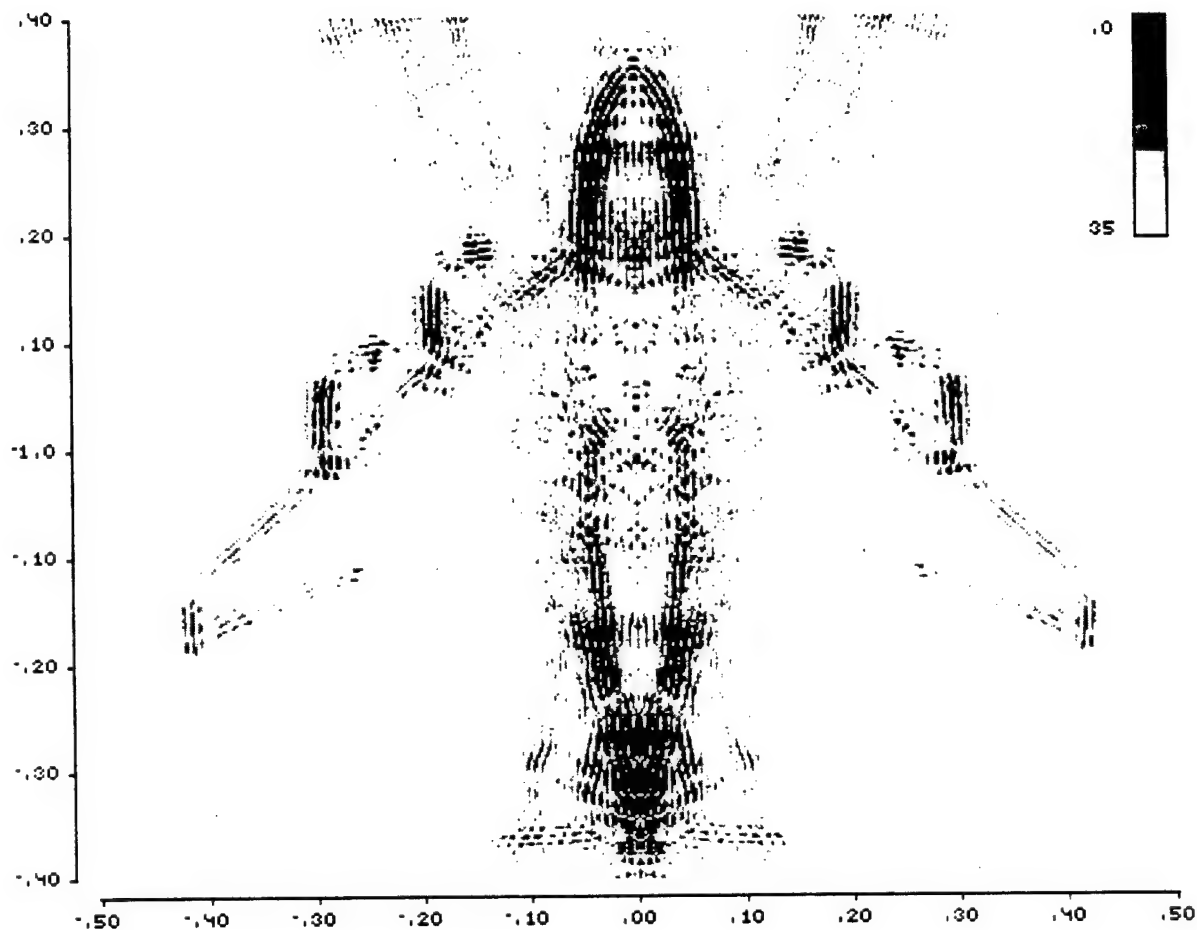


**Figure 21.** Image of B-52 from 0°-180° data in band 7-13 GHz (after windowing).

## Appendix 10

### RADAR IDENTIFICATION AND DETECTION USING ULTRA-WIDEBAND/SHORT-PULSE RADARS

K.M. Chen, E. Rothwell, D. P. Nyquist, J. Ross, P. Ilavarasan,  
R. Bebermeyer, Q. Li, C. Y. Tsai, and A. Norman

Department of Electrical Engineering  
Michigan State University  
East Lansing, MI 48824

#### INTRODUCTION

An ultra-wideband/short-pulse (UWB/SP) radar has promising potential for target identification due to its ultra-high resolution capability and for target detection due to its clutter-suppression capability. This paper describes various research topics studied at Michigan State University on target identification and detection using a UWB/SP radar.

First the measurement of transient responses of airplane models illuminated by a short EM pulse is described. Then target identification schemes using these primarily early-time target responses are discussed. These target ID schemes include a time-domain imaging technique, a wavelet-transform technique and a neural network technique. Finally, schemes for detecting a target in a severe sea clutter environment using the E-Pulse technique or using the relative motion of the target are presented.

#### MEASUREMENT OF SHORT-PULSE TARGET RESPONSES

Michigan State University has a ground-screen-based time-domain scattering range and a free-field, anechoic chamber scattering range. The latter is used to measure high-resolution, early time responses of airplane models illuminated by a short EM pulse (about 60 ps width) which is synthesized from swept frequency measurements in the range of 2 to 18 GHz. A computer-controlled rotatable target positioner is capable of orienting the target to a precision of 0.15° in aspect angle. The data acquisition procedure is fully computer controlled, with the system transfer function deconvolved using a metallic sphere as a known calibration target. A typical set of synthesized target pulse responses is given in Figure 1, which shows the transient response of a 1:48 scale model B-58 (63 cm from nose to tail, and 36 cm from wing-tip to wing-tip) for aspect angles between 0 to 90 degrees, stepped in a 0.45° increment.

Using these measured target pulse responses, several schemes for target identification have been developed. These include the E-Pulse technique<sup>1,2</sup>, a correlation scheme<sup>3</sup>, a time-domain imaging technique, a wavelet transform technique and a neural network technique. The latter three are described in this paper.

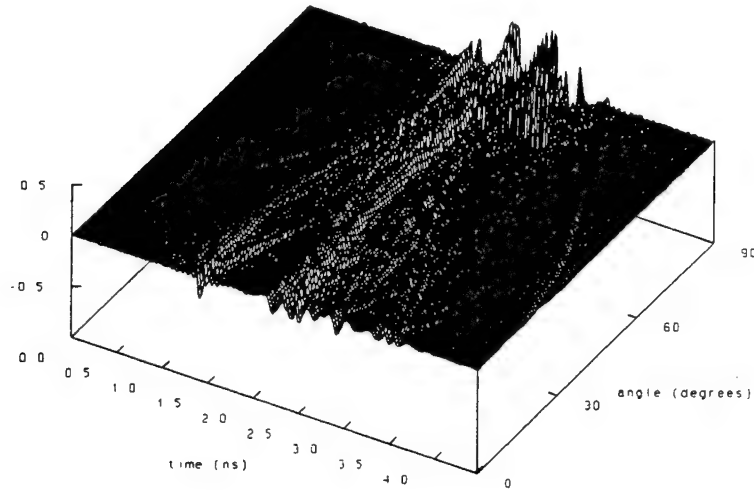


Figure 1. Transient response of 1:48 scale B-58 aircraft

#### TIME-DOMAIN IMAGING TECHNIQUE FOR TARGET IDENTIFICATION

The short-pulse response of a radar target provides significant information about the positions and strengths of scattering centers. If observations are made over a wide range of aspect angles, sufficient information is gained to obtain an image of the target.

Bojarski<sup>4</sup> proposed a simple inverse scattering identity based on the physical optics approximation. He showed that the characteristic function of a conducting scatterer (which is unity within the target geometry and zero elsewhere) is given by the three-dimensional inverse Fourier transform of the scattered field as a function of the incident plane-wave wave vector  $\vec{k}^i$ . If scattered field information is only available within a plane, then the two-dimensional inverse transform yields the thickness of the scatterer as a function of position in that plane.

In the MSU free-field scattering range, aspect angle variation is obtained by target rotation. It is thus convenient to write the inverse scattering identity in polar coordinates. The thickness is then shown to be proportional to the function

$$T_{\omega}(\vec{\rho}) = \text{Re} \left\{ \int_{\phi_i=0}^{2\pi} \int_{K_0=0}^{\infty} E^s(K_0, \phi_i) e^{-jK_0 \rho \cos(\phi - \phi_i)} \frac{dK_0}{K_0} d\phi_i \right\} \quad (1)$$

where  $\vec{\rho}$  is the position vector in the plane of the measurements,  $\phi_i$  is the plane wave incidence angle,  $E^s$  is the back-scattered field measured at frequency  $\omega$  and aspect angle  $\phi_i$ , and  $K_0 = 2k_0 = 2\omega/c$ . By performing the integral over  $K_0$  and recognizing this as the temporal inverse transform, the thickness function is proportional to

$$T_t(\vec{\rho}) = \int_0^{2\pi} r \left( -\frac{2\rho}{c} \cos(\phi - \phi_i), \phi_i \right) d\phi_i \quad (2)$$

where  $r(t)$  is the time-integral of the inverse transform of  $E^s$ , i.e. the step response of the target. This time-domain physical optics inverse scattering identity has a very clear physical interpretation. The quantity  $-2\rho \cos(\phi - \phi_i)/c$  is the two way transit time from the origin of coordinates to the point  $(\rho, \phi)$

along a plane wave incident at angle  $\phi_i$ . Thus, the integral (2) is the sum over all aspect angles of the step response value corresponding to scattering from the point  $(\rho, \phi)$ .

It is possible to enhance the edges of the image by merely using the impulse response (inverse transform of  $E^s$ ) rather than the step response, since this corresponds to a derivative of the thickness response. This has been done in the examples shown in Figure 2. A distinct image of each target results, with the edges of the fuselage, wings, etc., being clearly displayed. Note that the physical optics approximation does not accommodate the shadowed regions, and thus hidden edges such as the rear of the forward wings are not strongly present.

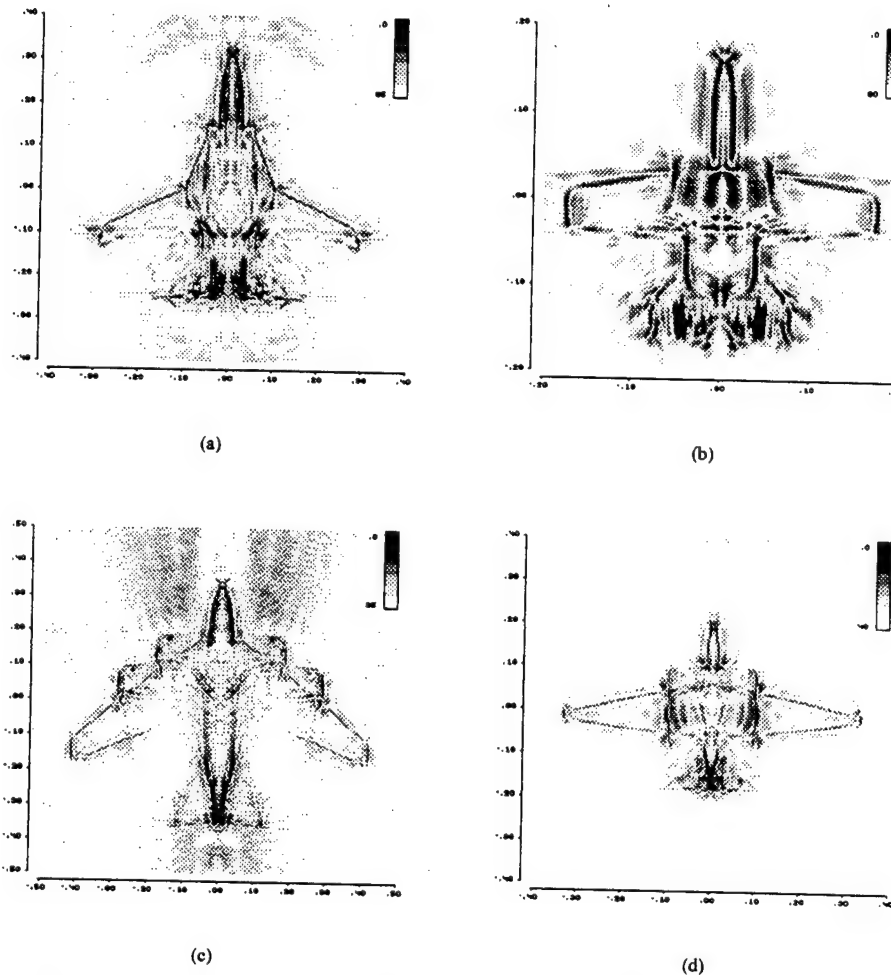


**FIGURE 2.** Images of aircraft found using time-domain, physical optics inverse scattering identity. Temporal waveforms synthesized from 2-18 GHz ultra-wideband responses, measured at 201 aspect angles between  $0^\circ$  (nose-on) and  $180^\circ$ . Information from unlit side supplied by symmetry. Axes are scaled to physical size in m, gray scale is in dB. (a) F-14 (1:32 scale), (b) A-10 (1:48), (c) B-52 (1:72), (d) TR-1 (1:48).

## WAVELET-TRANSFORM TECHNIQUES FOR TARGET IDENTIFICATION

The sparse nature of the discrete wavelet transform (DWT) of SP scattering signals allows for a significant reduction in the storage of early-time signals. The DWT provides a linear transformation of a discretized signal into the "wavelet domain" much in the same manner as the discrete Fourier transform<sup>5</sup>. The signal is represented as a linear combination of wavelet basis



functions (analogous to sinusoids for the Fourier transform) and can thus be reconstructed by

$$s_i = \sum_{j=1}^N a_j w_{ij} \quad 1 \leq i \leq N \quad (3)$$

Here  $s_i$  is the signal sampled at time  $t_i$ ,  $a_j$  is the amplitude of the  $j^{\text{th}}$  wavelet basis function,  $w_{ij}$  is the  $j^{\text{th}}$  wavelet basis function sampled at time  $t_i$ , and  $N$  is the length of the signal (usually a power of 2). Wavelet basis functions are constructed so that the wavelet coefficient vector  $\{a_j\}$  is sparse for a certain class of waveforms (polynomials of a chosen degree). Because of this sparseness, the DWT can be used to compress the signal.

As an example, consider the nose-on ( $0^\circ$ ) response of a 1:72 scale B-52 sampled at 256 time points, as shown in Figure 3. Figure 4 shows the wavelet spectrum  $\{a_j\}$  computed using a 256-point Lemarie DWT<sup>5</sup>. It is readily seen that only a small subset of the wavelet coefficients are significant. Note that the small values of coefficients  $a_{128}$  through  $a_{256}$  is due to an oversampling of the data by a factor of about 2. The DWT thus automatically compensates for frequency oversampling.

To see the effects of random noise on the wavelet reconstruction of data, zero-mean white Gaussian noise has been added to the nose-on response of the B-52, resulting in a waveform with a signal-to-noise ratio (SNR) of 10 dB. Figure 4 shows the wavelet spectrum of the noisy response. Although there is a perturbation of each of the wavelet coefficients, the values of the larger coefficients are changed only slightly. Thus, when only a few coefficients are retained in reconstructing the response, the result is a much more faithful representation than the original noisy waveform, as seen in Figure 3. In other words, much of the noise is represented by perturbation of very small wavelet coefficients which are neglected (effectively filtered out) in the reconstruction.

To provide an example of target identification using wavelet-stored data, the SP responses of five aircraft models -- B-52 (1:72 scale), B-58 (1:48), TR-1 (1:48), F-14 (1:48) and Mig-29 (1:48) -- were synthesized from frequency-domain measurements at 68 angles between  $0^\circ$  and  $30^\circ$ . The resulting signals were transformed using a 512 point Lemarie DWT and the spectra truncated to the largest 32 components. An identification scenario assumes that the  $18^\circ$  B-52 response arises from an unknown target. The measured response of the B-52 is correlated with the responses of all the other targets, at all aspects, reconstructed from their stored, truncated wavelet spectra. The result, shown in Figure 5, provides a correct identification, since the largest correlated output arises from the B-52. Also note that the target can be correctly identified over about a  $3^\circ$  range of angles. This gives a measure of the necessary aspect angle discretization needed when storing target SP signatures.

Finally, Figure 6 shows that contaminating the measured target signal with random noise at an SNR of 10 dB does not significantly reduce the identification capabilities of this technique.

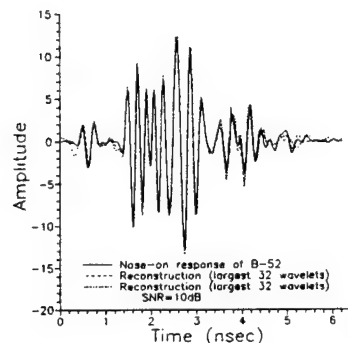


Figure 3. Nose-on ( $0^\circ$ ) response of B-52 aircraft model and 32 wavelet reconstruction.

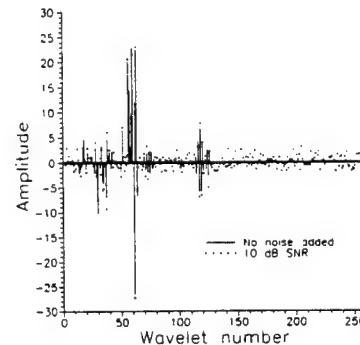


Figure 4. Wavelet spectrum of nose-on ( $0^\circ$ ) response of B-52 aircraft model.

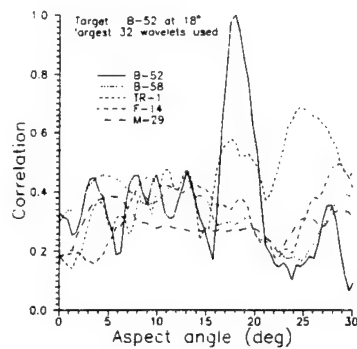


Figure 5. Maximum correlation of 18° B-52 response with responses from all targets. Target waveforms represented using 32 wavelets.

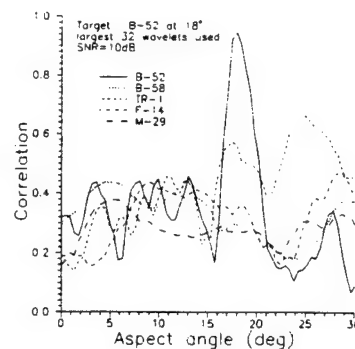


Figure 6. Maximum correlation of 18° B-52 noisy response with responses from all targets. Target waveforms represented using 32 wavelets. SNR = 10 dB.

## NEURAL NETWORK TECHNIQUES FOR TARGET IDENTIFICATION

Neural networks have great potential for storing and retrieving the large number of target signatures needed to perform aspect-dependent target identification (i.e., identification based on the early-time SP response). A number of neural network architectures for target identification were simulated, including feed-forward networks trained using back-propagation, and Hopfield networks. Particularly good success was observed with correlation associative memories, including generalized inverse networks (GI), exponential correlation associative memory networks (ECAM), and cascades of these networks (ECAM-GI). The wavelet transform technique described in the previous section has also been employed to reduce network size.

As an example, Figure 7 shows simulation results for the ECAM-GI cascaded network, designed to recognize three aircraft (F-14, B-58 and B-52) each at 19 different aspect angles between 0° and 90°. The results show that for low noise conditions, each of the 57 responses is correctly recognized. In fact, accurate identification is possible at noise levels of 0 dB SNR.

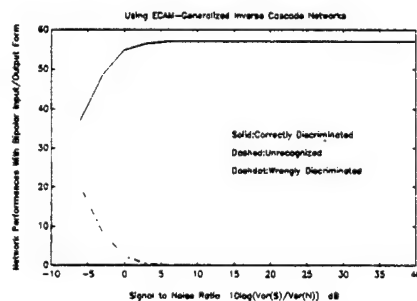


Figure 7. Overall performance of ECAM-GI cascade network, designed to recognize 3 aircraft at 19 aspect angles each.

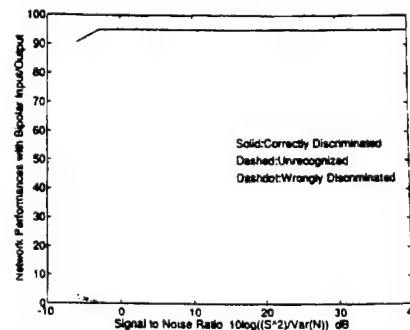


Figure 8. Performance of RDM-GI cascaded networks trained to recognize five target models each at 19 aspect angles. Analog inputs used.

More sophisticated networks are also being investigated, including recurrent dynamic correlation associative memory networks<sup>6,7</sup> (RDM). The performance of a network using the RDM technique cascaded with the Generalized-Inverse method (RDM-GI) with fixed analog input is shown in Figure 8. This network was trained to recognize five targets (B-52, B-58, F-14, Mig-29, TR-1), each at 19 different aspect angles. Superior performance is seen in these figures, with better than 95% correct identification at SNR levels as low as -5 dB.

## DETECTION OF TARGETS IN A SEA CLUTTER ENVIRONMENT USING UWB/SP RADAR

The detection of radar targets near the sea surface using transient signals is made difficult by the presence of a strong clutter return from the disturbed sea. However, if the scattering from water wave crests is primarily specular within the band of the interrogating signal, the E-pulse resonance cancellation technique can be used to eliminate the clutter return, thus increasing the probability of detection.

Assume that the sea surface consists of wave crests of nonuniform heights separated by water wavelength  $\lambda_w$ . If the scattering from these wave crests is nearly specular, the transient back-scattered electric field response will be a series of peaks separated in time by approximately  $2\lambda_w \cos \theta_i / c$ , where  $\theta_i$  is the incidence angle measured from grazing incidence. Because this is analogous to the early-time response from a radar target, a frequency-domain E-pulse can be constructed to eliminate the sea clutter as a post-processing step. This enhances the ratio of energy in the signal to the energy in the clutter and improves the probability of detecting the target.

Under certain circumstances the clutter cancellation can also be accomplished in the time domain through direct transmission of an appropriate "clutter reducing transmit waveform" (CRTW). If the wave crests are fairly similar in height, the time domain scattered field response will be nearly periodic, and can be approximated by a sum of complex exponentials. It is then possible to create an E-pulse to eliminate the sea clutter directly in the time domain. Furthermore, it is possible to shape the E-pulse such that its energy is concentrated within the band of maximum target response (perhaps near the dominant target resonance) so that the radar return when this pulse is radiated contains both an enhanced target response and an eliminated clutter. Since this is not a post-processing step, both the target-to-clutter ratio and the signal-to-noise ratio are enhanced. If the E-pulse waveform is too complicated for direct transmission, a simplified version can be synthesized and transmitted using a superposition of short-pulse CW waveforms.

To simulate the potential of the time-domain approach, an aluminum missile model has been placed above a conducting aluminum sinusoidal surface, as shown in Figure 9, and illuminated by a horizontally-polarized EM wave. The backscattered field has been measured for an aspect angle of  $30^\circ$  from the horizontal in the frequency band 1-7 GHz both with and without the missile present. The resulting time-domain waveforms, obtained through Fourier inversion, are shown in Figure 10. As can be seen, the missile response is embedded within the strong clutter signal, and difficult to detect. To eliminate the clutter, a CRTW has been constructed using the clutter response, and convolved with the clutter+missile response to simulate its transmission. Figure 11 shows the result, indicating that the clutter has been reduced significantly, and the target response (appearing after about 2 ns) is easily detected.

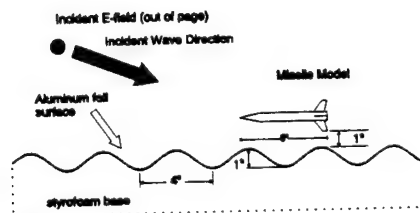


Figure 9. Simulated experimental sea surface environment.

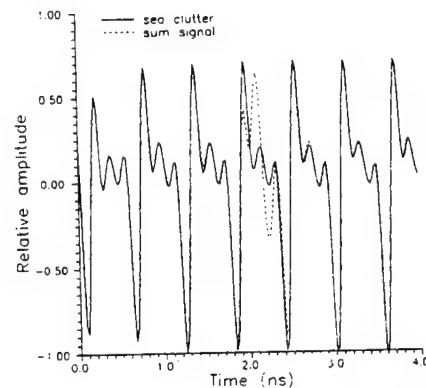
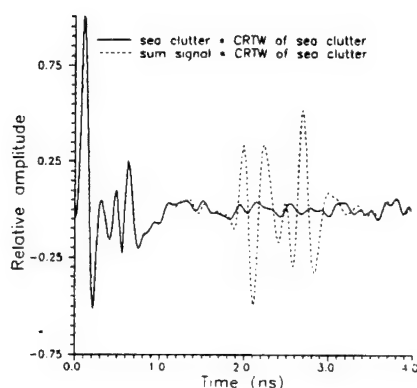
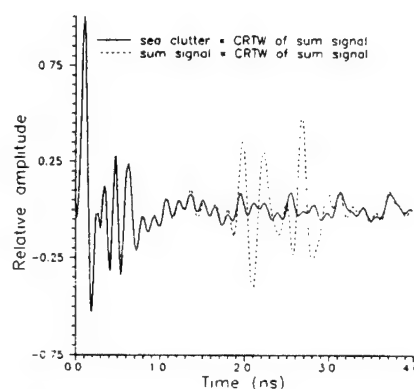


Figure 10. Measured response of simulated sea surface with and without 5 inch missile present.

In an actual application, it would not be known if the target was present, and thus the CRTW might be constructed using both target and clutter information. However, it is speculated that if the missile response is small, the resulting CRTW will eliminate the clutter without reducing the target response. To test this, a CRTW was created using the clutter + missile response of Figure 10 and convolved with the same response. The result, shown in Figure 12 demonstrates that while the clutter cancellation is not quite as good as when the CRTW was constructed from a pure clutter response, the missile response is still detectable over the clutter.



**Figure 11.** Convolution of measured response of sea surface with and without 5 inch missile with CRTW created from sea clutter response.



**Figure 12.** Convolution of measured response of sea surface with and without 5 inch missile with CRTW created from missile plus clutter response.

## SEPARATION OF TARGETS FROM CLUTTER USING UWB/SP RADAR AND RELATIVE TARGET MOTION

A UWB/SP radar can be used to detect targets which move with different velocities than that of the ocean waves.

Consider a situation where a fast-moving target (e.g., a missile) and a stationary target (e.g., a periscope) are in the presence of a slow-moving ocean wave. If the sea surface is interrogated by a short EM pulse, the radar return will consist of a periodic series of peaks (the sea clutter from the ocean wave) and two peaks representing responses of the moving and stationary targets. When another interrogating pulse is sent out after a time interval, the new radar return will have a series of peaks shifted slightly due to the slow moving ocean wave, while the peak of the moving target will have moved a much larger amount, and the peak of the stationary target will not have moved. With repetitive interrogating pulses and each subsequent radar return recorded, a diagram such as shown in Figure 13 can be constructed. The horizontal axis is a fast time scale (ns) representing the location of targets and ocean wave crests. The vertical axis is a slow time scale (s) representing the time when the radar return is received. This diagram clearly shows the traces of moving and stationary targets and ocean wave crests. Using this relative motion scheme, targets can be separated from clutter, thus facilitating their detection.

This detection scheme was recently studied by the Naval Command, Control and Ocean Surveillance Center using actual measurements.

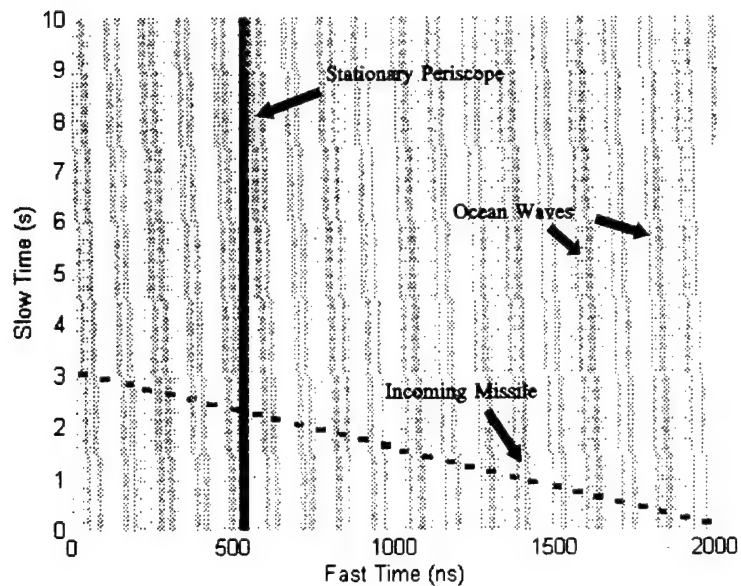


Figure 13. Traces of targets and ocean wave crests constructed using radar returns from repetitive interrogating EM pulses. Ocean wave velocity: 1 m/s, missile velocity: 100 m/s.

#### REFERENCES

1. E. Rothwell, K.M. Chen, D.P. Nyquist, P. Ilavarasan, J. Ross, R. Bebermeyer, and Q. Li, "Radar target identification and detection using short EM pulse and the E-pulse techniques", Ultra-Wideband, Short-Pulse Electromagnetics, Edited by H. Bertoni et al., Plenum Press, pp. 475-482, 1993.
2. J. Ross, P. Ilavarasan, E. Rothwell, R. Bebermeyer, K.M. Chen, D.P. Nyquist, and Q. Li, "Radar target discrimination using E-pulses with early-time and late-time responses", presented at 1993 IEEE-APS International Symposium/URSI Radio Science Meeting, June 28-July 2, 1993, University of Michigan, Ann Arbor, Michigan.
3. E. Rothwell, Q. Li, J. Ross, R. Bebermeyer, C.Y. Tsai, and K.M. Chen, "Non-Cooperative target recognition using ultra-wideband radars", Quarterly Report No. 5, Division of Engineering Research, Michigan State University, December 1993.
4. N.N. Bojarski, "A survey of the Physical Optics Inverse Scattering Identity," IEEE Transactions on Antennas and Propagation, vol. AP-30, No. 5, pp.980-989, September 1982.
5. W.H. Press, S.A. Teukolsky, W.T. Vetterling, and B.P. Flannery, Numerical Recipes in Fortran, 2nd ed., Cambridge University Press, 1992, chap. 13.
6. Tzi-Dar Chiueh and R.M. Goodman, "Recurrent Correlation Associative Memories," IEEE Trans. Neural Networks, vol. 2, pp. 275-284, March 1991.
7. Y. Kamp and M. Hasler, Recursive Neural Networks for Associative Memory, John Wiley & Sons, 1990.

#### ACKNOWLEDGEMENTS

The work was supported by Naval Command, Control and Ocean Surveillance Center under Contract N66001-91-C-6019, Office of Naval Research under Grant N00014-93-1-1272, and ThermoTrex Corporation under purchase order No. 22068.

# Appendix 11

## Measurement and processing of scattered ultrawide-band/short-pulse signals

Edward Rothwell, Kun-Mu Chen, Dennis Nyquist, John Ross, and Robert Bebermeyer

Department of Electrical Engineering, Michigan State University  
East Lansing, MI 48824

### ABSTRACT

High quality ultrawide-band measurements provide a basis for understanding the transient scattering phenomena necessary for the development of short-pulse radar target identification and detection schemes. This paper describes several techniques used at Michigan State University (MSU) for the acquisition, processing and interpretation of ultra-wideband scattering data. By performing measurements over a sufficiently large bandwidth, the early-time specular nature of a radar target and the late-time resonant behavior can be observed simultaneously within a single target signature. Special attention has been given at MSU to enhancing the equivalent bandwidth of the measurement system through a spectral splicing and extrapolation method. Observation and interpretation of the various scattering phenomena and their dependence on target aspect are then interpreted through several visualization techniques, including scattering plots, frequency-time plots and images.

**Key words** -- impulse radar, ultrawide-band radar, electromagnetic scattering measurements

### 1. INTRODUCTION

The development of viable short-pulse radar target identification systems<sup>1</sup> has prompted a need for understanding the basic phenomena of transient electromagnetic scattering from realistic targets. This is most easily accomplished through laboratory measurements over ultrawide frequency bandwidths. If the bandwidth is large enough, a target signature can be measured which contains both the early-time specular target response (a high frequency effect), and the late-time natural resonance response (a low frequency effect). Each of these components has been suggested for use in target identification schemes<sup>2</sup>, and with sufficient bandwidth both could be used in a single technique<sup>3</sup>.

A scattering range has been developed at Michigan State University (MSU) which allows calibrated measurements of the near backscattering properties of scale model targets over the effective frequency range of 0-18 GHz for all linear polarization combinations (hh, hv, vh, vv). The bandwidth is achieved through a combination of frequency scaling, splicing and extrapolation techniques which employ a genetic algorithm to enforce the causality of the equivalent time-domain signature. Details of the bandwidth enhancement are given in Section 2, along with a description of the range calibration technique. A computer controlled target rotator capable of a positioning accuracy of 0.15° allows a detailed study of the variation of target scattering as a function of aspect angle. The wide bandwidth combined with the fine angular resolution of the measurements results in a large amount of data for each target, the physical interpretation of which is facilitated by various visualization techniques. Several methods for visualizing the data are presented in Section 3, including scattering plots, frequency-time plots, and imaging based on physical optics. Images and scattering plots are useful for interpreting the early-time specular behavior of targets as a function of aspect angle, while frequency-time plots allow the identification of such interesting physical phenomena as the resonance of target substructures. The late-time behavior is described best through plots of the aspect variation of the late-time modal amplitudes.

### 2. MEASUREMENT TECHNIQUES

The free-field scattering measurement system at MSU is a swept-frequency system utilizing a Hewlett-Packard HP-8720B vector network analyzer. While the network analyzer is capable of performing measurements over the band 0.13-20 GHz, the practical measurement band is controlled by the rated antenna bandwidth. Two sets of TEM horn antennas are available for use, American Electronic Laboratories model AEL H-1734 (0.5-6 GHz rated bandwidth) and AEL-1498 (2-18 GHz). The first set of antennas is combined with a Picosecond Pulse Labs broadband amplifier (11 dB gain) to give a viable 0.4-7 GHz measurement band, while the second set of antennas is combined with a Hewlett Packard HP-8349B amplifier (20

dB gain) to give a viable measurement band of 2-18 GHz. By combining measurements from both bands, and using algorithms described in Section 2 to scale, splice and extrapolate the spectrum, an equivalent measurement bandwidth of 0-18 GHz is obtained.

The horn antennas are mounted within portholes cut into one wall of a 24x12x12 foot anechoic chamber which is lined with 6 inch pyramidal absorber. Scale model targets are placed on a low density foam pedestal mounted on an Arrick Robotics MD-2 Dual Stepper Motor computer controlled rotator located in the center of the chamber. The rotator is capable of 0.15 degree positioning accuracy from 0 to 360 degrees. At each aspect angle, the network analyzer acquires the data and sends it to a personal computer for processing and analysis.

A diagram of the measurement system is shown in Figure 1. As in any scattering system, the effects of the transmit/receive system transfer function, clutter, and target to chamber interactions must be removed to obtain accurate measurements. The calibration procedure is similar to that used by Morgan<sup>4</sup> except that the initial raw measurements are performed in the frequency domain. The methodology is sufficiently different to merit a detailed description.

## 2.1. Calibration Procedure

The raw measured response of a target obtained with the anechoic chamber system differs from the actual response for two distinct reasons. First, the response of the measurement system (network analyzer, cables, amplifiers, antenna, propagation path) will modify the actual response through a convolution process. Second, there will be systematic errors introduced through reflections from the chamber walls (clutter) and interactions between the target and the chamber. Each of these effects is modeled in the measurement system diagram shown in Figure 2.

The first step in the calibration procedure is to make a background measurement of the empty chamber. This measured response is modelled as

$$R^b(f) = S(f) \{H_a(f) + H_c(f)\} + N^b(f) \quad (1)$$

where  $H_a(f)$  describes the transfer function of the direct coupling from the transmit antenna to the receive antenna,  $H_c(f)$  models the transfer function of the coupling from the transmit antenna to receive antenna via the anechoic chamber, antenna supports, and target mount,  $N^b(f)$  is random noise and  $S(f)$  is the system transfer function

$$S(f) = H_r(f) H_t(f) E(f) \quad (2)$$

Here  $H_r(f)$  and  $H_t(f)$  are the transfer functions of the receive and transmit antennas from the transmission line into the free-field environment while  $E(f)$  represents the spectral content of the CW source.

Next, a calibration object with a known response is measured. For like-polarization measurements, a conducting sphere is used, with a known response calculated theoretically using the Mie series. For cross-polarization measurements, an inclined circular wire loop is used. This measurement gives

$$R^{c+b}(f) = S(f) \{H_a(f) + H_c(f) + H_s^c(f) + H_x^c(f)\} + N^{c+b}(f) \quad (3)$$

where  $N^{c+b}(f)$  is random noise,  $H_s^c(f)$  is the known transfer function of the calibration object, and  $H_x^c(f)$  is the transfer function of the interaction of the calibration object with the anechoic chamber. Note that the interaction term is causal in the time domain; it cannot not occur prior to the time required for the wave scattered from the target to reach the chamber walls and return to the receiving antenna. Note also that the interaction term is represented here as an additive effect.

The last measurement is of the target, giving

$$R^{t+b}(f) = S(f) \{H_a(f) + H_c(f) + H_t^t(f) + H_x^t(f)\} + N^{t+b}(f) \quad (4)$$

where  $N^{t+b}(f)$  is random noise,  $H_t^t(f)$  is the desired transfer function of the target and  $H_x^t(f)$  is the transfer function due to the interaction of the target with the anechoic chamber. Again, this term is causal in the time domain.

Once these three measurements have been completed and stored in the computer, data processing to obtain the actual target scattered field response can be undertaken. First, the background measurement is subtracted from the measurements of the calibration object and the target. Subtracting (1) from (3) and (4) gives the clutter-free responses

$$\begin{aligned} R^c(f) &= S(f) \{H_s^c(f) + H_x^c(f)\} + N^c(f) \\ R^t(f) &= S(f) \{H_s^t(f) + H_x^t(f)\} + N^t(f) \end{aligned} \quad (5)$$

with the noise terms  $N^c(f) = N^{cb}(f) - N^b(f)$ ,  $N^t(f) = N^{tb}(f) - N^b(f)$ . The next step in the calibration process depends on the quality of the anechoic chamber. If the anechoic chamber is of very high quality, then the interaction terms are small and can be neglected along with the noise terms giving

$$\begin{aligned} R^c(f) &= S(f) H_s^c(f) \\ R^t(f) &= S(f) H_s^t(f) \end{aligned} \quad (6)$$

Thus, the system transfer function can be determined from the known calibration response as

$$S(f) = \frac{R^c(f)}{H_s^c(f)} \quad (7)$$

Finally, the actual target response is given through

$$H_s^t(f) = \frac{R^t(f)}{S(f)} \quad (8)$$

For anechoic chambers of lesser quality, the interaction terms may be too large to be neglected. To solve this problem,  $R^c(f)$  can be transformed to the time domain and time gating can be used to eliminate any interaction terms that are sufficiently delayed beyond the end of the calibration object response. Define the time response of the calibration measurement as

$$r^c(t) = \mathcal{F}^{-1}\{R^c(f)\} \quad (9)$$

Time gating with a window function  $w(t)$  effectively excludes the interaction terms, giving

$$r^{cw}(t) = r^c(t)w(t) \quad (10)$$

Assuming that  $w(t)$  excludes all of the interaction terms, and that  $\mathcal{F}^{-1}\{S(f)H_s^c(f)\}$  is approximately time limited and not truncated by the window function, then

$$R^{cw}(f) = S(f)H_s^c(f) \quad (11)$$

where  $R^{cw}(f) = \mathcal{F}\{r^{cw}(t)\}$ . From this, the system transfer function  $S(f)$  can be obtained as

$$S(f) = \frac{R^{cw}(f)}{H_s^c(f)} \quad (12)$$

Then, from (5)

$$H_s^t(f) + H_x^t(f) = \frac{R^t(f)}{S(f)} \quad (13)$$

Finally to isolate  $H_s^t(f)$  the inverse Fourier transform is applied to obtain

$$H_s^t(t) + H_x^t(t) = \mathcal{F}^{-1}\left\{\frac{R^t(f)}{S(f)}\right\} \quad (14)$$

If the target response is approximately time limited, and the interaction term is causal and delayed beyond the end of the target



response, then the actual target response can be isolated using time gating to eliminate  $H_{sc}^i(t)$ .

To validate the calibration process, the response of a 0.0381 m diameter conducting sphere was measured using a 0.1778 m diameter sphere as a calibration object. The measured transfer function of the sphere is compared with its theoretical response in Figure 3 for the frequency band 2-18 GHz. Good agreement is seen throughout the band.

## 2.2 Splicing and extrapolation algorithm

If a target is measured within the two bands 0.4-7 and 2-18 GHz, the results can be combined to give an overall bandwidth of 0.4-18 GHz. It is found that if large scale model targets are used, good spatial resolution is obtained from the specular portion of the target response, but the major target resonances occur below 0.4 GHz. On the other hand, if a small target is used, the resonances are present but the spatial resolution is poor. This problem can be overcome by measuring a small target in the low frequency band and a larger version of the same target in the high frequency band. Assume the larger model, denoted A, has a scale of 1:A and the smaller model, denoted B, has a scale of 1:B. Then, frequency scaling for conducting targets allows the expression

$$R^A(f) = \left(\frac{B}{A}\right) R^B\left(\frac{A}{B}f\right) \quad (15)$$

where  $R^A(f)$  and  $R^B(f)$  are the measured responses of model A and B respectively. By using the above relation,  $R^B(f)$  is converted to the same scale as model A. Thus, by combining both measurements, the response of the larger model is obtained within the effective bandwidth (0.4A/B-18 GHz). Typically, a ratio of 2:1 is used between the two targets, giving an equivalent frequency range of 0.2-18 GHz.

The splicing of the two target spectra  $R^A(f)$  and  $R^{BS}(f) = (B/A)R^B(fA/B)$  in a way that permits accurate determination of the transient response via the inverse FFT is somewhat difficult due to unavoidable phase differences between  $R^A(f)$  and  $R^{BS}(f)$ . These phase differences are primarily due to variations in the effective range to models A and B. Any discontinuity in phase at the splicing frequency results in a non-causal, oscillatory signal being introduced into the transient response. A related problem arises from the abrupt termination of the band edges. If the data is inversely transformed into the time domain, oscillatory signals will again be introduced. The oscillation can be reduced by using an appropriate windowing function which tapers smoothly to zero at the band edges, but this will seriously reduce the presence of the low frequency resonances, resulting in a transient response with minimal late-time component.

To overcome these problems,  $R^{BS}(f)$  is extrapolated to zero frequency with a linear phase, polynomial spectral function  $R^E(f)e^{-j\alpha f}$ , and then is multiplied by a progressive phase shift factor  $\exp(-j\beta f)$ . The optimal values of  $\alpha$  and  $\beta$  are determined by minimizing the non-causal signal present before the beginning of the target response,  $t_0$ . A genetic algorithm<sup>5</sup> is used to minimize the energy

$$E = \int_{t_0-\Delta}^{t_0} [\mathcal{F}^{-1}\{W(f)(R^A(f) + [R^E(f)e^{-j\alpha f} + R^{BS}(f)]e^{-j\beta f})\}]^2 dt \quad (16)$$

where  $W(f)$  is a weighting function which rolls off only at high frequency (typically a Gaussian function).

As an example, consider a B-58 model with scales of 1:48 and 1:96 measured at wing-on incidence with the electric field polarized in the plane of the aircraft. The spectral magnitude of the spliced and extrapolated spectral scattered field response is shown in Figure 4. There is clearly a low-frequency resonant region with sharp spectral peaks, followed by a high-frequency specular region. The inset shows an expanded version of the lower frequencies, showing the resonances and the extrapolation to zero frequency (using a function proportional to  $\omega^2$ ). Figure 5 shows the time-domain response obtained via the inverse FFT. Here there is a clear distinction between the early-time specular response, occurring as the incident field passes across the target, and the late-time resonant response. The solid line in Figure 5 is a result of using the genetic algorithm to minimize the oscillating precursor signal. If splicing is done without this minimization, the unacceptably poor

signal shown as the dotted line is obtained.

### 3. TRANSIENT DATA ANALYSIS AND VISUALIZATION

It is evident from the above description that several steps are required to obtain an ultrawide-band, transient target response. To minimize the required amount of human effort, the system has been automated to the greatest extent possible. At the beginning of each measurement process a calibration object and the empty chamber are measured, and the results transferred to a computer via an HP-IB interface bus. A target is then placed upon a computer controlled rotatable platform, and the raw target response is automatically measured over a desired range of aspect angles with a step as fine as  $0.1^\circ$ . This data is sent to the computer and each set is processed to obtain a calibrated target response. The measurement process is repeated with a target of a different scale and the two sets of data are automatically spliced, extrapolated, and inverse transformed to give the final time-domain target responses.

A great deal of data can be rapidly accumulated for each target. To help understand the phenomenology of the scattering process, as is required before a successful target discrimination scheme can be developed, a significant effort must be put into analyzing the measured data. This encompasses two tasks: understanding the physics of the scattering process as a function of time, and understanding the dependence of the scattered field on aspect angle. To this end, several schemes have been developed to process the data and improve the visualization of the scattering effects.

Traditionally, the transient response of a radar target has been decomposed into two parts, an early-time specular response which occurs as the incident field waveform passes across the target, followed by a late-time natural mode response after the field has completely traversed the target. However, the measured data shows a more ambiguous delineation, complicated by the fact that small substructures may resonate during the period usually designated as early time, and global resonances may begin to be established before the onset of the late-time period. This effect can be observed quite clearly in Figure 6. Here the measured wing-on responses of 1:72 and 1:144 scale model B-52 aircraft have been combined together to obtain the short-pulse response. Overlaid with the response is the outline of the B-52. Clearly, there are specular reflections arising from the tip of the wing, the two engines, and the fuselage. Note also that the specular response is followed by a late-time natural mode response. However, an interesting effect is created by the shadowing of the leeward wing by the fuselage. There are no distinct specular reflections after the incident wave has passed the fuselage, but the natural mode series has obviously begun before the wave has completely passed the target. At this aspect angle, the natural response of the target is dominated by a fuselage resonance which begins to be established immediately after the incident wave has passed the fuselage. This is one instance of a natural response being imbedded within traditional early time. Examples of substructure resonances are also apparent. Plotted on the same graph is the transient response obtained using only the high-band (2-18 GHz) data. This data has no resonance information, which is easily seen by examining the difference between the curves in the late-time region. Note that there is also a difference following the specular reflection from the wing tip and from each engine. Since the difference is only due to low frequency information, there is a substructure resonance building after each specular reflection — the resonances of the wingtip and the engines.

The confusing mixture of specular and resonant information can be sorted out and more easily visualized using a frequency-time plot. These plots have been used recently as a visual aid in many areas of electromagnetic scattering<sup>6</sup>. The plot is usually created by sliding a windowing function through the waveform and Fourier transforming the product of the waveform and the window. Often the window is allowed to expand as it moves (wavelet concept). For a narrow window, specular events are more evident; a wider window reveals resonant events. Since there is a combination of both types of events at many points within the target data, it is necessary to use a window with an adaptable window width. Figure 8 shows the plot generated using a rectangular window whose right side progresses uniformly in time through the waveform (shown at the bottom) and whose left side is allowed to expand at the same rate until either side encounters a large slope. At that point a specular reflection is detected and the width is reduced to a minimum value of 0.05 ns. When the window moves into a region of resonance, it expands to encompass the entire resonance until another specular reflection is encountered. The vertical axis is a plot of the spectrum within the window when the right side is at a given value of time (shown as the curve on the left for the largest time plotted). Specular reflections appear as dark stripes with wide bandwidth, while resonances appear as horizontal stripes. Thus, the substructure resonances are seen beginning to form after each specular reflection, and then finally progressing into two very strong body resonances in late time. This plot allows a visualization of the onset and behavior of both specular reflections and target resonances of all types.

Once there is an understanding of the complexity of each target response, it is not surprising that there are many ways to view the aspect dependence of the data. A very straightforward approach is to view the data as a three-dimensional plot of amplitude vs. aspect angle. This is shown in Figure 7 for the B-58 aircraft, measured from 0°-180° with a 0.9° step size. It is easily seen that both the early and late-time components are highly aspect dependent. By separating early and late times, more physical insight is provided. For instance, Figure 9 is a scattering plot showing the log amplitude of the response of the B-58 vs. aspect angle. Here the variation of the specular reflections are more easily seen. For example, at nose-on incidence (0°), the first reflection is from the nose, and later reflections come from the engine mounts, horizontal stabilizer, etc. As the aspect progresses toward wing-on (90°) the nose and tail reflection move inward to coincide with the fuselage, and the engine mounts move outward. This aspect dependent information can be accumulated and used to produce a spatial plot of an aircraft's specular points. For each spatial point  $(\rho', \phi')$  an accumulation over aspect angles is given through

$$\pi(\rho', \phi') = \int_0^{2\pi} f\left\{\left[\rho - 2\rho'\cos(\phi' - \phi)\right]/c\right\} d\phi, \quad (17)$$

where  $[\rho - 2\rho'\cos(\phi' - \phi)]/c$  is the time delay to the point  $(\rho', \phi')$ . Figure 10 shows the result for a 1:48 model TR-1, and an obvious image is created. Formula (17) is directly related to the time domain physical-optics imaging identity<sup>7</sup>.

Finally, the late-time data is most easily interpreted as a sum of body resonances with aspect independent natural frequencies and aspect dependent amplitudes and phases. By extracting these resonances using a genetic algorithm, a description of the aspect dependence is provided by plotting the variation of amplitude and phase vs. aspect angle. Figure 11 shows the modal amplitudes of the B-58 model. It is seen that the first dominant mode (perhaps a wing resonance) is very constant with aspect angle while the second mode (perhaps a fuselage resonance) shows a variation similar to thin wire structures.

#### 4. ACKNOWLEDGEMENT

This work is supported by the Office of Naval Research under Grant No. N00014-93-1-1272.

#### 5. REFERENCES

1. C. Phillips, P. Johnson, K. Garner, G. Smith, A. Shek, R.C. Chou and S. Leong, "Ultra-high-resolution radar development and test," in *Second Conference on Ultra-Wideband, Short-Pulse Electromagnetics*, New York, April 5-7, 1994.
2. Edward J. Rothwell, Kun-Mu Chen, Dennis P. Nyquist, Ponniah Ilavarasan, John E. Ross, Robert Bebermeyer, and Qing Li, "A general E-pulse scheme arising from the dual early-time/late-time behavior of radar scatterers," *IEEE Trans. on Ant. Propagat.*, vol. 42, no. 9, pp. 1336-1341, Sept. 1994.
3. J. Ross, P. Ilavarasan, E. Rothwell, R. Bebermeyer, K. M. Chen, D. Nyquist, and Q. Li, "Radar target discrimination using E-pulses with early-time and late-time responses," *IEEE AP-S International Symposium and URSI Radio Science Meeting*, Ann Arbor, MI, June 28-July 2, 1993.
4. M.A. Morgan, "Ultra-wideband impulse scattering measurements," *IEEE Trans. Ant. Propagat.*, vol. 42, no. 6 pp. 840-846, June 1994.
5. David E. Goldberg, *Genetic Algorithms*, Addison-Wesley, Reading, MA, 1989.
6. Lawrence Carin and Leopold B. Felsen, "Wave-oriented data processing for frequency- and time-domain scattering by nonuniform truncated arrays," *IEEE Antennas and Propagation Magazine*, vol. 36, no. 3, pp. 29-43, June 1994.
7. E.J. Rothwell, K.M. Chen, D.P. Nyquist and J.E. Ross, "Time-domain imaging of airborne targets using ultra wideband or short-pulse radar," *IEEE Trans. Ant. Propagat.*, vol. 43, no. 3, pp. 327-329, March 1995.

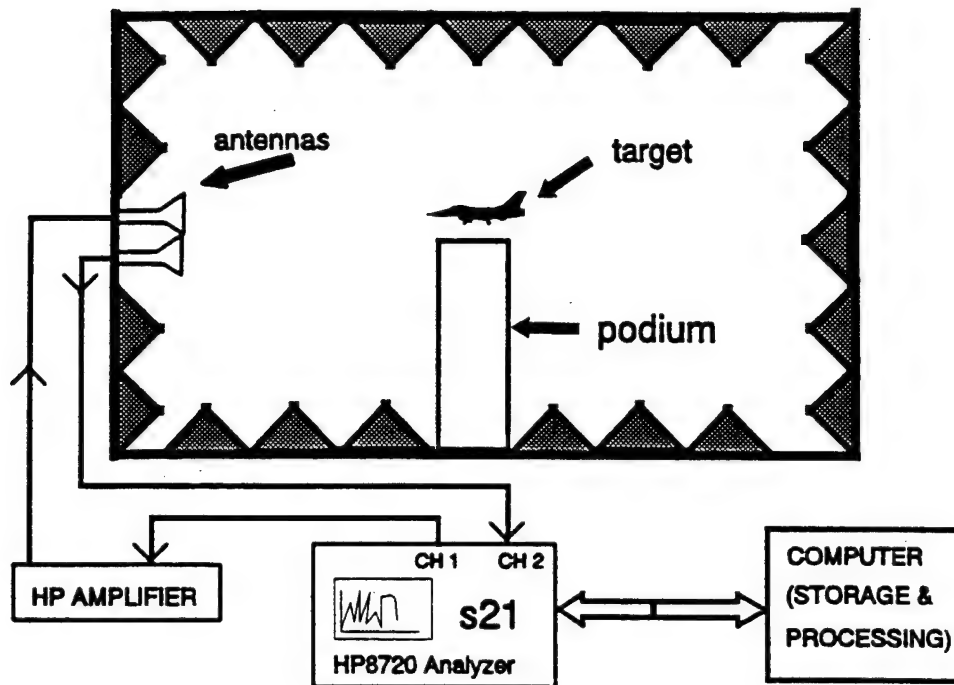


Figure 1. MSU ultrawide-band scattering range.

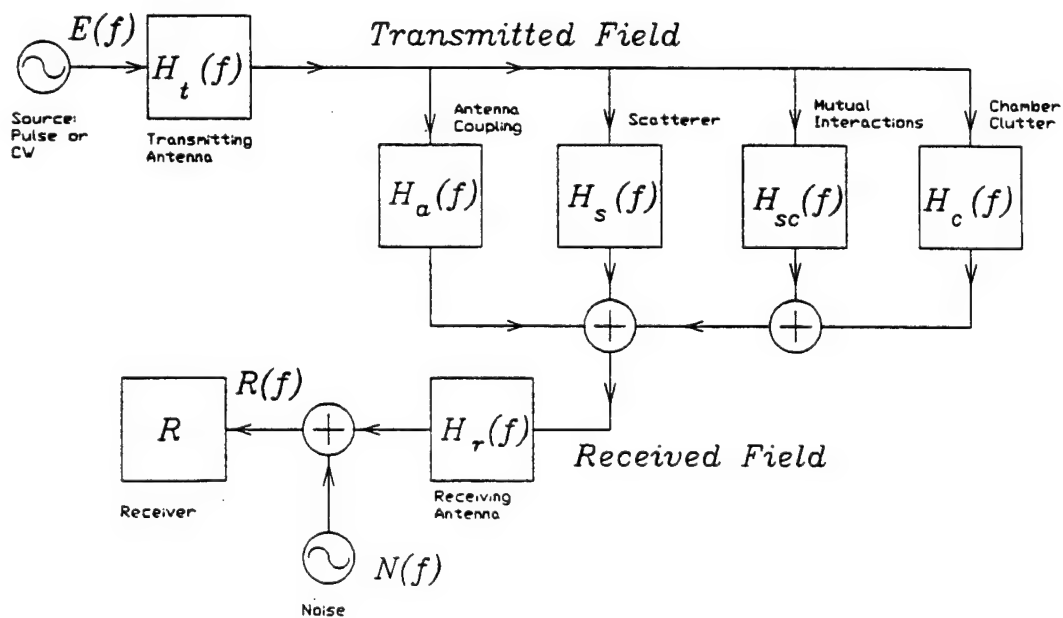
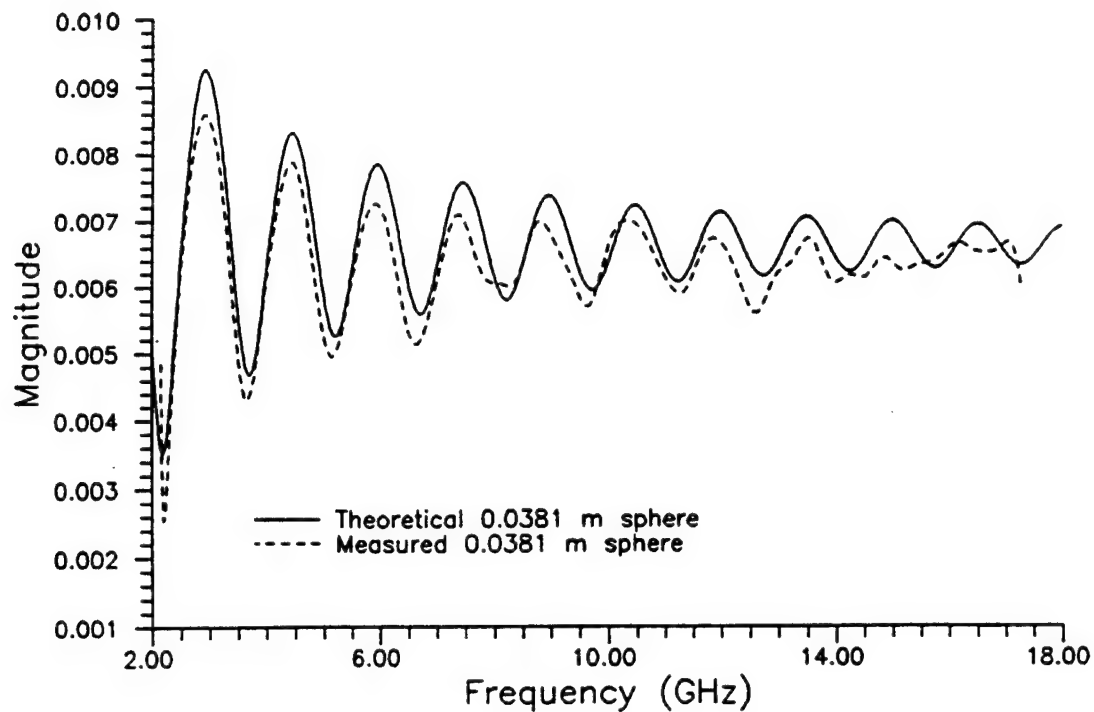
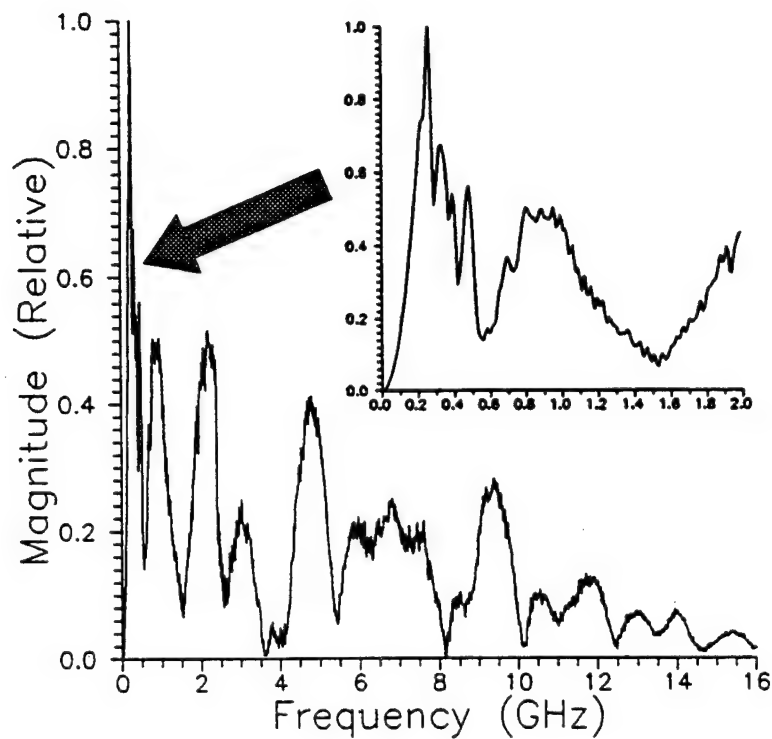


Figure 2. Block diagram model of measurement system.



**Figure 3.** Measured response of 0.0381 m diameter conducting sphere, and comparison with theory.



**Figure 4.** Spectral response of B-58 aircraft model. Inset shows expansion of low-frequency region. Wing-on (90°) incidence.

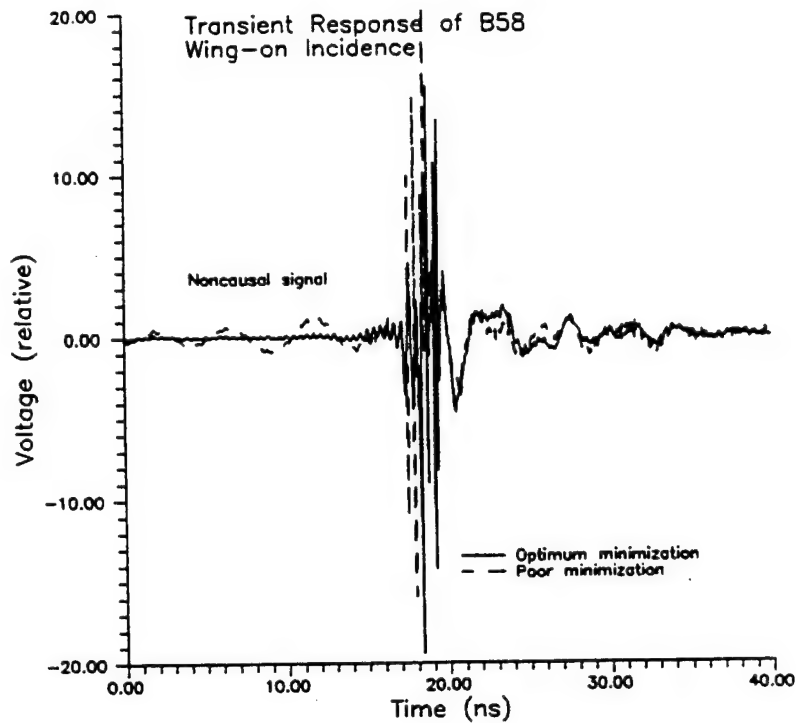


**Figure 5.** Transient response of B-58 showing early and late-time responses. Wing-on ( $90^\circ$ ) incidence.

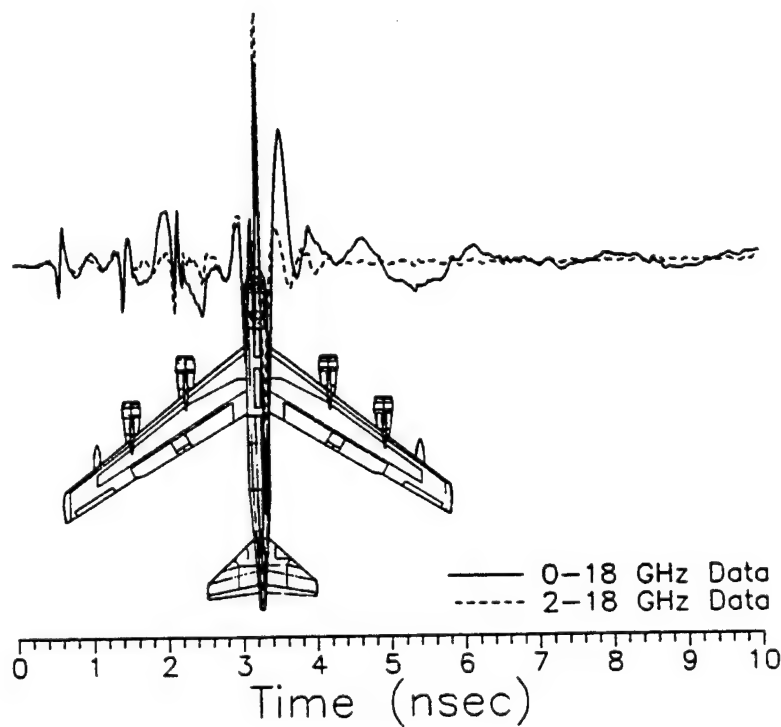


**Figure 6.** Transient response of B-52 showing specular reflections and substructure resonances. Wing-on ( $90^\circ$ ) incidence.

Transient Response Synthesized from 2-18 GHz Data

'b58b.dat' —

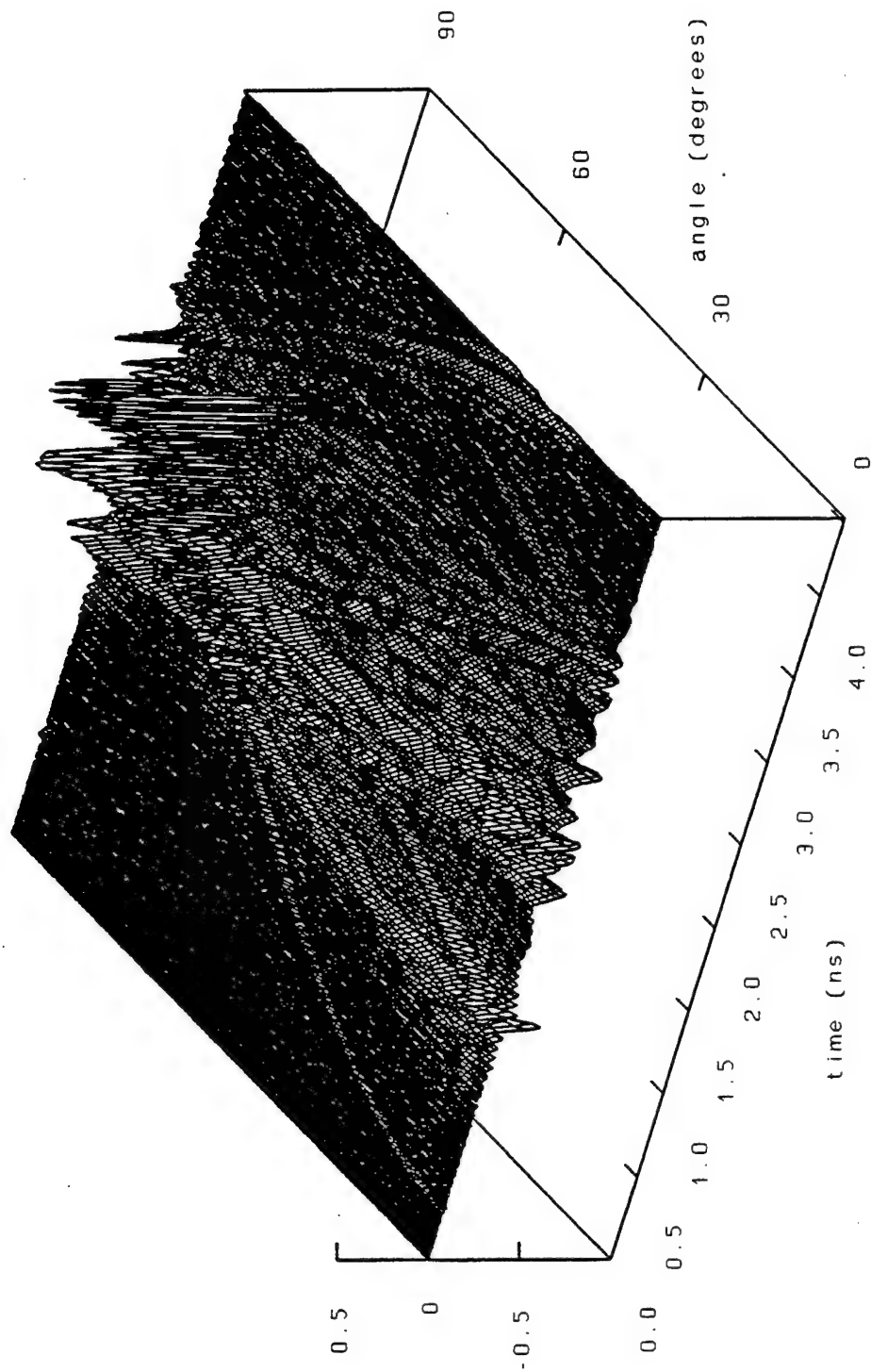
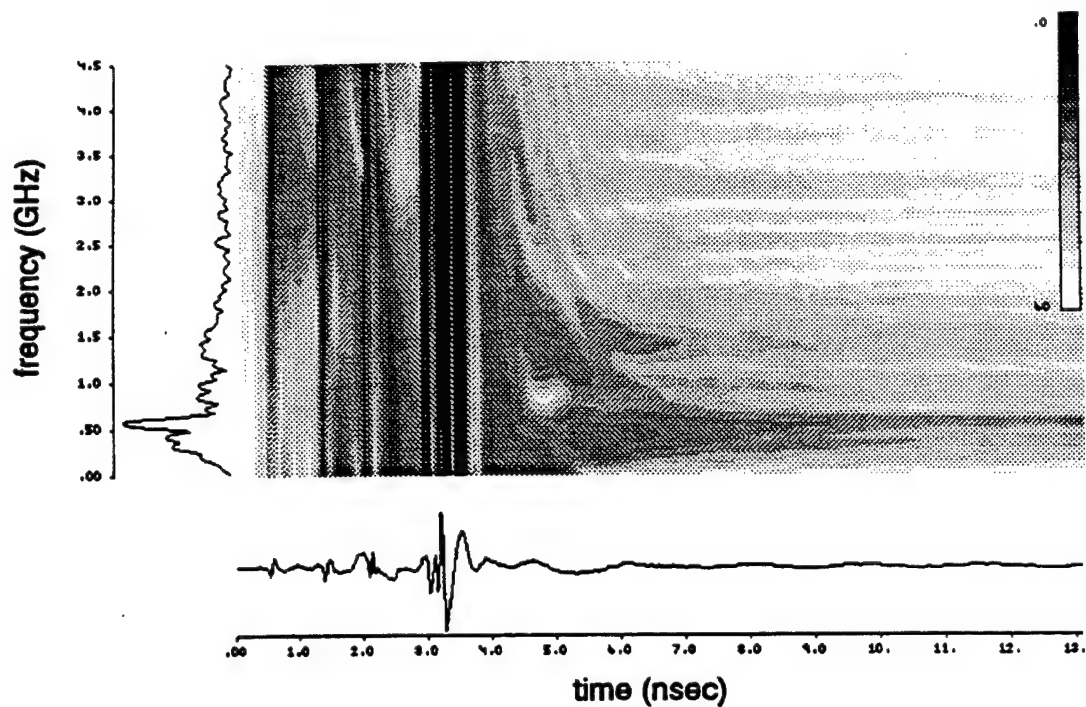
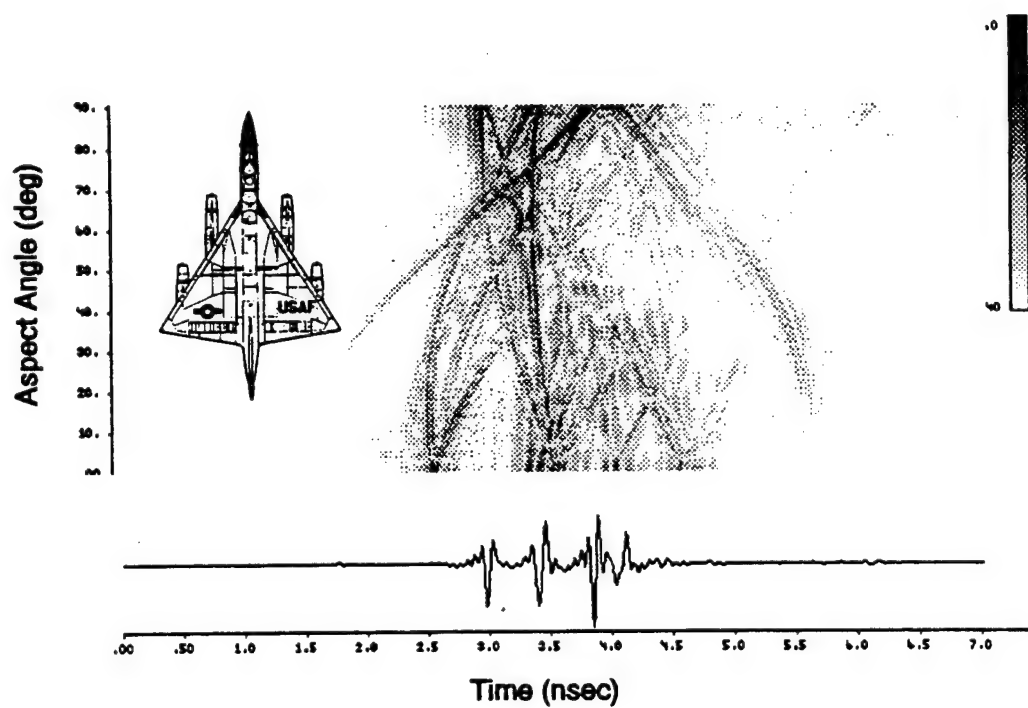


Figure 7. Transient response of B-58 as a function of aspect angle.



**Figure 8.** Frequency-time plot of transient B-52 response. Scale is in dB. Wing-on ( $90^\circ$ ) incidence.



**Figure 9.** Scattering plot of B-58 showing variation of transient response with aspect angle. Scale is in dB.



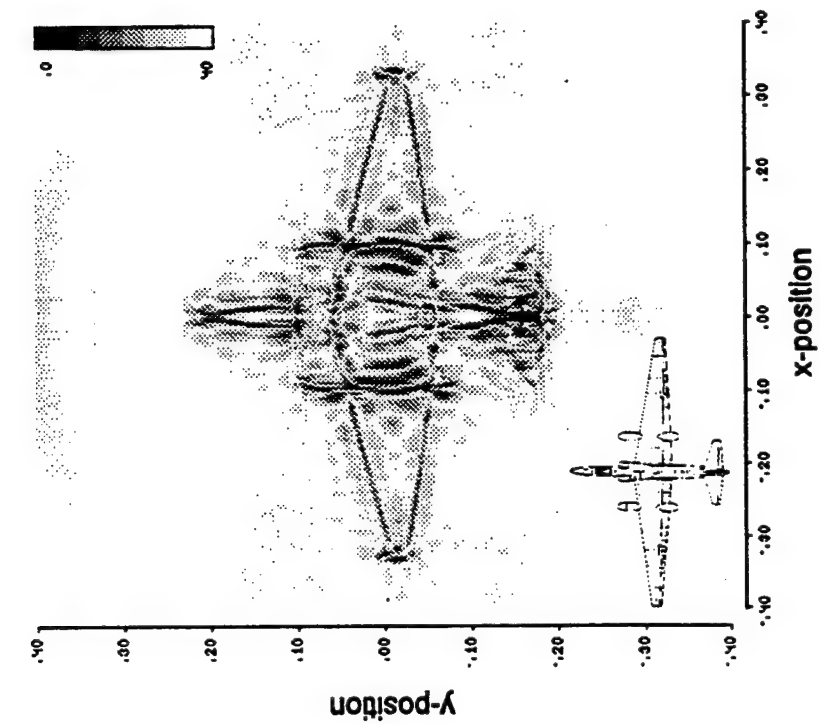


Figure 10. Image of TR-1. Scale is in dB.

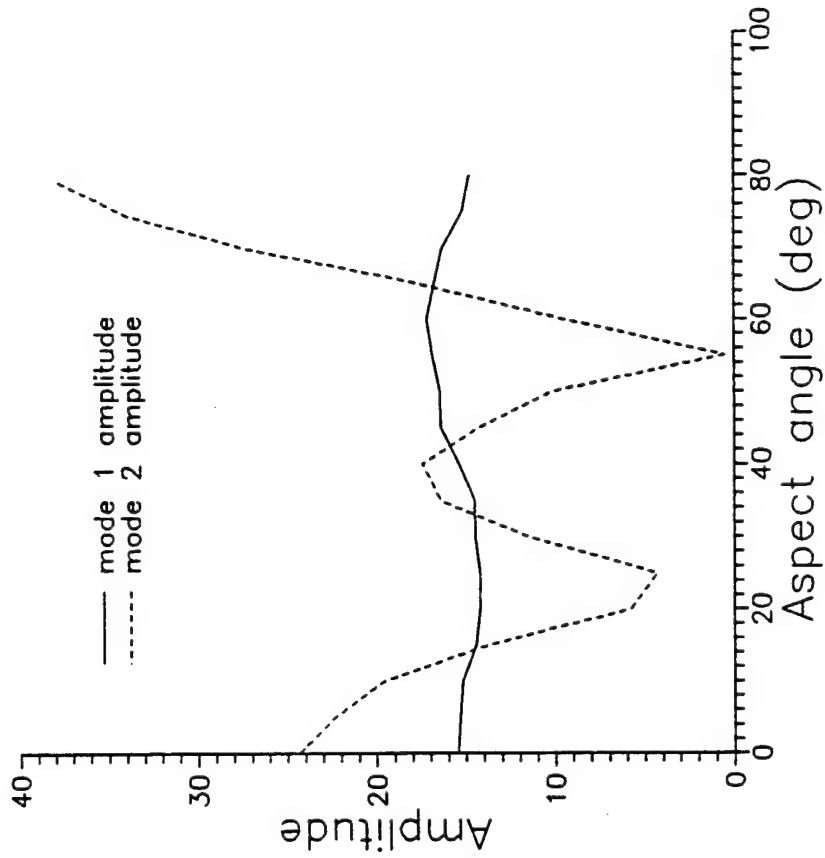


Figure 11. Variation in modal amplitudes of B-58 with aspect angle.

# Appendix 12

## Ultra-Wideband/Short-Pulse Radar for Target Identification and Detection -- Laboratory Study

K.M. Chen, E.J. Rothwell, D.P. Nyquist, R. Bebermeyer, Q. Li, C.Y. Tsai and A. Norman  
Department of Electrical Engineering  
Michigan State University  
East Lansing, MI 48824

**Abstract** - A laboratory study was conducted to investigate the schemes of radar target identification and detection using an ultra-wideband/short-pulse (UWB/SP) radar. In target identification, a correlation/wavelet transform scheme, a neural network technique and a time-domain imaging scheme were studied. To detect a target in a sea clutter environment, the E-pulse technique was utilized to minimize the sea clutter while enhancing the target response, thus facilitating its detection. It appears that a UWB/SP radar may provide higher resolution for target ID and more effective clutter suppression for target detection compared with conventional radars.

### 1. INTRODUCTION

We have undertaken a study in our laboratory at Michigan State University into various topics regarding the identification (ID) of complex targets and their detection in a sea clutter environment, using an ultra-wideband, short-pulse (UWB/SP) radar. In our experimental study, we have found that a UWB/SP radar can provide higher resolution for target ID and more effective clutter suppression for target detection compared with conventional radars. The baseband pulse used in our experiments has a temporal width in the order of 100 ps, or about one tenth of the dimension of our experimental target models. This short pulse has frequency components in the band 2-18 GHz.

A UWB/SP radar provides a unique capability for the identification of complex targets. When a target is illuminated by a short baseband pulse, the return consists of an early-time response which has a series of peaks representing the specular reflections from the scattering centers of the target, and a late-time response which represents the resonant response of the target. The early-time response can be used to identify the target if the locations and the transfer functions of the target scattering centers are known as functions of the aspect angle of the incident short pulse. We have developed various target ID schemes based on the early-time response, including a correlation/wavelet transform scheme and a neural network technique. If the early-time response of a target can be measured over a range of aspect angles, a sharp, clear target image can be created using a time-domain imaging scheme.

A UWB/SP radar can be used to detect targets in a severe clutter environment due to the significant difference in the short-pulse responses of the target and the environment; this allows the clutter to be suppressed. We have studied the case of a target airborne above a disturbed sea surface where the sea clutter overwhelms the target response. The E-pulse concept [1,2] can be used to minimize the sea clutter while at the same time enhancing the target response, thus increasing the probability of detection. We have also studied the detection technique based on separating the target response from the sea clutter by making use of the relative motion of the target with respect to the ocean wave. These schemes and laboratory test results will be briefly described.

### 2. TARGET IDENTIFICATION USING A UWB/SP RADAR

The interrogating baseband pulse used in our study, as shown in Fig. 1, has a temporal width of about 100 ps with frequency components covering the range of 2-18 GHz. When the short pulse illuminates a 1:48 scale model B-58 aircraft (63 cm fuselage length and 36 cm wingspan) over a range of aspect angles from 0°-90°, stepped in a 0.45° increment, the early-time responses produce the 3-D diagram shown in Fig. 2. It is seen that the early-time response of a complex target is strongly dependent on the illumination angle of the interrogating pulse.

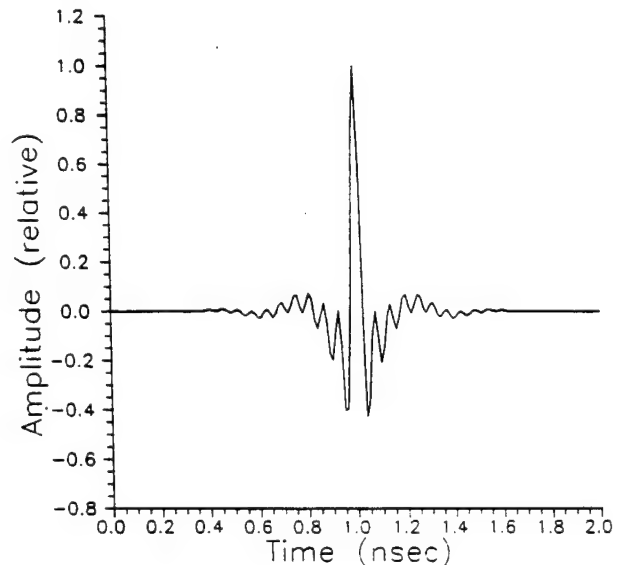


Figure 1. Incident short pulse waveform.

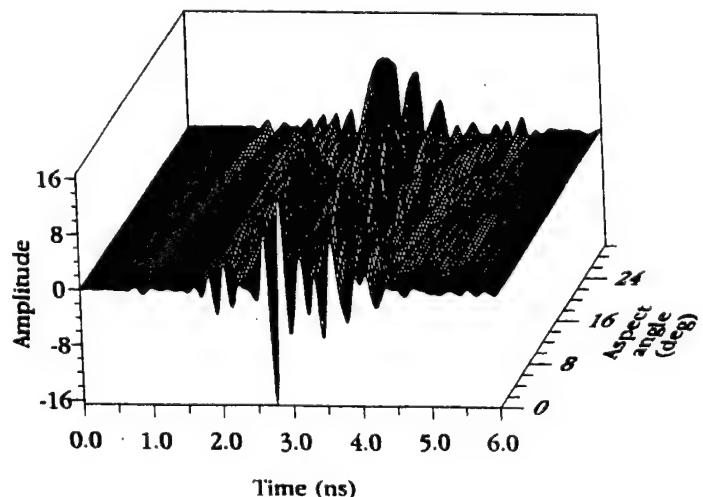


Figure 2. Early-time response of 1:48 scale B-52 aircraft.

Using sets of early-time responses of all relevant targets, we have developed various target ID schemes which include the correlation/wavelet transform technique, the neural network scheme, and the time-domain imaging technique. Brief descriptions of these schemes follow.

## 2.1. Correlation/Wavelet Transform Technique for Target Identification

Since the early-time response of a target is a strong function of the aspect angle, responses from many aspect angles are needed to perform target ID. If many different targets are to be discriminated, a burdensome amount of computer storage space is required. This difficulty can be overcome by using the sparse nature of the discrete wavelet transform [3,4] to compress the early-time data. For example, Fig. 3 shows the early-time response of the B-52 model measured at the nose-on ( $0^\circ$ ) aspect angle and sampled at 256 time points. However, using a 256-point Lemarie discrete wavelet transform [3], the wavelet spectrum of this response can be found as shown in Fig. 4. It is seen that only a small subset of the wavelet coefficients are significant. Figure 3 also shows the B-52 response reconstructed using only the 32 largest wavelet coefficients. With the early-time target responses for a range of aspect angles stored in terms of wavelet basis function amplitudes, a correlation of measured and stored waveforms provides an efficient means of target ID. The unknown target is identified with the target whose stored response produces the maximal (unity, for no noise) correlation.

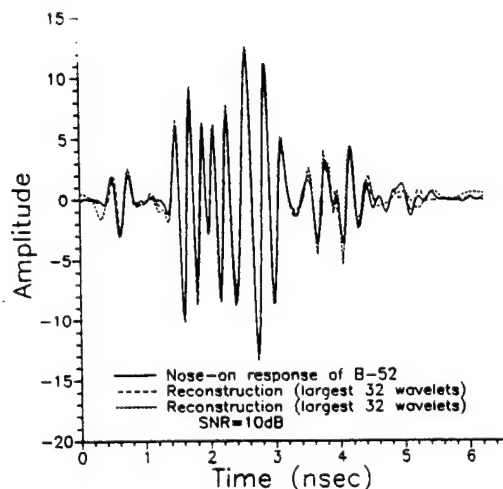


Figure 3. Nose-on ( $0^\circ$ ) response of B-52 aircraft model and 32 wavelet reconstruction.

As an example of target ID using wavelet-stored data, the early-time responses of five aircraft models -- B-52 (1:72 scale), B-58 (1:48), TR-1 (1:48), F-14 (1:48), and Mig-29 (1:48) -- were stored at 68 aspect angles between  $0^\circ$  and  $30^\circ$ . An identification scenario assumes that the  $18^\circ$  B-52 response arises from an unknown target. This response is correlated with the responses of all targets at all aspect angles, reconstructed from their stored, truncated wavelet spectra. The result, shown in Fig. 5, provides a correct identification since the largest correlation output arises from the B-52. Figure 6 shows that contaminating the measured target signal with white Gaussian noise at an SNR of 10 dB does not significantly reduce the identification capability of this technique.

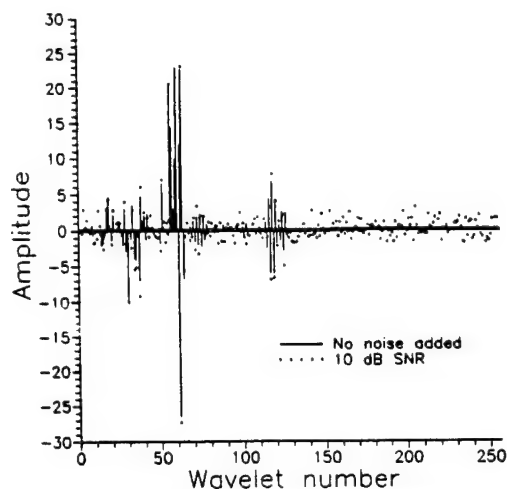


Figure 4. Wavelet spectrum of nose-on ( $0^\circ$ ) response of B-52 aircraft model.

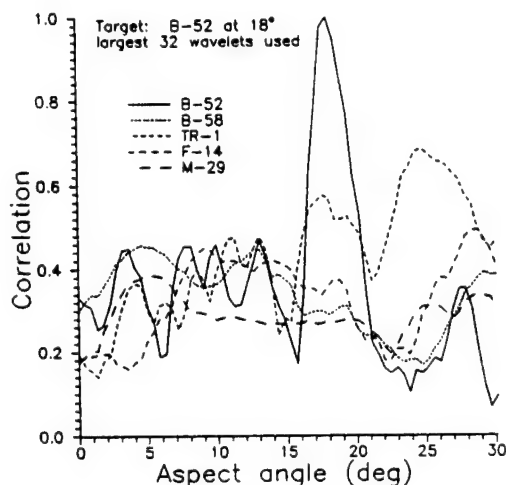


Figure 5. Maximum correlation of  $18^\circ$  B-52 response with responses from all targets. Target waveforms represented using 32 wavelets.

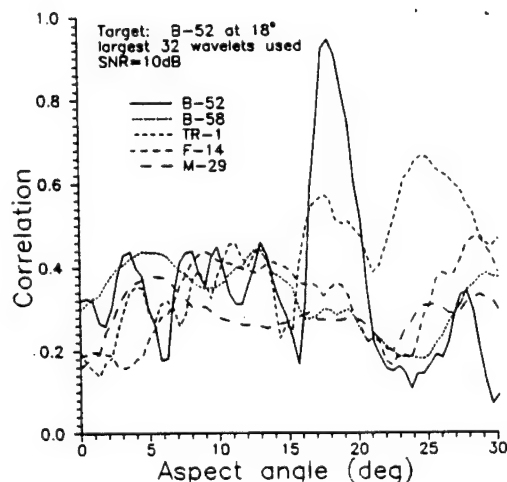


Figure 6. Maximum correlation of  $18^\circ$  B-52 noisy response with responses from all targets. Target waveforms represented using 32 wavelets. SNR = 10 dB.

## 2.2. Neural Network Techniques for Target Identification

Neural networks have great potential for storing and retrieving a large number of target signatures needed to perform aspect-dependent target identification. A number of neural network architectures for target ID have been simulated, including feed-forward networks trained using back-propagation, and Hopfield networks. Particularly good success has been obtained using correlation associative memories, including generalized inverse (GI) networks, exponential correlation associative memory (ECAM) networks, and cascades of these networks (ECAM-GI). The performance of a network using the ECAM cascaded with the generalized-inverse network (ECAM-GI) is shown in Fig. 7. This network was trained to recognize four targets (B-52, B-58, F-14 and TRI) each at 17 different aspect angles with a total of 68 patterns. Good performance is seen in this figure with nearly 100% correct identification at a SNR level of 5 dB.

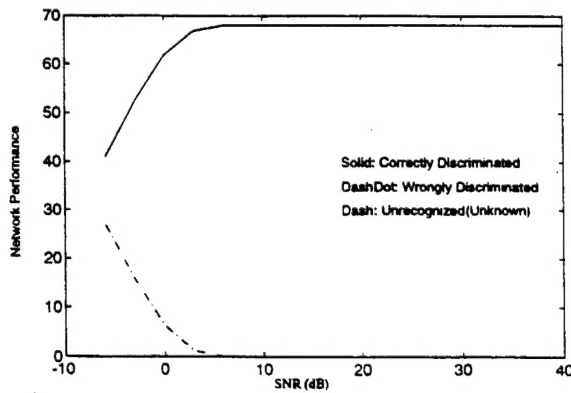


Figure 7. Performance of ECAM-GI cascaded networks trained to recognize four target models each at 17 aspect angles (total of 68 patterns).

More sophisticated networks have also been investigated, including recurrent dynamic correlation associative memory (RDM) networks [5,6]. The performance of a network using the RDM technique cascaded with the generalized-inverse method (RDM-GI) with fixed analog input is shown in Fig. 8 when it was trained to recognize the same patterns used in Fig. 7. Excellent performance is seen in this figure, with nearly 100% correct identification at SNR levels as low as -5 dB. This network not only has excellent performance, but also offers the flexible decision strategy and less computation scale space.

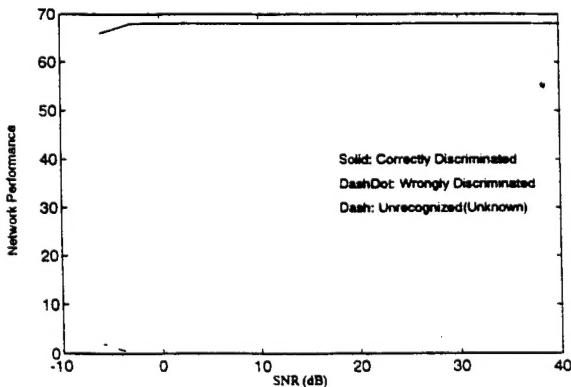


Figure 8. Performance of RDM-GI cascaded networks trained to recognize four target models each at 17 aspect angles (total of 68 patterns). Analog inputs used.

In a practical noise-limited situation, finding the same beginning response time used in training is very difficult. Therefore, the network must also store or train several time-shift neighborhoods of the time segment pattern for each aspect angle to increase tolerance for time-shifted patterns. This is impractical, since it dramatically reduces the network capacity. To overcome this difficulty, we have used spectral magnitude of the target response, which is time-invariant, as the network process information. The performance of a spectrum process RDM-GI cascade network with fixed analog input for the same 68 stored aspect patterns used in Figs. 7 and 8 is shown in Fig. 9. In this case, nearly 100% correct identification can be achieved at a SNR level of 0 dB. Although we used less information here than the time domain process, we have found this alternative process technique to be effective after some extra processes [7].

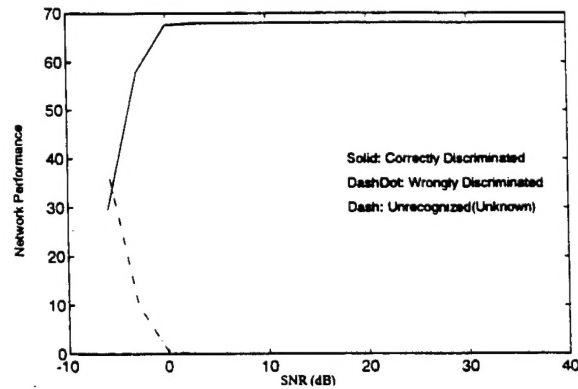


Figure 9. Spectrum process performance of RDM-GI cascaded networks trained to recognize four target models each at 17 aspect angles (total of 68 patterns). Analog inputs used.

## 2.3. Time-Domain Imaging Technique for Target Identification

The short-pulse response of a radar target provides significant information about the positions and strengths of scattering centers. If observations are made over a wide range of aspect angles, sufficient information is gained to obtain an image of the target.

Bojarski [8] proposed a simple inverse scattering identity based on the physical optics approximation. He showed that the characteristic function of a conducting scatterer (which is unity within the target geometry and zero elsewhere) is given by the three-dimensional inverse Fourier transform of the scattered field as a function of the incident plane-wave vector  $\vec{k}^i$ . If scattered field information is only available within a plane, then the two-dimensional inverse transform yields the thickness of the scatterer as a function of position in that plane.

In the MSU free-field scattering range, aspect angle variation is obtained by target rotation. It is thus convenient to write the inverse scattering identity in polar coordinates. The thickness is then shown to be proportional to the function

$$T_{\omega}(\vec{\rho}) = \text{Re} \left\{ \int_{\phi_1=0}^{2\pi} E^s(K_o, \phi_1) e^{-jK_o \rho \cos(\phi - \phi_1)} \frac{dK_o}{K_o} d\phi_1 \right\} \quad (1)$$

where  $\vec{\rho}$  is the position vector in the plane of the measurements,  $\phi_1$  is the plane wave incidence angle,  $E^s$  is the back-scattered field measured at frequency  $\omega$  and aspect angle  $\phi_1$ , and  $K_o = 2k_o = 2\omega/c$ .

By performing the integral over  $K_n$  and recognizing this as the temporal inverse transform, the thickness function is proportional to

$$T_r(\vec{\rho}) = \int_0^{2\pi} r\left(-\frac{2\rho}{c} \cos(\phi - \phi_1), \phi_1\right) d\phi_1 \quad (2)$$

where  $r(t)$  is the time-integral of the inverse transform of  $E^s$ , i.e., the ramp response of the target. This time-domain physical optics inverse scattering identity has a very clear physical interpretation.

The quantity  $-2\rho \cos(\phi - \phi_1) / c$  is the two-way transit time from the origin of coordinates to the point  $(\rho, \phi)$  along a plane wave incident at angle  $\phi_1$ . Thus, the integral (2) is the sum over all aspect angles of the ramp response value corresponding to scattering from the point  $(\rho, \phi)$ .

It is possible to enhance the edges of the image by merely using the impulse response (inverse transform of  $E^s$ ) rather than the ramp response, since this corresponds to a derivative of the thickness response. This has been done in the examples shown in Figs. 10 and 11. A distinct image of each target results, with the edges of the fuselage, wings, etc., being clearly displayed. Note that the physical optics approximation does not accommodate the shadowed regions, and thus hidden edges such as the rear of the forward wings are not strongly present.

It seems that the target images created by a UWB/SP radar are sharper and clearer than those created by other microwave imaging techniques with other types of radars.

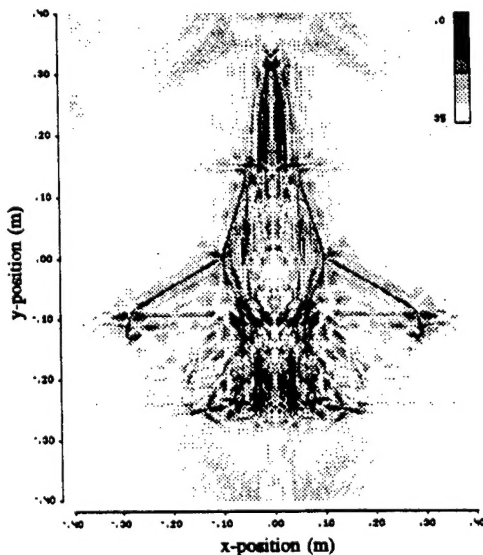


Figure 10. Image of F-14 aircraft model found using time-domain, physical optics inverse scattering identity. 2-18 GHz band, 201 aspect angles. Gray scale is in dB.

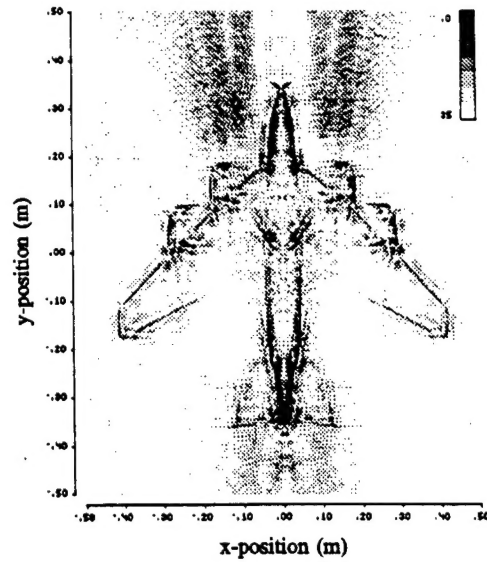


Figure 11. Image of B-52 aircraft model found using time-domain, physical optics inverse scattering identity. 2-18 GHz band, 201 aspect angles. Gray scale is in dB.

### 3. TARGET DETECTION IN A SEA CLUTTER ENVIRONMENT USING A UWB/SP RADAR AND THE E-PULSE TECHNIQUE

The detection of a target near the sea surface using conventional radar is difficult because the target response is usually overwhelmed by the strong sea clutter signal. This difficulty may be reduced if a UWB/SP radar is used, because the sea clutter created by a short pulse is a periodic series of peaks which can be suppressed using the E-pulse technique [1,2]. On the other hand, if the short pulse is properly shaped the target response can be enhanced, and thus the probability of target detection is increased.

When a short pulse illuminates a sea surface which is represented by a periodic ocean wave, the backscattered field (sea clutter) consists of a periodic series of peaks representing the reflections from the ocean wave crests. We have theoretically calculated the sea clutter created by a short pulse illuminating two models of the sea surface: (1) a sinusoidally-varying perfectly conducting surface, and (2) a sinusoidal interface between air and the imperfectly conducting sea. The theoretical results for the first model are shown in Fig. 12 and for the second model in Fig. 13.

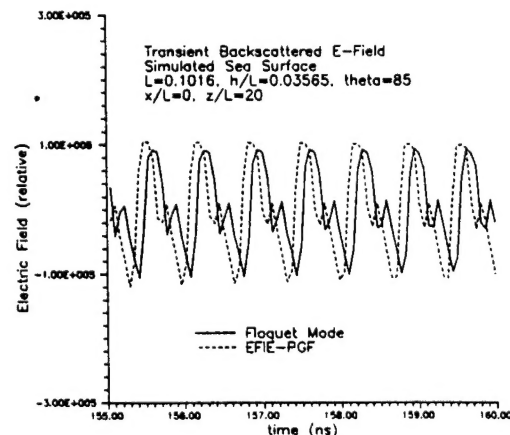


Figure 12. Transient backscattered H-field from simulated sea surface for TE excitation.

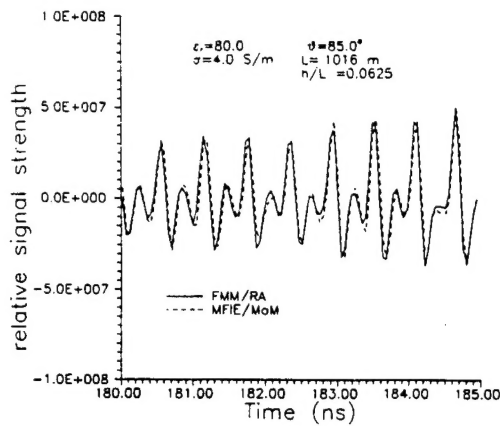


Figure 13. Comparison of Rayleigh and MFIE-PGF methods for computing backscattered transient response of imperfectly conducting surface.

The physical dimensions of the sea surface model are those of the scale model used in our experiment. The incidence angle of the short pulse illumination is  $5^\circ$  from grazing. For the imperfectly conducting sea surface, a conductivity of 4 S/m and a relative permittivity of 80 were used. From the results shown in Figs. 12 and 13, the sea clutter created by a short pulse illuminating a disturbed sea is a series of peaks representing the specular reflections from the ocean wave crests. Note that because the illumination of the sea surface occurs over an extremely short period of time, the random nature of the ocean wave is neglected.

To demonstrate the E-pulse scheme to detect a target in a sea clutter environment, we have constructed a conducting sea surface by milling a sinusoidal surface into a styrofoam block (48 x 22 x 2.5 inches, 11 wave crests) and attaching aluminum foil to the surface, as shown in Fig. 14. The ocean wavelength is 4 inches and the Ocean wave height is 1 inch. A 2 inch long missile is placed 1.5 inches above the sea surface.

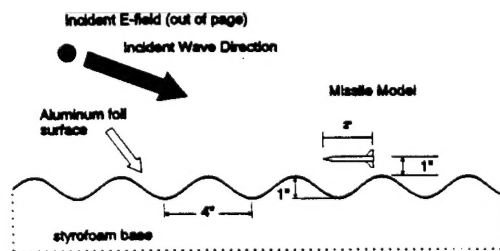


Figure 14. Conducting periodic surface with missile model.

When this sinusoidal surface with a missile present is illuminated by a short pulse, the measured transient response is shown in Fig. 15, where the target response is superimposed with the measured clutter in the middle of the response. Note that the large response at the beginning is the reflection from the front edge of our finite sea surface model, and it should be ignored.

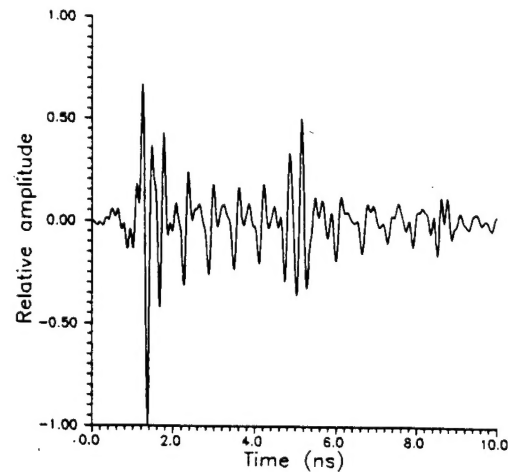


Figure 15. Measured transient response of sea surface with missile.

Based on the measured transient response of Fig. 15 and using the E-pulse technique, a "clutter-reducing transmit waveform" (CRTW) can be synthesized as shown in Fig. 16. When this CRTW is convolved with the sea clutter, the output is nearly zero (solid line in Fig. 17). If this same CRTW is convolved with a clutter plus missile response, the output (dotted line in Fig. 17) reveals the clear presence of the missile within the suppressed sea clutter. It is evident that if an interrogating pulse such as the CRTW can be transmitted, the return response from the sea surface with a target present will be like that shown in Fig. 17.

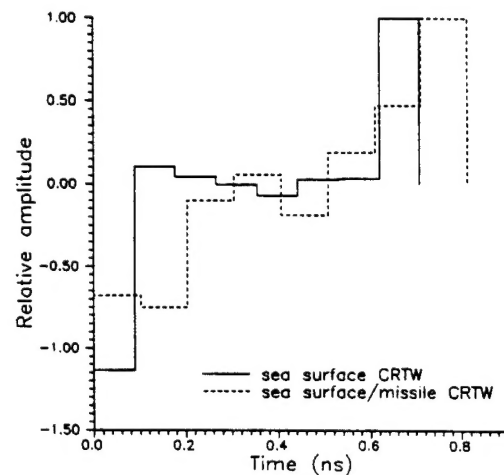


Figure 16. Clutter reducing transmit waveforms for sea surface with and without missile.



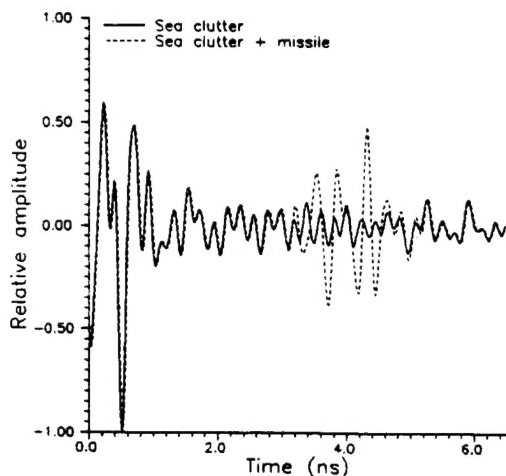


Figure 17. Simulated response of the sea surface, with and without missile, to the sea surface CRTW.

#### 4. SEPARATION OF TARGETS FROM CLUTTER USING UWB/SP RADAR AND RELATIVE TARGET MOTION

A UWB/SP radar can be used to detect targets which move with different velocities than the ocean waves.

Consider a situation where a fast-moving target (e.g., a missile) and a stationary target (e.g., a periscope) are in the presence of a slow-moving ocean wave. If the sea surface is interrogated by a short EM pulse, the radar return will consist of a periodic series of peaks (the sea clutter from the ocean wave) and two peaks representing responses of the moving and stationary targets. When another interrogating pulse is sent out after a time interval, the new radar return will have a series of peaks shifted slightly due to the slow moving ocean wave, while the peak of the moving target will have shifted a much larger amount, and the peak of the stationary target will not have shifted at all. With repetitive interrogating pulses and each subsequent radar return recorded, a diagram such as that shown in Fig. 18 can be constructed. The horizontal axis is a fast time scale (ns) representing the location of the targets and the ocean wave crests. The vertical axis is a slow time scale (s) representing the time when the radar return is received. This diagram clearly shows the traces of moving and stationary targets and ocean wave crests. Using this relative motion scheme, targets can be separated from clutter, thus facilitating their detection.

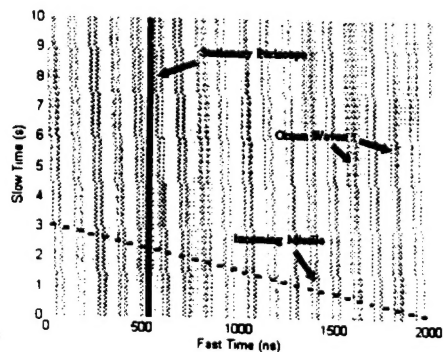


Figure 18. Traces of targets and ocean wave crests constructed using radar returns from repetitive interrogating EM pulses. Ocean wave velocity: 1 m/s; missile velocity: 100 m/s.

#### REFERENCES

- [1] E. Rothwell, K.M. Chen, D.P. Nyquist, P. Ilavarasan, J. Ross, R. Bebermeyer and Q. Li, "Radar target identification and detection using short EM pulses and the E-pulse technique," *Ultra-Wideband, Short-Pulse Electromagnetics*, Edited by H. Bertoni, et. al., Plenum Press, pp. 475-482, 1993.
- [2] E. Rothwell, K.M. Chen, D.P. Nyquist, P. Ilavarasan, J. Ross and R. Bebermeyer, "A general E-pulse scheme arising from the dual early-time/late-time behavior of radar scatterers," *IEEE Trans. on Antennas and Propagation*, vol. 42, no. 9, pp. 1336-1341, September 1994.
- [3] W.H. Press, S.A. Teukolsky, W.T. Vetterling and B.P. Flannery, *Numerical Recipes in Fortran*, 2nd ed., Cambridge University Press, 1992, chap. 13.
- [4] E. Rothwell, K.M. Chen, D.P. Nyquist, J. Ross and R. Bebermeyer, "A radar target discrimination scheme using the discrete wavelet transform for reduced data storage," *IEEE Trans. on Antennas and Propagation*, vol. 42, no. 7, pp. 1033-1037, July 1994.
- [5] Tzi-Dar Chiueh and R.M. Goodman, "Recurrent Correlation Associative Memories," *IEEE Trans. Neural Networks*, vol. 2, pp. 275-284, March 1991.
- [6] Y. Kamp and M. Hasler, *Recursive Neural Networks for Associative Memory*, John Wiley & Sons, 1990.
- [7] C.Y. Tsai, E. Rothwell and K.M. Chen, "Target discrimination using neural networks with time domain or spectrum magnitude response," to appear in *Journal of Electromagnetic Waves and Applications*, 1995.
- [8] N.N. Bojarski, "A Survey of the Physical Optics Inverse Scattering Identity," *IEEE Trans. Ant. Propagat.*, vol. AP-30, no. 5., pp. 980-989, September 1982.

#### ACKNOWLEDGEMENTS

This work was supported by the Office of Naval Research under grant N00014-93-1-1272, by the Naval Command, Control and Ocean Surveillance Center under Contract N66001-91-C-6019, and by the ThermoTrex Corporation under purchase order No. 22068.